Biochemomechanical model of aneurysm growth

Horvat, Nino

University of Zagreb

Faculty of Mechanical Engineering and Naval Architecture

Nino Horvat

BIOCHEMOMECHANICAL MODEL OF ANEURYSM GROWTH

DOCTORAL DISSERTATION

Zagreb, 2022

University of Zagreb

Faculty of Mechanical Engineering and Naval Architecture

Nino Horvat

BIOCHEMOMECHANICAL MODEL OF ANEURYSM GROWTH

DOCTORAL DISSERTATION

Supervisor:

Prof. Igor Karšaj, PhD

Zagreb, 2022

Sveučilište u Zagrebu

Fakultet strojarstva i brodogradnje

Nino Horvat

BIOKEMIJSKO-MEHANIČKI MODEL RASTA ANEURIZME

DOKTORSKI RAD

Mentor:

prof. dr. sc. Igor Karšaj

Zagreb, 2022.

BIBLIOGRAPHY DATA

UDC:	616.13-007.64:616.136
Keywords:	abdominal aortic aneurysm, intraluminal thrombus, growth and remodeling, fluid-solid growth, fiber dispersion
Scientific area:	Technical sciences
Scientific field:	Mechanical engineering
Institution:	Faculty of Mechanical Engineering and Naval Architecture
Thesis supervisor:	Prof. Igor Karšaj, PhD
Number of pages:	35
Number of pages (in total):	165
Number of figures:	21
Number of tables:	1
Number of references:	75
Date of examination:	25.10.2022.

Thesis defense committee:

Prof. Zdravko Virag, PhD - Chairman of the defense commission

Prof. Željko Tuković, PhD - member

Prof. Gerhard A. Holzapfel, PhD - member

Archive:	Faculty of Mechanical Engineering and Naval Architecture

ACKNOWLEDGMENTS

I want to express my sincere gratitude to my mentor and supervisor, Professor Igor Karšaj, for the given opportunity, continuous support and guidance, and for always looking out for my best interest. Furthermore, I would like to thank my friend and colleague Lana Virag for all the help with my research. She was like a second mentor to me, and without her, this work would not be at this level. Many thanks go to my colleagues in my faculty, and to all my friends. Our discussions, lunch, and coffee breaks always made my day more exciting and fulfilling.

I want to thank Professor Gerhard A. Holzapfel for his collaboration on my first two journal articles and for all the help and suggestions he gave me. Also, I would like to thank Professor Jay D. Humphrey for the valuable and inspirational conversations during our meetings at conferences and summer schools. I would also like to thank Professor Seungik Baek, Byron Zambrano, and all the research group members at Michigan State University for their warm welcome and help with my research during my two visits.

Furthermore, I would like to express my sincere gratitude to my family for the unconditional support they gave me throughout my education and entire life. I owe a great deal to my girlfriend Nikolina for always being there for me and tolerating my long working hours. I will always be extremely grateful for all the love, support, and encouragement she gives me.

Nino Horvat

Zagreb, May 2022

SPECIAL ACKNOWLEDGMENT

I wish to express my sincere gratitude to the Croatian Science Foundation for supporting the research conducted in this thesis through the project "BioChemoMechanical Modeling of Aneurysmal Growth" (IP-2014-09-7382, I. Karšaj) and the project Training of New Doctoral Students (DOK-2015-10-3164).

Nino Horvat

Zagreb, May 2022

ABSTRACT

An abdominal aortic aneurysm (AAA) is a local and irreversible dilatation of the aorta caused by an imbalance in production and degradation of the extracellular matrix. It has a high mortality rate, and it is common among the elderly, especially men, with a prevalence rate estimated between 1 and 9%. Most AAAs develop an intraluminal thrombus (ILT), i.e., a blood clot attached to the inner aortic wall. The role of ILT in AAA evolution remains controversial. On the one hand, it decreases peak wall stress, but on the other hand, it biochemically degrades and weakens the wall. To improve our understanding of the disease and our capabilities for predicting rupture, growth and remodeling (G&R) models of AAA were developed. However, in the present literature, there is still a lack of G&R models that consider the biochemomechanical effect of ILT, not to mention an absence of models that determine thrombus deposition based on hemodynamics analyses.

Therefore, this doctoral thesis aimed to develop a comprehensive fluid-solid growth (FSG) numerical model of AAA that could unite the G&R model of an aortic wall, the ILT deposition model based on hemodynamic analysis, and models describing biochemical and biomechanical interaction between the ILT and the aortic wall. The FSG model was developed in several stages. Each stage was tested, verified with clinical observation, and used to further study AAA progression. In the first stage, a 3D constrained mixture G&R theory was implemented into a finite element program (FEAP). FE implementation enabled the simulation of more realistic aneurysm geometries (e.g., axisymmetric and asymmetric fusiform AAAs). Next, an algorithm for adding finite elements of the new ILT layers during G&R simulation was developed and programmed into FEAP. During the deposition of new ILT layers, the algorithm defines node coordinates, element connectivity, boundary condition, connection to the underlying surface, and loading.

The algorithm was first developed to add an ILT at predefined luminal radii. Since it is believed that thrombus formation and its further deposition depend primarily on hemodynamics, the logical next step was to couple the ILT deposition algorithm and the hemodynamics. Hemodynamic analyses (i.e., computational fluid dynamics (CFD) analyses of blood flow) are performed in OpenFOAM, and time-averaged wall shear stress (TAWSS) is used to predict the location of new ILT layer deposition. Due to large differences in time scales (seconds for hemodynamics analyses, days for G&R analyses), CFD is loosely coupled with the ILT deposition algorithm and the G&R model. In other words, CDF analyses are run

every several G&R times steps to check whether TAWSS values are below the threshold, i.e., to investigate whether the thrombus layer would deposit.

Finally, in the last stage, the G&R model in FEAP was extended with the biochemomechanical model of ILT. This means that the degradation of proteins in the wall is not described by a predefined spatiotemporal function but depends on protease distribution. In the finalized FSG model, during every step in the G&R analysis of the wall and ILT, the biochemical model runs separate 3D FEM analyses to calculate enzyme concentration in every point of the AAA model.

The developed FSG model can describe a rather realistic AAA behavior, deposition of thrombus, and its biochemomechanical influence on the aortic wall. Obtained results agree with clinically observed phenomena, and they offer great insight into the complex effect of ILT on AAA evolution.

Keywords: abdominal aortic aneurysm, intraluminal thrombus, growth and remodeling, fluid-solid growth, fiber dispersion

PROŠIRENI SAŽETAK (Extended Abstract in Croatian)

Aneurizma abdominalne aorte (AAA) je lokalno i trajno proširenje infrarenalne abdominalne aorte uzrokovano neravnotežom u proizvodnji i razgradnji konstituenata izvanstaničnog matriksa. AAA se često pojavljuje među starijom populacijom te uzrokuje od 1 do 3% smrti kod muškaraca starosti 65 do 85 godina u razvijenijim zemljama. Procjenjuje se da je prevalencija od 1,3 do 8,9% kod muškaraca te od 1 do 2,2% kod žena, [1]. Aneurizma raste kroz duži period od nekoliko desetaka godina, a do rupture, koja ima vrlo visoku stopu smrtnosti, dolazi naglo kada naprezanja u stijenci aorte prijeđu njenu čvrstoću.

Patogeneza AAA još uvijek nije u potpunosti razjašnjena, međutim, postoji veliki broj bioloških, kliničkih, histoloških i mehaničkih podataka o ovoj bolesti. Primarni rizični faktori uključuju spol, starost, pušenje i visoki krvni tlak. Unatoč znatnom napretku u posljednjih dvadesetak godina u području numeričkog modeliranja (pregled modela sumiran u [2] i [3]), ishod bolesti (ruptura, stabilizacija ili kontinuirani rast) i dalje nije moguće točno i pouzdano predvidjeti. Liječenje AAA svodi se na operativni zahvat, a odluka liječnika o tretmanu još uvijek se donosi na osnovi jednostavnih kriterija: veličine aneurizme (obično kad najveći promjer dosegne 5 do 5,5 cm) ili brzine rasta koja često nije dostupna (obično kad povećanje najvećeg promjera prekorači 0,5 do 1 cm u godini dana). Veličina aneurizme nije pouzdan kriterij jer do rupture dolazi i kod manjih aneurizmi, dok s druge strane postoje velike aneurizme koje ostaju stabilne kroz duže periode, [4], [5]. Ta činjenica naglašava potrebu za dodatnim alatima koji bi povećali razumijevanje ove bolesti, a jedna od skupina alata koja definitivno može pomoći su računalne simulacije temeljene na numeričkim modelima AAA.

Sve AAA veće od 6 cm, kao i većina manjih, sadrže intraluminalni tromb (ILT), [6], [7]. Tromb je krvni ugrušak prilijepljen na unutarnju stijenku aorte, a sastoji se od fibrinske strukture s upletenim krvnim stanicama (prvenstveno eritrocitima i leukocitima). Uloga tromba u evoluciji aneurizme je i dalje kontroverzna. S jedne strane tromb služi kao mehanička zaštita i smanjuje opterećenje na stijenku aorte, dok s druge strane proteolitičko djelovanje njegovog luminalnog sloja razgrađuje i dodatno oslabljuje stijenku [8], [9]. Stoga je vrlo bitno razviti nove ili unaprijediti postojeće numeričke modele kako bi se mogli otkriti i ispitati kompleksni utjecaji ILT-a na progresiju AAA.

Primarni cilj ovog rada je razvoj realističnog numeričkog modela s kojim bi se mogao opisati nastanak i razvoj AAA. Za realistični opis aneurizme, potrebno je razmotriti tri glavna

aspekta koja uključuju: rast i remodeliranje stijenke aorte, strujanje krvi, te stvaranje tromba i njegov biokemijsko-mehanički utjecaj na stijenku aorte. Dosadašnji modeli bavili su se jednim aspektom ili kombinacijom dvaju, međutim ne postoji 3D model koji bi obuhvatio sva tri aspekta te ih spojio u jednu cjelinu. U nastavku je dan kratki pregled literature i postojećih numeričkih modela vezanih uz modeliranje krvih žila i AAA.

Pregled literature i postojećih numeričkih modela AAA

Stijenka aorte sastoji se od tri sloja: intime, medije i adventicije. Svaki od tih slojeva sadrži različite udjele tri strukturalno najbitnija konstituenta: elastina, kolagena i glatkih mišićnih stanica. Zbog složene strukture, aktivnog odaziva glatkih mišićnih stanica, nelinearnog i anizotropnog ponašanja konstituenata te njihove kontinuirane proizvodnje i razgradnje, numeričko modeliranje rasta i promjene strukture (eng. *growth and remodeling*, G&R) aorte vrlo je kompleksno.

Prvi G&R modeli fokusirali su se na matematičko opisivanje kinematike rasta mekih tkiva bez razmatranja temeljnih procesa koji uzrokuju sam rast. Taj pristup predstavili su Rodriguez et al. [10], a u kasnijim radovima pristup je nadograđen za opisivanje adaptacije krvnih žila na promjene krvnog tlaka i protoka, [11]–[14].

Humphrey i Rajagopal [15] 2002. godine predlažu fundamentalno drugačiji pristup koji se fokusira na opisivanje promjena pojedinih konstituenata i izvanstaničnog matriksa kao posljedice promjene mehaničkih i biokemijskih podražaja. Na taj način, rast mekih tkiva (npr. krvih žila) nije direktno propisan već je posljedica spomenutih promjena. Uz to, predlažu teoriju spregnutih smjesa po kojoj je više različitih konstituenata, proizvedenih u različitim trenucima, spojeno u jednu cjelinu, tj. smjesu (npr. *in vivo* arteriju), unutar koje konstituenti mogu imati različita naprezanja, ali su im deformacije ograničene i jednake deformaciji cjelokupne smjese. Mnoštvo daljnjih radova temeljilo se na ovom principu i do danas to je jedan od najznačajnih pristupa u modeliranju mekih tkiva. Nekih od tih radova uključuju membranske modele za opisivanje ponašanja cerebralnih aneurizmi [16], [17] i bazilarnih arterija [18]. Iako su ti modeli limitirani na 2D membransko stanje naprezanja, daju dobar uvid u mehanizme rasta i promjene strukture (npr. ovisnost o naprezanju te koncentraciji vazodilatatora i vazokonstriktora).

Prvi G&R model koji opisuje rast AAA predstavili su Watton et al. u [19], a u kasnijem radu [20] korištenjem tog modela ispitali su utjecaj materijalnih parametara na rast AAA. Utjecaj materijalnih parametara ispitivali su i Wilson et al. [21], [22] pomoću G&R modela

implementiranog u membranske konačne elemente. Odmak od membranskih modela napravili su Karšaj et al. [23], [24] razvojem 3D G&R numeričkog model s primjenom na adaptacije krvnih žila na promjene u krvnom tlaku i protoku. Horvat et al. [25] kasnije rade implementaciju tog modela u 3D konačne elemente što omogućuje odmak od cilindričnih modela i simuliranje složenije geometrije fuziformnih AAA.

Cyron et al. [26] predstavljaju novi pristup homogenizirane spregnute smjese koji pokušava spojiti numeričku efikasnost kinematskih modela sa mikrostrukturalnom osnovom klasičnih modela temeljenih na teoriji spregnutih smjesa. Kasnije Braeu et al. [27] rade implementaciju homogeniziranog modela u 3D konačne elemente te analiziraju rast AAA.

Intraluminalni tromb je sastavni dio većine AAA. Inzoli et al. [28] prvi su predložili hipotezu da tromb služi kao mehanički štit i da smanjuje naprezanja u stijenci aorte. Niz kasnijih studija potvrdio je tu tezu, [6], [29], [30]. Mehanička svojstva tromba dobro su dokumentirana u radu [31] gdje je nakon provedenih eksperimentalnih mjerenja predložen jednostavni linearni model za modeliranje tromba. Kasniji radovi s eksperimentalnim mjerenjima [32], [33] predlažu izotopni materijalni model temeljen na funkciji energije deformiranja, dok Tong et al. [34] prvi rade dvoosne testove te predlažu anizotropni konstitutivni materijalni model. Uz mehanički utjecaj, novija istraživanja ukazala su i na biokemijski utjecaj tromba te je ustanovljeno da luminalni sloj preko proteolitičke aktivnosti razgrađuje i oslabljuje stijenku, [7], [35]–[37]. Detaljan pregled biokemomehanike ILT-a napravljen je u [9]. Na temelju tog pregleda, Virag et al. u radu [38] predstavljaju novi 3D numerički model AAA, koji je uz G&R stijenke opisivao nastanak i rast ILT-a te njegov biokemijski i mehanički utjecaj na stijenku aorte. Iako je model bio ograničen na cilindričnu geometriju, dao je iznimno vrijedan uvid u utjecaj tromba na rast aneurizme.

Proces stvaranja tromba nije potpuno razjašnjen, ali je prihvaćeno mišljenje da je povezan sa strujanjem krvi kroz aneurizmu. Kompleksna geometrija uzrokuje pojavu vrtloga, za koje se vjeruje da su ključni pri nastanku tromba jer omogućuju aktivaciju trombocita u području visokih posmičnih naprezanja te njihovu akumulaciju u području nižih posmičnih naprezanja [39]. Zambrano et al. [40], analizirajući strujanje krvi na geometrijama AAA dobivenim iz CT snimaka, zaključili su da nisko vremenski osrednjeno posmično naprezanje na stijenci promovira akumulaciju tromba. Di Achille et al. [39], također analizirajući hemodinamiku u stvarnim AAA, definiraju novi parametar za predviđanje nastanka tromba nazvan „potencijal stvaranja tromba“, koji kombinira vremenski osrednjeno posmično naprezanje na stijenci, oscilaciju posmičnog naprezanja te potencijal aktivacije trombocita.

Korištenje G&R modela arterija u sprezi sa strujanjem fluida prvi put je prikazano u [41], a kasnije je unaprijeđeno u [42] gdje je predstavljen generalni okvir za modeliranje rasta na temelju analize hemodinamike. Taj pristup naziva se *fluid-solid growth* (FSG). Kasniji radovi koristili su FSG model za analizu cerebralnih aneurizmi [43], za modeliranje stijenke aorte [44] te za analizu aneurizmi na realističnoj (*patient-specific*) geometriji [45], [46]. Međutim, ni jedan od tih radova nije modelirao i uzeo u obzir utjecaj tromba.

Još jedna klasa model koja spaja analizu stijenke aorte s analizom hemodinamike su FSI (f*luid-solid interaction*) modeli. Međutim, ti modeli ne razmatraju rast i remodeliranje stijenke, već promatraju elastični odaziv i raspodjelu naprezanja u stijenci aorte tijekom srčanog ciklusa. FSI modeli se često koriste za analizu naprezanja kod aneurizmi dobivenih iz CT snimaka, [47]–[49].

Metode

U sklopu ovog rada razvijen je FSG model koji objedinjuje G&R model stijenke aorte, analizu hemodinamike, stvaranje i rast ILT-a te njegov mehanički i biokemijski utjecaj na stijenku. Koncept razvijenog modela prikazan je na slici 1.

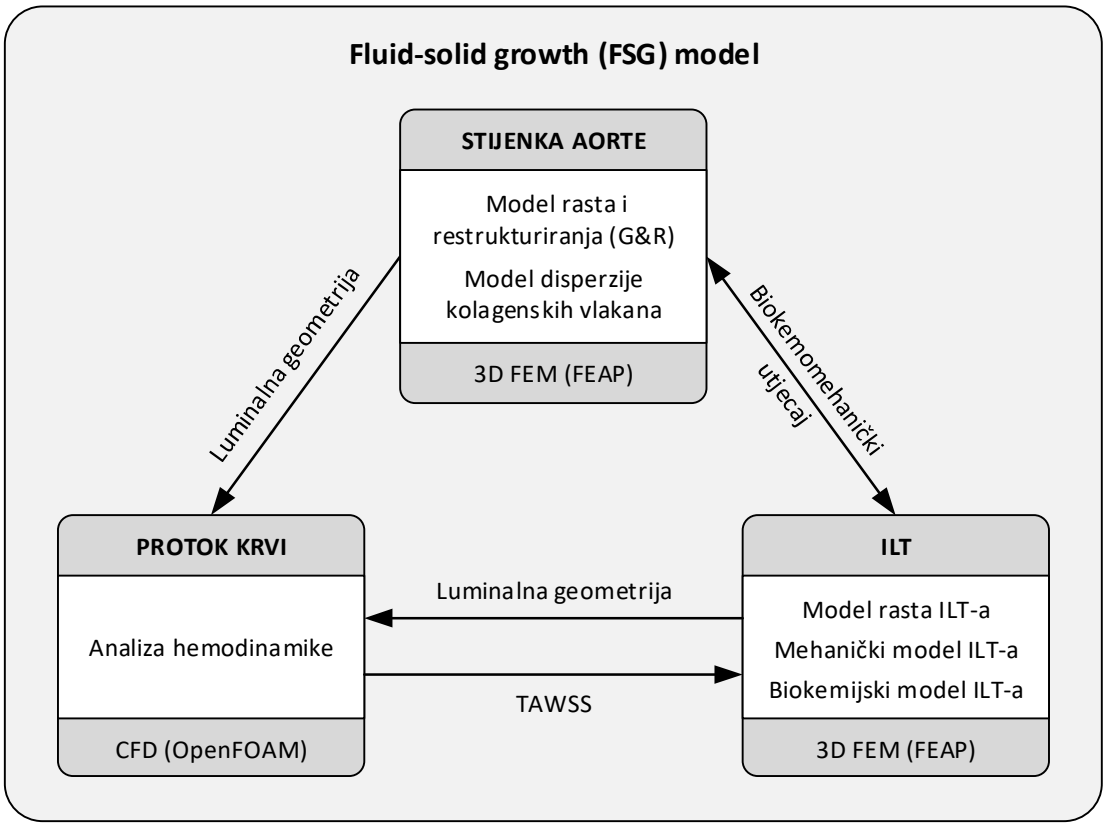

Slika 1. Koncept razvijenog FSG modela.

Za modeliranje stijenke aorte korišten je G&R model predstavljen u [24], a njegova implementacija u 3D konačne elemente tj. u program za konačne elemente (FEAP, [50]) detaljno je opisana prvom priloženom članku (PAPER 1, [25]). Model se temelji na teoriji spregnutih smjesa, prema kojoj su svi konstituenti ograničeni na zajedničko deformiranje, ali svaki od njih može imati vlastito stanje naprezanja. Pomoću ovog modela moguće je pratiti promjene svakog konstituenta zasebno (npr. promjena mase, orijentacije, naprezanja itd.).

Dodatno unaprjeđenje modela postignuto je implementacijom disperzije kolagenskih vlakana. Po prvi puta je u 3D G&R model stijenke implantiran model disperzije kolagenskih vlakana temeljen na generaliziranom strukturnom tenzoru. Detaljan opis implementacije i dobiveni reprezentativni rezultati prikazani su u drugom priloženom članku (PAPER 2, [51]).

Sljedeći korak bilo je dodavanje ILT-a u G&R model. Za tu namjenu razvijen je algoritam za generiranje dodatnih konačnih elemenata tromba tijekom G&R simulacije rasta aneurizme. Za svaki novo dodani sloj tromba, algoritam mora definirati koordinate čvorova, povezanost čvorova u elemente, rubne uvjete, opterećenje i povezanost sa slojem ispod. Rad algoritma i implementacija mehaničkog modela tromba opisani su detaljnije u trećem priloženom članku (PAPER 3, [52]). Uz to, analiziran je rast AAA te su dobiveni zanimljivi rezultati vezani uz mehanički utjecaj tromba na tijek bolesti.

Nakon mehaničkog utjecaja, dodatno je implementiran biokemijski utjecaj ILT-a na stijenku. Proteolitički aktivan luminalni sloj tromba te *vasa vasorum* kapilare, koje se nalaze s vanjske strane stijenke aorte, izvor su enzima koji svojim djelovanjem utječu na razgradnju stijenke. Difuzija enzima određena je u svakom koraku G&R analize preko zasebno pokrenutih 3D FEM analiza. Implementacija biokemijskog modela te intrigantni rezultati dobiveni analizom biokemomehaničkog utjecaja ILT-a na progresiju AAA opisani su u četvrtom priloženom članku (PAPER 4, [53]).

Zadnji dio koji je nedostajao kako bi se formirao i zaokružio FSG model bio je analiza hemodinamike. G&R model stijenke i tromba implementiran je u program za konačne elemente FEAP dok se za analizu hemodinamike koristi CFD simulacija u OpenFOAM programu. Kao što je prikazano na slici 1, G&R analiza AAA (stijenka aorte + ILT) daje luminalnu geometriju kao ulaz za analizu strujanja krvi, a iz analize hemodinamike izvlače se rezultati vremenski osrednjenog naprezanja na stijenci koji se zatim učitavaju u G&R analizu te se na temelju njih dodaje novi sloj tromba. Ovaj postupak ilustriran je u petom priloženom radu (PAPER 5, [54]).

Cilj i hipoteza istraživanja

Glavni cilj ovog istraživanja je razvoj realističnog numeričkog modela koji može opisati razvoj aneurizme abdominalne aorte, uključiti analizu hemodinamike te uzeti u obzir složeni biokemijski i mehanički utjecaj novonastalog intraluminalnog tromba na razvoj bolesti.

Hipoteze istraživanja su:

1. Mjesto i smjer nastanka novih slojeva ILT-a može se odrediti na osnovi:

a) analize hemodinamike,

b) oslabljenja stijenke aorte zbog biokemijskih i mehaničkih utjecaja tromba.

2. Način taloženja ILT-a direktno utječe na brzinu i smjer rasta aneurizme te nastajanje novih slojeva tromba.

3. Klinički opažene načine rasta aneurizme moguće je opisati preko prostorne promjene proteolitičke aktivnosti tromba.

Znanstveni doprinos

Najvažniji znanstveni doprinos ovog rada je razvijeni realistični FSG (*fluid-solid growth*) numerički model koji se može koristiti za simuliranje i analizu nastanka i razvoja AAA. Tri glavne strane koje treba razmotriti kako bi modeliranje AAA bilo što realističnije su rast i remodeliranje stijenke aorte, strujanje krvi, te stvaranje intraluminalnog tromba i njegov biokemomehanički utjecaj na stijenku. U literaturi postoji niz numeričkih modela koji se bave jednom od tih strana ili kombinacijom dviju njih, međutim ne postoji 3D model koji bi obuhvatio sve tri strane i zaokružio ih u jednu cjelinu. Iz tog razloga, u sklopu ovog rada razvijen je i kroz nekoliko znanstvenih članaka predstavljen jedan takav numerički model.

Model je implementiran u 3D konačne elemente što omogućuje simulacije fuziformnih i sakularnih aneurizmi kompleksnije geometrije. Za modeliranje stijenke je korištena G&R teorija temeljena na metodi spregnutih smjesa koja omogućuje praćenje veličina (npr. mase, naprezanja, orijentacije vlakana) na razini individualnih konstituenata stijenke. Nadalje, G&R model je povezan s analizom strujanja krvi i rast tromba se može bazirati na rezultatima prostorne raspodjele vremenski osrednjenog posmičnog naprezanja na stijenci. Uz mehanički utjecaj tromba, implementiran je i biokemijski utjecaj gdje proteolitička aktivnost tromba, ovisna o njegovoj prostorno promjenjivoj debljini, direktno utječe na promjene u stijenki.

Zbog navedenih mogućnosti, razvijeni FSG model omogućuje bolju predikciju ishoda AAA (brzina rasta, ruptura, stabilizacija), u odnosu na do sada dostupne numeričke modele.

U postojećim G&R modelima, kolagenska vlakna su obično modelirana kao diskretne 1D strukture orijentirane u četiri različita smjera. Eksperimentalna mjerenja pokazala su da postoji znatna disperzija kolagenskih vlakana unutar stijenke i shodno tome razvijeno je nekoliko modela za opisivanje disperzije. Dodatan znanstveni doprinos je implementacija modela disperzije kolagenskih vlakana u G&R model koja je po prvi put predstavljena unutar ovog istraživanja.

Osim razvojem novog modela, rad doprinosi i mnoštvom rezultata koji su dobiveni korištenjem modela za analiziranje rasta i razvoja AAA. Tu se posebice ističu rezultati koji pokazuju mehanički i biokemijski utjecaj tromba na stijenku aorte i evoluciju aneurizme. Oko utjecaja tromba se vodi mnoštvo rasprava zbog njegovog oprečnog djelovanja na stijenku. S jedne strane ILT mehanički štiti stijenku i smanjuje naprezanja u njoj, dok ju s druge strane proteolitičkim djelovanjem razgrađuje. Stoga su dobiveni rezultati i mogućnost modela da opiše mehanički i biokemijski utjecaj tromba od izuzetne važnosti.

Ključne riječi: aneurizma abdominalne aorte, intraluminalni tromb, model rasta i restrukturiranja, *fluid-solid growth*, disperzija vlakana

CONTENTS

LIST OF FIGURES

LIST OF TABLES

LIST OF ABBREVIATIONS

Label	Full meaning
AAA	Abdominal aortic aneurysm
AI	Angular integration
CFD	Computational fluid dynamics
FE	Finite element
FEM	Finite element method
FEAP	Finite element analysis program
FSG	Fluid-solid growth
FSI	Fluid-solid interaction
G&R	Growth and remodeling
GST	Generalized structure tensor
ILT	Intraluminal thrombus
MMPs	Matrix metalloproteinases
OSI	Oscillatory shear index
PLAP	Platelet activation potential
SMC	Smooth muscle cell
TAWSS	Time-averaged wall shear stress
TFP	Thrombus formation potential

LIST OF AUTHOR'S PUBLICATIONS

CROSBI profile: https://www.bib.irb.hr/pregled/profil/33883

Google Scholar profile: https://scholar.google.hr/citations?user=dgRfcj0AAAAJ&hl=hr

List of Scientific Journal Papers:

(PAPER 1) **Horvat, Nino**, Virag, Lana, Holzapfel, Gerhard A., Sorić, Jurica, Karšaj, Igor: A finite element implementation of a growth and remodeling model for soft biological tissues: Verification and application to abdominal aortic aneurysms. Computer Methods in Applied Mechanics and Engineering, 352: pp. 586-605, 2019, doi.org/10.1016/j.cma.2019.04.041

(PAPER 2) **Horvat, Nino**, Virag, Lana, Holzapfel, Gerhard A., Karšaj, Igor: Implementation of collagen fiber dispersion in a growth and remodeling model of arterial walls. Journal of the Mechanics and Physics of Solids, 153(3): 104498, 2021, doi.org/10.1016/j.jmps.2021.104498

(PAPER 3) **Horvat, Nino**, Virag, Lana, Karšaj, Igor: Mechanical role of intraluminal thrombus in aneurysm growth: a computational study. Biomechanics and Modeling in Mechanobiology, 20(5):1819-1832, 2021, doi.org/10.1007/s10237-021-01478-w

Živić, Josip, Virag, Lana, **Horvat, Nino**, Smoljkić, Marija, Karšaj, Igor: The risk of rupture and abdominal aortic aneurysm morphology: A computational study. International Journal for Numerical Methods in Biomedical Engineering, 38(3): e3566, 2022, doi.org/10.1002/cnm.3566

(PAPER 4 - manuscript) Virag, Lana, **Horvat Nino**, Karšaj Igor: A computational study of bio-chemo-mechanics of thrombus-laden aneurysms. The manuscript has been submitted to Journal of the Mechanics and Physics of Solids

List of Book Chapters:

(PAPER 5) Virag, Lana, **Horvat Nino**, Karšaj Igor: Bio-chemo-mechanical role of intraluminal thrombus deposition on arterial tissue growth and remodeling. In: Solid (Bio)mechanics: Challenges of the Next Decade, editors: Gerhard Sommer, Kewei Li, Daniel

Ch. Haspinger, Raymond W. Ogden, publisher: Springer Cham, 2022, doi.org/10.1007/978-3-030-92339-6_5

List of Scientific Conference Papers:

Horvat, Nino; Virag, Lana; Karšaj, Igor: Analiza utjecaja mišićnih stanica na ponašanje aorte pomoću konačnih elemenata. Zbornik radova sedmog susreta Hrvatskog društva za mehaniku / Mavrović, Pavao; Galić, Mirela; Krstulović-Opara, Lovre (ur.)., Split: Kartular d.o.o., 2016. str. 85-90

Virag, Lana; Righi, Boris; **Horvat, Nino**; Karšaj, Igor: Ispitivanje biološkog utjecaja tromba na fiziformnu aneurizmu. Zbornik radova sedmog susreta Hrvatskog društva za mehaniku / Mavrović, Pavao; Galić, Mirela; Krstulović-Opara, Lovre (ur.). Split: Kartular d.o.o., 2016. str. 211-216

Horvat, Nino; Zambrano, Byron; Baek, Seungik; Karšaj, Igor: Numerical modeling of fluid solid growth in abdominal aortic aneurysm. Proceedings of 5th International Conference on Computational and Mathematical Biomedical Engineering / Nithiarasu, Perumal; Robertson, Anne M. (ur.)., Pittsburgh: Zeta Computational Resources Ltd., 2017. str. 172-175

Virag, Lana; Karšaj, Igor; **Horvat, Nino**: A computational study of influence of changes in blood pressure on growth of abdominal aortic aneurysm. Proceedings of 5th International Conference on Computational and Mathematical Biomedical Engineering / Nithiarasu, Perumal; Robertson, Anne M. (ur.)., Pittsburgh: Zeta Computational Resources Ltd., 2017. str. 1236-1239

Horvat, Nino; Krizmanić, Severino; Karšaj, Igor: Numeričko modeliranje stvaranja tromba u analizi rasta abdominalne aneurizme. Zbornik radova osmog susreta Hrvatskog društva za mehaniku / Penava, Davorin; Guljaš, Ivica; Klečina, Mirjana Bošnjak (ur.)., Osijek: Grafika d.o.o., 2017. str. 77-82

Horvat, Nino; Virag, Lana; Karšaj, Igor: Finite Element Growth Model of Abdominal Aortic Aneurysm. Proceedings of the 9th International Congress of Croatian Society of Mechanics / Marović, Pavao; Krstulović-Opara, Lovre; Galić, Mirela (ur.)., Split: Croatian Society of Mechanics, 2018. 44, 9

Horvat, Nino; Karšaj, Igor: Utjecaj disperzije kolagenskih vlakana na rast aneurizme abdominalne aorte. Zbornik radova 9. susreta Hrvatskog društva za mehaniku - "50 godina

Društva" / Skozrit, Ivica; Tonković, Zdenko; Karšaj, Igor; Jarak, Tomislav; Lesičar, Tomislav (ur.)., Zagreb, 2019. str. 313-318

Virag, Lana; **Horvat, Nino**; Karšaj, Igor: Utjecaj morfoloških karakteristika aneurizme abdominalne aorte na vjerojatnost rupture. Zbornik radova 9. susreta Hrvatskog društva za mehaniku - "50 godina Društva" / Skozrit, Ivica; Tonković, Zdenko; Karšaj, Igor; Jarak, Tomislav; Lesičar, Tomislav (ur.)., Zagreb, 2019. str. 337-342

Živić, Josip; Batistić, Ivan; **Horvat, Nino**; Karšaj, Igor: Modeliranje strujanja u aneurizmatičnoj abdominalnoj aorti korištenjem metode kontrolnih volumena. Zbornik radova Desetog susreta Hrvatskog društva za mehaniku / Damjanović, Darko; Kozak, Dražan; Konjatić, Pejo; Katinić, Marko (ur.)., Slavonski Brod: Grafika d.o.o., 2021. str. 307-312

1. INTRODUCTION

An abdominal aortic aneurysm (AAA), see Figure 1, is an irreversible focal dilatation of the infrarenal abdominal aorta defined by a 1.5 or more-fold increase in diameter or simply a diameter larger than 3 cm. AAA is a common cause of preventable deaths among the elderly, with prevalence rates estimated between 1.3 and 8.9% in men and between 1.0 and 2.2% in women [1]. AAAs are caused by an imbalance in production and degradation of the extracellular matrix. They tend to grow over several decades but can rupture suddenly, often without warning and with fatal outcome, when wall stress exceeds wall strength. The primary risk factors associated with AAAs are male gender, aging, cigarette smoking, and hypertension. Although the pathogenesis is still not well understood, there is a wealth of biological, clinical, histopathological, and mechanical data on AAAs, and there has been significant progress in the biomechanical modeling of these lesions [2], [55]. Nevertheless, our ability to predict whether a specific lesion will remain, continue to enlarge either slowly or rapidly, or ultimately rupture remains wanting.

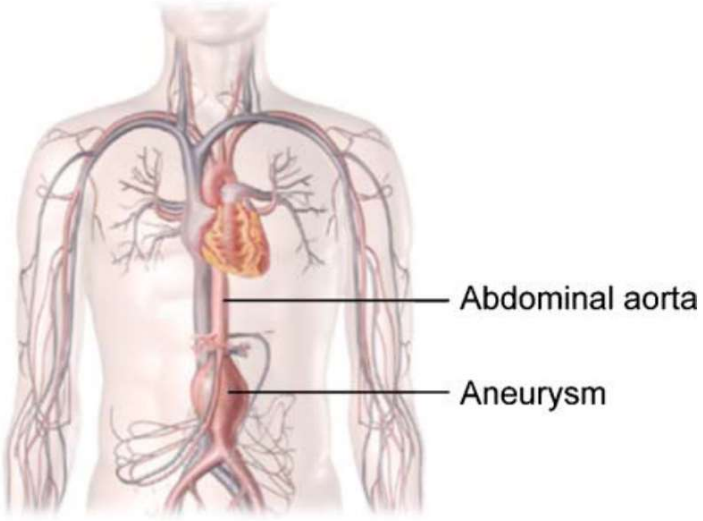

Figure 1. Abdominal aortic aneurysm. Taken from [56].

Clinical interventions are based primarily on the maximum dimension (typically when the maximum diameter of the lesion reaches 5-5.5 cm) or expansion rate of the lesion (typically when the maximal diameter increases more than 0.5-1 cm in one year) as well as symptoms (e.g., pain). However, many small lesions rupture, whereas larger lesions may remain asymptomatic and do not rupture over long periods [4], [5]. There is clearly a need for an increased understanding and for tools that could provide further insight and aid in

decisions regarding clinical interventions. Since biomechanical factors play fundamental roles in the history and evolution of AAAs, one class of tools that could be used are computer simulations equipped with mechanical and biochemical numerical models.

1.1. Intraluminal thrombus

One possible reason for the variable clinical outcomes is the intraluminal thrombus (ILT) that is present in about 75% of AAAs, [6]. A large population-based study has shown that all AAAs larger than 6 cm and the majority of smaller ones contain ILTs [7]. ILT can vary in thickness from a few millimeters to several centimeters. Thick ILT usually has a layered structure (Figure 2) with three recognizable layers. The luminal layer is closest to the blood, and it is characterized by the aggregation of activated platelets and entrapment of erythrocytes (hence the red color) and leukocytes within an evolving fibrin mesh. Its thickness is limited by the depth to which blood can penetrate fibrin mesh, and based on experimental results, it is around 2 mm thick. At first, ILT was considered an inert structure, however, later it was found that the luminal layer is proteolytically very active and causes activation of matrix metalloproteinases (MMPs), enzymes that degrade proteins (elastin and collagen) and as a result weaken the aortic wall [9]. Over time, luminal thrombus gets buried by successive clot deposition. It develops into a medial and finally abluminal layer as biochemical reactions degrade blood cells trapped within it. A more detailed overview of the structure, histology, and biochemomechanics of ILT in AAA can be found in [8] and [9].

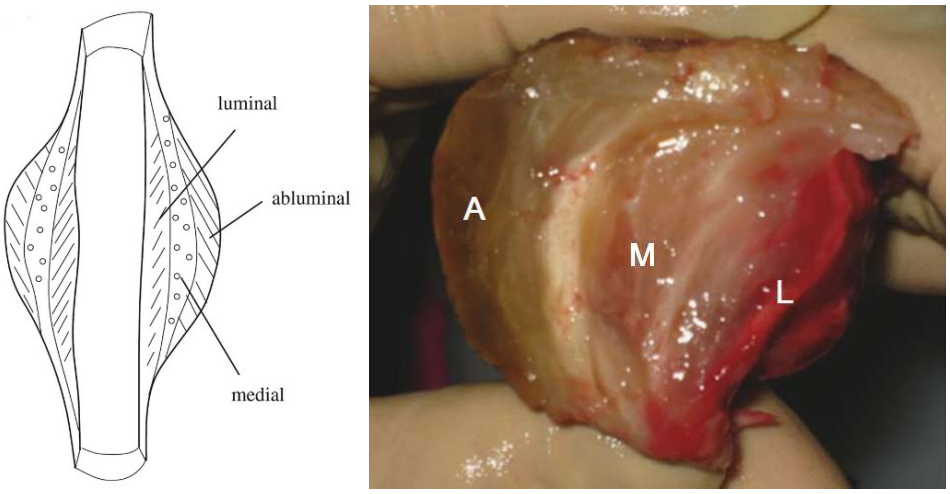

Figure 2. Illustrative sketch (left, taken from [8]) and ILT specimen (right, taken from [57]) with three visible layers: abluminal (A), medial (M), and luminal (L) layer.

Due to its complex natural history and structure, the biological and mechanical role of ILT in the progression and potential rupture of AAAs remains controversial. On the one hand,

through proteolytic activity, ILT may degrade and weaken the aortic wall, while on the other hand, it may stress-shield the aortic wall and thereby reduce intramural stress. An increased insight gained with numerical models and the ability to understand the biochemomechanical properties of ILT and its influence on the evolution of the aneurysmal wall could resolve some of that controversy. Furthermore, it could also guide future clinically motivated experimental and computational efforts to understand, predict, and therapeutically address the roles of ILT in challenging vascular pathology [9].

1.2. Abdominal aortic wall structure

To be able to successfully model an aortic wall and an AAA, it is first necessary to know its structure and material properties. The aortic wall is a composite structure organized in layers of different mixtures of cells and extracellular matrix proteins [58]. The healthy aortic wall consists of three layers: intima, media, and adventitia (Figure 3). Every layer has a different ratio of elastin, collagen, and smooth muscle cells (SMCs), which are structurally the most important constituents. Their ratio varies with age since elastin is produced only prenatally, while collagen and SMCs constantly turnover. During disease progression (e.g., AAA), aortic wall structure and mass fractions of the wall constituent can vary dramatically. Elastic fibers and smooth muscle cells can be degraded to the point that it is difficult to distinguish between the intima and the media [59].

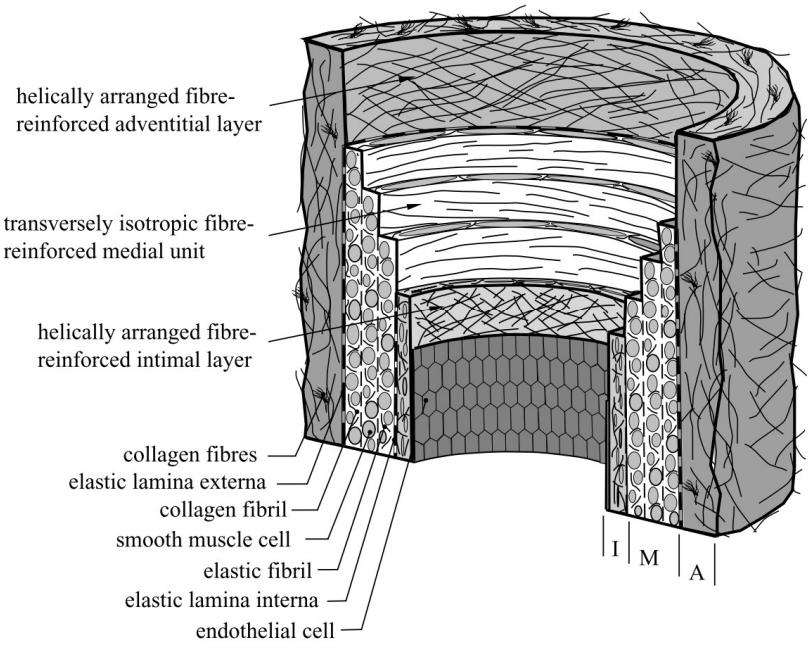

Figure 3. The composite layered structure of the aortic wall. Taken from [60].

Although structurally not important, endothelial cells at the luminal surface of the aortic wall are crucial for wall remodeling and adaptation of an artery to insults. They serve as a protective barrier between the blood and the aortic tissue and thus prevent blood clotting. Furthermore, endothelium cells can detect alterations in blood flow by sensing changes in wall shear stress, and based on that, they can release chemicals that control vascular relaxation and contraction.

1.3. Previous and related studies

The three main aspects of the AAA progression are G&R of the aortic wall, formation of ILT, and blood flow which is crucial for wall G&R and thrombus deposition. Many attempts have been made to mathematically model one or more of those aspects and their interactions. As new information from experimental and histological studies became available, numerical models became more complex. Their ability to describe a more realistic AAA behavior increased and each new numerical model provided further insight into the complex mechanobiological processes. This section will outline existing numerical models and give an overview of previous studies that were used to describe and analyze AAA.

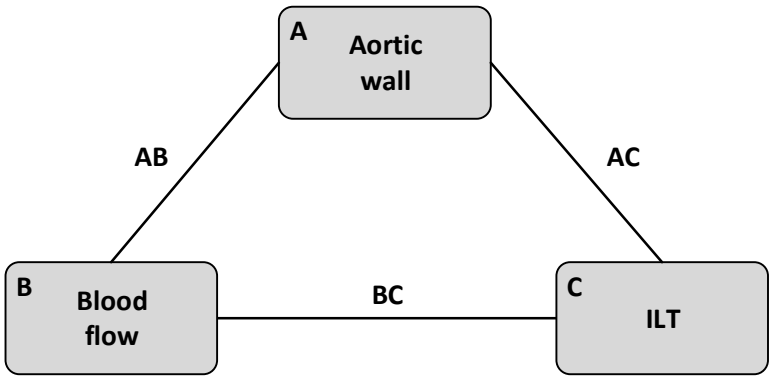

Figure 4. Three main parts of AAA modeling.

In Figure 4, three main parts of AAA modeling are schematically shown and indicated with the letters A, B, and C. Interactions between these parts are illustrated by lines labeled AB, AC, and BC. Furthermore, Table 1 summarizes numerical models and relevant studies from the literature. Each study is labeled with the abovementioned letters indicating which aspect or aspects of an AAA the study focuses on. Note that fluid-solid interaction (FSI) models have parentheses around label A because they use the aortic wall model but without growth and remodeling. Studies and their contributions are examined in more detail in the following subsections.

Table 1 - Summary of previous studies that are related to one or more parts of AAA modeling shown in Figure 4. Studies are grouped by numerical model type indicated in the first column, and they are linked to Figure 4 through labels in the last column.

Model type	Study	Figure 4 label
Finite volumetric growth model	Rodriguez et al. (1994), [10]	A
	Taber and Eggers (1996), [11]	A
	Rachev (2000), [12]	A
	Eriksson et al. (2014), [13]	A
	Grytsan et al. (2017), [14]	A
Constrained mixture G&R model	Humphrey and Rajagopal (2002), [15]	-
	Baek et al. (2005, 2006), [16], [17]	A
	Valentin and Humphrey (2009), [18]	A
	Karšaj et al. (2010, 2012), [23], [24]	A
	Horvat et al. (2019), [25]	A
Homogenized constrained mixture model	Cyron et al. (2016), [26]	A
	Braeu et al. (2017), [27]	A
AAA model	Watton et al. (2004), [19]	A
	Watton and Hill (2009), [20]	A
	Wilson et al. (2012), [21], [22]	A
ILT model	Di Martino et al. (1998), [31]	C
	Wang et al. (2001), [32]	C
	Geest et al. (2006), [33]	C
	Tong et al. (2011), [34]	C
	Virag et al. (2015), [38]	AC, C
ILT formation based on hemodynamics analyses	Biasetti et al. (2012), [61]	BC
	Zambrano et al. (2016), [40]	BC
	Achille (2014, 2017), [9], [39]	BC
Fluid-solid interaction snapshot analyses on patient-specific geometries	Scotti (2007), [48]	(A)B
	Rissland et al. (2009), [47]	(A)B
	Chandra et al. (2013), [49]	(A)B
Fluid-solid growth model	Figueroa et al. (2009), [42]	AB
	Watton et al. (2009), [43]	AB
	Sheidaei et al. (2011), [44]	AB
	Wu and Shadden (2015), [45]	AB
	Grytsan et al. (2015), [46]	AB

1.3.1. Growth and remodeling models of the aortic wall

Due to the composite structure, active smooth muscle stress, constituents' nonlinear and anisotropic behavior, and turnover of constituents, numerical modeling of G&R of the aorta is very complex. Special attention has been directed towards the mathematical modeling of arterial growth (i.e., changes in mass) and remodeling (i.e., changes in microstructure) and the development of an arterial G&R theory. Within the G&R theory, homeostasis is achieved with negative feedback loops and with rates of production and removal (degradation) changing in response to the changes in the mechanical environment. However, different constitutive models can be used to connect tissue deformations and stresses.

The work by Skalak [62] was the first that provided some crucial insight into the modeling of soft tissue growth using nonlinear elasticity. In a later work, Rodriguez et al. [10] attempted to model G&R by focusing on the description of growth kinematics, which led to the widely used theory of finite volumetric growth. The approach was later upgraded by Rachev [12] and Taber and Eggers [11] to describe the adaptation of blood vessels to alterations in blood pressure and flow. More recent use of volumetric growth can be found in the studies [13] and [14].

The finite volumetric growth approach focuses primarily on the consequences of G&R without considering the underlying mechanisms that cause tissue growth. In 2002, Humphrey and Rajagopal [15] proposed a fundamentally different approach based on changes in the rates and extents of cellular and extracellular matrix turnover in response to perturbations of the mechanical stimuli from baseline values. They introduced a new model concept of the constrained mixture in which different structurally significant constituents, produced at different times, are constrained in the mixture (i.e., artery). In this approach, the overall growth of soft tissue, i.e., mixture, is not directly described but is a consequence of the change in mass of individual constituents.

Soon after, the first finite element implementation of constrained mixture G&R theory followed. This included work by Baek et al. [16], [17] for cerebral aneurysms, and work by Valentín and Humphrey [18], who conducted a parameter sensitivity study of an arterial constrained mixture G&R model. Although their models were limited to membrane formulations, they provided insight into the G&R mechanisms (i.e., the dependence of mass change on the stress state and the concentration of vasoconstrictor/vasodilator ratio in the wall), and they gave boundary values of model parameters that cannot be determined experimentally.

The first mathematical G&R model to describe AAA evolution was presented by Watton et al. [19]. Since aortic wall constituents can remodel during aneurysm development, they emphasized the importance of using a constitutive model that can capture changes in the aorta microstructure. They used the general constitutive model proposed by Holzapfel et al. [60] that explicitly accounts for the individual contributions of elastin and collagen in the arterial wall. In their later work [20], they used the model to test the influence of different material parameters on AAA growth. Further use of G&R theory on AAA was presented by Wilson et al. [21], [22]. They used membrane finite element implementation of G&R model to study the influence of specific model parameters on AAA.

Further advancement was made by Karšaj et al. [23], [24], who developed a 3D G&R model that can describe changes in geometry and structure of arteries in response to altered hemodynamics (changes in blood flow and pressure) for one-layered and for three-layered artery models. The three-layered G&R model was later implemented into a 3D finite element code by Horvat et al. [25]. This implementation enabled detailed analyses of radial, axial and circumferential changes within the axisymmetric and asymmetric finite element computational model of AAA.

Cyron et al. [26] introduced a new homogenized constrained mixture model for G&R of soft tissues. This new class of models tries to combine the conceptual simplicity and computational efficiency of kinematic growth models with the microstructurally founded classical constrained mixture models. Later Braeu et al. [27] extended this model for anisotropic volumetric growth, implemented it into 3D finite elements, and used it to analyze AAA.

1.3.2. Numerical models of intraluminal thrombus

The thrombus was treated as a homogeneous inert material until the early 90s when Inzoli et al. [28] first suggested that ILT might act as a mechanical shield to the aortic wall, decreasing its peak stress and, in consequence, reducing the risk of rupture. This was confirmed in some of the studies that analyzed the effect of thrombus on AAA mechanics [6], [29], [30]. On the other hand, newer studies have shown that ILT is also proteolytically active and that it degrades and weakens the aortic wall [7], [35]–[37].

Mechanical data regarding ILT was well documented by a study in [31], suggesting a linear stress-strain relation for ILT. After conducting numerous uniaxial extension tests, Wang et al. [32] concluded that ILT is an isotropic material with a nonhomogeneous structure that is

stronger and stiffer in the luminal region. They used a two-parameter, isotropic material model for the ILT, while the study by Vande Geest et al. [33] used a general form of isotropic strain-energy function for modeling. Tong et al. [34] were the first to document biaxial mechanical responses of fresh thrombi, and for constitutive modeling, they used an anisotropic strain-energy function originally developed for arterial walls.

A detailed review of ILT biochemomechanics was performed in [9] and based on that, a new 3D numerical model of AAA was developed by Virag et al. [38]. Apart from modeling G&R of ILT constituents using the constrained mixture theory, the model can describe the biochemical and mechanical influence of ILT on the aortic wall. Despite its limitation to cylindrical geometry, the model gave an important insight into the effect of thrombus on aneurysm growth and emphasized the importance of modeling ILT in AAA models. Encouraged by these results, Horvat et al. [52] used a 3D finite element constrained mixture G&R model of the aortic wall with added ILT finite elements to study the mechanical effect of ILT on AAA growth. Since only the mechanical influence of ILT was considered, their next step is to implement a numerical model and explore the biochemical influence of ILT.

1.3.3. Hemodynamics analyses of blood flow

It is believed that hemodynamics is a crucial factor in the development of ILT. Complex AAA geometry creates vortices inside the lumen that causes sufficiently high shear stress needed to activate platelets. In contrast, low wall shear stress at injured endothelium allows activated platelets to accumulate and start fibrinogenesis. Fibrin fibers are then stabilized by crosslinking into a network with blood cells intertwined. Biasetti et al. [61] proposed a model that couples fluid and chemical domains and provides an integrated mechanochemical picture that could help unveil ILT formation and development mechanisms. Zambrano et al. [40] analyzed the hemodynamics in AAA obtained from CT scans and concluded that low TAWSS promotes thrombus accumulation. After analyzing the hemodynamics of patient-specific AAAs, Di Achille et al. [39] defined a new parameter for predicting thrombus deposition called thrombus formation potential (TFP), which combines TAWSS, shear stress oscillation, and platelet activation potential.

1.3.4. Fluid-solid interaction models

FSI models are frequently used to analyze patient-specific geometries obtained from CT scans [47]–[49]. However, analyses with these models typically study aneurysms at a certain point without considering G&R; thus, they are often referred to as snapshot analyses. An

aortic wall model is used to calculate the distribution of wall stresses, while a hemodynamic simulation updates the mechanical load on the wall. In this way, the elastic response of the aortic wall to varying blood flow loading during the cardiac cycle can be studied. A simple material model is often used for the wall since multiple iterations are necessary for every increment to achieve equilibrium between the aortic wall and the blood flow.

1.3.5. Fluid-solid growth models

FSG models couple vascular G&R with hemodynamics analysis. They use loose coupling, mainly due to the vastly different time scale, one second for hemodynamics analysis and days to months for G&R analysis. FSG modeling was first used in 2007 by Ateshian [41] but was generally advanced in 2009 by Figueroa et al. [42] where they presented a computational framework for FSG modeling in cardiovascular simulations. Watton et al. [43] coupled the hemodynamic environment to the evolution of cerebral aneurysms. Sheidaei et al. [44] used the FSG model with membrane G&R model of the aortic wall, while Wu and Shadden [45] used an FSG model with constrained mixture G&R model to study vascular G&R in a patient-specific geometry. Grytsan et al. [46] also analyzed patient-specific geometry but with a thick-walled G&R model of AAA. None of these studies considered the influence of ILT in their model.

1.4. Objectives and research hypotheses

The objective of this research is to develop a comprehensive FSG numerical model of an AAA that could unite the G&R model of an aortic wall, deposition of ILT, hemodynamic simulation, and biochemical and mechanical influence of ILT on the aneurysmal aortic wall.

Hypotheses of the research are:

1. Location and direction of deposition of new thrombus layers can be determined based on:
    a) hemodynamic analysis,
    b) weakening of the aortic wall due to the biochemical and mechanical influence of thrombus.
2. Thrombus accumulation directly affects the rate and direction of aneurysm growth, as well as the deposition of new thrombus layers.
3. Patterns of clinically observed aneurysm growth can be described using different spatial proteolytic activity of thrombus.

1.5. Scientific contribution

The existing 3D G&R model of the arteries can describe growth and changes in the aortic wall structure during aneurysm evolution. At the same time, hemodynamic analysis can determine the mechanical loading and predict thrombus deposition. Furthermore, a numerical model that can describe ILT biochemomechanical influence was developed and presented in the literature. Nevertheless, hitherto developed FSG models have not yet managed to combine all three mentioned areas (G&R of the artic wall and ILT, biochemomechanical influence of ILT, and the role of hemodynamics in a deposition on new thrombus layers). Hence, there is a pressing need for a numerical model that couples all these areas and describes a realistic AAA behavior on complex geometry. The development of such a model was the main objective of this work, and it has successfully been realized.

Therefore, the main scientific contribution of this thesis is the developed FSG numerical model of aortic aneurysms that couples the 3D finite element G&R model of the aortic wall, the 3D finite element model of ILT, the thrombus deposition based on results from the hemodynamics analysis, and the spatially varying biochemomechanical influence of the proteolytically active ILT on the aortic wall. Compared to currently available numerical models, the developed FSG model gives a deeper insight into the AAA and can better predict its outcomes (growth rate, rupture, stabilization).

Furthermore, in existing G&R models, collagen fibers are usually modeled as 1D structures oriented in several discrete directions. However, experimental measurements have revealed significant fiber dispersion within the aortic wall, prompting the development of several numerical models of collagen fiber dispersion. The additional scientific contribution of this paper is the very first implementation of the collagen fiber dispersion model based on the GST approach in a constrained mixture G&R model of an aortic wall.

Apart from the new model, this work delivers a multitude of results obtained while analyzing AAAs. Because of the controversial ILT role in AAA progression, results regarding ILT mechanical and biochemical effects are of great interest and importance.

2. DISCUSSION OF METHODS AND RESULTS

This thesis presents a development of an FSG model of AAAs and a study of the mechanical and biochemical influence of ILT on the aortic wall and aneurysm evolution. The concept of the developed FSG model is depicted in Figure 5. The aim was to incorporate all three main aspects of an AAA into one comprehensive numerical model. As can be seen, the developed model combines 3D finite element G&R analysis of an aortic wall, CFD analysis of blood flow (i.e., hemodynamics analysis), ILT formation and growth, and the ILT mechanical and biochemical influence on the aortic wall and AAA evolution. The review in the previous chapter has shown that some parts of the FSG model already exist as individual models in the literature, but there is no comprehensive FSG model that combines all the abovementioned parts into an overall model that can be used in a 3D finite element environment.

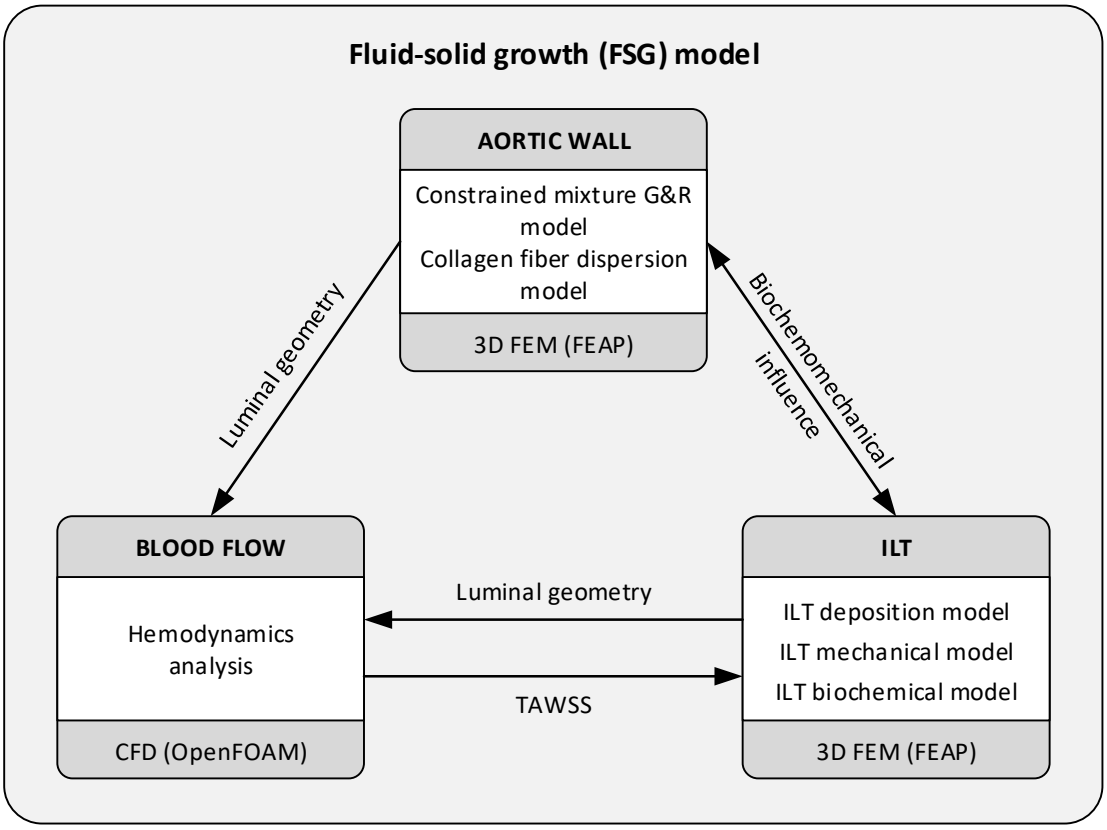

Figure 5. Graphical overview of the developed FSG model.

The development of the FSG model consisted of several steps, and each step was detailed in one of the attached papers. The first step was the implementation of the constrained mixture G&R model into the 3D finite element software FEAP [50]. This step

was described in detail in PAPER 1 [25]. Apart from the FE implementation, the G&R model was verified based on clinically observed phenomena and applied for modeling AAA growth.

PAPER 2 [51] presented the very first implementation of a fiber dispersion model based on the generalized structure tensor approach into a constrained mixture G&R model of the aortic wall. The implemented non-symmetric collagen fiber dispersion model further advanced and enriched the existing G&R model.

The next step was to incorporate the ILT in the G&R model to study its mechanical and biochemical influence on the aortic wall. A numerical model and an algorithm for depositing new finite elements representing ILT in the FE AAA model during the G&R analysis needed to be developed. The developed algorithm and ILT mechanical model implementation were presented in PAPER 3 [52]. Since only the mechanical influence of ILT was modeled in PAPER 3 [52], the natural next step was to expand the ILT numerical model to consider the biochemical influence on the aortic wall. This was done in PAPER 4 [53].

Finally, the last missing part that needed to be connected was the hemodynamics analysis. Hemodynamics was loosely coupled with the ILT deposition algorithm, and it was used to determine a location for depositing new layers of ILT. The framework for this coupling is illustrated in PAPER 5 [54] and later in this thesis.

As explained above, each paper deals with a particular aspect of the developed FSG model, and when combined, they form a complete picture of the FSG model. The following sections describe each development step in more detail and discuss the key results that were obtained.

2.1. Constrained mixture growth and remodeling model of the aortic wall

Constrained mixture G&R models are commonly used in the numerical modeling of arterial walls and aortic aneurysms because of their ability to describe processes inside the aortic wall and response of the aorta to different mechanical (e.g., stress) and chemical (e.g., diffusion of vasoconstrictors and vasodilatators) stimuli. The G&R model used in this study was presented in [23] for one layered and in [24] for multilayered aortic walls. The model uses the constraint mixture theory and the theory of evolving configurations to describe changes in the geometry and structure of the aorta. According to the constrained mixture theory, constituents (elastin, collagen, and SMC) deform together with the mixture, while each can possess a different stress state. The theory of evolving configuration tracks the production and degradation of constituents, and at any given moment, the mixture is

comprised of constituents created at different times in the past. Each of the constituents can have a different natural configuration and, therefore, a different deformation gradient. Furthermore, at the time of production, a constituent is embedded into the matrix with a certain pre-stretch which must be taken into account when calculating the constituent's overall deformation.

Changes in mass can significantly impact stresses; thus, it is essential to model mass production and degradation correctly. Due to the relatively short natural half-life (70-80 days), collagen and SMC turnover continuously, while elastin is produced prenatally and only degraded during maturity. Since elastin does not have production, loss of elastin mass can have a major impact and cause irreversible damage to the aortic wall. In homeostasis, the production of collagen and SMC is equal to degradation, and their overall mass is preserved. Changes in external stimuli can change mass production and degradation: increased stresses in the aortic wall cause increased production and degradation, while an increase in wall shear stress due to the increased blood flow causes a reduction in mass production. A more detailed description of the G&R model with all the expressions that govern the kinematics and kinetics of AAA, as well as stress calculation, can be found in PAPER 1 [25].

2.1.1. Implementation of G&R model in finite elements

Finite element implementation of the G&R model was presented and detailly described in PAPER 1 [25]. The model was implemented in the FE analysis software FEAP [50] thru subroutines for a user-defined material model. Within the subroutines, it was necessary to define the Cauchy stress tensor and the elasticity tensor in every integration point. An Augmented Lagrange method and elements with a mixed variational approach were used to deal with material incompressibility. Specifically, 3D hexahedral Q1P0 elements were used.

Integral-based formulation of the G&R model requires a precise tracking of the constituent's kinematics and kinetics. To perform numerical time integration of G&R expressions at an integration point level, it is necessary to track the history of variables used in expressions from the beginning of a simulation. For example, to integrate the current total mass of a constituent, it is necessary to know the production and degradation of that constituent for all previous time increments. In every time increment and for every integration point, it is necessary to store 70 variables (54 variables for the kinematics of constituents, 9 for the total deformation gradient **F**, 5 for mass production, 1 for the current simulation time, and 1 for the active stretch computation of SMCs). Additional six variables of the Cauchy

stresses, needed for mass calculation, are stored only for the previous increment. For example, for the mesh with 720 elements, each with eight integration points, and for the simulation with 1000 timesteps, the number of stored variables would be over 400 million. This would make the model computationally and memory-wise extremely demanding, especially considering the needed integration of those variables in every increment.

Collagen and SMC fibers have a relatively short half-life (70-80 days) compared to the total simulation time (years, even decades). Thus, it is possible to reduce the size of the required history field by setting the maximum lifespan of fibers to seven half-lives or roughly 500 days. In that case, history variables need to be stored only for the last 500 days (i.e., 50 increments, for the increment size of 10 days). This reduces the size of the history field by a factor of 20 and makes numerical integration much faster without compromising the result, given that less than 0.1% of the fiber mass remains after that time.

Since we have defined a maximum life span, the history field can have a fixed size of 3500 (70 variables × 50 time increments) for one integration point. Figure 6 illustrates how variables are stored in the history field. Numbers represent time increments, each containing 70 history variables. Arrows indicate the integration direction, while S and E represent the start and end of each integral, respectively. During integration, variables are read from the memory location S (start) to the location E (end). Incremental variables are written from the beginning towards the end of the field (case a); however, when the history field is filled (case b), variables from new increments are written at the beginning of the field (case c). In that way, variables are written in the memory only once, and they remain at the same memory location until they are overwritten 50 time increments later.

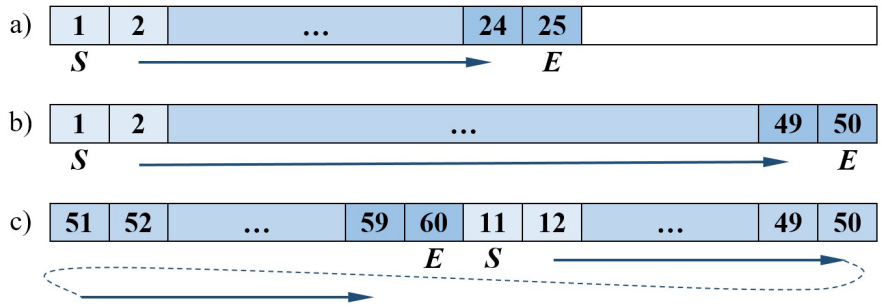

Figure 6. Schematic representation of the history field. Taken from [63].

2.1.2. Computational models

Several types of computational models were used for AAA in this work. A simple cylindrical model was used for G&R model development and testing, calibration of model

parameters, and getting fast and preliminary results. For the simulations of fusiform AAA, an axisymmetric model was used. A portion of a cylinder (as shown in Figure 7) with imposed axisymmetric boundary conditions was used for both models. In the case of a cylindrical model, only one element in the axial direction was used, with 12 elements in the radial direction. The fusiform model was discretized with 6 elements radially and 120 elements in the axial direction. Finally, for asymmetric AAA, half of the cylinder was used with 50, 16, and 3 elements in the axial, circular, and radial directions, respectively. Figure 8 illustrates the difference in geometry of the developed axisymmetric (a) and asymmetric (b) fusiform AAA. Note that in both cases, the initial geometry is a straight cylinder (c).

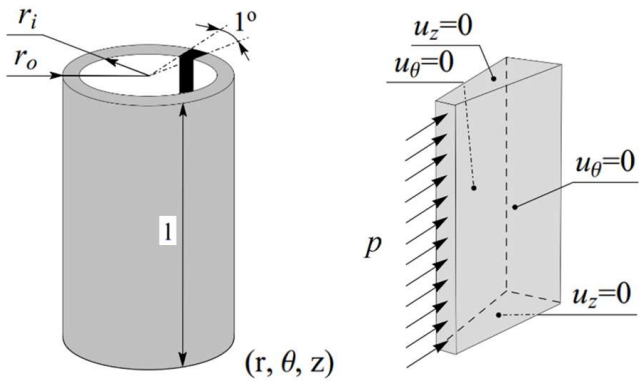

Figure 7. Geometry and boundary conditions of the computational model used for the cylindrical and axisymmetric fusiform aneurysm. Taken from [63].

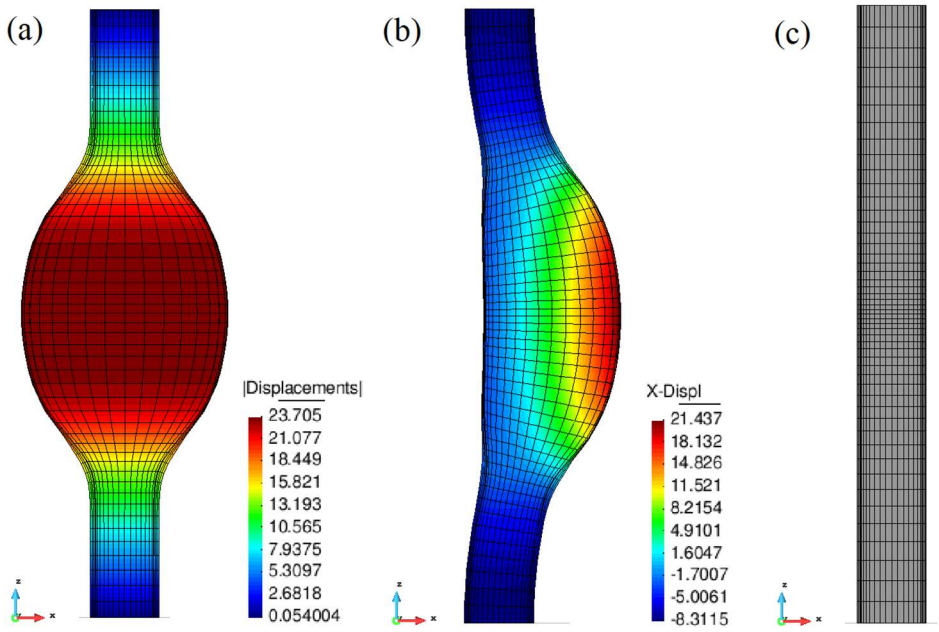

Figure 8. Example of axisymmetric (a) and asymmetric (b) fusiform aneurysm. The initial geometry was a straight cylinder (c). Taken from [63].

As explained in the introduction, the aortic wall has three distinct layers. Each layer has a different ratio of structural constituents (i.e., elastin, collagen, and smooth muscle cells) and can generally have different values of material parameters. In addition to a realistic 3-layer model, in some cases, a simpler 1-layer model with averaged values of material parameters was used. In the case of a 3-layer model, two additional transitional layers were added to avoid sharp changes in the material parameters that can cause numerical instabilities. Structural parameters in these zones change linearly from the values of one layer to the values of the adjacent layer. This applies to mass fractions of the constituents, pre-stretches of the constituents, mean fiber angles of the collagen, and parameters of the collagen dispersion.

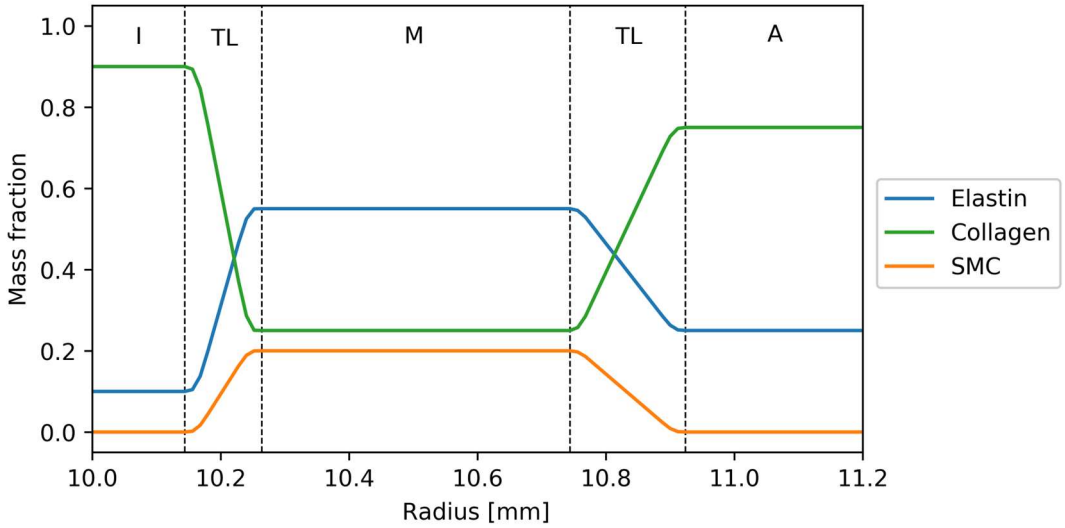

Figure 9. Mass fractions of three main structural constituents through the aortic wall thickness. Transitional layers (TL) can be seen between intima (I) and media (M), and media and adventitia (A).

The existence of the transitional zones has been confirmed by the second harmonic generation (SGH) imaging [64], and the widths of the zones were defined relative to the observed ones. For example, Figure 9 illustrates the mass fractions of the three main constituents through the aortic wall thickness. The transitional layers (TL) can clearly be seen between the intima (I) and media (M), and the media and adventitia (A).

2.1.3. Model verification

The G&R model implementation was verified using clinically observed phenomena. Cases of aortic adaptations to hemodynamic changes, specifically changes in blood flow and pressure of a non-idealized aorta, were analyzed. Figure 10 shows an adaptation of the non-idealized aorta to the abrupt 50% increase in blood pressure. To achieve the non-idealized geometry of the aorta, a rather small inhomogeneous degradation of elastin was used on the

initially idealized cylindrical geometry. After 400 days of the G&R process, the aorta achieved a new non-cylindrical equilibrium shown with dash curves in Figure 10(c). The location of the initial small elastin degradation is marked with the letter A. Following the abrupt blood pressure increase, the aorta immediately expanded due to the increased loading; however, in response to the increased intramural stress, the G&R process reacted by producing more mass, which returned the inner diameter to almost its initial value. Note that in this newly reached homeostatic state, the aortic wall thickness is increased to deal with increased loading. These results showed a good agreement with the membrane theory, animal models, and clinical observations. That confirms the validity of the model implementation. The same conclusion was drawn in the case of adapting the non-idealized aorta to the abrupt increase in blood flow, see PAPER 1 [25] for more detail.

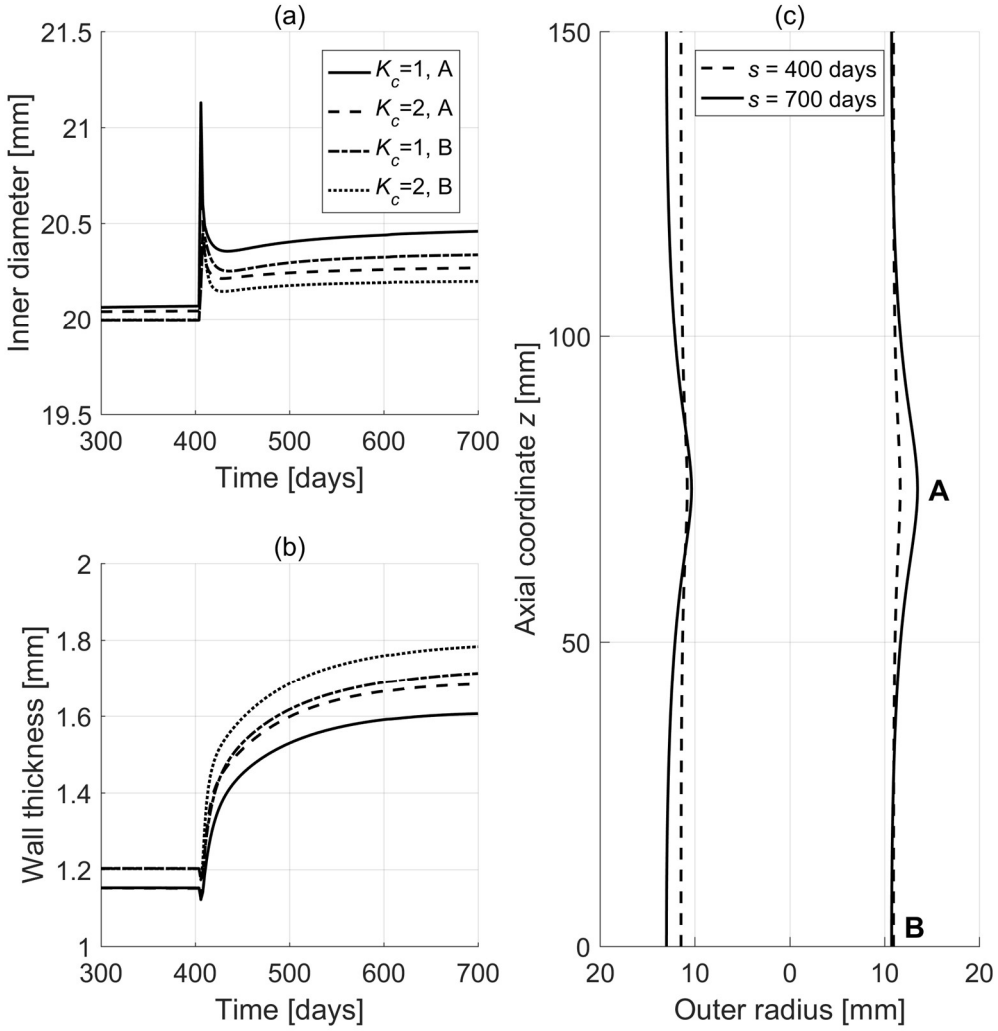

Figure 10**.** Evolution of the inner diameter (a) and the wall thickness (b) at the locations A and B noted in (c) for different production rates of collagen and SMC (partly governed by indicated K_C parameter); contours of a healthy artery (dashed curve) and the artery after the new homeostatic state is reached (solid curve) after a 50% blood pressure increase for K_C = 1 (c). Taken from PAPER 1 [25].

2.2. Collagen fiber dispersion model

G&R models typically divide collagen fibers into several families and model them as perfectly aligned with no dispersion. Some G&R models feature four collagen fiber families (e.g., [24], [25], [65]) with axial, circumferential, and two helical directions instead of the two that are typically observed in imaging of the abdominal aorta [64], [66]. The use of two additional fiber families can, to some degree, mimic certain mechanical effects of the fiber dispersion, but only in the tangential plane. For healthy aortic walls, this could be enough; however, for AAA with more expressed dispersion, the use of a dispersion model would be more appropriate. Since the underlying microstructure strongly influences the mechanical response of the arterial wall, it is crucial to model the microstructure as detailed as possible to obtain more accurate results and to increase the predictive power of numerical models (e.g., prediction of aneurysm growth and rupture). Therefore, the used G&R model was further advanced and made more realistic by implementing collagen fiber dispersion.

In the context of soft tissue mechanics, two different approaches for modeling fiber dispersion were developed. Firstly, Lanir [67] introduced the angular integration (AI) approach, where the fiber dispersion is directly incorporated in a strain-energy function through a probability density function. The strain energy of a single fiber within a dispersion is considered as a function of stretch, and the total strain energy is obtained by its integration over a unit sphere. In the second approach, the fiber dispersion is represented by a second-order tensor called a generalized structure tensor (GST). Gasser et al. [68] first formulated the approach for rotationally symmetric fiber dispersion, which was later, extended to a more general case of non-symmetric fiber dispersion by Holzapfel et al. [69]. The study [70] shows that the predictive power of the two models is equivalent; however, the GST approach is much simpler to implement and computationally less demanding. These approaches enable the calculation of mural stresses within arteries at a specific instant. Nevertheless, to account for long-term changes in the structure and thus an altered stress response of healthy and diseased arterial walls, a constrained mixture G&R model is needed.

Hence, PAPER 2 [51] introduced the very first implementation of the collagen fiber dispersion model based on the GST approach in a finite element constrained mixture G&R model of an aortic wall. A non-symmetric fiber dispersion model developed in [69], was used and incorporated into the G&R model, as detailed in PAPER 1 [25]. In the arterial wall, the fibers are synthesized and deposited into a ground matrix with a certain deposition stretch, which is a crucial part of the aortic wall adaptation mechanism. The GST approach does not

include fiber pre-stretch, so a special emphasis needs to be made on the new proposed definition of the fiber pre-stretch tensor. Appendix A in PAPER 2 [51] explains the proposed fiber pre-stretch tensor in detail and gives a flowchart for its calculation.

The studies [71], [72] have shown that excluding the compressed fibers from the overall strain-energy function can significantly affect the mechanical response of the aortic wall. Due to the wavy shape of collagen fibers, they are often considered to have load-bearing capabilities only in tension. Therefore, in the implemented dispersion model, the contribution of compressed collagen fibers is excluded through the simple tension-compression switch, as suggested in [72].

Recently, second harmonic generation (SHG) imaging made data on the aortic wall structure more available and detailed [64], [66], [73]. The realistic measured values presented in [64] for collagen mean fiber orientations and fiber dispersion in the tangential plane and out-of-plane were used in this study.

To verify the dispersion model implementation and the pre-stretch tensor definition, residual stresses during vascular adaptation to hypertension were investigated (Section 3.1 in PAPER 2, [51]). Results showed a reasonable residual stress distribution (compression on the inner side and tension on the outer side) and a development of the opening angle that corresponds to the animal model. After successful verification, the influence of collagen fiber dispersions and mean fiber angles on AAA growth and the distribution of stresses inside the aortic wall were studied. A three-layered axisymmetric and non-symmetric computational model of fusiform AAA was used, and the dispersion parameters were varied in the range of measured values. Results show that changes in fiber dispersions and mean fiber angles significantly influence the aneurysm evolution and the stress distribution. For example, the mean fiber direction closer to the circumferential direction resulted in a stiffer response in the aortic inflation analysis and decreased growth rate of AAA. Simulations with increased fiber dispersion in the intima or the media showed a slower aneurysm growth, while the opposite was true for the adventitia. SHG imaging showed a considerable difference in the healthy and aneurysmatic aortic wall structure [64]. Change in the collagen out-of-plane dispersion is especially pronounced. To account for that, the last example in PAPER 2 [51] varied fiber dispersion over time with respect to the inner diameter of the aneurysm. Changes in the initial collagen mean orientation towards the circumferential direction resulted in a stiffer mechanical response (and consequently slower growth), non-axisymmetric growth, and more bending of the aneurysm. Furthermore, a significant reorientation of the collagen fibers of

around 10–20° was observed. Therefore, apart from spatial variations, temporal variation of the structural parameters should also be considered in G&R simulations. However, more detailed measurements of the aneurysm structure are required.

2.3. ILT deposition model

In order to add ILT in analyses of thrombus-laden aneurysms, an algorithm for the deposition of additional finite elements representing ILT during the AAA G&R simulation was developed. The algorithm is implemented through new subroutines in FEAP and executed when a condition for adding additional finite elements of ILT is met (e.g., expansion of inner radius by more than one ILT element thickness, TAWSS from hemodynamics analyses falls below a threshold). At that point, the G&R simulation is paused, and the algorithm's subroutines are called. When executed, the algorithm creates new finite elements that fill the void between the existing luminal surface and the targeted luminal surface. For newly created elements, the subroutines of the algorithm define nodes, element connectivity data, boundary conditions, loading, and connectivity to underlaying surface. New elements are deposited on the deformed geometry of the aortic wall and/or existing ILT surface, and at the time of deposition, they are in a stress-free state with zero displacements. Furthermore, the blood pressure loading is transferred from the old luminal surface to the new elements. This novel approach has not been shown in the literature, since most AAA studies do not include ILT.

The targeted luminal surface is the critical factor determining how ILT is deposited. Again, the algorithm works by filling the space between the existing and targeted luminal surface with new ILT; thus, the shape of the targeted luminal surface directly impacts the shape of the deposited ILT. There are multiple options within the developed model for capturing the targeted luminal surface. Mainly, it can be defined as a simple cylinder with a constant radius (e.g., with a radius equal to the initial aorta radius for a fully thrombosed aneurysm), it can change over time to simulate gradual thrombus growth, or it can be defined based on hemodynamics analysis. The first two definitions were used and explained in more detail in PAPER 3 [52]. The flowchart in Figure 11 illustrates how the algorithm works for these options. An example of ILT growth in an asymmetric fusiform AAA aneurysm is shown in Figure 12. The first option with a constant predefined targeted luminal radius equal to the initial radius was used for ILT deposition in this example.

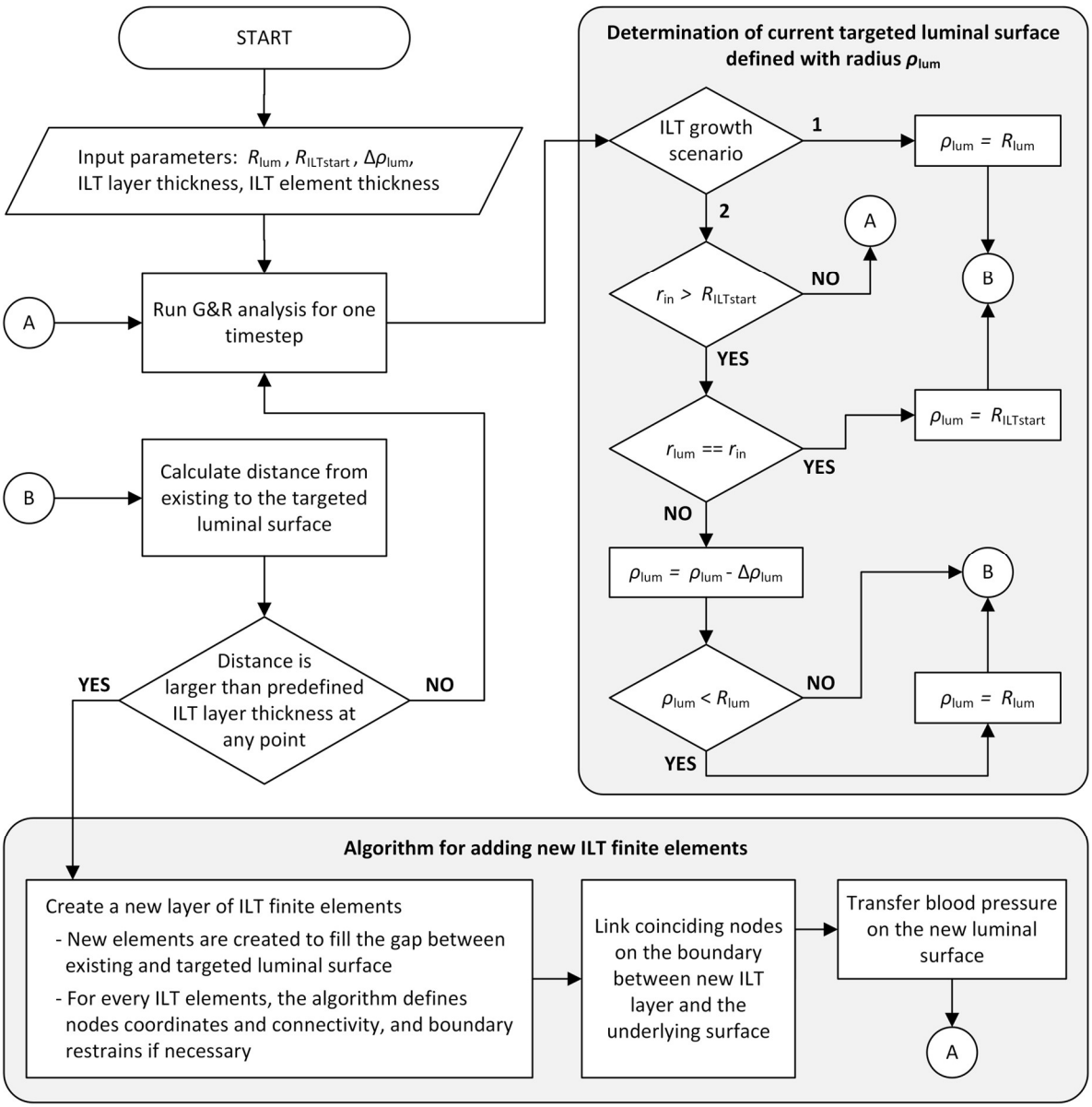

Figure 11. Flowchart for thrombus deposition process based on the predefined (constant and variable) targeted luminal surface. Taken from PAPER 3 [52].

Next, the flowchart in Figure 13 illustrates how the FSG approach adds ILT elements. The definition of the targeted luminal surface is now based on the spatial distribution of TAWSS calculated in hemodynamics analysis. The targeted luminal surface is first set to equal the existing luminal surface. Then on every part of the surface where TAWSS is lower than a set limit value (e.g., 0.4 Pa), the surface radius is decreased for one ILT element thickness. In that way, the algorithm will add new ILT elements only and everywhere where the TAWSS criterion is met. Note that the luminal surface is no longer cylindrical but can be arbitrarily shaped. G&R analysis and hemodynamic analysis are loosely coupled because of vastly different timescales. Hemodynamics analysis runs over several cardiac cycles (i.e.,

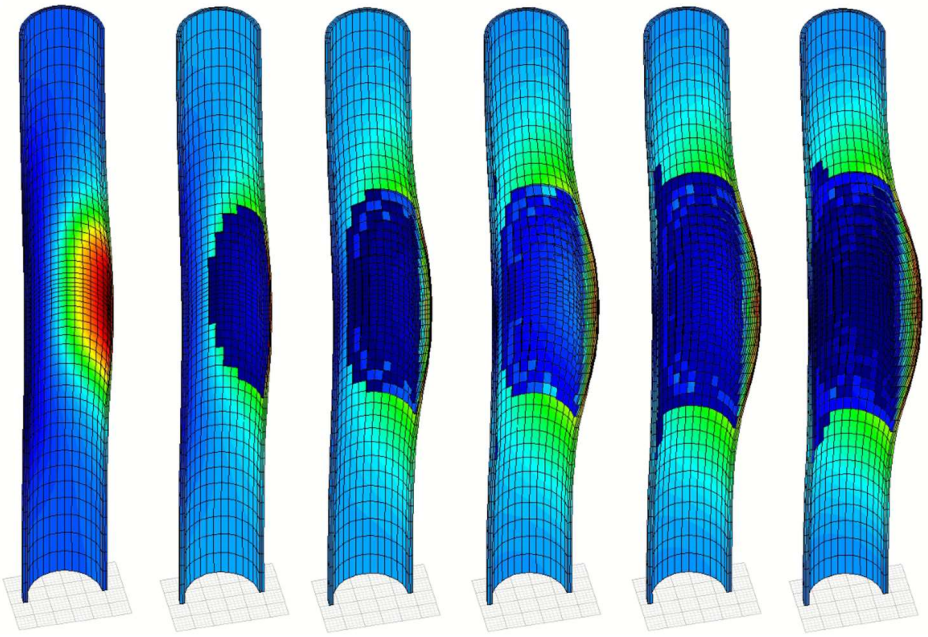

Figure 12. Example of the ILT growth in asymmetric fusiform AAA aneurysm. ILT deposition option with a constant predefined targeted luminal radius is used, explained in Figure 11. Colors represent total displacement ranging from dark blue for zero displacements to dark red for the maximum displacement. Since the newly added thrombus layer has zero displacements, it can be seen as dark blue elements.

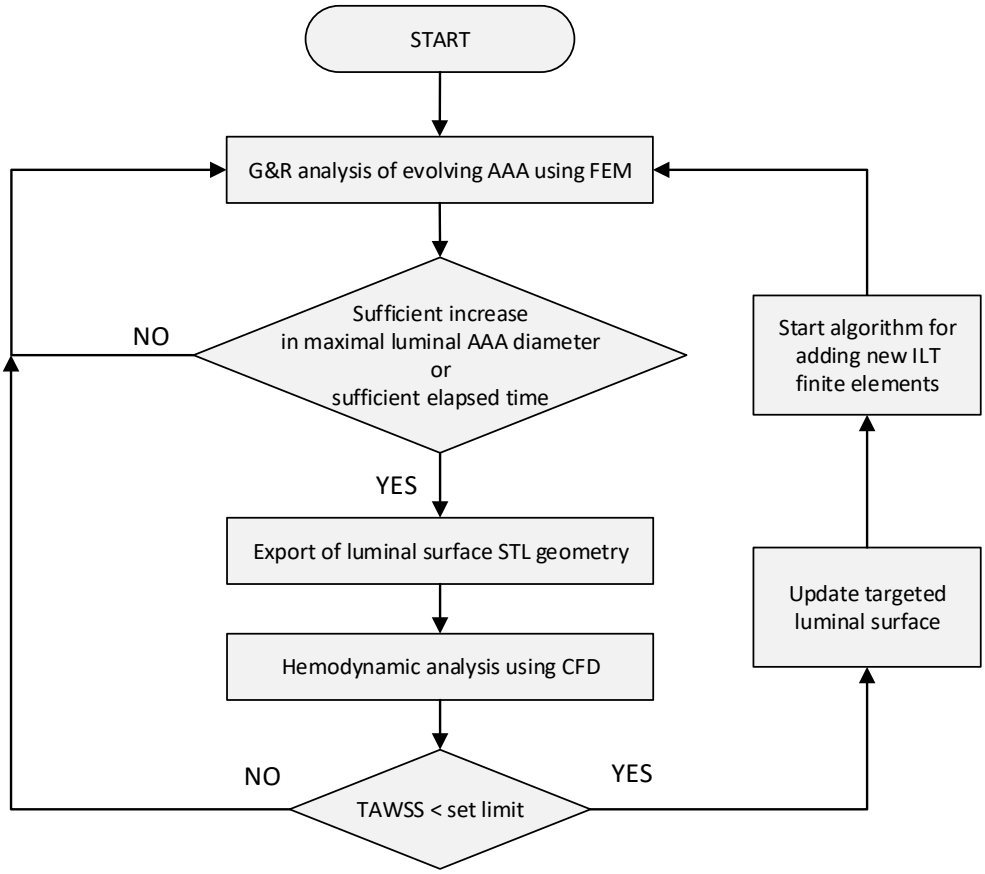

Figure 13. Flowchart for the thrombus deposition process based on the FSG approach.

several seconds), whereas the G&R model of the wall and underlying thrombus tracks changes over several decades. Thus, hemodynamics analyses are run every several G&R times steps to check whether TAWSS values are below the set threshold, or in other words, to investigate whether and where a new thrombus layer would deposit.

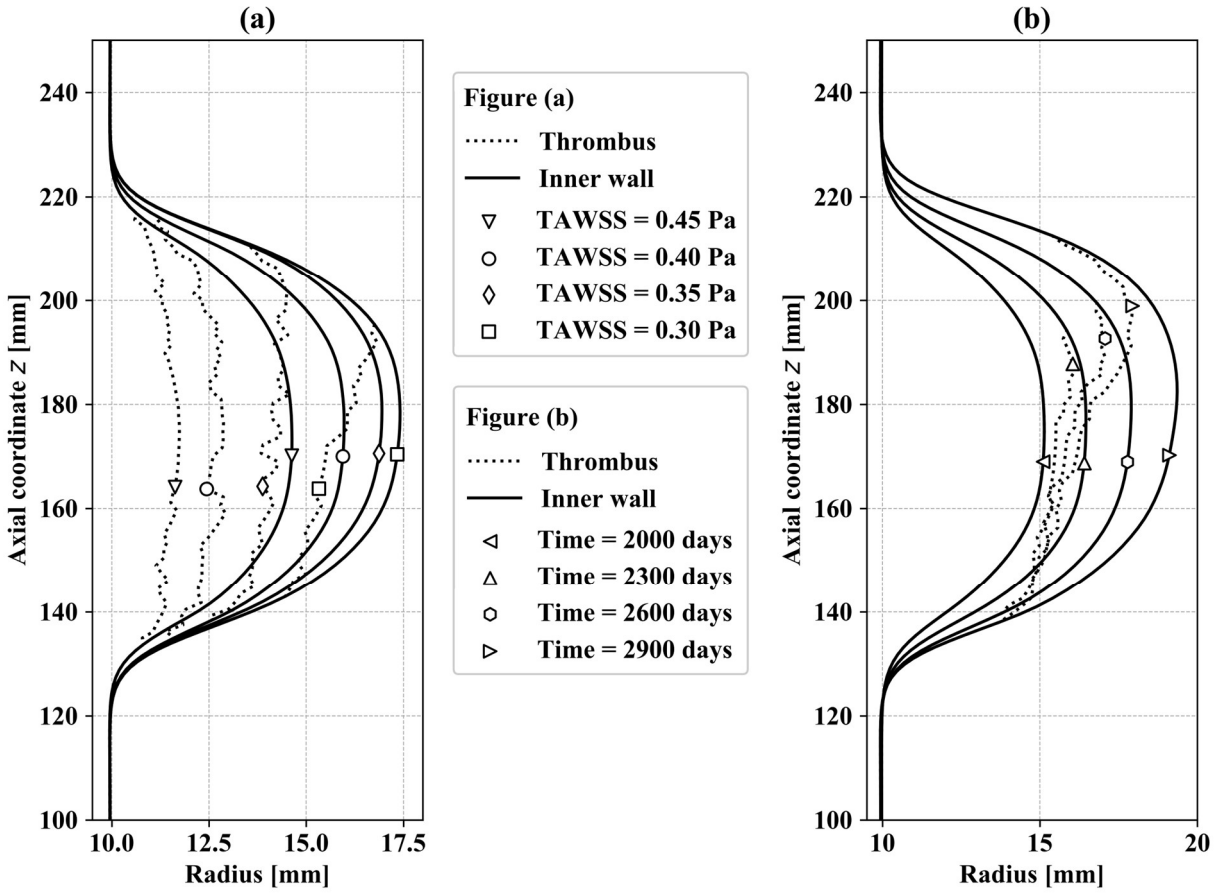

Figure 14. Contours of ILT/wall interface radii (solid curves) and luminal radii (dotted curves) at the same G&R time (2500 days) for different threshold values of TAWSS (a), and contours at different times during evolutions of AAA when the threshold value is set to 0.3 Pa (b). Taken from PAPER 5 [54].

When the FSG approach is used, deposition of ILT becomes more asymmetrical and is shifted downstream. This, in turn, leads to asymmetrical wall deformation, and the apex of AAA is no longer at the middle surface but shifted upwards. That can be seen in Figure 14, which shows the contours of ILT/wall interface radii and luminal radii for different values of TAWSS criteria and different times during AAA evolution.

2.4. Hemodynamics analysis

When specific criteria for running a hemodynamics analysis in the FSG framework are met, the G&R simulation is paused, and another custom-made FEAP subroutine generates an

STL file of luminal surface. To avoid numerical instabilities and minimize the influence of boundary conditions in CFD analysis, an extension on the inlet side and a bifurcation with iliac branches on the outlet side are added. The exported STL geometry is shown in Figure 15, with (b) and without added extensions (a). Idealistic time-dependent volume flow rate and pressure waves, based on data presented in Olufsen et al. [74], are prescribed at the inlet and the outlets, respectively. CFD hemodynamics simulations are performed in OpenFOAM with the assumption of a laminar flow and rigid walls. Blood is modeled as an incompressible (ρ = 1060 kg/m3) non-Newtonian fluid described by Carreau–Yasuda model [75]. Five cardiac cycles with 1000 timesteps per cycle are analyzed, and results only from the last cardiac cycle are used to calculate TAWSS. This is done to minimize the influence of the initial conditions. Contours of calculated TAWSS can be seen in Figure 15(c).

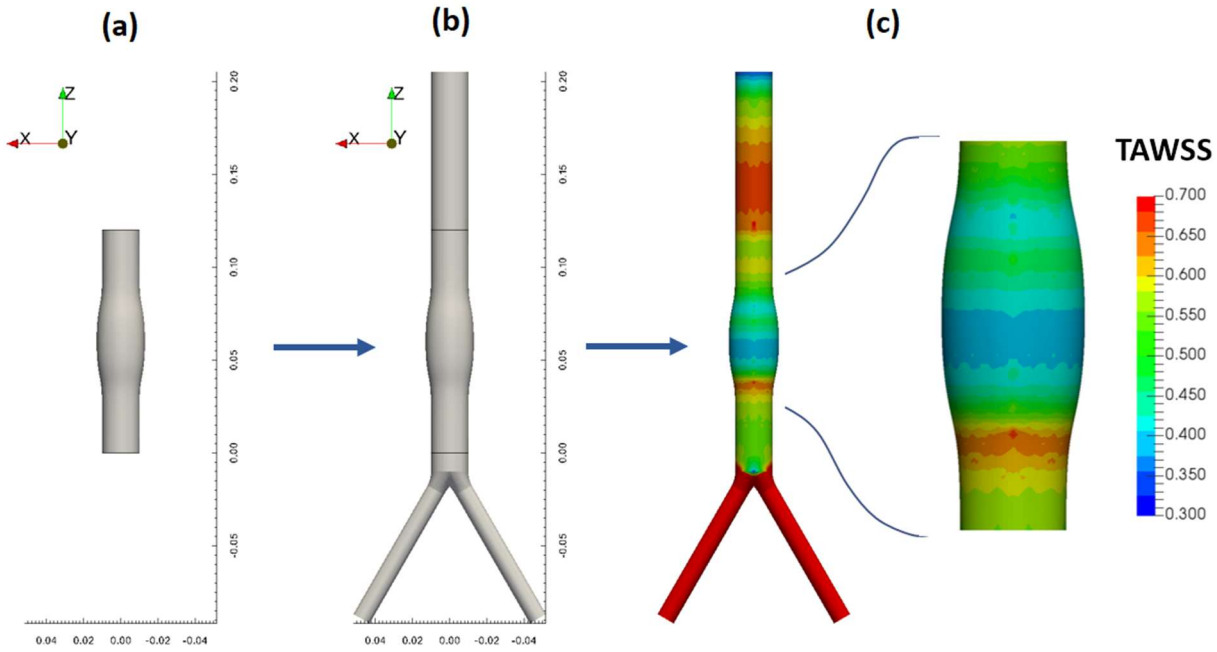

Figure 15. STL geometry of AAA luminal surface obtained from G&R analysis (a), STL geometry used for hemodynamics analysis with an extension on the inlet side and iliac branches on the outlet side (b), and contour of TAWSS calculated from CFD hemodynamics simulation (c).

For the axisymmetric FEM model of a fusiform aneurysm, TAWSS is further circumferentially averaged. The distribution of circumferentially averaged TAWSS along the axial direction is plotted in Figure 16 for the case from Figure 15. The area marked with a blue dashed rectangle has TAWSS below the set threshold value, and the ILT deposition algorithm will here add a layer of thrombus elements when G&R simulation continues. Note that this area is shifted downstream from the middle of AAA.

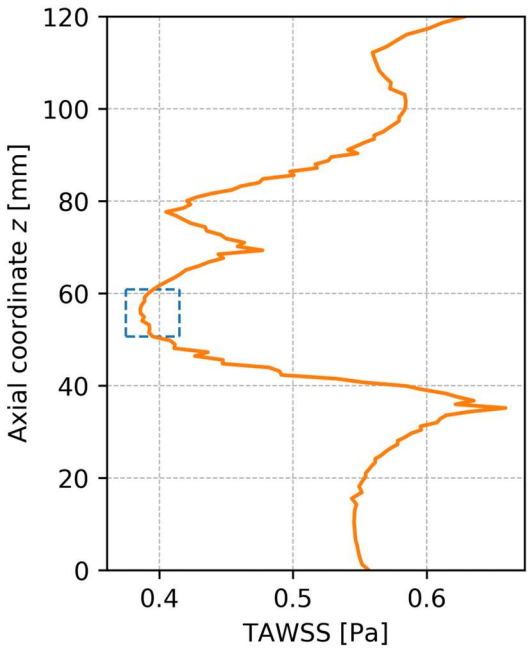

Figure 16. Circumferentially averaged TAWSS obtained from the CFD hemodynamics analysis of an axisymmetric AAA (TAWSS shown in Figure 15 (c)). TAWSS is only plotted for the aortic segment used in G&R analysis (Figure 15(b)).

2.5. ILT mechanical model

For describing the mechanical characteristics of ILT, the material model proposed in [34] was used. The model is based on the exponential strain-energy function initially developed for an arterial wall. The model can account for ILT anisotropy; however, most tested thrombi in the study behaved isotropically. Thus, the expression was slightly simplified by omitting its anisotropic part. ILT was assumed to be incompressible and discretized with the same finite elements as the aortic wall. In this study, individual mechanical properties of each thrombus layer were measured by biaxial tests, and material model parameters were calculated for each layer (Table 4 in [34]). Measured stiffness of the luminal thrombus layer was highest, and it decreased towards the abluminal layer. To capture that effect and avoid sharp changes in the material properties, a function illustrated in Figure 17 was used to gradually change the ILT material parameters from the luminal values to the abluminal values according to the thrombus thickness. The thickness of the luminal layer was set to 2 mm, while the medial layer thickness was set between 5 and 15 mm. PAPER 3 [52] describes the ILT mechanical model in more detail, and it gives the expressions for calculating the material parameters using the function shown in Figure 17.

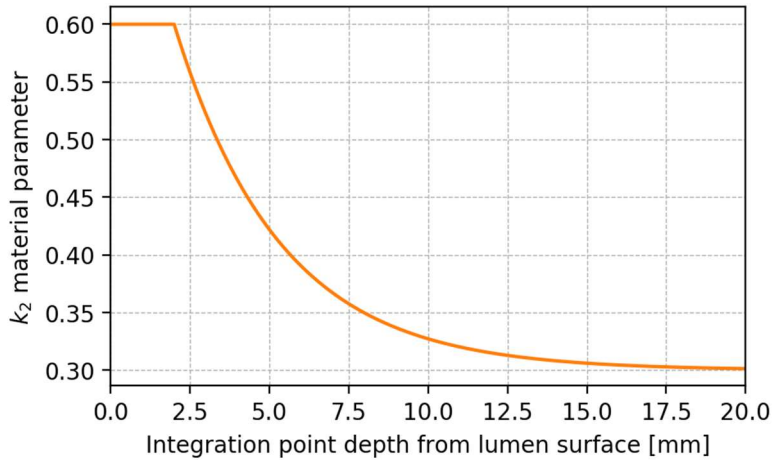

Figure 17. Example of ILT material parameter change depending on integration point depth.

In addition to the implementation of the mechanical ILT model, PAPER 3 [52] focuses on exploring the mechanical influence of the ILT on AAA progression. Two scenarios shown in Figure 11 were used for thrombus deposition. Figure 18 shows part of the results revealing the essence of the mechanical ILT influence. In this example, a deposition scenario with a constant luminal surface was used. It can be seen that the addition of ILT slowed down and stabilized the aortic expansion so much that not even an aneurysm was formed (blue vs black curve).

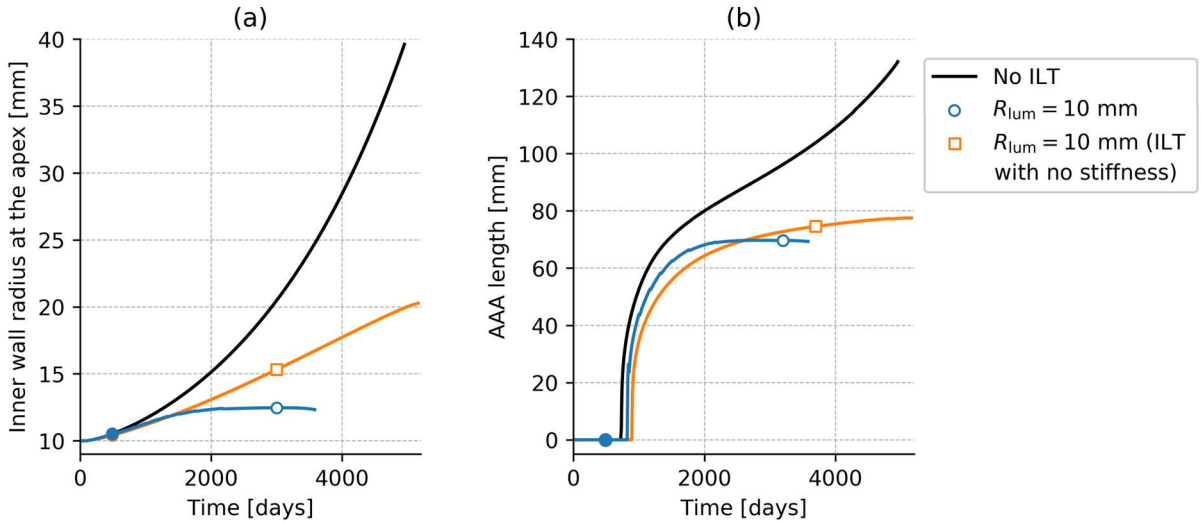

Figure 18. Radial (a) and axial (b) growth of AAA without ILT (no marker), completely thrombosed AAA with ILT stiffness (blue circle), and completely thrombosed AAA without ILT stiffness (orange square). The moment of the first ILT deposition is denoted with a solid dot.

PAPER 3 [52] discussed two ILT mechanical effects that slow down aorta expansion. First, the overall stiffness of the thrombus-laden AAA increases due to added ILT. Second, the ILT changes blood pressure distribution and thus reduces the axial tensile force on the

AAA apex. The second effect was tested using the example of a completely thrombosed aneurysm with neglected mechanical properties of the ILT. In this case, blood pressure redirection was present, but without affecting the overall stiffness of the aorta. The example is illustrated with the orange curve in Figure 18, and the results indicate that the change in blood pressure distribution is a significant part of the mechanical influence of the ILT.

Figure 18 shows only a small fraction of the results; see PAPER 3 [52] for the rest. It is important to note that PAPER 3 [52] shows the modeling of the biochemical influence as a predefined spatiotemporal function since the proteolytical activity of ILT has not yet been implemented. Thus, this stage of the G&R model likely overestimated the stability of AAA growth. PAPER 4 [53] expands the G&R model to include the biochemical influence of thrombus and gives a more realistic picture of the influence of ILT on AAA progression.

2.6. ILT biochemical model

After implementing the mechanical ILT model, the next step was to implement the biochemical ILT model. A simplified version of the model presented by Virag et al. [30] was used in this work. The original model is based on the constrained mixture theory, similarly to the aortic wall, and can track the evolution of individual constituents within the ILT, as well as biochemical processes. Using a complete model formulation on top of the large 3D G&R aortic wall model would be computationally demanding. Therefore, a simplified version was created. The simplified model is described in detail in PAPER 4 [53].

In G&R simulations of AAA performed prior to the implementation of the ILT biochemical model in FEAP, the elastin degradation was modeled with a spatiotemporal function (see PAPER 1 [25] and PAPER 3 [52] for a detailed description of the function). Contrary, in G&R simulations of thrombus-laden AAA with included ILT biochemical effects, elastin is only initially locally degraded (by 15%) to create an insult that causes a slight aorta dilatation sufficient for deposition of the first thrombus layer. All subsequent elastin degradation is due to the biochemical effect of enzymes emanating from the thrombus luminal layer and the *vasa vasorum* on the outer surface of the aortic wall. The concentration of enzymes can be calculated in these sources by using equations of the biochemical model. The luminal concentration depends most notably on the thickness of the thrombus luminal layer; it increases with luminal layer thickness up to the maximum thickness of 2 mm and afterwards it remains constant. Concentration in the *vasa vasorum* is dependent on the amount of degraded elastin in the wall. As the amount of degraded elastin increases during AAA

progression, the enzyme concentration in the *vasa vasorum* also increases. To calculate the concentration of enzymes in all other points of the model, an external 3D FEM analysis is used. More precisely, at the beginning of each increment in the G&R simulation of a thrombus-laden AAA, a custom-made FEAP subroutine is called, which runs a separate external 3D diffusion analysis that uses the FEAP thermal analysis solver. The same differential equations govern thermal diffusion and chemical diffusion; thus an existing FEAP thermal solver can be used. The flowchart of this process is shown in Figure 19.

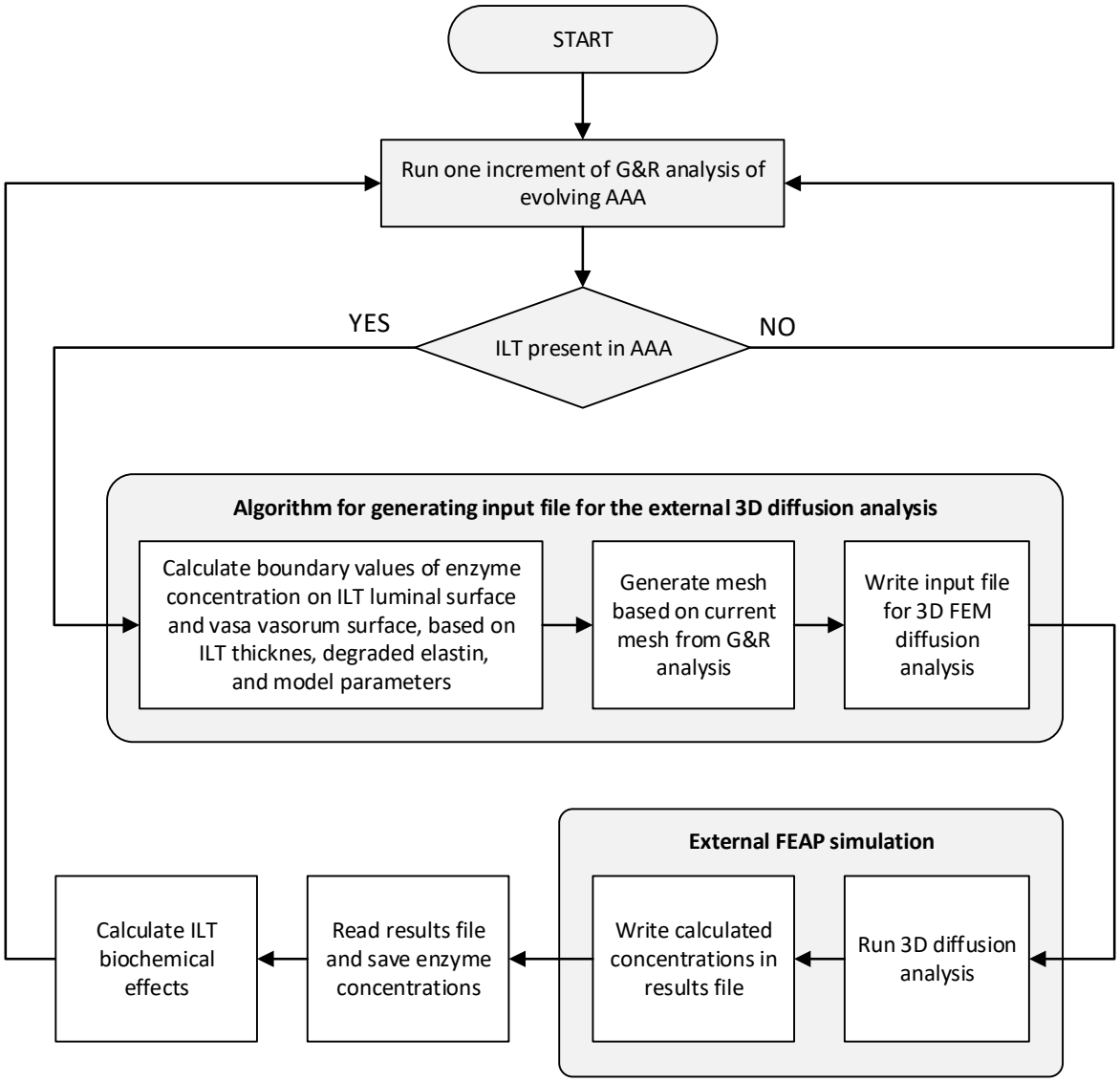

Figure 19. Flowchart for incorporating biochemical ILT effects into G&R analysis of thrombus-laden AAA.

The subroutine first creates an input file containing all the necessary data to perform a diffusion analysis. These data include: mesh that is a copy of the current AAA mesh in the G&R simulation, concentration of enzymes (defined in the luminal layer and the *vasa*

vasorum) that act as a temperature boundary condition, and commands for running the analysis. The enzyme concentration in all model nodes is written in a file at the end of the diffusion analysis. This file is then read by the G&R simulation and the concentrations are stored for later use at an integration point level, where enzyme concentration directly affects wall mechanics by degrading its constituents.

Some of the parameters used in the implemented simplified biochemical model were taken from the original biochemical model by Virag et al. [38]. However, due to the differences in the models (simplified vs. full formulation) and the used methods (3D-FEM vs. semi-analytical), some of the mechanical and biochemical parameters needed to be calibrated to replicate the results from the original model. The final values of the parameters are listed in Table 1 in PAPER 4 [53]. Calibration was performed in several steps. First, biochemical model parameters were adjusted to replicate the enzyme's (i.e., elastases and collagenases) spatial and temporal distribution during AAA progression. Second, the range of the weighting factor, which correlates the concentration of elastases and increased elastin degradation, was chosen so that 10-20% of the functional elastin remained 20 years after the formation of the aneurysm. Third, mechanical ILT parameters were chosen to give an appropriate spatiotemporal distribution of the stresses within the wall and thrombus. Finally, the range of the weighting factor that correlates the concentration of collagenases and increased collagen degradation was chosen to make the AAA growth rate realistic.

Apart from the introduction to the implementation of the biochemical model, PAPER 4 [53] has shown very interesting results. Besides confirming already accepted hypotheses, it brought some new and exciting insights into biochemomechanical processes within the AAA. Furthermore, the results indicate that later ILT formation leads to higher growth rates of the maximum AAA diameter than its early deposition, despite lower peak protease activity and related degradation of the extracellular matrix. In addition, thrombus deposition significantly affects the aneurysmal sac shape and volume, see PAPER 4 [53] for more detail.

Figure 20(a) shows an example of the aorta with a sudden initial degradation of 15% of elastin. Without a thrombus (black curves), this initial insult is not enough to cause the formation of an aneurysm, and the aorta finds a new homeostatic state with a slightly increased radius. However, if an ILT is deposited (orange curve), a thin proteolytically active luminal ILT layer degrades the aortic wall and causes rapid aorta dilatation and aneurysm formation. In this example, a full thrombosis scenario with a constant luminal radius was used. In Figure 20(b), the axial length was calculated as the distance between the sections

with a diameter 10% larger than the healthy one. If the thrombus does not deposit, the diameter never reaches this value and the AAA length remains zero (black curve). However, as thrombus deposits, the AAA length initially expands steeply, and after the first medial layer of the ILT layer forms, growth slows (orange curve), see PAPER 4 [53] for a more detailed discussion. Figure 20(c) shows the contours of the inner radius at three different G&R times. The growth of AAA and changes in the shape and volume of the AAA sac can easily be understood from the contours.

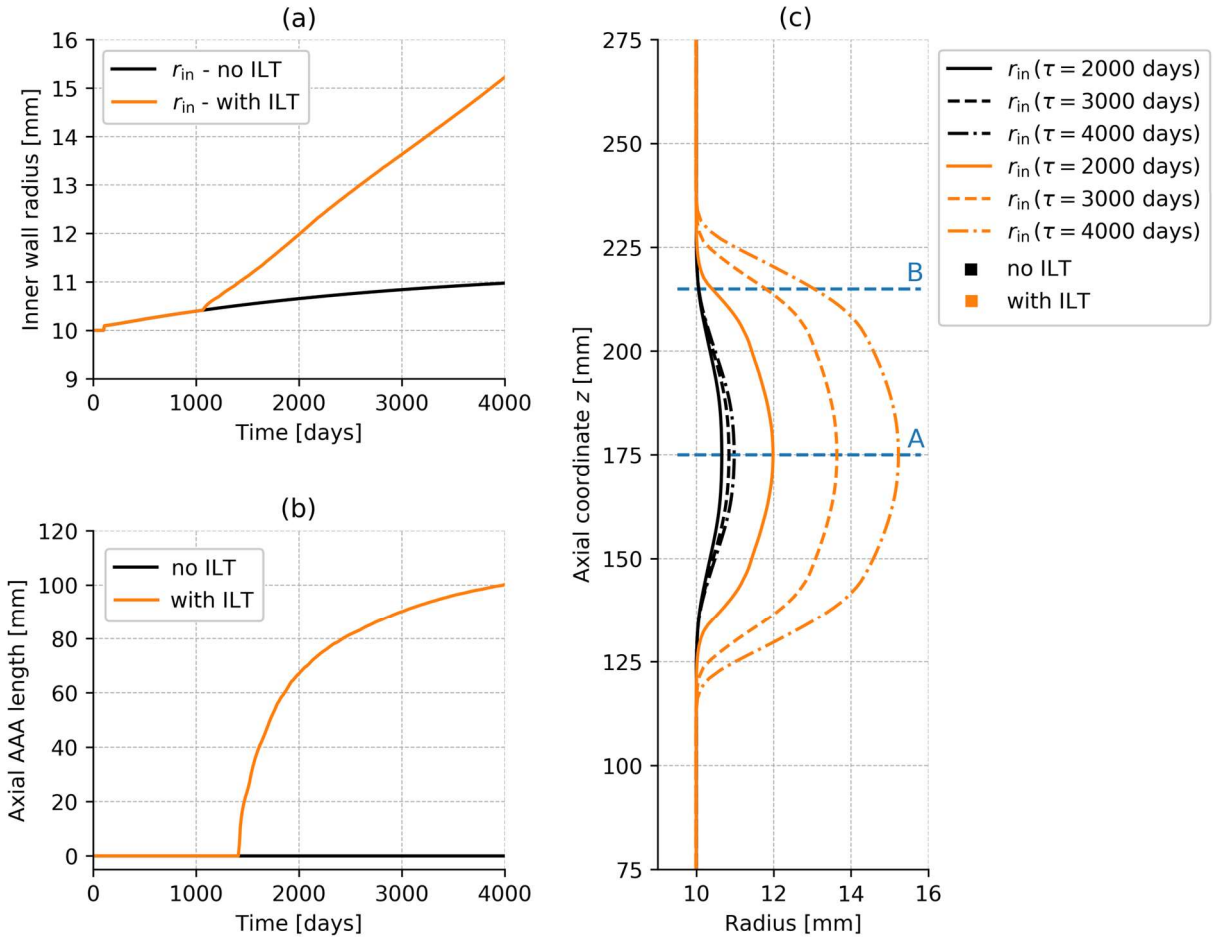

Figure 20. Radial (a) and axial (b) growth of the aorta without thrombus after a sudden degradation of 15% of elastin (black curve), the evolution of a completely thrombosed aneurysm (orange curve), and contours of the inner radii at different G&R times (c). Taken from PAPER 4 [53].

Two sections (A and B) are indicated in Figure 20(c), and in Figure 21(b), the time distribution of the normalized enzyme concentration is plotted for those sections. Enzyme concentration on the inner surface of the aortic wall increases with ILT thickness up until the maximum thickness of the ILT luminal layer is reached (set as 2 mm). With a further increase in the ILT thickness, a medial layer starts to form. Since it stands as a barrier between the proteolytically active luminal layer and the inner aortic wall, the enzyme concentration at the

inner radius decreases. This is also visible in Figure 21(a) from the axial distribution of enzyme concentration at the inner radius. With the formation of the medial layer, the concentration of enzymes at the apex decreases; however, it remains high on the AAA neck, where thin proteolytically active ILT is present. For ease of comparison, the amount of enzyme was normalized by its initial amount at the apex on the outer radius of the wall. Figure 21(c) illustrates an example of enzyme concentration contours for the three G&R times used in Figure 21(a). It can be seen (by the red color in the contour plot) that luminal enzyme concentration initially increases as ILT reaches 2 mm in thickness and then remains constant. Furthermore, the area with the maximum luminal enzyme concentration (red color) expands axially as ILT grows.

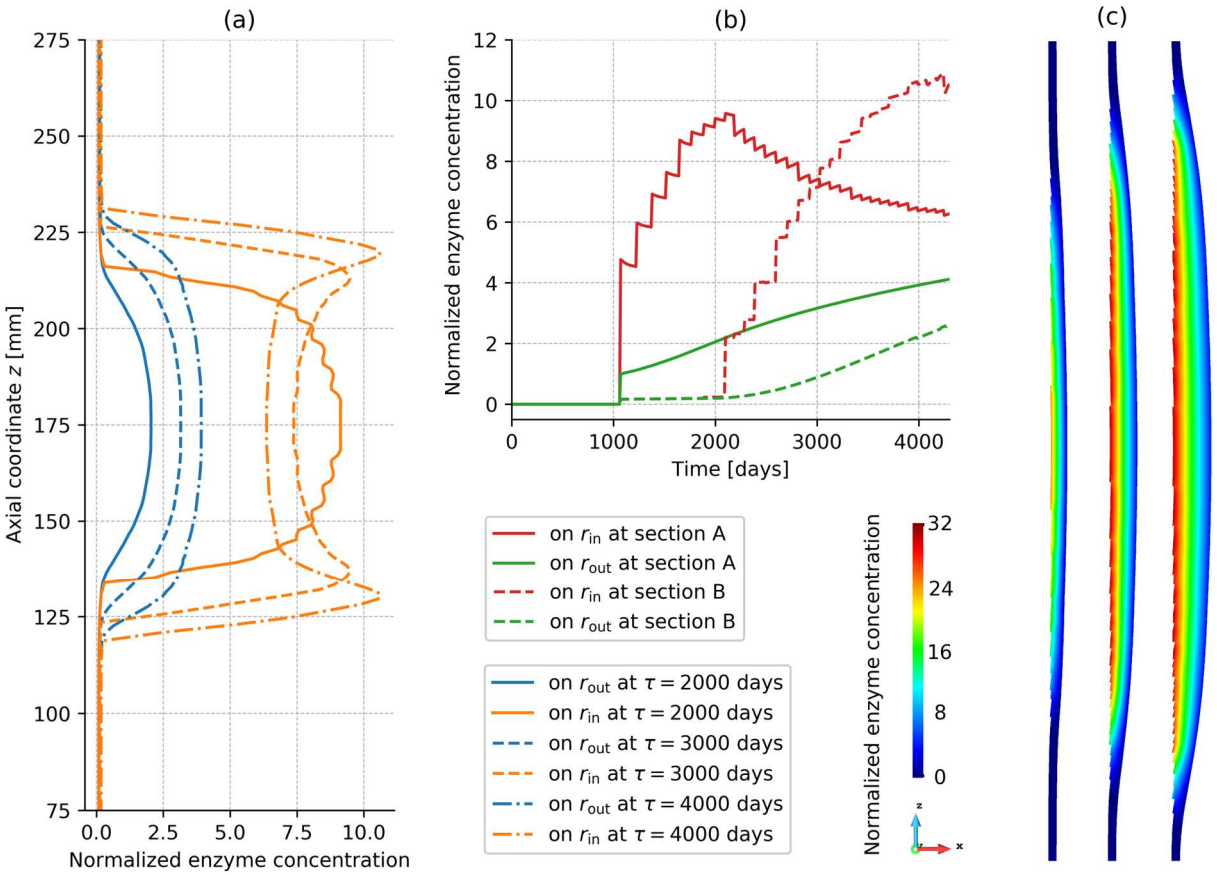

Figure 21. Axial distribution of normalized elastases concentration at inner and outer radius at different G&R times (a), the evolution of normalized elastases activity at the inner and outer wall radius at sections A and B (sections marked in Figure 20) (b), and contour plots of the normalized elastases concentration at three different corresponding G&R times (c).

2.7. Model limitation

As in every model, certain limitations need to be mentioned. The G&R model aims to describe the *in vivo* aortic wall, while specific model parameters are measured *ex vivo* on the

unloaded configuration of the aortic wall (e.g., fiber mean angles and dispersion). Due to the constituent's pre-stretches in the aortic wall, structural parameters *in vivo and ex vivo* are not equal. Still, these parameters must be used in the absence of *in vivo* data. Furthermore, surrounding tissues were neglected, and the aorta was considered as an isolated organ.

Little is known about the causes of AAA formation and protease distribution or their sources in AAAs without thrombus. For this reason, in analyses of the biochemical influence of ILT, an initial insult was needed to cause a slight expansion of the aorta which then initiated the ILT deposition process. This initial insult was simplified as a sudden local degradation of elastin. In analyses without any biochemical ILT influence, the elastin degradation was described with a spatiotemporal function.

In CFD hemodynamics analyses, blood flow was assumed as laminar. Even though this is a reasonable assumption for a healthy aorta, it may not be for the AAA, where turbulent flow may occur due to the changes in expanded luminal geometry.

Although the model can describe the realistic behavior of the aortic wall and AAA, it is difficult to use it for patient-specific modeling. Model parameters can vary significantly from patient to patient and most of them cannot be determined for the *in vivo* state. For example, the composition of each patient's aortic wall is unique and can only be measured *ex vivo*. Likewise, the constituent pre-stretching, which massively influences the result, can only be calculated from the opening angle of the excised aortic wall segment.

3. CONCLUSION AND FUTURE WORK

3.1. Conclusion

Describing the behavior of a complex mechanobiological system like an AAA, is a very demanding task. To be realistic, the model must consider for the evolving composite layered structure of the aortic wall, with constituents that exhibit nonlinear and anisotropic behavior and are constantly degraded and produced in response to external stimuli. Moreover, new constituents are embedded in the matrix with a certain pre-stretch during the production, which is crucial for the aortic wall adaptive capabilities. In addition, smooth muscle cells have an active response that is controlled by the endothelial cell response to perturbation of wall shear stress. At the same time, collagen fibers show a non-axisymmetric dispersion around the mean fiber direction. Furthermore, most AAAs contain ILT, the formation of which is strongly believed to be influenced by hemodynamics, i.e., blood flow. Its mechanical properties and biochemical influence through proteolytic activity on the aortic wall have a significant impact on AAA progression.

The main aim of this research was to develop a comprehensive and realistic 3D numerical model that would consider all the abovementioned properties of AAA. This thesis and corresponding papers presented here give a detailed overview of the developed FSG model. To the author's knowledge, such a complex FSG model has not yet been developed and presented in the literature and presents an extraordinary scientific contribution. Each included paper introduces a part of the FSG model and its scientific contribution. Nonetheless, if all papers are considered as a whole, they form a unity that surpass the impact of individual papers.

PAPER 1 [25] and PAPER 2 [51] are focused on the development of a realistic model of the aortic wall. It is necessary to have a unique formulation that can describe healthy aortic walls, as well as changes in the wall structure during disease development. Introducing the constrained mixture G&R theory in a 3D finite element formulation was an essential first step, which was the focus of the first paper (PAPER 1, [25]). FE implementation enables realistic computer simulations of a fusiform AAA, while the constrained mixture G&R theory enables tracking individual constituent's properties (e.g., mass, stress, fiber orientation). This approach significantly increases model predicting capabilities (e.g., AAA growth rate, rupture). The model implementation was validated by analyzing cases of aortic adaptations to

hemodynamics changes, i.e., changes in blood flow and pressure of a non-idealized aorta. The results showed a good agreement with the membrane theory, animal models, and clinical observations. The second paper (PAPER 2, [51]) introduced the very first implementation of the collagen fiber dispersion model based on the GST approach in a constrained mixture G&R model of an aortic wall. In addition, a new definition of the fiber pre-stretch tensor compatible with the fiber dispersion model and considering pre-stretches perpendicular to the mean fiber direction has been proposed. The results in the paper showed that changes in the aortic wall structure (i.e., changing fiber dispersion and mean fiber direction) have significant effects on the mechanical response, the stress distribution within the wall, and the growth of AAA. The fiber dispersion model is based directly on the results of multiphoton microscopy and is therefore an important step towards a realistic wall model.

The third and fourth papers (PAPER 3 and 4, [52], [53]) focused on the development of a 3D finite element model describing the formation and structural transformation of the ILT. The developed G&R model can simulate the expansion of the aortic wall with the addition of considering the ILT's mechanical and biochemical influence on the wall structure. The third paper (PAPER 3, [52]) presents the computational model and an algorithm for adding new finite elements, representing a new ILT layer added during the G&R analysis of thrombus-laden AAA. The algorithm must define node coordinates, node connectivity, boundary conditions, loading, and connection to the underlaying surface for each new layer. The fourth paper (PAPER 4, [53]) focuses on the calculation of the concentrations of enzymes (collagenases and elastases) in the entire aortic wall and ILT. The spatiotemporal distribution of enzyme concentrations is essential for realistic modeling of biochemical interactions between the ILT and the aortic wall. At each step of the G&R simulation, a separate external 3D FEM analysis is performed to calculate the enzyme distribution. Apart from the introduction of numerical models, both papers have shown very interesting results. Besides confirming already accepted hypotheses, they brought some new and exciting insights into biochemomechanical processes within the AAA.

Finally, the fifth paper (i.e., a book chapter, PAPER 5, [54]) completed the FSG model by presenting a framework for connecting the hemodynamics analysis. Hemodynamics is loosely coupled with the ILT deposition algorithm. A TAWSS from the CFD analysis is used to determine a location for depositing new ILT layers. Compared to currently available numerical models, the developed FSG model can provide a deeper insight into processes within the AAA and better predict the AAA outcome (growth rate, rupture, stabilization).

3.2. Future work

In future work, the developed FSG model will be used for further simulations and analyses of ILT growth and its biochemomechanical influence on the AAA progression. In the included paper (PAPERS 4, [53]), where the biochemical influence of ILT was studied in detail, the ILT deposition was not based on the hemodynamics analysis. Therefore, the next step is to make a comprehensive set of analyses to examine the ILT biochemical influence with activated hemodynamics options, i.e., to use the full potential of the FSG model. In the current version of the FSG model, TAWSS is used to predict the location of ILT growth. Another goal is to expand the model to use additional indicators of thrombus deposition that exist in the literature, such as the oscillatory shear index (OSI), platelet activation potential (PLAP), and thrombus formation potential (TFP). As one can assume, the developed FSG G&R model is computationally intensive due to its complexity. In fact, some of the AAA simulations performed during this research took up to a week to complete. Another idea for future work is to use the FSG model as a benchmark for testing and developing simpler but computationally much faster models.

BIBLIOGRAPHY

[1] N. Sakalihasan, R. Limet, and O. D. Defawe, "Abdominal aortic aneurysm," *Lancet*, vol. 365, pp. 1577–89, 2005, doi: 10.1016/S0140-6736(05)66459-8.

[2] J. D. Humphrey and G. A. Holzapfel, "Mechanics, mechanobiology, and modeling of human abdominal aorta and aneurysms," *Journal of Biomechanics*, vol. 45, pp. 805–814 Contents, 2012, doi: 10.1016/j.jbiomech.2011.11.021.

[3] J. D. Humphrey, "Constrained Mixture Models of Soft Tissue Growth and Remodeling – Twenty Years After," *Journal of Elasticity*, 2021, doi: 10.1007/s10659-020-09809-1.

[4] R. C. Darling, C. R. Messina, D. C. Brewster, and L. W. Ottinger, "Autopsy study of unoperated abdominal aortic aneurysms. The case for early resection.," *Circulation*, vol. 56, no. 3 Suppl, pp. II161-4, Sep. 1977.

[5] M. Mehta, R. Darling, B. Chang, P. Paty, S. Roddy, P. Kreienberg, K. Ozsvath and D. Shah, "Does Sac Size Matter? Findings Based on Surgical Exploration of Excluded Abdominal Aortic Aneurysms," *Journal of Endovascular Therapy*, vol. 12, pp. 183–188, 2005, doi: 10.1583/04-1402.1.

[6] D. H. J. Wang, M. S. Makaroun, M. W. Webster, and D. A. Vorp, "Effect of intraluminal thrombus on wall stress in patient-specific models of abdominal aortic aneurysm," *Journal of Vascular Surgery*, vol. 36, no. 3, pp. 598–604, 2002, doi: 10.1067/mva.2002.126087.

[7] C. Behr-Rasmussen, N. Grondal, M. B. Bramsen, M. D. Thomsen, and J. S. Lindholt, "Mural thrombus and the progression of abdominal aortic aneurysms: A large population-based prospective cohort study," *European Journal of Vascular and Endovascular Surgery*, vol. 48, no. 3, pp. 301–307, 2014, doi: 10.1016/j.ejvs.2014.05.014.

[8] J. Tong and G. A. Holzapfel, "Structure, Mechanics, and Histology of Intraluminal Thrombi in Abdominal Aortic Aneurysms," *Annals of Biomedical Engineering*, vol. 43, no. 7, pp. 1488–1501, 2015, doi: 10.1007/s10439-015-1332-5.

[9] J. S. Wilson, L. Virag, P. di Achille, I. Karšaj, and J. D. Humphrey, "Biochemomechanics of Intraluminal Thrombus in Abdominal Aortic Aneurysms,"

Journal of Biomechanical Engineering, vol. 135, no. 2, p. 021011, 2013, doi: 10.1115/1.4023437.

[10] E. K. Rodriguez, A. Hoger, and A. D. Mcculloch, "Stress-dependent finite growth in soft elastic tissues," *Pergamon .I. Biomchanics*, vol. 21, no. 4, pp. 455–467, 1994.

[11] L. A. Taber and D. W. Eggers, "Theoretical Study of Stress-Modulated Growth in the Aorta," *Journal of Theoretical Biology*, vol. 180, pp. 343–357, 1996.

[12] A. Rachev, "A Model of Arterial Adaptation to Alterations in Blood Flow," *Journal of Elasticity*, vol. 61, pp. 83–111, 2000, doi: 10.1023/A:1010800703478.

[13] T. S. E. Eriksson, P. N. Watton, X. Y. Luo, and Y. Ventikos, "Modelling volumetric growth in a thick walled fibre reinforced artery," *Journal of the Mechanics and Physics of Solids*, vol. 73, pp. 134–150, 2014, doi: 10.1016/j.jmps.2014.09.003.

[14] A. Grytsan, T. S. E. Eriksson, P. N. Watton, and T. C. Gasser, "Growth description for vessel wall adaptation: a thick-walled mixture model of abdominal aortic aneurysm evolution," *Materials*, vol. 10, no. 9, p. e994, 2017, doi: 10.3390/ma10090994.

[15] J. D. Humphrey and K. R. Rajagopal, "A constrained mixture model for growth and remodeling of soft tissues," *Mathematical Models and Methods in Applied Sciences*, vol. 12, no. 03, pp. 407–430, Mar. 2002, doi: 10.1142/S0218202502001714.

[16] S. Baek, K. R. Rajagopal, and J. D. Humphrey, "Competition between radial expansion and thickening in the enlargement of an intracranial saccular aneurysm," *Journal of Elasticity*, vol. 80, pp. 13–31, 2005, doi: 10.1007/s10659-005-9004-6.

[17] S. Baek, K. R. Rajagopal, and J. D. Humphrey, "A theoretical model of enlarging intracranial fusiform aneurysms," *Journal of Biomechanical Engineering*, vol. 128, no. 1, pp. 142–149, 2006, doi: 10.1115/1.2132374.

[18] A. Valentín and J. D. Humphrey, "Parameter sensitivity study of a constrained mixture model of arterial growth and remodeling," *Journal of Biomechanical Engineering*, vol. 131, no. 10, p. 101006, 2009, doi: 10.1115/1.3192144.

[19] P. N. Watton, N. A. Hill, and M. Heil, "A mathematical model for the growth of the abdominal aortic aneurysm," *Biomechanics and Modeling in Mechanobiology*, vol. 3, pp. 98–113, 2004, doi: 10.1007/s10237-004-0052-9.

[20] P. N. Watton and N. A. Hill, "Evolving mechanical properties of a model of abdominal aortic aneurysm," *Biomechanics and Modeling in Mechanobiology*, vol. 8, no. 1, pp. 25–42, 2009, doi: 10.1007/s10237-007-0115-9.

[21] J. S. Wilson, S. Baek, and J. D. Humphrey, "Importance of initial aortic properties on the evolving regional anisotropy, stiffness and wall thickness of human abdominal aortic aneurysms," *Journal of the Royal Society Interface*, vol. 9, no. 74, pp. 2047–2058, 2012, doi: 10.1098/rsif.2012.0097.

[22] J. S. Wilson, S. Baek, and J. D. Humphrey, "Parametric study of effects of collagen turnover on the natural history of abdominal aortic aneurysms," *Proceedings of the Royal Society A: Mathematical, Physical and Engineering Sciences*, vol. 469, no. 2150, p. 20120556, 2012, doi: 10.1098/rspa.2012.0556.

[23] I. Karšaj, J. Sorić, and J. D. Humphrey, "A 3-D framework for arterial growth and remodeling in response to altered hemodynamics," *International Journal of Engineering Science*, vol. 48, no. 11, pp. 1357–1372, 2010, doi: 10.1016/j.ijengsci.2010.06.033.

[24] I. Karšaj and J. D. Humphrey, "A multilayered wall model of arterial growth and remodeling," *Mechanics of Materials*, vol. 44, pp. 110–119, 2012, doi: 10.1016/j.mechmat.2011.05.006.

[25] N. Horvat, L. Virag, G. A. Holzapfel, J. Sorić, and I. Karšaj, "A finite element implementation of a growth and remodeling model for soft biological tissues : Verification and application to abdominal aortic aneurysms," *Computer Methods in Applied Mechanics and Engineering*, vol. 352, pp. 586–605, 2019, doi: 10.1016/j.cma.2019.04.041.

[26] C. J. Cyron, R. C. Aydin, and J. D. Humphrey, "A homogenized constrained mixture (and mechanical analog) model for growth and remodeling of soft tissue," *Biomechanics and Modeling in Mechanobiology*, vol. 15, no. 6, pp. 1389–1403, 2016, doi: 10.1007/s10237-016-0770-9.

[27] F. A. Braeu, A. Seitz, R. C. Aydin, and C. J. Cyron, "Homogenized constrained mixture models for anisotropic volumetric growth and remodeling," *Biomechanics and Modeling in Mechanobiology*, vol. 16, no. 3, pp. 889–906, 2017, doi: 10.1007/s10237-016-0859-1.

[28] F. Inzoli *et al.*, “Biomechanical Factors in Abdominal Aortic Aneurysm Rupture,” *European Journal of Vascular and Endovascular Surgery*, vol. 7, no. 6, pp. 667–674, Nov. 1993.

[29] F. Ene, C. Gachon, P. Delassus, R. Carroll, F. Stefanov, P. O'Flynn and L. Morris, “In vitro evaluation of the effects of intraluminal thrombus on abdominal aortic aneurysm wall dynamics,” *Medical Engineering & Physics*, vol. 33, no. 8, pp. 957–966, 2011, doi: 10.1016/j.medengphy.2011.03.005.

[30] F. Riveros, G. Martufi, T. Gasser, and J. Rodriguez, “Influence of Intraluminal Thrombus Topology on AAA Passive Mechanics,” *Computing in Cardiology 2010*, vol. 40, pp. 899–902, 2013.

[31] E. di Martino *et al.*, “Biomechanics of abdominal aortic aneurysm in the presence of endoluminal thrombus: Experimental characterisation and structural static computational analysis,” *European Journal of Vascular and Endovascular Surgery*, vol. 15, no. 4, pp. 290–299, Apr. 1998, doi: 10.1016/S1078-5884(98)80031-2.

[32] D. H. J. Wang, M. Makaroun, M. W. Webster, and D. A. Vorp, “Mechanical Properties and Microstructure of Intraluminal Thrombus From Abdominal Aortic Aneurysm,” *Journal of Biomechanical Engineering*, vol. 123, no. 6, pp. 536–539, Dec. 2001, doi: 10.1115/1.1411971.

[33] J. P. vande Geest, M. S. Sacks, and D. A. Vorp, “A planar biaxial constitutive relation for the luminal layer of intra-luminal thrombus in abdominal aortic aneurysms,” *Journal of Biomechanics*, vol. 39, no. 13, pp. 2347–2354, Jan. 2006, doi: 10.1016/j.jbiomech.2006.05.011.

[34] J. Tong, T. Cohnert, P. Regitnig, and G. A. Holzapfel, “Effects of age on the elastic properties of the intraluminal thrombus and the thrombus-covered wall in abdominal aortic aneurysms: Biaxial extension behaviour and material modelling,” *European Journal of Vascular and Endovascular Surgery*, vol. 42, no. 2, pp. 207–219, Aug. 2011, doi: 10.1016/j.ejvs.2011.02.017.

[35] W. Bosman, J. Hinnen, W. Kopp, T. Van Der Steenhoven, B. Kaptein, O. Koning and J. Hamming, “Influence of aneurysm wall stiffness and the presence of intraluminal thrombus on the wall movement of an aneurysm - An in vitro study,” *Vascular*, vol. 20, no. 4, pp. 203–209, 2012, doi: 10.1258/vasc.2011.oa0324.

[36] S. Marbacher *et al.*, "Loss of mural cells leads to wall degeneration, aneurysm growth, and eventual rupture in a rat aneurysm model," *Stroke*, vol. 45, no. 1, pp. 248–254, 2014, doi: 10.1161/STROKEAHA.113.002745.

[37] D. Koole *et al.*, "Intraluminal abdominal aortic aneurysm thrombus is associated with disruption of wall integrity," *Journal of Vascular Surgery*, vol. 57, no. 1, pp. 77–83, 2013, doi: 10.1016/j.jvs.2012.07.003.

[38] L. Virag, J. S. Wilson, J. D. Humphrey, and I. Karšaj, "A computational model of biochemomechanical effects of intraluminal thrombus on the enlargement of abdominal aortic aneurysms," *Annals of Biomedical Engineering*, vol. 43, no. 12, pp. 2852–2867, 2015, doi: 10.1007/s10439-015-1354-z.

[39] P. di Achille, G. Tellides, C. A. Figueroa, and J. D. Humphrey, "A haemodynamic predictor of intraluminal thrombus formation in abdominal aortic aneurysms," *Proceedings of the Royal Society A: Mathematical, Physical and Engineering Sciences*, vol. 470, no. 2172, pp. 20140163–20140163, 2014, doi: 10.1098/rspa.2014.0163.

[40] B. A. Zambrano, H. Gharahi, C. Lim, F. Jaberi, J. Choi, W. Lee and S. Baek, "Association of Intraluminal Thrombus, Hemodynamic Forces, and Abdominal Aortic Aneurysm Expansion Using Longitudinal CT Images," *Annals of Biomedical Engineering*, vol. 44, no. 5, pp. 1502–1514, 2016, doi: 10.1007/s10439-015-1461-x.

[41] G. A. Ateshian, "On the theory of reactive mixtures for modeling biological growth," *Biomechanical Modeling in Mechanobiology*, vol. 6, pp. 423–445, 2007.

[42] C. A. Figueroa *et al.*, "A Computational Framework for Fluid-Solid-Growth Modeling in Cardiovascular Simulations," *Computer Methods in Applied Mechanics and Engineering*, vol. 198, no. 45–46, pp. 3583–3602, 2009, doi: 10.1016/j.cma.2008.09.013.

[43] P. N. Watton, N. B. Raberger, G. A. Holzapfel, and Y. Ventikos, "Coupling the Hemodynamic Environment to the Evolution of Cerebral Aneurysms: Computational Framework and Numerical Examples," *Journal of Biomechanical Engineering*, vol. 131, no. 10, Oct. 2009, doi: 10.1115/1.3192141.

[44] A. Sheidaei, S. C. Hunley, S. Zeinali-Davarani, L. G. Raguin, and S. Baek, "Simulation of abdominal aortic aneurysm growth with updating hemodynamic loads using a

realistic geometry," *Medical Engineering & Physics*, vol. 33, no. 1, pp. 80–88, 2011, doi: 10.1016/j.medengphy.2010.09.012.

[45] J. Wu and C. Shadden, "Coupled simulation of hemodynamics and vascular growth and remodeling in a subject-specific geometry," *Annals of Biomedical Engineering*, vol. 43, no. 7, pp. 1543–1554, 2015, doi: 10.1007/s10439-015-1287-6.

[46] A. Grytsan, P. N. Watton, and G. A. Holzapfel, "A thick-walled fluid–solid-growth model of abdominal aortic aneurysm evolution: application to a patient-specific geometry," *Journal of Biomechanical Engineering,* vol. 137, no. 3, p. 031008, 2015, doi: 10.1115/1.4029279.

[47] P. Rissland, Y. Alemu, S. Einav, J. Ricotta, and D. Bluestein, "Abdominal Aortic Aneurysm Risk of Rupture: Patient-Specific FSI Simulations Using Anisotropic Model," *Journal of Biomechanical Engineering*, vol. 131, pp. 031001-1-031001–10, 2009, doi: 10.1115/1.3005200.

[48] C. M. Scotti, S. L. Cornejo, and E. A. Finol, "Biomechanics of Abdominal Aortic Aneurysms: Flow-Induced Wall Stress Distribution," *ICCES*, vol. 1, no. 1, pp. 41–47, 2007.

[49] S. Chandra, S. Raul, A. Jana, R. Biederman, M. Doyle, S. Muluk and E. Finol, "Fluid-Structure Interaction Modeling of Abdominal Aortic Aneurysms: The Impact of Patient-Specific Inflow Conditions and Fluid/Solid Coupling," *Journal of Biomechanical Engineering*, vol. 135, no. 8, Aug. 2013, doi: 10.1115/1.4024275.

[50] R. L. Taylor, "FEAP - Finite Element Analysis Program, Version 8.4." University of California at Berkeley, Berkeley (CA)., 2013.

[51] N. Horvat, L. Virag, G. A. Holzapfel, and I. Karšaj, "Implementation of collagen fiber dispersion in a growth and remodeling model of arterial walls," *Journal of the Mechanics and Physics of Solids*, vol. 153, p. 104498, Aug. 2021, doi: 10.1016/j.jmps.2021.104498.

[52] N. Horvat, L. Virag, and I. Karšaj, "Mechanical role of intraluminal thrombus in aneurysm growth: A computational study," *Biomechanics and Modeling in Mechanobiology*, vol. 20, no. 5, pp. 1819–1832, 2021, doi: 10.1007/s10237-021-01478-w.

[53] L. Virag, N. Horvat, and I. Karšaj, "A computational study of bio-chemo-mechanics of thrombus-laden aneurysms," *Subbmited manuscript*.

[54] L. Virag, Horvat Nino, and Karšaj Igor, "Bio-chemo-mechanical role of intraluminal thrombus deposition on arterial tissue growth and remodeling," in *Solid (Bio)mechanics: Challenges of the Next Decade*, G. Sommer, K. Li, D. Ch. Haspinger, and R. W. Ogden, Eds. Springer Cham, 2022.

[55] J. D. Humphrey and C. A. Taylor, "Intracranial and Abdominal Aortic Aneurysms: Similarities, Differences, and Need for a New Class of Computational Models," *Annual Review of Biomedical Engineering*, vol. 10, pp. 221–246, 2008, doi: 10.1146/annurev.bioeng.10.061807.160439.

[56] J. C. Lasheras, "The Biomechanics of Arterial Aneurysms," *Annual Review of Fluid Mechanics*, vol. 39, no. 1, pp. 293–319, 2007, doi: 10.1146/annurev.fluid.39.050905.110128.

[57] J. H. Ashton, J. P. vande Geest, B. R. Simon, and D. G. Haskett, "Compressive mechanical properties of the intraluminal thrombus in abdominal aortic aneurysms and fibrin-based thrombus mimics," *Journal of Biomechanics*, vol. 42, pp. 197–201, 2009, doi: 10.1016/j.jbiomech.2008.10.024.

[58] J. D. Humphrey, *Cardiovascular Solid Mechanics: Cells, Tissues, and Organs*. Springer Science+Business Media New York, 2002. doi: 10.1007/978-0-387-21576-1.

[59] J. Tong *et al.*, "Variations of dissection properties and mass fractions with thrombus age in human abdominal aortic aneurysms," *Journal of Biomechanics*, vol. 47, no. 1, pp. 14–23, 2014, doi: 10.1016/j.jbiomech.2013.10.027.

[60] G. A. Holzapfel, T. C. Gasser, and R. W. Ogden, "A new constitutive framework for arterial wall mechanics and a comparative study of material models," *Journal of Elasticity*, vol. 61, pp. 1–48, 2000, doi: 10.1023/A:1010835316564.

[61] J. Biasetti, P. G. Spazzini, J. Swedenborg, and T. Christian Gasser, "An integrated fluid-chemical model toward modeling the formation of intra-luminal thrombus in abdominal aortic aneurysms," *Frontiers in Physiology*, vol. 3, pp. 266 1-266 16, 2012, doi: 10.3389/fphys.2012.00266.

[62] R. Skalak, "Growth as A Finite Displacement Field," in *Proceed IUTAM Symposium Finite Elasticity*, 1981, pp. 347–355.

[63] N. Horvat, L. Virag, and I. Karšaj, "Finite Element Growth Model of Abdominal Aortic Aneurysm," in *Proceedings of the 9th International Congress of Croatian Society of Mechanics*, 2018.

[64] J. A. Niestrawska, C. Viertler, P. Regitnig, T. U. Cohnert, G. Sommer, and G. A. Holzapfel, "Microstructure and mechanics of healthy and aneurysmatic abdominal aortas: experimental analysis and modelling," *Journal of the Royal Society Interface*, vol. 13, no. 124, p. 20160620, 2016, doi: 10.1098/rsif.2016.0620.

[65] A. Valentín, J. D. Humphrey, and G. A. Holzapfel, "A finite element-based constrained mixture implementation for arterial growth, remodeling, and adaptation: Theory and numerical verification," *International Journal for Numerical Methods in Biomedical Engineering*, vol. 29, no. 8, pp. 822–849, 2013, doi: 10.1002/cnm.2555.

[66] A. J. Schriefl, A. J. Reinisch, S. Sankaran, D. M. Pierce, and G. A. Holzapfel, "Quantitative assessment of collagen fibre orientations from two-dimensional images of soft biological tissues," *Journal of the Royal Society Interface*, vol. 9, no. 76, pp. 3081–3093, 2012, doi: 10.1098/rsif.2012.0339.

[67] Y. Lanir, "Constitutive equations for fibrous connective tissues," *Journal of Biomechanics*, vol. 16, no. 1, pp. 1–12, 1983, doi: 10.1016/0021-9290(83)90041-6.

[68] T. C. Gasser, R. W. Ogden, and G. A. Holzapfel, "Hyperelastic modelling of arterial layers with distributed collagen fibre orientations," *Journal of the Royal Society Interface*, vol. 3, no. 6, pp. 15–35, 2006, doi: 10.1098/rsif.2005.0073.

[69] G. A. Holzapfel, J. A. Niestrawska, R. W. Ogden, A. J. Reinisch, and A. J. Schriefl, "Modelling non-symmetric collagen fibre dispersion in arterial walls," *Journal of the Royal Society Interface*, vol. 12, p. 20150188, 2015, doi: 10.1098/rsif.2015.0188.

[70] G. A. Holzapfel and R. W. Ogden, "Comparison of two model frameworks for fiber dispersion in the elasticity of soft biological tissues," *European Journal of Mechanics, A/Solids*, vol. 66, pp. 193–200, 2017, doi: 10.1016/j.euromechsol.2017.07.005.

[71] G. A. Holzapfel and R. W. Ogden, "On fiber dispersion models: exclusion of compressed fibers and spurious model comparisons," *Journal of Elasticity*, vol. 129, no. 1–2, pp. 49–68, 2017, doi: 10.1007/s10659-016-9605-2.

[72] G. A. Holzapfel and R. W. Ogden, “On the tension-compression switch in soft fibrous solids,” *European Journal of Mechanics, A/Solids*, vol. 49, pp. 561–569, 2015, doi: 10.1016/j.euromechsol.2014.09.005.

[73] T. C. Gasser, S. Gallinetti, X. Xing, C. Forsell, J. Swedenborg, and J. Roy, “Spatial orientation of collagen fibers in the abdominal aortic aneurysm ’ s wall and its relation to wall mechanics,” *Acta Biomaterialia*, vol. 8, no. 8, pp. 3091–3103, 2012, doi: 10.1016/j.actbio.2012.04.044.

[74] M. S. Olufsen, C. S. Peskin, W. Yong Kim, E. M. Pedersen, A. Nadim, and J. Larsen, “Numerical Simulation and Experimental Validation of Blood Flow in Arteries with Structured-Tree Outflow Conditions,” *Annals of Biomedical Engineering*, vol. 28, pp. 1281–1299, 2000.

[75] F. J. H. Gijsen, F. N. van de Vosse, and J. D. Janssen, “Wall shear stress in backward-facing step flow of a red blood cell suspension,” *Biorheology*, vol. 35, no. 4–5, pp. 263–279, 1998, doi: 10.1016/S0006-355X(99)80010-9.

CURRICULUM VITAE

Nino Horvat was born on the 11th of April 1991 in Čakovec. In 2010, he finished High school Josip Slavenski Čakovec in Čakovec and started his studies at the Faculty of Mechanical Engineering and Naval Architecture, University of Zagreb. He graduated in 2015 with the topic of his master's thesis: Numerical implementation of G&R theory in finite element software. During his studies, he received several awards, such as the "Davorin Bazjanac" award and the Medal of the Faculty of Mechanical Engineering and Naval Architecture for the best students. He was a member of the student group FSB Racing Team where he took part in developing and building a race car ArctosR for the 2014 Formula Student competition in Silverstone. In 2016 he started working as a Research Assistant at the Faculty of Mechanical Engineering and Naval Architecture (University of Zagreb) on a scientific project called "BioChemoMechanical Modeling of Aneurysmal Growth". He attended three international summer schools with programs regarding numerical modeling of soft tissues, and he spent six weeks at Michigan State University in the USA. Since 2020 he has been working as an Assistant at the Chair of Mechanics and Strength of Materials. He authored and co-authored four scientific papers published in renowned journals, a book chapter, and nine scientific conference papers. Apart from numerical modeling, his interest is in designing and building mechanical devices and machines. In 2019, he received a gold medal at the 17th ARCA International Innovation Exhibition for a machine that automatically treats potatoes with the powder sprouting inhibitor during storage. He is currently working on his own on the design, construction, and control software development of a machine that will be used for experimental mechanical characterization of polymer material and the flow measurement in 3D printed replicas of human aortas.

.

PAPER 1

Version of Record of the journal article reproduced with permission from Elsevier.

Horvat, Nino, Virag, Lana, Holzapfel, Gerhard A., Sorić, Jurica, Karšaj, Igor: A finite element implementation of a growth and remodeling model for soft biological tissues: Verification and application to abdominal aortic aneurysms. Computer Methods in Applied Mechanics and Engineering, 352: pp. 586-605, 2019, doi.org/10.1016/j.cma.2019.04.041

Available online at www.sciencedirect.com
ScienceDirect
Comput. Methods Appl. Mech. Engrg. 352 (2019) 586–605
Computer methods in applied mechanics and engineering
www.elsevier.com/locate/cma

A finite element implementation of a growth and remodeling model for soft biological tissues: Verification and application to abdominal aortic aneurysms

Nino Horvat[a], Lana Virag[a], Gerhard A. Holzapfel[b,c], Jurica Sorić[a], Igor Karšaj[a,*]

[a] University of Zagreb, Faculty of Mechanical Engineering and Naval Architecture, Zagreb, Croatia
[b] Graz University of Technology, Institute of Biomechanics, Graz, Austria
[c] Norwegian University of Science and Technology (NTNU), Department of Structural Engineering, Trondheim, Norway

Received 6 July 2018; received in revised form 29 January 2019; accepted 26 April 2019
Available online 7 May 2019

Highlights

- General soft tissue growth and remodeling model implemented in finite element code.
- Adaptation of vessel to change in hemodynamics agrees well with clinical observations.
- Fiber production in aneurysms is mediated more by wall shear than intramural stress.
- Evolution of aneurysmal geometry and stresses agrees well with expectations.
- Reestablishment of the endothelium is important for aneurysm stabilization.

Abstract

The general framework for growth and remodeling (G&R) of soft biological tissues shows a great potential for expanding our current understanding of biochemical and biomechanical processes, and to predict disease progression. Yet, its use is held up by the lack of a reliable and verified 3D finite element (FE) implementation capable of describing G&R processes of soft biological tissues. Thus, in this study we present the implementation of a 3D constrained mixture G&R model in a FE analysis program. In contrast to traditional finite strain FE formulations, we show that the volumetric–isochoric decomposition not only introduces numerical problems and instabilities, it also provides unphysical results. As a verification of the implementation we present adaptations of realistic aorta models to changes in the hemodynamics, i.e. changes in blood flow and pressure. The obtained results show a correspondence with the membrane theory and with clinical expectations. Application to a fusiform aneurysm model provided realistic growth rates, evolution of thickness and stress, whereas changes in the kinetic parameters show good agreement to animal models. Finally, we present simulated expansions of an asymmetric fusiform aneurysm. Non-axisymmetric elastin degradation increased the curvature of the aorta, which is characteristic for abdominal aortic aneurysms.

Keywords: Finite elements; Vascular adaptation; Collagen turnover; Fusiform aneurysm; Asymmetric fusiform aneurysm; Growth and remodeling

* Correspondence to: University of Zagreb, Faculty of Mechanical Engineering and Naval Architecture, Ivana Lučića 5, Zagreb, 10000, Croatia.
E-mail address: igor.karsaj@fsb.hr (I. Karšaj).

https://doi.org/10.1016/j.cma.2019.04.041

1. Introduction

Models that seek to describe fundamental mechanisms by which changes in the mechanical environment govern biological growth and remodeling (G&R) have been increasingly in use in order to improve our current understanding of biochemical and biomechanical (biochemomechanical) processes and to predict disease progression. For the description of soft biological tissue behavior various constitutive models have been proposed. However, G&R models have shown to capture the behavior the best, as they incorporate anisotropic hyperelastic deformation of structurally important constituents (elastin, collagen, smooth muscle), as well as biochemical influences, which are based on the changes of homeostatic stress and biomechanical dependence of the current stress state of the previous loading.

The general framework for G&R of soft biological tissues, as proposed by Humphrey and Rajagopal [1], can be used for modeling various tissues and diseases, from tendon healing [2] and myocardial hypertrophy [3], to the prediction of arterial adaptations in health (e.g., after a change in flow and blood pressure [4–6] or during aging [7]) and disease (e.g., abdominal aortic aneurysms [8–12]). Yet, its application is limited due to the lack of reliable, verified and validated finite element (FE) implementations capable of describing G&R processes of soft biological tissues. Several attempts to implement G&R models into FE codes have been conducted in the past. Models were first implemented by using membrane FEs that allowed the modeling of axisymmetric (fusiform) aneurysm enlargement [13]. Using these membrane models, geometrical changes and expansion rates during the aneurysm growth were studied for different kinetic parameters [14], with the importance to study the influence of initial aortic properties and collagen turnover on the evolution of fusiform abdominal aortic aneurysms (AAAs) without a thrombus [8,15]. Furthermore, a computational framework that couples vascular G&R with blood flow by using a 3D patient-specific geometry was presented in [16]. Nevertheless, albeit undoubtedly useful, membrane models are incapable of capturing distributions and parameter changes through the wall. Radial distributions of stresses and masses could be important for the evolution of aneurysms, especially for thrombus-laden aneurysms [17], and thus for modeling the biochemical influence of a thrombus on the aneurysmal wall more accurately, the mean values might not suffice. Additionally, membrane FEs limit the application to thin-walled soft biological tissue structures.

The first constrained mixture G&R model implementation into a 3D FE code was presented by Valentin et al. [18]. This approach was accompanied by some numerical problems, including instabilities and divergence of solutions with increased G&R time, management of computational requirements for storing histories of kinetics and motions, high CPU time, difficulties with enforcing isochoric responses, but also contra-intuitive responses of the tissue to prescribed changes in the arterial structure. Subsequently, several other groups implemented G&R models using a 3D FE framework. For example, Braeu et al. [19] proposed a homogenized constrained mixture model and compared isotropic growth to anisotropic (in-thickness) one. Their verification of the implementation using a case of the vessel adaptation to a minor increase in blood pressure showed that, while anisotropic growth might lead to expected new homeostatic state depending on model parameters, isotropic growth was mechanobiologically unstable. This opposes 1D studies on vascular adaptations to altered blood flow and pressure presented in [6,20]. In a further study, Grytsan et al. [11] also investigated differences in isotropic and various anisotropic volume growths (in-plane, in-thickness). Unfortunately, the authors provided no verification of their FE results. Smooth muscle cell contributions, along with respective active stress, were ignored in the model. The authors showed that different types of volume growth can lead to the opposite, sometimes unintuitive and implausible results. The latest paper on G&R implementation within a FE framework was documented by Lin et al. [12]. The authors implemented a simplified G&R theory in the commercial software Abaqus by using the user subroutine UMAT, without active and passive contributions of smooth muscle cells and they used simplified growth expressions with stretch-induced parameters. Furthermore, implemented strain-energy functions for the collagen behavior are based on a volumetric–isochoric split of the deformation gradient, which was shown not to be suitable for 1D constituents [21–24]. Also in the present paper, in Section 2.1., we will show that such a decomposition leads to an unphysical behavior.

To conclude, we consider all these studies dealing with G&R implementation in a FE code to be a guideline for achieving specific goals, e.g., to show the influence of different types of growth on the biomechanical response, or to provide illustrative AAA enlargements. In addition, these various papers were orientated towards simplified axisymmetric geometries without an active contribution of smooth muscle cells. However, we know that cell activation has a great influence on the mechanical response even on the distribution of stresses, and it allows an adaptation to sudden changes in the structure or loading of the aortic wall [25,26].

In the present study, we present the implementation of a comprehensive constrained mixture G&R model into a 3D nonlinear FE code. This implementation can be used for general soft tissue G&R problems. The theory is implemented by using the user subroutine UMAT within the FE analysis program *FEAP* [27], but it is not restricted to it and can be applied to any open FE code. Although the general theory was presented in previous studies (see, e.g., [5,6,13,18]) in order to provide full insights into all capabilities of the implemented model, we added a short overview of the constrained mixture G&R theory in Appendix A. Nevertheless, in Section 2 the most important expressions necessary for the FE implementation are explained. In addition, we discuss the necessity of avoiding the volumetric–isochoric split for fiber constituents. In Section 3, using realistic non-symmetrical geometries and non-homogeneous material, we tried to verify our implementation by showing results for some known phenomena such as hypertension and the change in blood flow. The full potential of the G&R theory we show through examples of symmetric fusiform growth of a three-layered aortic aneurysm in Section 4.1., and an asymmetric fusiform aneurysm in Section 4.2. For these cases we analyze the capability of the model to describe a realistic behavior of an aneurysm, as reported by clinicians (rupture, linear growth, stabilization, realistic growth rates and stresses in the aortic wall, staccato growth). Moreover, we show the necessity of using a 3D FE model through options of tracking stress changes and wall constituents' ratios through time and in different directions (radial, circumferential, axial). Finally, in Section 5 we summarize the major capabilities and discuss restrictions of the model.

Additionally, in order to facilitate the reproduction of the results, we have also included a condensed flowchart of the implemented procedure for obtaining the solution in Appendix C, but also our findings on the reduction of necessary CPU time, memory storage and numerical stabilities in Appendix D.

2. Methods

Similar to previous studies, the G&R model is based on continuum mechanics, and assumptions are used so that the artery follows the constrained mixture of elastin, and four families of collagen fibers and smooth muscle cells. Detailed constitutive model equations can be found in Appendix A. Here we only present the model equations that differ from other studies.

2.1. Finite element description

For our simulations an 8-node hexahedral Q1P0 element was used with three degrees of freedom at each node. Near incompressibility is ensured by a modified quadratic penalty function, i.e.

$$W_{\text{sph}} = \frac{1}{d_1}\left(J - \frac{M(s)}{M(0)}\right)^2, \tag{1}$$

where d_1 denotes a penalty parameter. The Jacobian is calculated as $J = \det\left({}^{s}_{0}\mathbf{F}\right)$ (see Appendix A for more details), and $M(0)$ and $M(s)$ are initial and targeted current total mass of a certain FE, respectively. Furthermore, we use the augmented Lagrangian method to cope with the quasi-incompressibility condition by changing the parameter d_1 in each iteration.

2.2. Volumetric-isochoric split vs. full deformation gradient formulation

Several studies (e.g., [21–24]) suggested that, while a volumetric–isochoric split of the deformation gradient can be justified and systematically derived for isotropic materials, in the case of fiber-reinforced material a multiplicative decomposition must be executed with care in order to avoid violation of certain physical requirements [24]. However, some implementations of the G&R theory, documented in [12,18], employed a volumetric–isochoric split of the deformation gradient and the strain-energy function, similar to traditional (finite strain) FE formulations. Thus, we compared results obtained with a volumetric–isochoric decomposition and a full gradient formulation for a fiber-reinforced hyperelastic material (i.e. an aorta).

The formulation using the full deformation gradient is described in Appendix A. The total strain-energy function W can be written in a decoupled form as

$$W = W_{\text{sph}} + W_{\text{dis}}, \tag{2}$$

where W_{sph} is the spherical (volumetric) part, Eq. (1), and $W_{\text{dis}} = \sum_k \overline{W}^k$ is the sum of the elastic constituents contributing to the isochoric deformations. For the fibers k, the isochoric contribution is calculated as

$$\overline{W}^k = \frac{k_2^k}{4k_3^k}\left\{\exp\left[k_3^k(\mathbf{m}(\tau)^k\,\overline{\mathbf{C}}^k_{n(\tau)}\mathbf{m}(\tau)^k - 1)^2\right] - 1\right\}, \tag{3}$$

where $\overline{\mathbf{C}}^k_{n(\tau)}$ is the so-called modified right Cauchy–Green tensor $\overline{\mathbf{C}}^k_{n(\tau)} = \left(\overline{\mathbf{F}}^k_{n(\tau)}\right)^{\mathrm{T}}\overline{\mathbf{F}}^k_{n(\tau)}$, and $\overline{\mathbf{F}}^k_{n(\tau)}$ is the distortional component of the deformation gradient $\overline{\mathbf{F}}^k_{n(\tau)}(s) = \left(J_{n(\tau)}(s)\right)^{-1/3}\mathbf{F}^k_{n(\tau)}(s)$, while k_2^k and k_3^k are material parameters. The deformation gradient $\mathbf{F}^k_{n(\tau)}(s)$ is a mapping from the natural configurations of each constituent produced at time τ to a current mixture configuration at time s, and $J_{n(\tau)}(s)$ is the volume ratio between instance s and τ. The orientation of each fibrillar constituent at the time of production of fiber τ is defined by the unit vector $\mathbf{m}^k(\tau)$. For more details see Figure 1 in [18].

On the other hand, the full gradient formulation does not include the decomposition of the strain-energy function. The strain-energy function $W_{\text{dis}} = \sum_k W^k$ is simply defined as

$$W^k = \frac{k_2^k}{4k_3^k}\left\{\exp\left[k_3^k(\mathbf{m}(\tau)^k\,\mathbf{C}^k_{n(\tau)}\mathbf{m}(\tau)^k - 1)^2\right] - 1\right\}. \tag{4}$$

All variables are defined in Appendix A. These different formulations lead to different forms of the Cauchy stress tensor $\boldsymbol{\sigma}$ and the elasticity tensor $\mathbb{C}$.

Illustrative example — Comparison of the two formulations

As the first step of a verification of the model implementation in the user material subroutine, a simple test example on a cylindrical geometry was designed. In this test, we have modeled aging (i.e. a gradual loss of elastin, with a half-life of approximately 40 years, without and with G&R of fibers. When a turnover of fibers was not allowed, the masses of collagen and smooth muscle were kept constant by setting the basal production m_B^k in Eq. (A.1) to zero, and by setting an infinite half-life of fibers so that there is no removal $q^k(s-\tau)$, see Eq. (A.3). Thus, the integrals from Eqs. (A.2) and (A.8) are eliminated. All other parameters are according to Table B.1. On the other hand, mass of elastin was degraded, hence the mass ratio is $J = M(s)/M(0) < 1$. Results are shown in Fig. 1(a) and compare the change in the inner diameter calculated by using two formulations: the volumetric–isochoric split (dashed curve) and the full deformation gradient formulation (solid curve). Not only the full gradient formulation has shown to be numerically more stable, but also, more importantly, the results indicate a rather opposite behavior. The use of the volumetric–isochoric split leads to a shrinkage of the aorta as elastin is degraded, whereas the full gradient formulation demonstrates a dilation.

Because this example is not physical, we have also modeled aortic aging, i.e. a gradual loss of elastin with turnover of fibers. Clinically, aging causes a monotonous dilation of the diameter, see Fig. 1 in [28]. A full gradient formulation provides results that demonstrate a continuous dilation of the aorta (solid curve in Fig. 1(b)). On the other hand, for the same model parameters, results obtained with the use of the volumetric–isochoric split show a shrinkage of the aorta for the first 6 years (dashed curve in Fig. 1(b)), before a rather steep increase in diameter occurs. This is clearly unphysical. Similarly, the dashed black curve in Fig. 1(a) shows a significant loss in mass, which is also unexpected during aging.

Based on these results and the previously mentioned studies on the volumetric–isochoric split of the deformation gradient [21–24], subsequently we use the full deformation gradient approach for our application.

2.3. Production of collagen and smooth muscle

Early G&R studies (e.g., [20,29]) suggested that vasoactive molecules, regulated by the endothelium in response to altered wall shear stress, also affect cell and matrix turnover. Furthermore, parametric studies have been conducted to define the range of values that provide physical responses [30]. Despite this, in the former G&R FE studies, the endothelial response was neglected, and only the intramural stress-mediated mass production (i.e., stress or stretch sensed by the fibers), was taken into account.

Illustrative example — Importance of the biochemically motivated parameter K_C

Effects of the parameters describing the influence of intramural (K_σ in Eq. (A.1)) and wall shear stresses (K_C) were previously investigated for the adaptation of an idealized cylindrical blood vessel to altered hemodynamics in

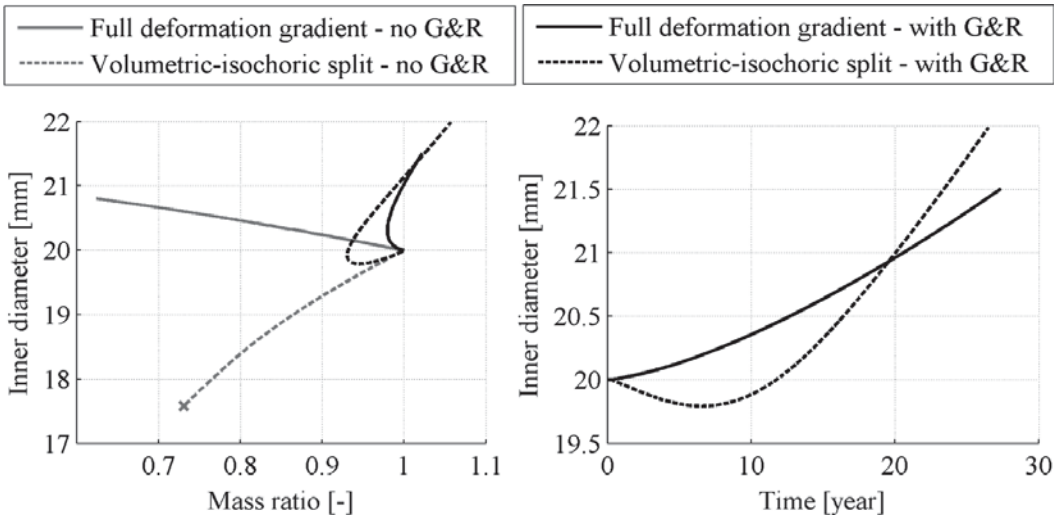

Fig. 1. Change in arterial inner diameter with change in mass for the case with no turnover of collagen and smooth muscle (gray curves) and during aging (black curves) (a); evolution of aortic inner diameter with aging in time (b). Dashed curves denote results obtained with the volumetric–isochoric split, and solid curves with the full deformation gradient formulation.

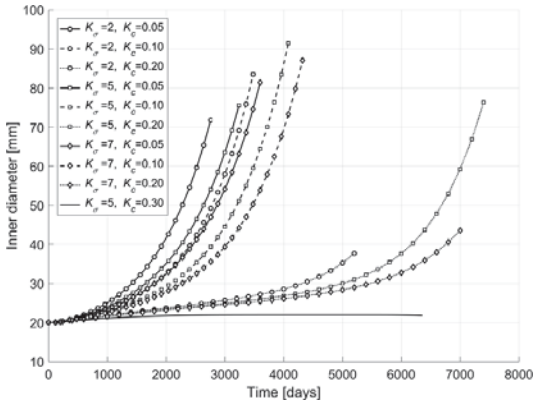

Fig. 2. Influence of parameters that model wall stress-mediated mass production (K_σ) and shear stress-mediated changes (K_C).

health [30,31]. However, in these cases, due to small deformations, the changes in wall shear stress and related mass production are negligible. Thus, the influence of the parameter K_C in a disease such as aneurysm, that significantly deforms the arterial geometry, and consequently considerably alters the wall shear stress, is unknown. For that reason, we studied the differences in a fusiform aneurysm growth (see Section 4.1. for more details) for different mass production parameters, while the other model parameters are according to Table B.1. Fig. 2 shows the evolution of the inner diameter over time, at axial position with highest elastin degradation, of the fusiform aneurysm for different fiber production parameters K_C and K_σ. It can be seen that for very small values of K_C, the stress-mediated growth significantly influences the growth of the aneurysm. On the other hand, for larger values of vasodilation-mediated growth, the change in K_σ has a minimal effect. However, it is important to note that the values and changes in K_C remained small when compared to values that were related to health (see, e.g., Figs. 3 and 7, or [6,20]). This could lead to the conclusion that vasoconstriction-mediated growth is more important for aneurysm growth.

The difference in the K_C values for health and disease can be explained by the fact that this parameter describes the response of endothelial cells. Increased wall shear stress upregulates endothelial cell production of nitric oxide, an inhibitor of collagen synthesis and smooth muscle cell proliferation, whereas decreased wall shear stress upregulates endothelial cell production of endothelin-1 (ET-1), a promoter of collagen synthesis and smooth muscle cell proliferation. Yet, functionality of endothelium in aneurysms is not clear. For intact endothelial cell layers, i.e. larger values of K_C, irreversible degradation of elastin does not lead to aneurysm formation, e.g., see the solid

curve without markers in Fig. 2 ($K_C = 0.3$). Although the change in structure leads to a new equilibrium, a slightly dilated state, the expansion of a few millimeters is not large enough to be called aneurysmal enlargement.

3. Verification on the basis of clinically observed phenomena

Before using the model for more complex applications, it is necessary to verify the implementation. This was performed using clinical observations, e.g., adaptation of the blood vessel to changes in blood flow or pressure. An idealized artery was represented by half of a cylinder (180° slice). Axial symmetry and distal-proximal symmetry were assumed. The model was discretized by 7200 finite elements (50 elements in the axial direction, 12 in the circumferential direction, and 12 in the radial direction). Three layers with different structures were defined according to data summarized in Table B.1, see Appendix B. In order to avoid numerical instabilities due to large gradients at the interface, where the layers are connected to each other, we defined a transition zone with a gradual change of the structure from one layer to another. Intensity plots showing collagen fiber orientation and dispersion through the healthy aortic wall thickness, as presented in [32], indicated the existence of "transition layers" in between the layers (intima, media, adventitia) with different fiber orientations (see Fig. 6 in [32]). Thus, the width of the transition zones was chosen to correspond to the width of the transition layers observed by second harmonic generation imaging.

Expectations based on membrane theory. It has been shown that for perturbations of the blood flow and the pressure, given by $Q = \varepsilon Q_h$ and $P = \gamma P_h$, where ε and γ indicate the perturbation parameters, both wall shear stress and circumferential stress tend to return to their homeostatic values, while stress-mediated G&R produces specific changes in the geometry. For example, it is expected that the inner radius in the new equilibrium state changes to $r_i = \varepsilon^{1/3} r_{i,h}$, and $h = \gamma \varepsilon^{1/3} h_h$, where $r_{i,h}$ and h_h are homeostatic values of the inner radius and the thickness before the change in hemodynamics, while r_i and h are inner radius and thickness after adaptation to the perturbation.

3.1. Change in blood flow

Clinical/experimental background. Clinically, widening of arteries with increased blood flow has been observed both in animal models (e.g., using anastomosis to increase blood flow of rabbits [33]) and in humans [34]. Time needed for vascular adaptation after an abrupt blood flow increase by 60% was reported to be approximately 2 months for rabbits. It is interesting to note that the diameters exceeded those of control arteries by 19%, which reasonably matches the membrane theory which predicts a 17% increase in the arterial diameter. On the other hand, a change in blood flow in humans was caused by an exercise, rather than a surgical procedure, making these measurements more difficult to control. However, although the change in arterial geometry varies among arteries (e.g., the difference in diameter of femoral arteries between athletes and sedentary subjects was reported to be 11–17.3%, yet carotid arteries were only slightly dilated [34]), both increase in diameter and wall thickness were shown.

Illustrative example. We performed FE simulations of adaptations to changes in the hemodynamics in three steps. Firstly, for the given idealized cylindrical geometry, the blood pressure and pre-stretches of constituents, as provided in Table B.1 of Appendix B, the material parameters for each constituent were calculated. Secondly, in order for the healthy aorta to be more realistic, we used an inhomogeneous (rather small) degradation of elastin from the idealized cylindrical vessel. After 400 days of the G&R process a new equilibrium, i.e. a healthy artery under normal hemodynamic conditions, was adjusted, which is presented by dashed curves in Fig. 3(c). The end stage of the G&R process can be seen in Fig. 3(a) and (b), for the time 300 to 400 days. Finally, we applied a 20% increase in the blood flow at the instance of 400 days. The increase in flow led to wall shear stress-induced changes in the production of fibers and an active response of smooth muscle cells. This triggered growth and a remodeling process, as shown in Fig. 3(a) (400 to 700 days). The outer contours of the new equilibrium state are shown in Fig. 3(c) (solid curves). From Fig. 3(a) and (b) it can also be seen that the parameter K_C influences the time needed for the vessel to find a new equilibrium, but it does not change the inner radius or the thickness of the new equilibrium state. For larger values of K_C, mass was deposited more quickly, and thus the thickness returned faster to a new homeostatic value. Furthermore, it can also be seen that in the middle cross-section ($z = 75$ mm), where a small fraction of elastin was degraded, the diameter of the healthy aorta is slightly greater than the diameter at the part with unchanged structure ($z = 0$ mm).

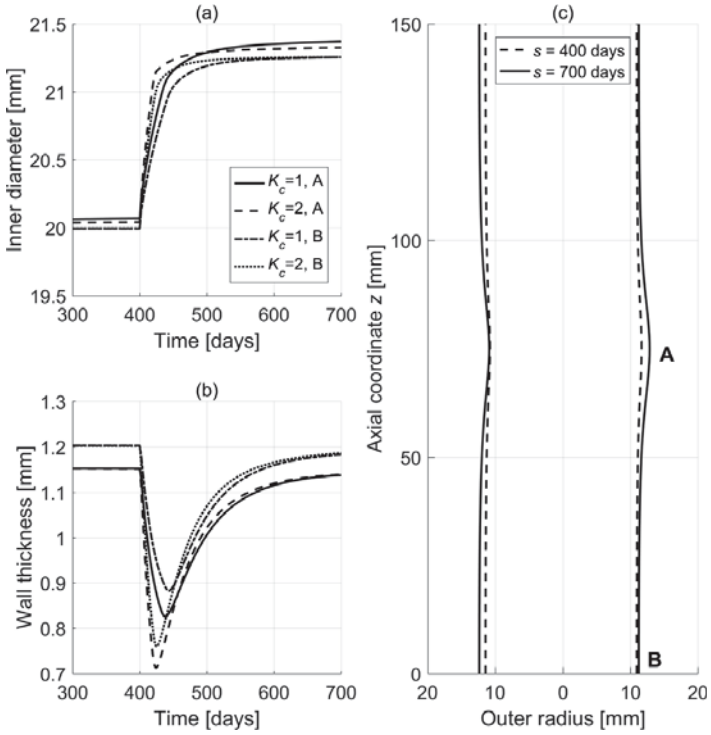

Fig. 3. Evolution of the inner diameter (a), and the wall thickness (b) at location A (middle cross-section at $z = 75$ mm) and at location B ($z = 0$ mm) for different production rates K_C; contours of a healthy artery (dashed curve) and the artery after the (new) homeostatic state is reached (solid curve), after 20% increase in the blood flow for $K_C = 1$ (c).

By using a membrane theory approximation, for the case that the blood flow is 20% above its homeostatic (normal) value ($\varepsilon = 1.2$), both the inner radius and the thickness should change $1.2^{1/3} = 1.06266$ times from the homeostatic value. Thus, an aorta with an inner diameter of 20 mm, the terminal inner diameter would amount to approximately 21.25 mm. Depending on the initial healthy diameter, the new homeostatic diameter, measured from the centerline, gained a value of 21.25–21.4 mm, which shows agreement with the membrane theory and expectations from the clinics.

3.2. Hypertension/hypotension

Clinical/experimental background. Similarly, after abrupt and sustained alterations in the pressure, relevant to a study of hypertension or hypotension, the most empirically observed response of the arterial wall is the change in wall thickness, however no long-term dilatation/shrinkage of the blood vessel was observed [35,36]. Again, this matches well the membrane theory.

Illustrative example. Analogous to the increase in flow, FE simulations were performed in three steps. In the first two steps, the geometry of non-cylindrical, healthy and normotensive arteries were found. Then, an abrupt 50% increase in blood pressure ($\gamma = 1.5$), at G&R time $s = 400$ days (Fig. 4(a) and (b)), was applied. The vessel immediately expanded due to the abrupt change in loading, see Fig. 4(a). However, G&R processes, primarily governed by an intramural stress-induced mass production, quickly ensured the return of the inner diameter to a smaller, almost initial value, see Fig. 4(a). It is interesting to note that FE simulations predicted a (hypertension-induced) increased arterial curvature of the artery (Fig. 4(c)). A correlation between hypertension and arterial curvature was also clinically observed [37,38].

According to the expectations from the membrane theory, the new thickness should increase approximately 50% with respect to the homeostatic value. Since the homeostatic thickness of the aorta is approximately 1.2 mm, after 50% increase in the blood pressure, the new thickness should be 1.8 mm. Again, the FE results presented in Fig. 4(b) match this expectation with good agreement.

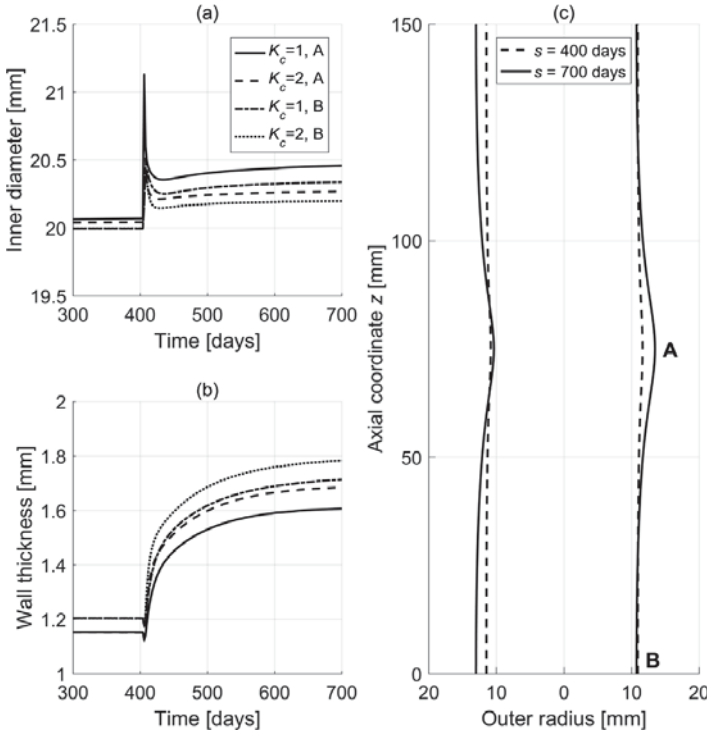

Fig. 4. Evolution of the inner diameter (a), the wall thickness (b) at the location A (middle cross-section at $z = 75$ mm) and at the location B ($z = 0$ mm) for different production rates; contours of a healthy artery (dashed curve) and the artery after the new homeostatic state is reached (solid curve) after 50% increase in the blood pressure for $K_C = 1$ (c).

4. Representative examples — application to an abdominal aneurysm

In order to show the full potential of the implemented constrained mixture G&R theory, we have applied the 3D FE model to cases of fusiform and asymmetric fusiform aneurysm enlargements occurring due to changes in the kinetic parameters. Subsequently, we study whether the calculated growth rates, the thicknesses, and the stresses can be compared with clinical observations.

4.1. Model for fusiform aneurysm

Geometrical changes and stress distributions

In order to exploit the axial symmetry of a fusiform aneurysm, a healthy aorta was modeled as a 2° cylindrical segment, with length $L = 150$ mm, and the AAA evolution was predicted. The modeling on one segment reduced significantly the computational cost. The segment is composed of three layers, and the FE mesh consists of 1 200 elements: 100 non-uniform elements in the axial direction (with finer mesh in the middle region, where an aneurysm was developed, and a coarser mesh where no change in the structure was expected), one in the circumferential direction, and 12 throughout the thickness of the wall.

Similar to previous studies, loss of mass in elastin initiates the aneurysm development according to

$$Q^{\mathrm{e}}(z,s) = \phi^{\mathrm{e}}_{\mathrm{rem}} + \left(1-\phi^{\mathrm{e}}_{\mathrm{rem}}\right)\left[1-\exp\left(-s/\tau^{\mathrm{e}}_{1/2}\right) f_1(z)\right], \tag{5}$$

where $\phi^{\mathrm{e}}_{\mathrm{rem}} = 0.2$ is the fraction of elastin not being degraded, s is the current time, and $\tau^{\mathrm{e}}_{1/2}$ is the half-life of elastin. The remaining functional elastin was set to correspond with data of Tong et al. [17], as these authors showed that even in large aneurysms some functional elastin remained. The function $f_1(z)$, defining the degradation of elastin in the axial direction z, is adapted from [15]. This function is defined as

$$f_1(z) = \begin{cases} \exp\left[-0.7\,(z-z_{down})^2\right] & z < z_{down}, \\ \exp\left[-0.7\left(z-z_{up}\right)^2\right] & z > z_{up}, \\ 1 & z_{down} \le z \le z_{up}. \end{cases} \tag{6}$$

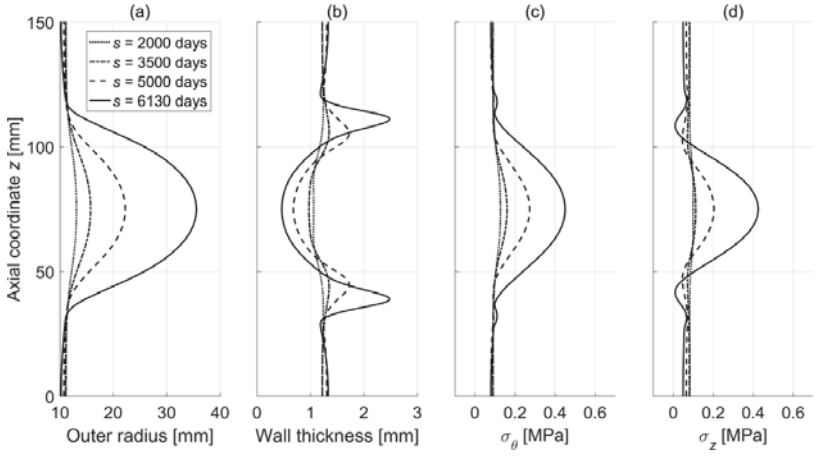

Fig. 5. Outer radius (a), wall thickness (b), circumferential stress σ_θ (c) and axial stress σ_z (d) at the inner radius for the model of a fusiform aneurysm along the axial coordinate z at several time instances.

In Eq. (6) $z_{down} = 65$ mm and $z_{up} = 85$ mm. In between these two coordinates, degradation of elastin is maximal and constant, while when z approaches 0 or L, $f_1(z)$ gradually tends to zero, leaving elastin intact in the healthy part. In response to a local irreversible elastin loss, a local dilatation forms.

Contours of the outer radius over time are shown in Fig. 5(a). As expected, the circumferential stress σ_θ was the highest in the apex region of this model at all times (Fig. 5(c)). The wall thickness in the corresponding time steps can be seen in Fig. 5(b). With the expansion of the AAA, the wall thickness at the apex decreased as the production was not sufficient to compensate for the expansion rate. It is interesting to note that the shoulder regions thickened. A similar thickness distribution was predicted by using the membrane model [15], but is also observed clinically using CT scans [39]. It is possible that wall thickening in the shoulder region decreases the wall stress, and thus prevents a rapid growth and consequently a rupture of the aneurysm. It was suggested before that the shoulder stress and the aneurysm expansion are correlated [40]. Thickening in the shoulder region does not seem to happen due to mass production. The inner radius, and thus the wall shear stress, is roughly constant at that location, and also the intramural stress (Fig. 5(b) and (c)). Consequently, mass production is not increased. However, it is interesting to note that the values of the axial stresses are roughly the same as the circumferential stresses (compare Fig. 5(c) with Fig. 5(d)). Axial stresses are the consequence of the blood pressure that is stretching the aneurysm axially, increasing tensile stress in the apex and compression of the shoulder regions. Additionally, this further thins down the apex region and thickens the shoulder region.

Radial distributions of the circumferential stress σ_θ and the axial stress σ_z at the aneurysm apex at certain time instances are illustrated in Fig. 6. In this figure, the normalized thickness at the radial position $r(\tau)$ was defined as the distance at that position from the inner radius $r_i(\tau)$ divided by the thickness $h(\tau)$ at the same time instance τ, i.e. $[r(\tau) - r_i(\tau)]/h(\tau)$. The non-continuous stress distributions are the consequence of the layered structure. Note that during AAA evolution, the axial stress component remains slightly smaller when compared with the circumferential stress, until the G&R time of $s = 6130$. However, rupture can probably be assumed when any normal component of the wall stress reaches 460 kPa [41]. High axial stresses are likely the consequence of the fusiform model restriction to out-of-plane deformations of the aortic centerline, i.e. the model does not allow aortic tortuosity or bending commonly seen in AAAs.

The vertical lines denote the interfaces between the wall layers. As can be seen, with loss of elastin, the media becomes thinner, while the intima and the adventitia thicken due to increased production of collagen. Intimal thickening is commonly seen in aneurysmal aortic tissue.

Influence of fiber production rate

The animal model presented by Franck et al. [42] suggested that stabilization of AAA expansion (i.e. decrease in growth rate or complete cessation of growth) can be achieved by an establishment of the endothelial lining that leads to the suspension of proteolysis, and thus an increased collagen production. This reconstitution of a new aortic wall has been associated with the stabilizing effect on rat AAAs. An increase in the endothelial functionality is described in the present model by parameter K_C, that captures changes in the mass production in response to altered wall shear stress sensed by endothelial cells. Thus, we simulated AAA expansion and the eventual endothelial layer

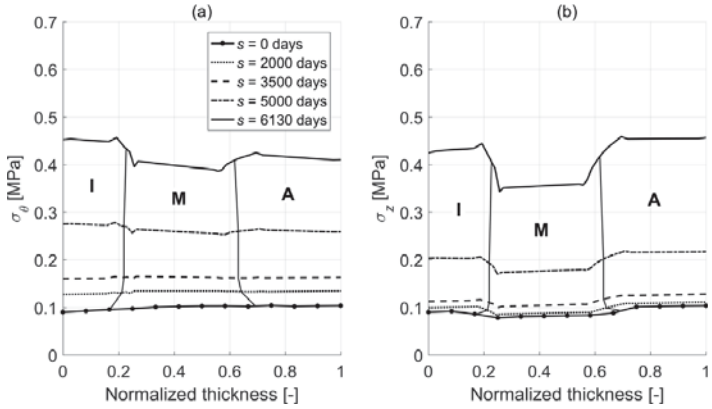

Fig. 6. Radial distribution (along normalized thickness) of circumferential stress σ_θ (a) and axial stress σ_z (b) at the apex of the fusiform aneurysm model at several time instances. The arterial layers, i.e. intima, media, and adventitia, are marked as "I", "M" and "A", respectively.

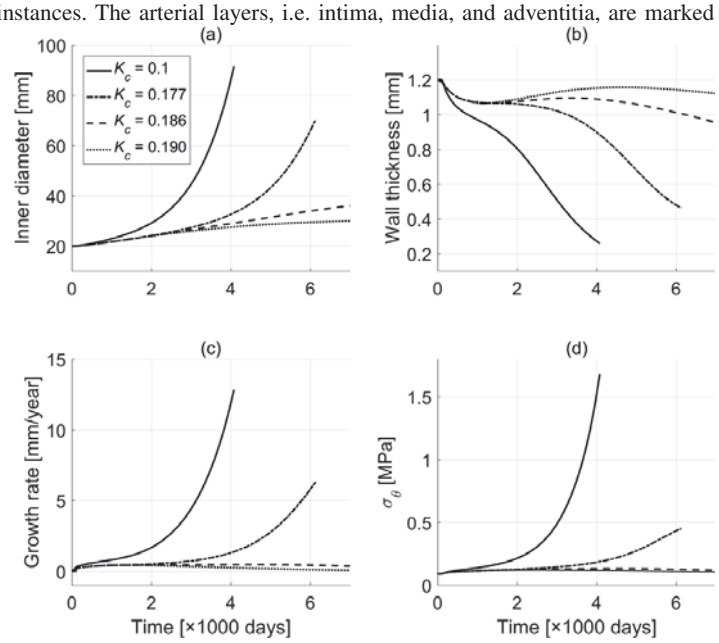

Fig. 7. Evolution of the inner diameter (a), the wall thickness (b), the growth rate (c), and the circumferential stress σ_θ (d) at the apex for the fusiform aneurysm model for different time-averaged production rates.

healing process by changing the values of K_C in time within the aneurysmal region. The results indicate that an increase in K_C in the AAA sac does indeed lead to a stabilization of the AAA growth, as can be seen in Fig. 7(a). The corresponding growth rates are shown in Fig. 7(c). As expected, high growth rates are related to rupture. For smaller production rates, the thickness decreases rapidly, while in cases with stabilization the thickness remains roughly the same, see Fig. 7(b). The evolution of the circumferential stress σ_θ needed to predict rupture can be seen in Fig. 7(d). In cases where AAA is stabilizing, i.e. where a new equilibrium state can be reached, the stresses tend to be restored towards the homeostatic value, whereas for cases of rupture they grow exponentially.

Again, note that small changes in K_C can change the AAA evolution significantly, and thus the production induced by wall shear stresses should not be neglected.

4.2. Model for asymmetric fusiform aneurysm

Non-axially symmetric AAAs are more common. Similar to the model used above to simulate a fusiform aneurysm, the aneurysm development is initiated by loss of elastin, but in this case, elastin degradation depends also on the circumferential coordinate ϑ, i.e.

$$Q^{\mathrm{e}}(z,s) = \phi^{\mathrm{e}}_{\mathrm{rem}} + \left(1-\phi^{\mathrm{e}}_{\mathrm{rem}}\right)\left(1-\exp\left(-s/\tau^{\mathrm{e}}_{1/2}\right) f_1(\vartheta)\, f_2(\vartheta)\right), \tag{7}$$

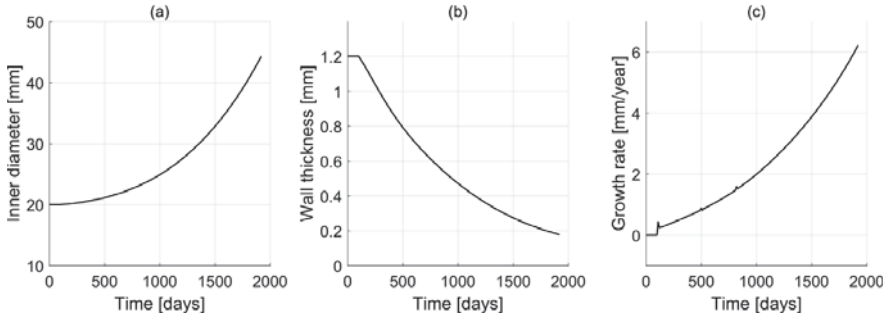

Fig. 8. Evolutions of the inner diameter (a), the wall thickness at the aneurysm apex (b), and the growth rate (c) of an asymmetric fusiform aneurysm model over 2000 days.

where the function f_2 is defined as

$$f_2(\vartheta) = \exp\left(-\frac{c_s \vartheta}{1.005\pi - \vartheta}\right)^2. \tag{8}$$

In the denominator 1.005π was chosen in order to avoid a division by zero. For the results shown herein the parameter $c_s = 1$ was used. Note that higher values of c_s lead to a steeper degradation function in the circumferential direction, and thus to a more stable aneurysm growth.

The initial model mesh of the cylindrical artery was used in a similar fashion as for the verification case. The geometry was then discretized by 50 elements in the axial direction, 16 in the circumferential direction, and 12 in the radial direction. The evolution of the asymmetric fusiform aneurysm model, simulated with the set of parameters of Table B.1, is shown in Fig. 8. Similar to ruptured fusiform aneurysm cases, the thickness at the apex decreased rapidly, and the growth rate increased to the value of 6 mm/year.

It is important to note that apart from the mass production other factors play a crucial role in the aneurysm outcome; i.e. rupture, continuous growth without rupture or stabilization (cessation of growth). For example, the above mentioned parameter c_s in the elastin degradation function (i.e., Eq. (8)) changes AAA stability. Additionally, it has been shown that the aneurysmal wall stiffens during the evolution of the aneurysm, not only because of loss of the compliant wall, but also due to stiffening of the collagen fibers [15,43–45]. Collagen stiffening can lead to a stabilization of the growth.

The outer contours of the asymmetric fusiform aneurysm model in the two symmetry planes at different G&R times are illustrated in Fig. 9. It is interesting to note that bending of the AAA occurs typically in plane 1 (i.e. the x-z symmetry plane), see Fig. 9(a). This increased arterial curvature of the aorta is the sole consequence of the non-axisymmetric elastin degradation, no additional boundary conditions were imposed (e.g., limitation of growth due to the spine). Arterial curvature could be more prominent if rotations of the upper and lower boundaries were allowed. Note that the asymmetric fusiform aneurysm requires the calculation of the centerline in each time step, because it does not remain vertical, unlike for the fusiform aneurysm.

Growth of the aneurysmal sac can also be seen in the horizontal plane 2 (i.e. the x-y plane), see Fig. 9(c). The circular cross-section becomes more elliptical with growth of the sac. Since elastin is degraded only on one side, the aneurysm tends to dilate mostly to that side. Yet, it does not mean that the opposite side remains unchanged. For example, Fig. 10(a) shows changes in the wall thickness along the axial coordinate at several time instances. As expected, thickness changes can mainly be found in the sac, and the wall also thickens on the opposite side of the sac. In the healthy part (where coordinate z is close to zero or L) the thickness remains the same. Similar to the fusiform aneurysm, there is a wall thickening in the shoulder region.

Intramural stresses are largest in the aneurysmal sac (Fig. 10(b) and (c)). In the healthy regions the stresses remain at the homeostatic level. However, unlike for the fusiform aneurysm, due to the increase in AAA curvature, the axial stress σ_z remains lower than the circumferential stress σ_θ all times, even when the stress exceeds the rupture point.

In addition to the changes in the axial direction, the thickness and the stress also change in the circumferential direction, see Fig. 11. In homeostasis, i.e. for G&R time $s = 0$, the thickness and the stress at the inner diameter do not change in the circumferential direction (see the solid curves in Fig. 11). From Fig. 11(a) it can be seen that the

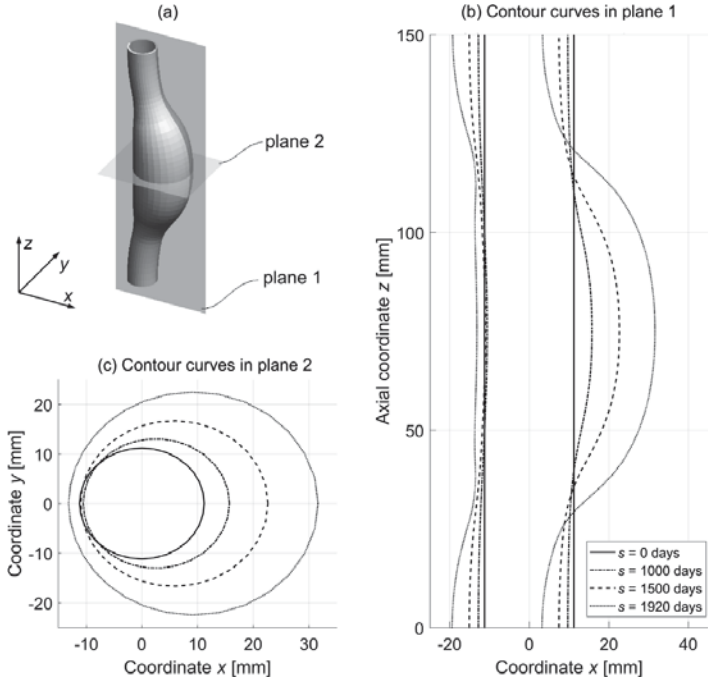

Fig. 9. Outer contours of an asymmetric fusiform aneurysm model in plane 1 (a) and plane 2 (c) at several time instances; definition of the planes is shown in (b).

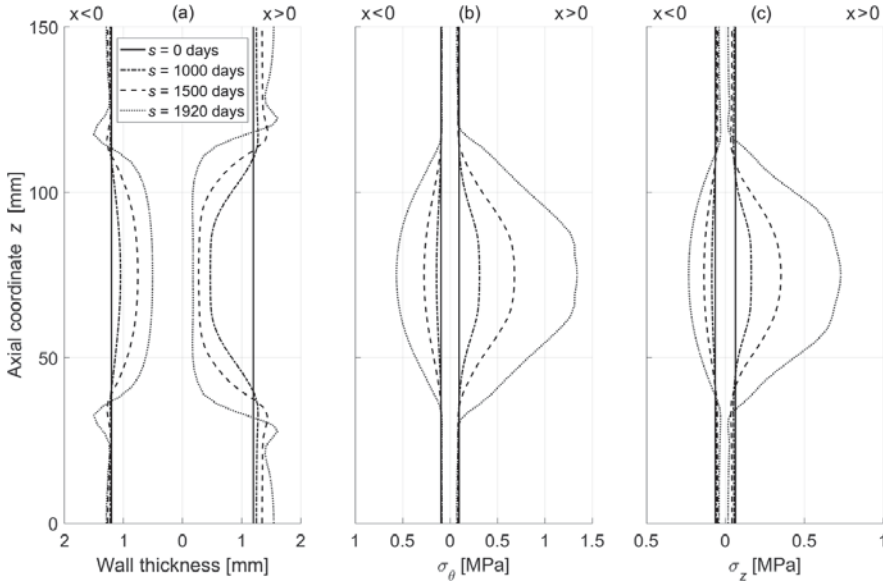

Fig. 10. Wall thickness (a), circumferential stress σ_θ (b) and axial stress σ_z (c) at the inner radius of an asymmetric fusiform aneurysm model along the axial coordinate z at several time instances.

thickness at the aneurysm apex (i.e., at the circumferential coordinate 0°) decreases with G&R time much quicker compared to the opposite side (at the circumferential coordinate 180°, where elastin is intact). Similarly, an increase in the stress is more significant at the aneurysm apex than at the opposite side, see Fig. 11(b) and (c).

5. Discussion and conclusions

In our preceding studies, we have used the semi-analytical method to model cylindrical thrombus-laden AAAs [9,45]. Yet, AAA is a large local dilatation of the infrarenal aorta, and therefore its geometry cannot be

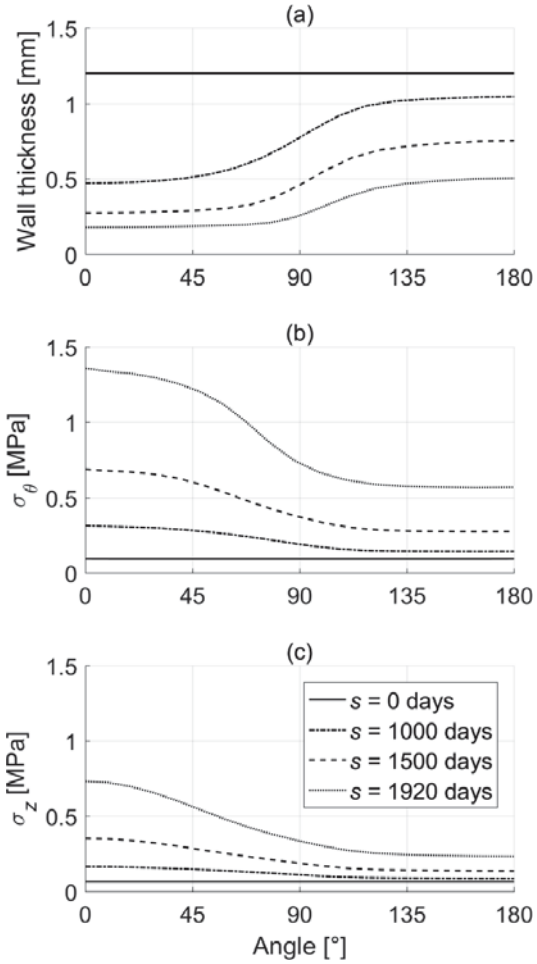

Fig. 11. Wall thickness (a), circumferential stress σ_θ (b) and axial stress σ_z (c) at the inner radius of an asymmetric fusiform aneurysm model at $z = 75$ mmalong the circumferential coordinate (given by the angle) at several time instances.

approximated by a cylinder. The semi-analytical solution of the biochemomechanical G&R model of thrombus-laden AAAs gave us important insights into the disease and empowered us to formulate certain hypotheses. However, these hypotheses should be tested on more realistic geometries, which can only be pursued by using the FE method. As an initial step, we implemented a constrained mixture G&R model of soft biological tissues in a FE code. It was suggested by several studies [21,22,24,46] that the use of a volumetric–isochoric split of the deformation gradient for fiber-reinforced materials provides non-physical results. In this paper we show that in case of G&R it may predict a completely opposite behavior. Thus, we use the (complete) deformation gradient for the calculation of the strain-energy.

We have validated the implementation of the model by analyzing cases of aortic adaptations to changes in the hemodynamics, i.e. changes in blood flow and pressure of a non-idealized aorta. The results show good agreement with the membrane theory, with animal models and clinical observations.

Furthermore, we have investigated the importance of intramural and wall shear stress-mediated mass productions on the outcome of aneurysm growth. Our results show that for an axisymmetric fusiform aneurysm the reestablishment of endothelial cells or the increase in their functionality (i.e. increased wall shear stress-induced production of fibers) leads to a stabilization of the aneurysm, as was also suggested by the animal model documented in [42]. Yet, it is important to keep in mind the functionality of endothelial cells in human aneurysms is not well understood. In the stabilization cases, the stress tends to return to the homeostatic level, whereas in the case of rupture, the stress increases rapidly in time, while the wall becomes significantly thinner at the model aneurysm apex. Note that homeostasis was maintained in the healthy regions, far from the aneurysm sac.

Application of a non-axisymmetric elastin degradation provided realistic deformation and wall stress distributions. Computed evolutions of wall thicknesses and stress components agreed well with clinical observations. The most important feature of the used non-axisymmetric aneurysm model was the increase in the arterial curvature, which is likely caused by the high axial stresses in the aneurysmal sac and the local weakening of the aortic wall.

Nevertheless, there are several limitations in the presented formulation. For example, wall shear stress is calculated by the simple and standard Hagen–Poiseuille formula that is valid for laminar flow through a cylindrical pipe. Such an assumption should not be used for more complex geometries, as shown in Figs. 5 and 9, where turbulent flow and development of vortices are expected. Yet, this can be partially compensated by changing the parameter K_C. Furthermore, elastin loss is defined by time- and space-depended functions. This is likely not realistic. As an additional simplification the surrounding tissues were neglected. We considered the aorta as an isolated organ, which is not realistic.

In conclusion, the presented results indicate a great potential. Hence, we suggest that this is an important step towards patient-specific modeling of soft tissue G&R.

Acknowledgment

This work was supported, in part, by grants from the Croatian Science Foundation (project IP-2014-09-7382 I. Karšaj, project IP-2013-11–2516 J. Sorić).

Appendix A

A.1. Kinematics of AAA

We use here a similar notation as described in [6]. Briefly, although we assume that each constituent deforms with the artery as a whole, each constituent can otherwise possess an individual stress-free configuration. Constituent k deposited at certain instant τ was incorporated within the extracellular matrix with a pre-stretch $\mathbf{G}^k(\tau)$ (mapping between natural configurations of the constituent at an instant τ, and the *in vivo* configuration of the mixture at the same instant). On the other hand, a mapping from the natural configurations of each constituent produced at time τ to a current mixture configuration at time s is defined by the deformation gradient $\mathbf{F}^k_{n(\tau)}(s)$ (see Figure 1 in [6] for clarification). The corresponding right Cauchy–Green tensor $\mathbf{C}^k_{n(\tau)}(s)$ can be calculated as $\mathbf{C}^k_{n(\tau)}(s) = \left(\mathbf{F}^k_{n(\tau)}(s)\right)^{\mathrm{T}} \mathbf{F}^k_{n(\tau)}(s)$. The deformation gradient ${}^s_0\mathbf{F}$ from the initial *in vivo* mixture configuration to the current configuration was calculated using the FE program. Subsequently, we denote this deformation gradient by $\mathbf{F}$, with the associated right Cauchy–Green tensor $\mathbf{C} = \mathbf{F}^{\mathrm{T}}\mathbf{F}$.

A.2. Kinetics of AAA

In accordance with previous G&R models, we let collagen and smooth muscle cells turnover continuously, whereas elastin is produced in the prenatal period and cannot be produced in maturity. In health, its mass is assumed either constant (for a short G&R time) or to decrease with a natural half-life of 40 years during aging. Turnover implicates that the constituent can be degraded and deposited with production rate $\dot{m}^k(\tau)$. Deposition in the arterial wall during homeostasis is constant, and has a basal production rate value m^k_B, whereas during adaptations after injury or during disease it is assumingly driven by deviations from the homeostatic intramural stress, measured as the Cauchy stress $\boldsymbol{\sigma}^k_{\mathrm{h}}$, and deviations from the wall shear stress $\tau^{\mathrm{w}}_{\mathrm{h}}$ that regulates vasoactive molecules so that

$$\dot{m}^k = m^k_B \left[1 + K^k_\sigma \left(\mathbf{m}(s)\, \boldsymbol{\sigma}^k(s)\, \mathbf{m}(s) - \mathbf{m}(0)\, \boldsymbol{\sigma}^k_{\mathrm{h}}(s)\, \mathbf{m}(0) \right) + K^k_C \frac{\tau^{\mathrm{w}} - \tau^{\mathrm{w}}_{\mathrm{h}}}{\tau^{\mathrm{w}}_{\mathrm{h}}} \right], \tag{A.1}$$

where $\boldsymbol{\sigma}^k$ and τ^{w} are the current Cauchy stress tensor and the wall shear stress, respectively, $\mathbf{m}(s)$ and $\mathbf{m}(0)$ denote the current and initial orientations, while K^k_σ and K^k_C are (gain-type) rate parameters that model wall stress- and

shear stress-mediated changes. The current mass of each constituent k was computed as

$$\begin{aligned} M^k(s) &= M^k(0)Q^k(s) + \int_0^s \dot{m}^k(\tau)\, q^k(s-\tau)\, \mathrm{d}\tau \qquad \text{for } s \le 7\tau_{1/2}^k \\ M^k(s) &= M^k(0)Q^k(s) + \int_{s-7\tau_{1/2}^k}^s \dot{m}^k(\tau)\, q^k(s-\tau)\, \mathrm{d}\tau \quad \text{for } s > 7\tau_{1/2}^k \end{aligned}, \tag{A.2}$$

where the survival function $q^k(s-\tau)$ defines a fraction of the constituent produced at the past time τ that remained at the current time s, with a special case $Q^k(s) = q^k(s-0)$, and $M^k(0)$ is the initial mass of the constituent; the half-life of the fibers is denoted by $\tau_{1/2}^k$. As there is no production of elastin, for elastin Eq. (A.2) reduces to $M^{\mathrm{e}}(s) = M^{\mathrm{e}}(0)Q^{\mathrm{e}}(s)$.

The survival function $q^k(s-\tau)$ was defined as

$$q^k(s-\tau) = \exp\left(-\int_\tau^s K_q^k(\widetilde{\tau})\,\mathrm{d}\widetilde{\tau}\right) Q^{k,\mathrm{e}}(s)\,, \tag{A.3}$$

where K_q^k is the mass removal rate-type parameter, and $Q^{k,\mathrm{e}}(s)$ equals 1 for all constituents but smooth muscle cells. To model apoptosis of smooth muscle cells caused by loss of attachment to the surrounding matrix (i.e., elastin), degradation of the smooth muscle was linked to degradation of the elastin such that $Q^{\mathrm{SMC,e}}(s) = Q^{\mathrm{e}}(s)$. The removal rate $K_q^k(\widetilde{\tau})$ was let to depend on the stress of the fiber compared to the homeostatic value as

$$K_q^k(\widetilde{\tau}) = \frac{1}{\tau_{1/2}^k} \frac{\exp\left(0.5\,(I_4(\widetilde{\tau})-1)^2\right)(I_4(\widetilde{\tau})-1)\,I_4(\widetilde{\tau})}{\exp\left(0.5\,(I_4(0)-1)^2\right)(I_4(0)-1)\,I_4(0)}. \tag{A.4}$$

The half-life of collagen and smooth muscle cells is denoted again by $\tau_{1/2}^k$, while

$$I_4(\widetilde{\tau}) = \mathbf{m}(\widetilde{\tau})^k\, \mathbf{C}_{n(\widetilde{\tau})}^k \mathbf{m}(\widetilde{\tau})^k\,.$$

A.3. Stress analysis

The Cauchy stress tensor related to the aortic wall was calculated as

$$\boldsymbol{\sigma} = \frac{2}{\det \mathbf{F}} \mathbf{F} \frac{\partial W}{\partial \mathbf{C}} \mathbf{F}^T + \sigma_{\mathrm{act}} \mathbf{m}^{\mathrm{SMC}} \otimes \mathbf{m}^{\mathrm{SMC}}. \tag{A.5}$$

Under the assumption of constrained mixture, the overall strain-energy function W was defined as $W = \sum_k W^k + W_{\mathrm{sph}}$. Finally, σ_{act} was the active stress contribution from the smooth muscle contractility oriented in the direction $\mathbf{m}^{\mathrm{SMC}}$ of the cells. The active stress was considered to be

$$\sigma_{\mathrm{act}}(s) = T_{\mathrm{m}} \phi^{\mathrm{SMC}}(s) \left(1 - e^{-C(s)^2}\right) \lambda_{\mathrm{act}}^{\mathrm{SMC}}(s) \left[1 - \left(\frac{\lambda_{\mathrm{m}} - \lambda_{\mathrm{act}}^{\mathrm{m}}(s)}{\lambda_{\mathrm{m}} - \lambda_0}\right)^2\right]. \tag{A.6}$$

In (A.6) T_{m} is the maximum actively generated stress, λ_{m} is the circumferential stretch at which the active stress is a maximum, λ_0 is the circumferential stretch at which the active stress goes to zero, ϕ^{SMC} is the mass fraction of the muscle cells, $C(s)$ is the net ratio of vasoconstrictors/vasodilators, and $\lambda_{\mathrm{act}}^{\mathrm{m}}(\tau) = \frac{\lambda^{\mathrm{SMC}}(\tau)}{\lambda^{\mathrm{A}}(\tau)}$. This is slightly modified from the original model [47], where $\lambda_{\mathrm{act}}^{\mathrm{m}}$ was defined as $\lambda_{\mathrm{act}}^{\mathrm{m}}(\tau) = \frac{r^{\mathrm{SMC}}(\tau)}{r^{\mathrm{A}}(\tau)}$, where r is the arterial radius. In general, the geometry does not need to stay axially symmetric, and thus the radius is not necessarily defined. Therefore, we have extended the model for more general geometries by replacing the ratio of radii with the ratio of stretches. Note that for a cylindrical geometry the value of the active stress is not changed by this modification. The stretch λ^A evolves via a first-order rate equation, similar to the original model. Thus,

$$\frac{\mathrm{d}\lambda^{\mathrm{A}}(\tau)}{\mathrm{d}s} = K_{\mathrm{act}}\left[\lambda^{\mathrm{SMC}}(\tau) - \lambda^{\mathrm{A}}(\tau)\right], \tag{A.7}$$

where $\lambda^{\mathrm{A}}(0) = \lambda^{\mathrm{SMC}}(0)$ in a normal artery, and K_{act} is a rate parameter.

Table B.1
Parameter values used for G&R of an aortic wall. Note that 'h' denotes homeostatic.

Class	Role	Parameter value
Observed	Physical constants	$\rho = 1050$ kg m^{-3}, $\mu = 0.0037$ Pa s, $r_i = 10$ mm
	Initial loading	$P_{\mathrm{h}} = 90$ mmHg, $\tau_{\mathrm{h}}^{\mathrm{w}} = 0.506$ Pa, $\sigma_{\mathrm{h}} = 100$ kPa
	Composition by layer	$\phi_{\mathrm{int}} = 0.16$, $\phi_{\mathrm{med}} = 0.52$, $\phi_{\mathrm{adv}} = 0.32$ $\phi_{\mathrm{int}}^{\mathrm{e}} = 0.1$, $\phi_{\mathrm{med}}^{\mathrm{e}} = 0.55$, $\phi_{\mathrm{adv}}^{\mathrm{e}} = 0.25$, $\phi_{\mathrm{med}}^{\mathrm{SMC}} = 0.20$ $\phi_{\mathrm{int}}^{\mathrm{c}} = 0.9$, $\phi_{\mathrm{med}}^{\mathrm{c}} = 0.25$, $\phi_{\mathrm{adv}}^{\mathrm{c}} = 0.75$
	Homeostatic kinetics	$\tau_{1/2}^{\mathrm{c}} = \tau_{1/2}^{\mathrm{SMC}} = 80$ days, $\tau_{1/2}^{\mathrm{e}} = 2$ years
	Passive elasticity	$c_3^{\mathrm{c}} = 22$, $c_3^{\mathrm{SMC}} = 3.5$
Bounded	Pre-stretches	$G_{\Theta\Theta}^{\mathrm{e}} = G_{zz}^{\mathrm{e}} = 1.4$, $G_{\mathrm{h}}^{\mathrm{SMC}} = 1.2$, $G_{\mathrm{h}}^{\mathrm{c}} = 1.08$
	SMC activation	$T_{\mathrm{m}} = 100$ kPa, $\lambda_{\mathrm{m}} = 2$, $\lambda_0 = 0.4$, $K_{\mathrm{act}} = 0.05$
	Production	$K_\sigma^{\mathrm{c}} = 5$, $K_\sigma^{\mathrm{SMC}} = 5$, $K_C^{\mathrm{c}} = 0.1$, $K_C^{\mathrm{SMC}} = 0.1$
Calculated	Passive elasticity	$c_2^{\mathrm{c}} = 560.3$ kPa, $c_2^{\mathrm{SMC}} = 62.1$ kPa, $c^{\mathrm{e}} = 33.96$ kPa

Since fibers deposited into the matrix at different times possess different deformation gradients, they also possess different energies. The strain-energy function is accordingly defined as

$$W^k(s) = \frac{M^k(0)}{\sum_k M^k(s)} \hat{W}^k\left(\mathbf{C}^k_{n(0)}(s)\right) Q^k(s) + \int_0^s \frac{\dot{m}^k(\tau)}{\sum_k M^k(s)} \hat{W}^k\left(\mathbf{C}^k_{n(\tau)}(s)\right) q^k(s-\tau)\, \mathrm{d}\tau \qquad \text{for } s \le 7\tau^k_{1/2}$$
$$W^k(s) = \frac{M^k(0)}{\sum_k M^k(s)} \hat{W}^k\left(\mathbf{C}^k_{n(0)}(s)\right) Q^k(s) + \int_{s-7\tau^k_{1/2}}^s \frac{\dot{m}^k(\tau)}{\sum_k M^k(s)} \hat{W}^k\left(\mathbf{C}^k_{n(\tau)}(s)\right) q^k(s-\tau)\, \mathrm{d}\tau \qquad \text{for } s > 7\tau^k_{1/2} \tag{A.8}$$

The isotropic elastin is modeled as a neo-Hookean material, while collagen and smooth muscle were modeled as fiber-like structures without compressive stiffness and with a specific exponential strain-energy function $\hat{W}$ in tension [48]. Collagen fibers in aneurysms may disperse in plane, but also re-orient out of the cylindrical plane [32], yet due to lack of adequate experimental data this was not modeled here. Trapezoidal integration scheme and Simpson rule were used for time integration.

Appendix B

As can be seen from Table B.1, some parameters are fixed (e.g., initial mass fractions, homeostatic values of stretch and stress, and some mechanical properties), and others are calculated to ensure equilibrium. This inverse problem is difficult to solve in finite elements, and thus the remaining parameters are calculated, meaning that they can only be obtained for a cylindrical geometry. For that reason, we model the expansion of the aneurysms with an initially healthy aorta. Furthermore, by starting from the healthy aorta we avoid to make assumptions on the initial mass fractions, orientations and the mechanical properties of a diseased aorta.

In Table B.1, ρ refers to a mass density, which is assumed to be constant, μ is the viscosity, P_{h} is the homeostatic mean pressure, $\tau_{\mathrm{h}}^{\mathrm{w}}$ is the homeostatic shear stress on the endothelial layer, r_i is the inner radius, and σ_{h} is the assumed stress in the wall. Furthermore, the index "int" refers to the intima, "med" stands for media while "adv" for adventitia, "h" refers to the homeostatic state. The upper indices "c", "SMC" and "e" refer to collagen, smooth muscle cell and elastin, respectively. The mass fraction of the constituent k is defined as $\phi^k = M^k/M$. The initial collagen fraction was subdivided among the four collagen fiber families with the ratio 1:1:4:4 for axial, circumferential, and two helical directions, respectively. Furthermore, $\tau_{1/2}$ denotes the half-life of each constituent, G are prostrates, and c are stiffness parameters. The maximal actively generated stress is T_{m}, λ_{M} is the circumferential stretch at which the active stress is a maximum, while λ_0 is the circumferential stretch at which the active stress goes to zero.

Appendix C

1. *Zeroth time step – homeostasis*
READ input file with data for homeostasis
LOOP until convergence of the augmented Lagrange scheme
    UPDATE geometry
    GET deformation gradient ${}^{s}_{0}\mathbf{F}$
    LOOP over integration points until convergence of the Newton-Raphson scheme
        CALL user material (UMAT) subroutine
        INPUT deformation gradient ${}^{s}_{0}\mathbf{F}$
        READ history variables
        CALCULATE constituents' masses and orientations, stresses
        WRITE to history fields the masses, orientations, deformation gradient, stresses
        OUTPUT: components of the stress tensor $\boldsymbol{\sigma}$, elasticity tensor $\mathbb{C}$
    END LOOP (equilibrium)
END LOOP (augmented Lagrange)
WRITE data

2. *Growth and remodeling*
LOOP for time
    UPDATE geometry
    GET deformation gradient ${}^{s}_{0}\mathbf{F}$
    LOOP over integration points until convergence of the augmented Lagrange scheme
        LOOP until convergence of the Newton-Raphson scheme
            CALL user material (UMAT) subroutine
            INPUT deformation gradient ${}^{s}_{0}\mathbf{F}$
            READ history variables
            CALCULATE mass production, fiber orientations
            LOOP for time
                CALCULATE survival functions, strain-energy function
            END LOOP (time)
            CALCULATE masses, stresses
            WRITE to history fields the masses, orientations, deformation gradient, stresses
            OUTPUT components of the stress tensor $\boldsymbol{\sigma}$, elasticity tensor $\mathbb{C}$
        END LOOP (equilibrium)
    END LOOP (augmented Lagrange)
WRITE data
END LOOP (time)

Appendix D

Solid mechanics elements in *FEAP* are available based on displacement, mixed, and enhanced-strain formulations. A FE formulation, which is free from locking at the incompressible or nearly incompressible limit, may be developed from a mixed variational approach using, e.g., the Hu–Washizu variational principle. In that principle, the

displacements appear up to first derivatives, while the stresses and strains appear without derivatives. Accordingly, the continuity conditions that may be used in FE approximations are C^0 for the displacements and C^{-1} for the stresses and strains (a C^{-1} function is one whose first integral is continuous). Thus, we use Q1P0 elements in *FEAP*. Note that the formulation is not restricted for the use of first-order 3D FEs but according to *FEAP*, a follower pressure can only be analyzed with this type of element.

The G&R theory requires an explicit tracking of the kinetics and the motion, see Appendix C. The integral-based formulation requires a storage of the history of the intervals in order to perform the related numerical integration. Thus, in every integration point we store 70 variables for every time step within the observed life-span (54 variables relate to elastin and fiber kinematics, nine to the deformation gradient ${}^{s}_{0}\mathbf{F}$, five are related to mass production, one to the simulation time of the current time step, and one to the active stretch computation of smooth muscle cells). Additionally, six stress components are stored only for the previous time step. Here it is noted that the minimum necessary number of stored variables is actually lower; it is 17 (nine components for the deformation gradient ${}^{s}_{0}\mathbf{F}$, six for the Cauchy stresses, one variable for the simulation time, and another one for the active stretch computation), while the remaining variables can be computed afresh at every time increment. Yet, our simulations showed that a decrease in the storage of history variables led to a significant increase in the process time. Therefore, we decided to optimize the process time at the expense of memory requirements. Due to that, the memory requirements were five times higher; however the process time was roughly two times shorter.

In order to additionally reduce the process time, the maximal life-span of fibers was set to seven half-lives. By using time steps of ten days, this means that only approximately 50 increments (with 70 variables per integration point) were stored in the history, and integrated at every increment. This did not influence the result, as in homeostasis less than 0.1% of the fiber mass remains after that time. Moreover, in the case of aneurysms, fibers produced more than seven half-lives days ago are likely overstressed to the point they would rupture, and could not bear load anymore. By not considering those fibers that also led to more stable simulations.

Both decision to store more variables and definition of maximal life-span reduced the computational requirements significantly. On average, it takes about 30 h to complete the simulation of fusiform aneurysm growth on one core of an Intel Xeon E5-2630 processor for a mesh with 1200 elements. This can be further decreased by shortening the maximal life-span to 300 days (like Wilson et al. [15] suggested) or by increasing the time step to, say 15 days. Unfortunately, parallel computation, which usually drastically reduces the process time, is difficult to apply to this type of problem, because both spatial and temporal discretizations are needed to find a solution. On the other hand we can run multiple simulations at the same time (up to the number of processor cores), and thus compensate for a longer process time of a single simulation.

References

[1] J.D. Humphrey, K.R. Rajagopal, A constrained mixture model for growth and remodelling of soft tissues, Math. Model. Methods Appl. Sci. 12 (2002) 407–430, http://dx.doi.org/10.1142/S0218202502001714.

[2] A.R. Akintunde, K.S. Miller, Evaluation of microstructurally motivated constitutive models to describe age-dependent tendon healing, Biomech. Model. Mechanobiol. 17 (2018) 793–814, http://dx.doi.org/10.1007/s10237-017-0993-4.

[3] C.M. Witzenburg, J.W. Holmes, A comparison of phenomenologic growth laws for myocardial hypertrophy, J. Elasticity 129 (2017) 257–281, http://dx.doi.org/10.1007/s10659-017-9631-8.

[4] W. Wan, L. Hansen, R.L. Gleason, A 3-d constrained mixture model for mechanically mediated vascular growth and remodeling, Biomech. Model. Mechanobiol. 9 (2010) 403–419, http://dx.doi.org/10.1007/s10237-009-0184-z.

[5] I. Karšaj, J. Sorić, J.D. Humphrey, A 3-D framework for arterial growth and remodeling in response to altered hemodynamics, Internat. J. Engrg. Sci. 48 (2011) 1357–1372, http://dx.doi.org/10.1016/j.ijengsci.2010.06.033.A.

[6] I. Karšaj, J.D. Humphrey, A multilayered wall model of arterial growth and remodeling, Mech. Mater. 44 (2012) 110–119, http://dx.doi.org/10.1016/j.mechmat.2011.05.006.

[7] A. Valentín, J.D. Humphrey, G.A. Holzapfel, A multi-layered computational model of coupled elastin degradation, vasoactive dysfunction, and collagenous stiffening in aortic aging, Ann. Biomed. Eng. 39 (2011) 2027–2045, http://dx.doi.org/10.1007/s10439-011-0287-4.

[8] J.S. Wilson, S. Baek, J.D. Humphrey, Importance of initial aortic properties on the evolving regional anisotropy, stiffness and wall thickness of human abdominal aortic aneurysms, J. R. Soc. Interface 9 (2012) 2047–2058, http://dx.doi.org/10.1098/rsif.2012.0097.

[9] L. Virag, J.S. Wilson, J.D. Humphrey, I. Karšaj, Potential biomechanical roles of risk factors in the evolution of thrombus-laden abdominal aortic aneurysms, Int. J. Numer. Method. Biomed. Eng. 33 (2017) e2893, http://dx.doi.org/10.1002/cnm.2893.

[10] C.J. Cyron, R.C. Aydin, J.D. Humphrey, A homogenized constrained mixture (and mechanical analog) model for growth and remodeling of soft tissue, Biomech. Model. Mechanobiol. 15 (2016) 1389–1403, http://dx.doi.org/10.1007/s10237-016-0770-9.

[11] A. Grytsan, T.S.E. Eriksson, P.N. Watton, T.C. Gasser, Growth description for vessel wall adaptation: A thick-walled mixture model of abdominal aortic aneurysm evolution, Materials (Basel). 10 (2017) e994, http://dx.doi.org/10.3390/ma10090994.

[12] W.J. Lin, M.D. Iafrati, R.A. Peattie, L. Dorfmann, Growth and remodeling with application to abdominal aortic aneurysms, J. Eng. Math. 109 (2017) 113–137, http://dx.doi.org/10.1007/s10665-017-9915-9.
[13] S. Baek, K.R. Rajagopal, J.D. Humphrey, A theoretical model of enlarging intracranial fusiform aneurysms, J. Biomech. Eng. 128 (2006) 142–149, http://dx.doi.org/10.1115/1.2132374.
[14] S. Zeinali-Davarani, A. Sheidaei, S. Baek, A finite element model of stress-mediated vascular adaptation: Application to abdominal aortic aneurysms, Comput. Methods Biomech. Biomed. Eng. 14 (2011) 803–817, http://dx.doi.org/10.1080/10255842.2010.495344.
[15] J.S. Wilson, S. Baek, J.D. Humphrey, Parametric study of effects of collagen turnover on the natural history of abdominal aortic aneurysms, Proc. R. Soc. A Math. Phys. Eng. Sci. 469 (2012) 20120556, http://dx.doi.org/10.1098/rspa.2012.0556.
[16] J. Wu, S.C. Shadden, Coupled simulation of hemodynamics and vascular growth and remodeling in a subject-specific geometry, Ann. Biomed. Eng. 43 (2015) 1543–1554, http://dx.doi.org/10.1007/s10439-015-1287-6.
[17] J. Tong, T. Cohnert, P. Regitnig, J. Kohlbacher, R. Birner-Gruenberger, A.J. Schriefl, et al., Variations of dissection properties and mass fractions with thrombus age in human abdominal aortic aneurysms, J. Biomech. 47 (2014) 14–23, http://dx.doi.org/10.1016/j.jbiomech.2013.10.027.
[18] A. Valentín, J.D. Humphrey, G.A. Holzapfel, A finite element-based constrained mixture implementation for arterial growth, remodeling, and adaptation: Theory and numerical verification, Int. J. Numer. Methods Biomed. Eng. 29 (2013) 822–849, http://dx.doi.org/10.1002/cnm.2555.
[19] F.A. Braeu, A. Seitz, R.C. Aydin, C.J. Cyron, Homogenized constrained mixture models for anisotropic volumetric growth and remodeling, Biomech. Model. Mechanobiol. 16 (2017) 889–906, http://dx.doi.org/10.1007/s10237-016-0859-1.
[20] A. Valentin, L. Cardamone, S. Baek, J.D. Humphrey, Complementary vasoactivity and matrix remodelling in arterial adaptations to altered flow and pressure, J. R. Soc. Interface 6 (2009) 293–306, http://dx.doi.org/10.1098/rsif.2008.0254.
[21] C. Sansour, On the physical assumptions underlying the volumetric-isochoric split and the case of anisotropy, Eur. J. Mech. A/Solids 27 (2008) 28–39, http://dx.doi.org/10.1016/j.euromechsol.2007.04.001.
[22] S. Federico, Volumetric-distortional decomposition of deformation and elasticity tensor, Math. Mech. Solids 15 (2009) 672–690, http://dx.doi.org/10.1177/1081286509105591.
[23] J. Helfenstein, M. Jabareen, E. Mazza, S. Govindjee, On non-physical response in models for fiber-reinforced hyperelastic materials, Int. J. Solids Struct. 47 (2010) 2056–2061, http://dx.doi.org/10.1016/j.ijsolstr.2010.04.005.
[24] O. Gültekin, H. Dal, G.A. Holzapfel, On the quasi-incompressible finite element analysis of anisotropic hyperelastic materials, Comput. Mech. 63 (2019) 443–453, http://dx.doi.org/10.1007/s00466-018-1602-9.
[25] D.M. Milewicz, D.-C. Guo, V. Tran-Fadulu, A.L. Lafont, C.L. Papke, S. Inamoto, et al., Genetic basis of thoracic aortic aneurysms and dissections: focus on smooth muscle cell contractile dysfunction, Annu. Rev. Genomics Hum. Genet. 9 (2008) 283–302, http://dx.doi.org/10.1146/annurev.genom.8.080706.092303.
[26] J.G. Walmsley, M.R. Campling, H.C. Chertkow, Interrelationship among wall structure, smooth muscle orientation, and contraction in human major cerebral arteries, Stroke. 14 (1983) 781–790.
[27] R.L. Taylor, A Finite Element Analysis Program, Version 8.4. 2014.
[28] T. Länne, B. Sonesson, D. Bergqvist, H. Bengtsson, D. Gustafsson, Diameter and compliance in the male human abdominal aorta: influence of age and aortic aneurysm, Eur. J. Vasc. Surg. 6 (1992) 178–184.
[29] A. Valentin, J.D. Humphrey, Evaluation of fundamental hypotheses underlying constrained mixture models of arterial growth and remodelling, Philos. Trans. R. Soc. A Math. Phys. Eng. Sci. 367 (2009) 3585–3606, http://dx.doi.org/10.1098/rsta.2009.0113.
[30] A. Valentín, J.D. Humphrey, Parameter sensitivity study of a constrained mixture model of arterial growth and remodeling, J. Biomech. Eng. 131 (2009) 101006, http://dx.doi.org/10.1115/1.3192144.
[31] I. Karšaj, J. Sorić, J.D. Humphrey, A 3-d framework for arterial growth and remodeling in response to altered hemodynamics, Internat. J. Engrg. Sci. 48 (2010) 1357–1372, http://dx.doi.org/10.1016/j.ijengsci.2010.06.033.
[32] J.A. Niestrawska, C. Viertler, P. Regitnig, T.U. Cohnert, G. Sommer, G.A. Holzapfel, Microstructure and mechanics of healthy and aneurysmatic abdominal aortas: experimental analysis and modelling, J. R. Soc. Interface 13 (2016) 20160620, http://dx.doi.org/10.1098/rsif.2016.0620.
[33] R.D. Brownlee, B.L. Langille, Arterial adaptations to altered blood flow, Can. J. Physiol. Pharmacol. 69 (1991) 978–983, http://dx.doi.org/10.1139/y91-147.
[34] A. Schmidt-Trucksäss, A. Schmid, C. Brunner, N. Scherer, G. Zäch, J. Keul, et al., Arterial properties of the carotid and femoral artery in endurance-trained and paraplegic subjects, J. Appl. Physiol. 89 (2000) 1956–1963, http://dx.doi.org/10.1152/jappl.2000.89.5.1956.
[35] P. Fridez, M. Zulliger, F. Bobard, G. Montorzi, H. Miyazaki, K. Hayashi, et al., Geometrical, functional, and histomorphometric adaptation of rat carotid artery in induced hypertension, J. Biomech. 36 (2003) 671–680, http://dx.doi.org/10.1016/S0021-9290(02)00445-1.
[36] J.J. Hu, T.W. Fossum, M.W. Miller, H. Xu, J.C. Liu, J.D. Humphrey, Biomechanics of the porcine basilar artery in hypertension, Ann. Biomed. Eng. 35 (2007) 19–29, http://dx.doi.org/10.1007/s10439-006-9186-5.
[37] H.N. Ntsinjana, G. Biglino, C. Capelli, O. Tann, A. Giardini, G. Derrick, et al., Aortic arch shape is not associated with hypertensive response to exercise in patients with repaired congenital heart diseases, J. Cardiovasc. Magn. Reson. 15 (2013) 101, http://dx.doi.org/10.1186/1532-429X-15-101.
[38] D. Craiem, G. Chironi, M.E. Casciaro, A. Redheuil, E. Mousseaux, A. Simon, Three-dimensional evaluation of thoracic aorta enlargement and unfolding in hypertensive men using non-contrast computed tomography, J. Hum. Hypertens. 27 (2013) 504–509, http://dx.doi.org/10.1038/jhh.2012.69.
[39] G. Martufi, A. Satriano, R.D. Moore, D.A. Vorp, E.S. Di Martino, Local quantification of wall thickness and intraluminal thrombus offer insight into the mechanical properties of the aneurysmal aorta, Ann. Biomed. Eng. 43 (2015) 1759–1771, http://dx.doi.org/10.1007/s10439-014-1222-2.

[40] Z.Y. Li, U. Sadat, J. U.-K.ing-Im, T.Y. Tang, D.J. Bowden, P.D. Hayes, et al., Association between aneurysm shoulder stress and abdominal aortic aneurysm expansion: A longitudinal follow-up study, Circulation. 122 (2010) 1815–1822, http://dx.doi.org/10.1161/CIRCULATIONAHA.110.939819.

[41] M.F. Fillinger, S.P. Marra, M.L. Raghavan, F.E. Kennedy, Prediction of rupture risk in abdominal aortic aneurysm during observation: Wall stress versus diameter, J. Vasc. Surg. 37 (2003) 724–732, http://dx.doi.org/10.1067/mva.2003.213.

[42] G. Franck, J. Dai, A. Fifre, S. Ngo, C. Justine, S. Michineau, et al., Reestablishment of the endothelial lining by endothelial cell therapy stabilizes experimental abdominal aortic aneurysms, Circulation. 127 (2013) 1877–1887, http://dx.doi.org/10.1161/CIRCULATIONAHA.113.001677.

[43] J.P. Vande Geest, M.S. Sacks, D.A. Vorp, The effects of aneurysm on the biaxial mechanical behavior of human abdominal aorta, J. Biomech. 39 (2006) 1324–1334, http://dx.doi.org/10.1016/j.jbiomech.2005.03.003.

[44] J. Tong, T. Cohnert, P. Regitnig, G.A. Holzapfel, Effects of age on the elastic properties of the intraluminal thrombus and the thrombus-covered wall in abdominal aortic aneurysms: Biaxial extension behaviour and material modelling, Eur. J. Vasc. Endovasc. Surg. 42 (2011) 207–219, http://dx.doi.org/10.1016/j.ejvs.2011.02.017.

[45] L. Virag, J.S. Wilson, J.D. Humphrey, I. Karšaj, A computational model of biochemomechanical effects of intraluminal thrombus on the enlargement of abdominal aortic aneurysms, Ann. Biomed. Eng. 43 (2015) 2852–2867, http://dx.doi.org/10.1007/s10439-015-1354-z.

[46] S. Federico, Volumetric-distortional decomposition of deformation and elasticity tensor, Math. Mech. Solids. 15 (2009) 672–690, http://dx.doi.org/10.1177/1081286509105591.

[47] S. Baek, A. Valentín, J.D. Humphrey, Biochemomechanics of cerebral vasospasm and its resolution: II. Constitutive relations and model simulations, Ann. Biomed. Eng. 35 (2007) 1498–1509, http://dx.doi.org/10.1007/s10439-007-9322-x.

[48] G.A. Holzapfel, T.C. Gasser, R.W. Ogden, A new constitutive framework for arterial wall mechanics and a comparative study of material models, J. Elasticity 61 (2000) 1–48, http://dx.doi.org/10.1023/A:1010835316564.

PAPER 2

Version of Record of the journal article reproduced with permission from Elsevier.

Horvat, Nino, Virag, Lana, Holzapfel, Gerhard A., Karšaj, Igor: Implementation of collagen fiber dispersion in a growth and remodeling model of arterial walls. Journal of the Mechanics and Physics of Solids, 153(3): 104498, 2021, doi.org/10.1016/j.jmps.2021.104498

J. Mech. Phys. Solids 153 (2021) 104498

Contents lists available at ScienceDirect

Journal of the Mechanics and Physics of Solids

journal homepage: www.elsevier.com/locate/jmps

Implementation of collagen fiber dispersion in a growth and remodeling model of arterial walls

Nino Horvat [a], Lana Virag [a], Gerhard A. Holzapfel [b,c], Igor Karšaj [a,*]

[a] University of Zagreb, Faculty of Mechanical Engineering and Naval Architecture, Zagreb, Croatia
[b] Graz University of Technology, Institute of Biomechanics, Graz, Austria
[c] Norwegian University of Science and Technology (NTNU), Department of Structural Engineering, Trondheim, Norway

ARTICLE INFO

Keywords:
Finite element
Arterial growth and remodeling
Collagen fiber dispersion
Aortic aneurysm

ABSTRACT

Imaging studies have shown, and more recently quantified, the collagen fiber dispersions within the aortic wall. Simultaneously, experimental and numerical studies highlight a significant influence of the dispersion on the aortic mechanical response. On the other hand, none of the numerical studies describing the adaptation of healthy and diseased aortas in response to different stimuli take fiber dispersion into account. In this study, we present the first implementation of a fiber dispersion model based on the generalized structure tensor approach into a constrained mixture growth and remodeling model of the aortic wall. Additionally, a new definition of the fiber pre-stretch tensor compatible with fiber dispersion is proposed. The new extended model was implemented into a finite element analysis program, and the influence of collagen fiber dispersions and mean fiber angles on aneurysm growth and the distribution of stresses inside the aortic wall were studied on a three-layered axisymmetric model of a fusiform abdominal aortic aneurysm as well as on non-symmetric aneurysm. In the analyses, the dispersion parameters and the mean fiber angles were varied in the range of measured values for healthy abdominal aortas and aneurysms. Results show a reasonable behavior during an extension-inflation test and the expected evolution of residual stresses during adaptation due to hypertension. Moreover, they show that changes in fiber dispersions and mean fiber angles have a significant influence on the aneurysm evolution and the stress distribution. For example, simulations with increased fiber dispersion in the intima or the media showed a slower aneurysm growth, while the opposite was true for the adventitia. Mean fiber direction closer to the circumferential direction resulted in a stiffer response in the aortic inflation analysis, and it also decreased the aneurysm growth rate.

1. Introduction

The aorta is a multilayered composite structure assembled from a ground matrix, embedded collagen fibers, and smooth muscle cells. Collagen fibers are dispersed within the matrix; however, they can be grouped into families (typically two in each layer) with distinctive mean orientation and dispersion in the tangential plane and out-of-plane (Holzapfel et al., 2015; Niestrawska et al., 2016). A healthy aortic wall has three distinguishable layers, intima, media, and adventitia, each with a different microstructure and function. The microstructure of a diseased aorta significantly changes, in some cases to the point that the layer-specific structure can no longer be

* Corresponding author.
E-mail address: igor.karsaj@fsb.hr (I. Karšaj).

https://doi.org/10.1016/j.jmps.2021.104498
Received 11 September 2020; Received in revised form 20 March 2021; Accepted 15 May 2021
Available online 24 May 2021

recognized, as is the case of an aneurysmal abdominal aorta (for clarification see, e.g., (Niestrawska et al., 2016; Hellenthal et al., 2009), with references therein). Since the mechanical response of the arterial wall is strongly influenced by the underlying microstructure, it is crucial for the microstructure in numerical models to be modeled as detailed as possible in order to obtain accurate results. This also increases the predictive power of models (e.g., prediction of aneurysm growth and rupture).

Dispersion of collagen was first studied in the 1980s, with the development of imaging techniques such as polarized light microscopy. The first studies on the complex structure of arterial walls were performed by Canham and co-workers on coronary and brain arteries and on intracranial aneurysms (see, e.g., Smith et al., 1981; Canham et al., 1989; MacDonald et al., 2000, with related review in Holzapfel, 2008). Recently, using second harmonic generation (SHG), data on the aortic wall structure are becoming more available and detailed (Niestrawska et al., 2016; Schriefl et al., 2012; Gasser et al., 2012).

Based on the obtained imaging data, two different approaches for modeling fiber dispersion in the context of soft tissue mechanics were developed. The first, the angular integration (AI) approach was introduced by Lanir (Lanir, 1983). Within this approach, the fiber dispersion is directly incorporated in a strain-energy function through a probability density function. The strain energy of a single fiber within a dispersion is considered as a function of stretch, and the total strain energy can be obtained by its integration over a unit sphere. In the second approach, the fiber dispersion is represented by a second-order tensor called generalized structure tensor (GST). This approach was first formulated in Gasser et al. (2006) for rotationally symmetric fiber dispersion and later it was extended to a more general case including non-symmetric fiber dispersion (Holzapfel et al., 2015). The predictive power of the two models is equivalent, hence neither of these two models is superior to the other as shown in Holzapfel and Ogden (2017); however the GST approach is simpler to implement and is computationally less demanding. For a more detailed review of the main existing continuum mechanics models with included fiber dispersion see Holzapfel et al. (2015) and Holzapfel et al. (2019).

These two approaches enable the calculation of mural stresses within arteries in a certain instant. However, in order to take into account long-term changes in the structure, and thus an altered stress response of healthy and diseased arterial walls, constrained mixture growth and remodeling (G&R) models are needed. They are microstructurally motivated models that take into account biological processes within the tissue, i.e. production and degradation of structurally important constituents (elastin, collagen, and smooth muscle cells) due to different mechanical (stress-related) and chemical stimuli (e.g., diffusion of vasoconstrictors and vasodilators). The general framework for constrained mixture G&R models of soft tissue was presented by Humphrey and Rajagopal (Humphrey and Rajagopal, 2002). Due to relatively simple geometry G&R models are often used for modeling arteries and abdominal aortic aneurysms (AAAs) (e.g. see Wan et al., 2010; Karšaj et al., 2010; J.S. Wilson et al., 2012; Virag et al., 2017), yet it can be used for modeling various tissues and diseases, from tendon healing (Akintunde and Miller, 2018) to myocardial hypertrophy (Witzenburg and Holmes, 2017).

In order to use the full potential of G&R models for any given geometry, the model is usually implemented in a finite element (FE) software. Early studies used an implementation in a membrane FE formulation, e.g., the first mathematical model of the AAA evolution using membrane FEs was presented by Watton et al. (Watton et al., 2004). Subsequent studies also used membrane elements to model aneurysm growth (Baek et al., 2006), and to study the influence of different aortic properties and kinetic parameters on aneurysm evolution (Wilson et al., 2012a,b; Zeinali-Davarani et al., 2011). Some of the more recent studies with membrane FEs include the work presented in Wu and Shadden (2015). It coupled G&R with a blood flow simulation in a 3D patient-specific geometry, and the computational analysis studied the influence of the spine on AAA growth (Farsad et al., 2016). Although membrane models are very insightful, they are not able to capture some changes or to model a different structure throughout the aortic wall thickness, as 3D models can. The first implementation of a constrained mixture G&R model into 3D finite elements was presented by Valentín et al. (Valentín et al., 2013). Some of the further 3D implementations were performed by Eriksson et al. (Eriksson et al., 2014) for a volumetric growth model of arteries and its application to AAA evolution, and by Grytsan et al. (Grytsan et al., 2015) for a fluid-solid-growth model of AAA applied to a patient-specific geometry, and a thick-walled mixture model of AAA evolution with anisotropic volumetric growth was proposed in Grytsan et al. (2017). Cyron et al. (Cyron et al., 2016) introduced a new homogenized constrained mixture model for G&R of soft tissues. Later Braeu et al. (Braeu et al., 2017) extended this model for anisotropic volumetric growth, implemented it into 3D finite elements, and used it to analyze AAA. In the study (Virag et al., 2015) the G&R theory was used not just for the modeling of an aneurysmatic wall but also to describe the development of intraluminal thrombus and its influence on AAA development. The latest FE implementation of a constrained mixture G&R model was presented in Horvat et al. (2019), together with verification examples and applications to AAA.

Nevertheless, although several collagen fiber dispersion models were developed, G&R models typically consider several perfectly aligned collagen families and neglect their dispersion. Some G&R models feature four collagen fiber families (in axial, circumferential, and two helical directions, see, e.g., Valentín et al., 2013; Karšaj and Humphrey, 2012) instead of two that are typically observed in imaging of the abdominal aorta (Niestrawska et al., 2016; Schriefl et al., 2012). By varying the mass fractions of fiber families, this might, to some degree, emulate certain effects of the fiber dispersion, but only in the tangential plane. This could be adequate for modeling healthy aortic walls; however, in the case of an aneurysm with more expressed dispersion, the use of a dispersion model would be more appropriate. As several numerical studies have shown (see, e.g., Holzapfel et al., 2015; Niestrawska et al., 2018), collagen fiber dispersion has a significant effect on the mechanical response of the aorta and, therefore, should be considered. The study by Ren (Ren, 2013) has taken into account fiber dispersion within a growth model; however, only a simple analytical model with a kinematic growth approach and rotationally symmetric fiber dispersion was considered.

The aim of this work is twofold. Firstly, to extend an existing G&R model that we presented in Horvat et al. (2019), to incorporate a non-symmetric collagen fiber dispersion model. The existing G&R model is a FE model of the abdominal aorta that can be used to analyze the response of an aorta in health (by investigating adaptation to changes in blood flow or pressure) and disease (by considering the formation and growth of an aneurysm). Noting the simplicity and lower computational demands of the GST approach

compared to the AI approach, without affecting the accuracy of the result, in this study the GST approach will be used to model non-symmetric fiber dispersion. Secondly, to use the new extended model to analyze the influence of collagen fiber dispersion on the stress distribution inside the aortic wall and its influence on vascular adaptation, in particular hypertension and growth of AAAs.

2. Methods

In this section, we briefly review the existing constrained mixture G&R model, presented in more detail in Horvat et al. (2019), and the non-symmetric fiber dispersion model developed in Holzapfel et al. (2015), with a special emphasis on their interconnection. Noting that pre-stretch was not included in the original dispersion model, a new definition of the fiber pre-stretch tensor is proposed, and the implementation into finite elements is described.

2.1. G&R model of the aortic wall

The growth and remodeling model used in this study is an extension of a multilayered aortic wall model that was thoroughly described by Horvat et al. (Horvat et al., 2019). To facilitate the procedure of keeping track of model details, the same notation as in Horvat et al. (2019) will be used. Thus, only modifications of the model will here be addressed. The model is based on continuum mechanics and the aortic wall is viewed as a constrained mixture of isotropic elastin, circumferentially oriented smooth muscle cells (SMC), and collagen fibers grouped into several families. The G&R model used in Horvat et al. (2019) had four collagen fiber families (in axial, circumferential, and two helical directions) with no dispersion, whereas the current extended G&R model considers two symmetric helically-oriented families of collagen fibers with a non-symmetric fiber dispersion around the mean fiber direction. Elastin is assumed to be produced only in the prenatal period, while SMC and collagen fibers can turnover continuously in response to deviations of wall (normal/shear) stresses from the homeostatic values. SMCs are assumed to be perfectly aligned in the circumferential direction and, apart from the passive response, they can generate active stresses.

2.2. Implementation of fiber dispersion in the G&R model

A non-symmetric fiber dispersion was modeled using the GST approach, as introduced in Holzapfel et al. (2015), capturing different dispersions in the tangential plane and the out-of-plane. As was described in Horvat et al. (2019), the overall strain-energy function W of the aortic wall, required to calculate the stress tensor, can be written in a decoupled form as

$$W = \sum_k W^k + W_{\text{sph}}, \tag{1}$$

where the first part is the sum of the elastic contribution of all constituents k and W_{sph} is the spherical (volumetric) part defined as

$$W_{\text{sph}} = \frac{1}{d_1}\left(J - \frac{M(s)}{M(0)}\right)^2, \tag{2}$$

where d_1 is a penalty parameter, J is the Jacobian, and $M(s)$ and $M(0)$ denote the current and the initial total mass, respectively.

2.2.1. Collagen strain-energy function

The collagen strain-energy function, used in Horvat et al. (2019), is herein extended to incorporate fiber dispersion. Accordingly, the specific strain-energy function of a collagen fiber family k, at the current time s, is defined as

$$W^k(s) = \frac{c_2^k}{4c_3^k}\left\{\exp\left[c_3^k\left(I_4^k(s) - 1\right)^2 - 1\right]\right\}, \quad k = 1, 2, \tag{3}$$

where c_2^k and c_3^k are material parameters. In the previous G&R models (e.g., Horvat et al., 2019; Karšaj and Humphrey, 2012) with assumed perfect alignment of fibers, the invariant I_4^k depended on the direction $\mathbf{m}^k(\tau)$ of the fiber, produced at time instant τ, i.e.

$$I_4^k(s) = \left(\mathbf{m}^k(\tau)\right)^{\mathrm{T}} \mathbf{C}^k_{n(\tau)}(s)\mathbf{m}^k(\tau). \tag{4}$$

However, in the current model, the fourth invariant is defined as a function of the general structure tensor $\mathbf{H}^k$, i.e.

$$I_4^k(s) = \operatorname{tr}\left(\mathbf{H}^k(\tau)\mathbf{C}^k_{n(\tau)}(s)\right). \tag{5}$$

In the above expressions, $\mathbf{m}^k(\tau)$ denotes a unit vector of the collagen fiber family k along the mean direction at the fiber production time τ, while $\mathbf{C}^k_{n(\tau)}(s)$ is the right Cauchy-Green tensor that connects k constituent's stress-free configuration at τ to the mixture configuration at the current instant s (see Fig. 1 in Karšaj et al., 2010 for more detail). The GST $\mathbf{H}^k$ is a mathematical representation of the fiber dispersion incorporated into a strain-energy function, and thus into the G&R model.

2.2.2. Structure tensor for fiber dispersion

According to Holzapfel et al. (2015), the GST is a symmetric, second-order tensor defined for collagen fiber constituent k, and is

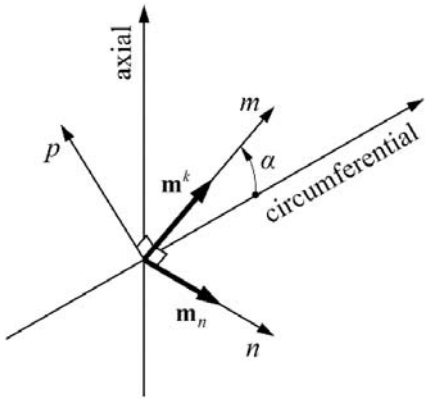

Fig. 1. Fiber coordinate system with a m axis aligned with the mean fiber direction, a p axis aligned in the tangential plane, and an n axis perpendicular to the tangential plane and along the direction of the unit vector $\mathbf{m}_n$. The mean fiber direction $\mathbf{m}^k$ lies in the tangential plane and it is defined by an angle α with respect to the circumferential direction.

given by

$$\mathbf{H}^k(\tau) = A\mathbf{I} + B\mathbf{m}^k(\tau) \otimes \mathbf{m}^k(\tau) + (1 - 3A - B)\mathbf{m}_n(\tau) \otimes \mathbf{m}_n(\tau), \quad k = 1, 2. \tag{6}$$

The vector $\mathbf{m}^k(\tau)$ of the fiber family k along the mean direction lies in the tangential plane of the aorta, while the unit vector $\mathbf{m}_n(\tau)$ is perpendicular to the tangential plane. The constants A and B are given as in Holzapfel et al. (2015). Thus,

$$A = 2\kappa_{\text{op}}\kappa_{\text{ip}}, \quad B = 2\kappa_{\text{op}}\left(1 - 2\kappa_{\text{ip}}\right), \tag{7}$$

where κ_{ip} and κ_{op} are structural parameters describing the dispersion in the tangential plane and the out-of-plane, respectively. The range of values for the dispersion parameters is $\kappa_{\text{ip}} \in [0, 1]$ and $\kappa_{\text{op}} \in [0, 1/2]$. The special case $\kappa_{\text{ip}} = 0$ and $\kappa_{\text{op}} = 1/2$ describes perfectly aligned fibers, while the case $\kappa_{\text{ip}} = 1/2$ and $\kappa_{\text{op}} = 1/3$ corresponds to an isotropic dispersion in both planes. Detailed definitions and interpretations of the dispersion parameters can be found in Holzapfel et al. (2015).

2.2.3. *Pre-stretch tensor definition*

Another major distinction from previous G&R models without fiber dispersion is in the definition of the fiber pre-stretch tensor. In the arterial wall, the fibers are synthesized and deposited into a ground matrix with a certain deposition stretch, i.e. pre-stretch. In the previous study (Horvat et al., 2019) the fiber pre-stretch tensor $\mathbf{G}$ was calculated in the cylindrical coordinate system of the vessel as

$$\mathbf{G}^k(\tau) = G^k\mathbf{m}^k(\tau) \otimes \mathbf{m}^k(\tau), \tag{8}$$

where G^k is a scalar value of the fiber constituent k deposition stretch. This expression is assuming perfectly aligned fibers where the pre-stretch is present only in the mean fiber direction. However, for dispersed fibers, a new definition of this tensor is needed that accounts for a pre-stretch perpendicular to the mean fiber direction. Therefore, we propose a new pre-stretch tensor for collagen fibers to be defined as

$$\mathbf{G}^k = \begin{bmatrix} G_m^k & 0 & 0 \\ 0 & G_p^k & 0 \\ 0 & 0 & G_n^k \end{bmatrix}, \tag{9}$$

using matrix notation, where G_m^k, G_p^k, and G_n^k are pre-stretch components defined in the fiber coordinate system, as shown in Fig. 1. The values of the pre-stretches in the three directions cannot be chosen arbitrarily. In Appendix A, a detailed explanation is provided on how these components are defined for a certain fiber dispersion.

Note that the pre-stretch tensor is defined in a local coordinate system of the fiber; it needs to be rotated into a global Cartesian coordinate system to calculate the total deformation gradient $\mathbf{F}_{n(\tau)}^k$ by multiplying the pre-stretch tensor $\mathbf{G}^k$ (in the Cartesian coordinate system) with the deformation gradient ${}_\tau^s\mathbf{F}$ mapping the *in vivo* mixture configuration from the arbitrary time τ to the current time s ($\mathbf{F}_{n(\tau)}^k(s) = \mathbf{G}^k\,{}_\tau^s\mathbf{F}$), and thus for the calculation of the strain-energy function and the stresses. Unlike collagen, it was assumed that SMCs are not dispersed, and their pre-stretch tensor is calculated according to (8).

2.2.4. *Exclusion of compressed collagen fibers*

Because of the wavy shape of collagen fibers, they are often considered to have load-bearing capabilities only in tension. Therefore, the contribution of the compressed fibers should be excluded from the overall strain-energy function. This can have a significant influence on the mechanical response of the aortic wall, as shown in (Holzapfel and Ogden, 2017; Holzapfel and Ogden, 2015). In this

Table 1
Fiber dispersion parameters κ_{ip}, κ_{op} and mean fiber angle α used in the subsequent analyses. Values were taken from Fig. 7 in Niestrawska et al. (2016) and correspond to minimal, maximal, and median measured values. AA denotes a healthy abdominal aorta and AAA an abdominal aortic aneurysm.

	κ_{ip}			κ_{op}			α		
	min	Median	max	min	median	max	min	median	max
AA intima	0.175	0.261	0.327	0.447	0.484	0.492	0.97°	3.25°	11.52°
AA media	0.135	0.208	0.341	0.471	0.487	0.492	2.71°	6.91°	14.91°
AA adventitia	0.132	0.232	0.352	0.440	0.466	0.486	58.03°	77.53°	87.20°
AA wall	0.205	0.237	0.324	0.469	0.479	0.487	22.37°	24.46°	34.86°
AAA wall	0.158	0.229	0.290	0.397	0.433	0.468	3.33°	14.67°	29.74°

work, we will use a simple tension-compression switch, as suggested in Holzapfel and Ogden (2015). It excludes all fibers with the mean fiber direction under compression, i.e. fibers that satisfy the condition

$$I_4^k(s) = \left(\mathbf{m}(\tau)^k\right)^{\mathrm{T}} \mathbf{C}^k_{n(\tau)} \mathbf{m}(\tau)^k < 1. \tag{10}$$

Note, however, that this condition does not exclude (all) compressed fibers within a dispersion for which the mean fiber direction is under extension. In Holzapfel and Ogden (2017) a method for the exclusion of compressed fibers within the GST approach was presented, where the dispersion parameter was modified at each Gauss point based on the corresponding deformation. However, expressions were derived only for a rotationally symmetric fiber dispersion for the 1D examples. Although this method can presumably be extended to the non-symmetric fiber dispersion, it has still not been reported in the literature.

2.3. Finite element implementation

The current G&R model with collagen fiber dispersion is an extension of the model (Horvat et al., 2019) that we already implemented in a FE code. In summary, the finite element analysis program FEAP (Taylor, 2013) was used, and the model was implemented through subroutines for a user-defined material model, where it is necessary to define the Cauchy stress and the elasticity tensors. A deformation gradient formulation was used, which does not include a volumetric-isochoric split of the strain energy. For the analyses, 8-node hexahedral Q1P0 finite elements were used, and incompressibility was enforced by the augmented Lagrangian method. For a more detailed description of the model implementation, as well as a comparison between the volumetric-isochoric split and the full deformation gradient, the reader is referred to Horvat et al. (Horvat et al., 2019).

2.4. Computational models

In the subsequent numerical examples, we show the effects of in-plane and out-of-plane dispersion on the pressure-extension test, the evolution of residual stresses during the development of hypertension and aneurysm growth. The aortic wall was modeled as a three-layered structure, except for the example with changing dispersion parameters in Section 3.4. where a one-layered aortic wall model was used. For each layer (i.e. intima, media, and adventitia) a different composition, mean fiber angle, and fiber dispersion parameters were defined. Fiber angles and dispersions are summarized in Table 1, while layer composition, and other model parameters that are not explicitly mentioned here, were the same as in Table B.1 in Horvat et al. (2019). Rate parameters that model wall stress- and shear stress-mediated changes in the mass production (see eq. (A.1) in Horvat et al. (2019) for the context of these parameters) were set to $K_\sigma = 1$ and $K_C = 0.13$, respectively. In order to avoid large differences in the material parameters and to increase numerical stability, we have modeled transitional zones between the layers, where the structural parameters changed linearly from values of one layer to values of another layer. The existence of the transitional zones has been confirmed by SHG imaging, and we have defined the width of the zones relative to the observed zones (see Fig. 6 in Niestrawska et al., 2016).

The pre-stretch of collagen fibers was defined according to Appendix A. For the one-layered model, the mass of each constituent (elastin, collagen, or SMC) was equal to the total mass of that constituent from the three-layered model. Mean fiber angles and dispersion parameters were taken from the last two rows of Table 1.

In scope of this work, we have used an axisymmetric fusiform aneurysm as well as non-symmetric aneurysm models to analyze the influence of the fiber dispersion on the abdominal aneurysm development. Each analysis started from a cylindrical geometry of a healthy aorta, for which all needed structural parameters are known, and the development of a AAA was predicted from this stage. However, before the FE analysis, the aortic wall thickness and the stiffness parameters of the constituents had to be calculated in order to ensure equilibrium at the initial step of the analysis. This inverse problem was solved using a 1D cylindrical semi-analytical model, and the unknown parameters were calculated for the given geometry, aortic wall structure, constituent pre-stretches, and the homeostatic stresses. In order to have equal material properties for elastin and SMCs in the mutually compared analyses with different fiber dispersion, the stiffness parameters were calculated in two steps. In the first step, for all three constituents the stiffness parameters were calculated under the assumption of perfectly aligned collagen fibers. In the second step, the collagen stiffness parameter was varied until equilibrium was reached for a given fiber dispersion. Therefore, different dispersion parameters κ_{ip} and κ_{op} in the compared G&R analyses had only an effect on the collagen material properties, while the elastin and SMC properties were equal.

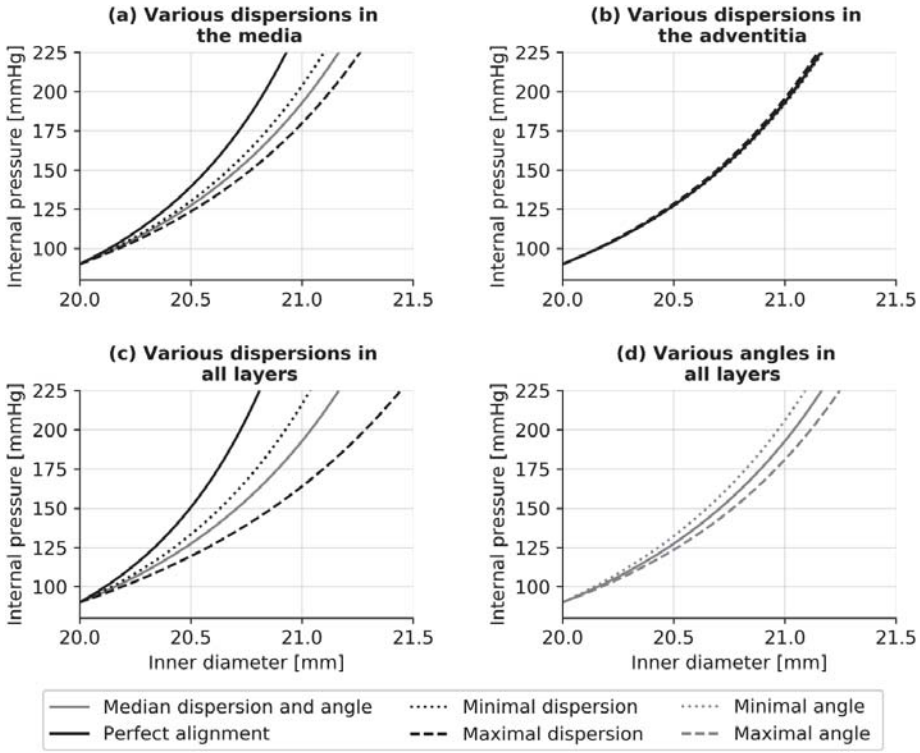

Fig. 2. Effect of the fiber dispersion change in (a) the media, (b) the adventitia, and (c) in all layers simultaneously on the stiffness of the aortic wall; (d) influence of a mean fiber angle change on the aortic wall stiffness.

2.4.1. *Axisymmetric model*

To benefit from the axial symmetry (i.e. to reduce computational cost), an initially healthy aorta was modeled as a 2° cylindrical segment, with a length of $L = 250$ mm and an inner radius of $r_{\text{in}} = 10$ mm. Axisymmetric boundary conditions were imposed on the segment lateral sides, while the top and bottom of the segment were constrained in the axial direction. Furthermore, for the three-layered aortic wall model, the segment was discretized with 2400 finite elements: 120 non-uniformly distributed elements in the axial direction (with finer mesh in the middle where changes due to the aneurysm development were present), one in the circumferential direction, and 20 in the radial direction. For the one-layered aortic wall model, the FE mesh consisted of 720 elements with 6 elements throughout the thickness of the wall. In the case of the inflation analysis, a segment with a length of $L = 5$ mm was used, discretized with one element in the circumferential and axial direction, and 20 elements in the radial direction.

2.4.2. *Non-symmetric model*

When considering an axially non-symmetric aneurysm, then half of a cylinder (180 °cylidrical segment) must be modeled. The length was chosen to be the same as for axially symmetric aneurysm (250 mm) but it was discretized with 50 non-uniform elements in the axial direction, 3 in the radial, and 16 in the circumferential direction.

3. Results and discussion

The illustrated numerical examples aim to show the influence of various fiber dispersions and mean fiber directions on the mechanical response of the abdominal aorta, on the stress distribution inside the aortic wall, residual stresses, and on the growth of an axially symmetric and non-symmetric fusiform AAA.

3.1. *Inflation of a cylindrical aorta*

The first example deals with an extension-inflation analysis of a pre-stretched straight cylindrical segment of an aortic wall. Studies have shown that the fiber dispersion and the mean fiber angle have a significant effect on the mechanical response of the aortic wall (see, e.g., Holzapfel et al., 2015; Gasser et al., 2006; Niestrawska et al., 2018). Therefore, with this example, we want to analyze the influence of the fiber dispersion and, by comparing our results to the results from the literature, verify our implementation of the fiber dispersion model in the constrained mixture G&R theory. A three-layered aortic wall model was used, and dispersion was varied individually in one layer or simultaneously in all three layers (for the respective values see Table 1).

In Fig. 2(a) and (b), the fiber dispersion was individually varied in the media and the adventitia, whereas the dispersion parameters and the mean fiber angles for the other two layers had median values, as listed in Table 1. Likewise, in Fig. 2(c), the fibers had median mean angles, while the dispersion parameters were varied simultaneously in all three layers. A minimal dispersion in the figure

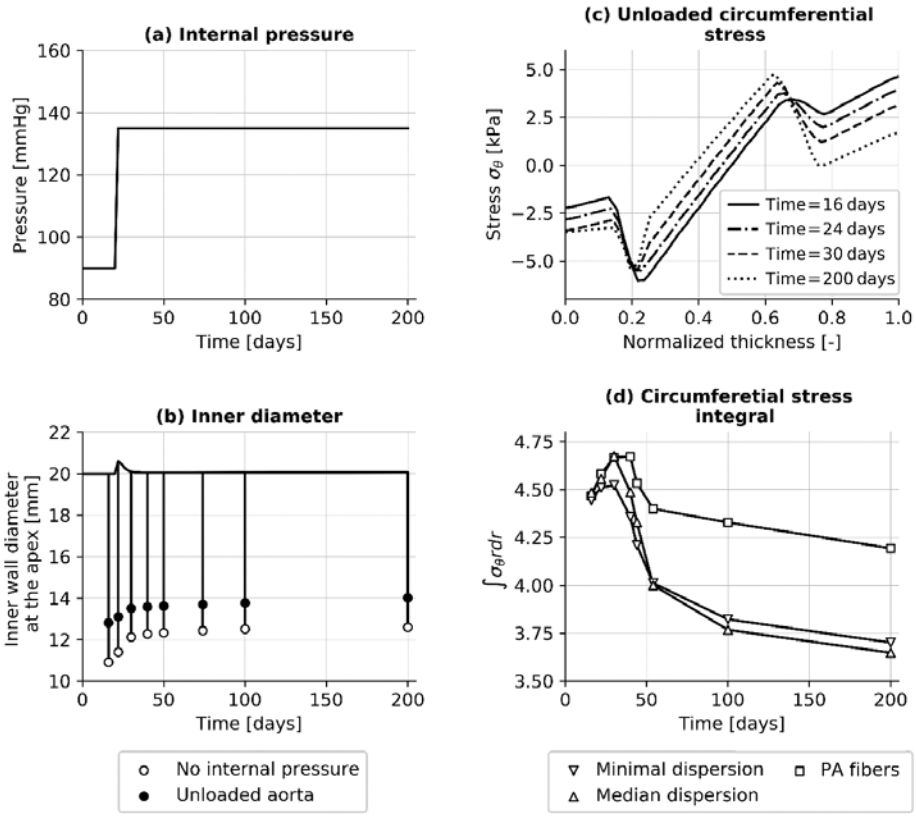

Fig. 3. Vascular adaptation during hypertension: (a) abrupt change of the mean blood pressure; (b) evolution of the *in vivo* inner diameter (solid line), diameter after removal of blood pressure (empty circle) and unloaded diameter (solid circle); (c) distribution of circumferential stress in the unloaded configuration for several time instances during adaptation for the median healthy dispersion; (d) measure of residual stresses – PA means "perfectly aligned".

corresponds to minimal values of κ_{ip} and maximal values of κ_{op} parameters, as listed in Table 1, while the opposite applies for a maximal dispersion. For the case with perfect alignment, the dispersion parameters are $\kappa_{\text{ip}} = 0$ and $\kappa_{\text{op}} = 1/2$. Cases with isotropic dispersion are not shown here because, as mentioned in Appendix A, the pre-stretch tensor definition is not valid for isotropic dispersion.

As can be seen in Fig. 2(a), an increase in the fiber dispersion of the media results in a stiffness decrease of the aortic wall. Similar behavior can be observed for the intima (not shown here). Conversely, for the adventitia (Fig. 2(b)), a higher dispersion slightly increases the aortic wall stiffness, mainly due to the fiber orientation, which is close to the axial direction. For a simultaneous change of the dispersion in all layers (Fig. 2(c)), differences in the mechanical response are more pronounced with the stiffest behavior for perfectly aligned fibers. The most similar analyses are documented in Niestrawska et al. (2018), where the influence of the fiber dispersion on the mechanical response of residually stressed and pre-stretch idealized aortic segment was studied. In study Holzapfel et al. (2015), Gasser et al. (2006), Niestrawska et al. (2018) the authors did not use a pre-stretch tensor, but included residual stresses through an opening angle and an axial pre-stretch, before loading the aorta with blood pressure. Similar to this model, it was shown that analyses with perfectly aligned fibers provided by far the stiffest response. Moreover, in Holzapfel et al. (2015), an analysis of the biaxial extension of a cube reinforced by two symmetric fiber families shows a similarly stiffer stress/stretch response for cases with less fiber dispersion.

Fig. 2(d) illustrates that the pressure/diameter response stiffens for mean fiber angles closer to the circumferential direction. Again, the values of angles in all three layers correspond to minimal and maximal layer angles, as listed in Table 1. The same behavior was reported in Gasser et al. (2006) for the inflation of an adventitial layer with two embedded families of collagen fibers (thin-wall approximation was used). Overall, from these results, we may conclude that the mechanical pressure/diameter response of the aortic wall model stiffens with a decrease of the fiber dispersion, and with a decrease of the mean fiber angle.

3.2. *Evolution of residual stresses during vascular adaptation due to hypertension*

For additional verification of the pre-stretch tensor **G**, and the implementation of the dispersion model during growth and remodeling, it is interesting to investigate residual stresses and their evolution during adaptation due to hypertension. After a 50% increase in mean blood pressure, from 90 to 135 mmHg, as shown in Fig. 3(a), first the inner diameter increases but returns to the homeostatic value, see Fig. 3(b). The presented results are for a median collagen dispersion. Interestingly, unlike the *in vivo* inner diameter, the diameter of the unloaded state increases monotonically. The unloaded state was calculated in two steps: (i) blood

Table 2
Orientations of the fibers in the three aortic layers in the *in vivo* and the unloaded state during adaptation due to hypertension.

	In vivo state			Unloaded state		
Time [day]	Intima	Media	Adventitia	Intima	Media	Adventitia
16	3.25°	6.91°	77.24°	3.62°	7.00°	76.58°
24	3.18°	6.75°	77.19°	3.63°	7.02°	76.39°
30	3.24°	6.82°	77.16°	3.64°	7.02°	76.39°
200	3.24°	6.77°	77.07°	3.66°	7.03°	76.36°

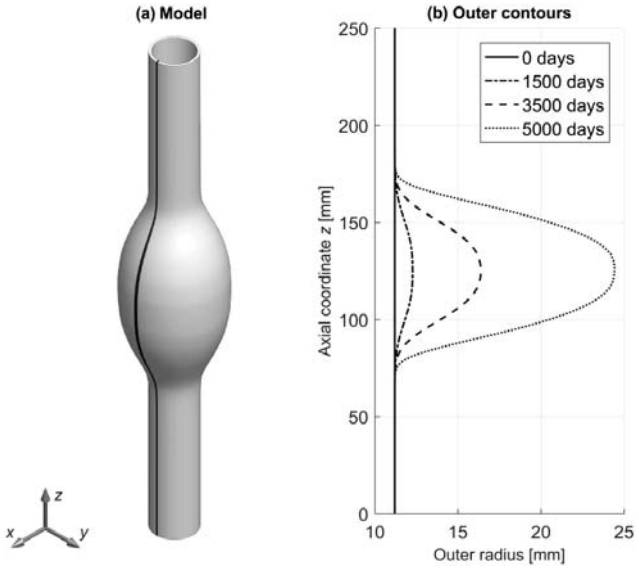

Fig. 4. Axisymmetric fusiform aneurysm model: (a) 3D representation; (b) outer contours at several time instances.

pressure was reduced to zero, and then (ii) the axial boundary condition was removed. In Fig. 3(b), an empty circle denotes the inner diameter of the aorta stressed only by the axial pre-stretch but with removed pressure, and a solid circle denotes the unloaded diameter. Note that the unloaded diameter depends on the thickness, which increases during adaptation due to hypertension, and the axial stretch decreases during hypertension, see, e.g., Bersi et al. (2017) for experimental data and Karšaj and Humphrey (2012) for numerically obtained data on the thickness and the axial stretch evolution. The two factors have opposing effects on the unloaded diameter, yet animal models in rats showed that the unloaded diameter increase slightly during vascular adaptation due to hypertension (Matsumoto and Hayashi, 1994). Circumferential stresses in the unloaded state for a median dispersion are shown in Fig. 3(c). At the inner side of the aorta (i.e. for normalized thickness close to 0) the compression is calculated, while at the outer side (at normalized thickness close to 1) the tension can be seen. This means that if the aortic ring is cut, then the opening of the ring decreases both compression on the inner side and tension on the outer side. Because the opening angle itself is difficult to assess numerically, using finite elements, as a measure of the opening angle, a net bending moment in the unloaded state was calculated according to $\int \sigma_\Theta r dr$ (for more details see Taber and Humphrey (Taber and Humphrey, 2001)). The evolution of the residual bending moment, as shown in Fig. 3(d), first increases rapidly and then decreases to a value lower than the nominal (healthy) value. The animal model presented by Fung and Liu (Liu and Fung, 1989) has demonstrated that opening angles during adaptation due to hypertension in rats changes in exactly the same manner.

Radial and axial residual stresses are not shown in Fig. 3(d), however, the radial stress is zero at the inner and the outer radius, and it takes on a very small negative value in the middle of the aortic thickness. The distribution of the axial stress in the unloaded configuration is similar to the circumferential stress – negative on the inner side and positive on the outer side, however, the calculated integral $\int \sigma_z r dr$, which represents axial force divided by 2π, is zero. This is not surprising because it is a boundary condition for the unloaded state.

A decrease in collagen dispersion influences significantly and leads to a decrease in the opening angle of the aorta adopted due to hypertension, however in the measured range for healthy aorta, the variation of the results is rather minor, see Fig. 3(d).

Note that the collagen orientation and the dispersion are, in general, experimentally measured in the unloaded state, but these measures are mainly used as input data for the *in vivo* state. Hence, we also investigated here the change in collagen orientation in the *in vivo* and the unloaded state. Table 2 shows the collagen angles in all three layers in the *in vivo* and the unloaded state at several time instances during adaptation due to hypertension. Note that for the *in vivo* state, on the 16th day (healthy aorta), the collagen orientation is taken from Table 1. As can be seen from Table 2, there is a surprisingly little difference in the collagen orientation between the *in vivo* and the unloaded state. It is, however, important to have in mind that the dispersion is assumed to be constant during unloading and that the unloaded state is still not a stress-free state in which the orientations were measured. Nor does this necessarily apply to an

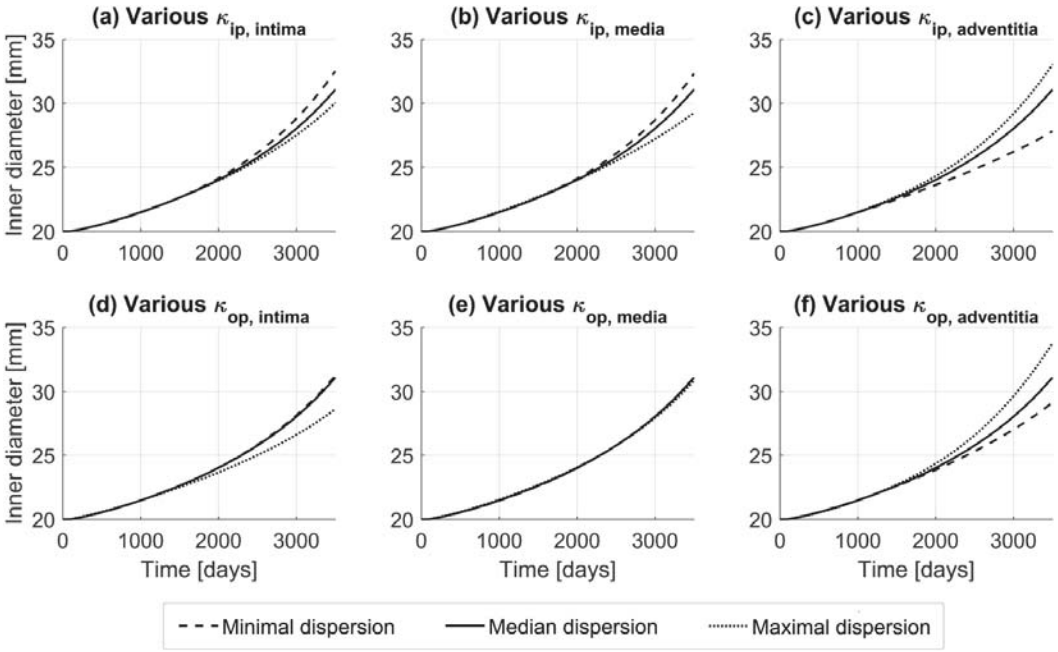

Fig. 5. Axisymmetric fusiform aneurysm model: (a)–(c) influence of the layer-specific change in in-plane dispersion, and (d)–(f) in out-of-plane dispersion on the growth. The inner diameter was measured at the apex of the aneurysm.

aneurysm in which much larger deformations are observed.

3.3. *Three-layered axially symmetric AAA with constant dispersion parameters*

In this section, the influence of the fiber dispersion and the mean fiber direction on a three-layered axially symmetric AAA model was analyzed. Dispersion parameters and fiber angles were set to a certain value at the beginning of each analysis and they did not change over time. The aneurysm development was initiated by a local degradation of elastin, the same way as it was done in Horvat et al. (2019). The elastin degradation function Q^{e} was defined as

$$Q^{\mathrm{e}}(z,s) = \phi^{\mathrm{e}}_{\mathrm{rem}} + \left(1-\phi^{\mathrm{e}}_{\mathrm{rem}}\right)\left[1-\exp\left(-s \,\Big/\, \tau^{\mathrm{e}}_{1/2}\right) f_1(z)\right], \tag{11}$$

where $\tau^{\mathrm{e}}_{1/2}$ is the half-life of elastin and $\phi^{\mathrm{e}}_{\mathrm{rem}} = 0.2$ is the fraction of the remaining not degraded elastin. Degradation in the axial direction z was defined by the function $f_1(z)$ as

$$f_1(z) = \begin{cases} \exp\left[-0.7(z-z_{\mathrm{down}})^2\right] & z < z_{\mathrm{down}}, \\ \exp\left[-0.7\left(z-z_{\mathrm{up}}\right)^2\right] & z > z_{\mathrm{up}}, \\ 1 & z_{\mathrm{down}} \le z \le z_{\mathrm{up}}, \end{cases} \tag{12}$$

with $z_{\mathrm{down}} = 115\mathrm{mm}$ and $z_{\mathrm{up}} = 135\mathrm{mm}$.

In Fig. 4, a 3D representation of an axisymmetric aneurysm model is shown together with the outer contours depicting the shape of the aneurysm at several time instances. As mentioned in Section 2.4, due to the axial symmetry, only a small segment of the aorta was used for the computational analysis. This segment is highlighted in Fig. 4(a) as it is also rotated for illustrative purposes to reveal the entire aorta.

3.3.1. *Influence of fiber dispersion on aneurysm growth*

In this example, we analyze how different degrees of in-plane and out-of-plane dispersions in the individual layers affect the aneurysm growth over time. The related results are shown in Fig. 5. For all six diagrams, median values for the dispersion parameters and the fiber angles were used for all three layers according to Table 1, with the exception of the dispersion parameter, which is listed in the diagram title and whose value has been varied. Again, the minimal dispersion in a particular layer corresponds to a minimal κ_{ip} parameter and a maximal κ_{op} parameter, and vice versa.

As can be seen in Fig. 5, the initially larger in-plane dispersions in the intima and the media result in a slower growth rate of an aneurysm. The opposite effect can be observed for the adventitia, with more pronounced differences between the cases with minimal and maximal dispersions in the layer. A similar behavior, but less pronounced, can be seen for the out-of-plane dispersion. Larger differences between the cases in Fig. 5(c) can be contributed to the largest range of the measured κ_{ip} for the adventitia. On the other hand, κ_{op} for the media had the smallest range (see Table 1). It is interesting to note that an increased dispersion of fibers with a mean orientation close to the circumferential direction has the opposite effect on the aneurysm growth than an increased dispersion of fibers

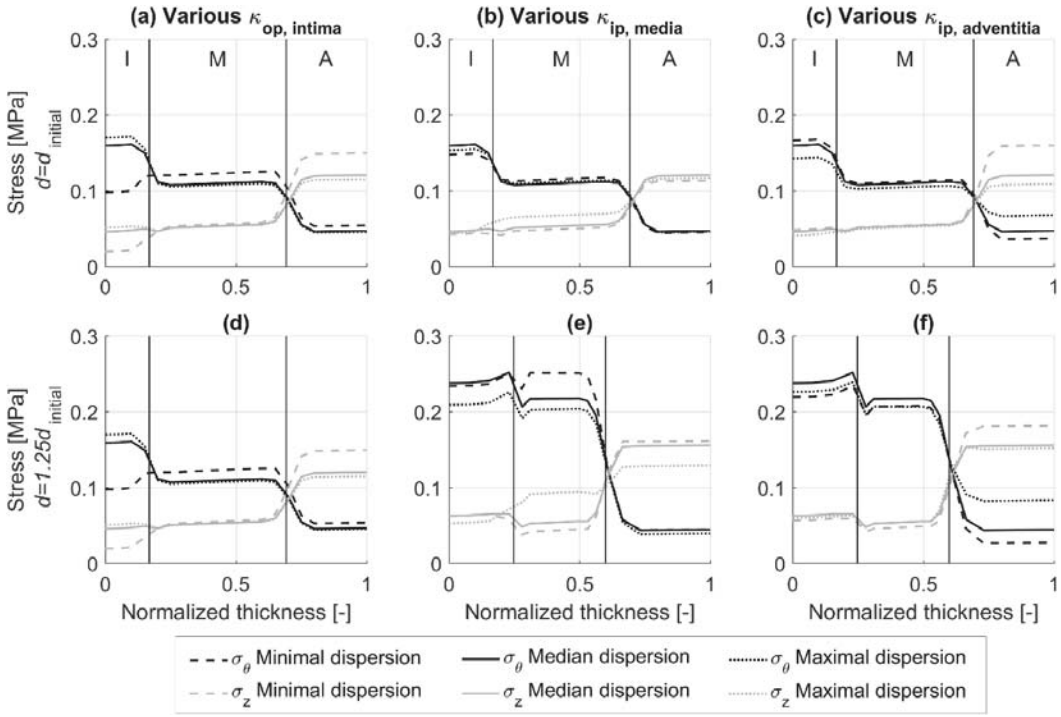

Fig. 6. Influence of layer-specific changes in (a, d) out-of-plane dispersion and in (b, c, e, f) in-plane dispersion on the distribution of the circumferential and the axial Cauchy stresses throughout the thickness of the aortic wall. The stress distribution is illustrated at the initial instant (first row), and at the instant with a 25% inner diameter increase (second row) at the apex of the aneurysm. Vertical lines show boundaries between the individual layers of the aortic wall.

close to the axial direction. This would suggest that aneurysm growth is strongly influenced by the mean fiber angle. According to Fig. 2(a), a minimal dispersion in the media causes a stiffer pressure/diameter response of the aorta, while in the present example it has caused a faster aneurysm growth, see Fig. 5(b). Similarly, for the adventitia, a stiffer pressure/diameter response due to an increased dispersion is associated with a faster aneurysm growth.

3.3.2. Influence of the fiber dispersion on stresses inside the aortic wall

In this section we analyze the influence of the fiber dispersion on the circumferential and axial stress distributions throughout the thickness of the aortic wall at the apex of the aneurysm. Like in the previous example, the dispersion parameters and the mean fiber angles had median values, with the exception of the parameter listed in the title, which has been varied. The first row in Fig. 6 shows the distribution of stresses at the initial moment, while the second row shows the stress distribution for moments when the inner diameter was 25% increased. The first column in Fig. 6 illustrates the stress distribution for various out-of-plane dispersions in the intima. As can be seen, a lower out-of-plane dispersion causes a decrease of both circumferential and axial stress in the layer, and an increase of stress in the other two layers. An opposite but less pronounced behavior is present for larger out-of-plane dispersions. Furthermore, it can be seen that with an increase of the inner diameter, the stress becomes greater and the differences between the dispersion cases are more prominent. An analogous behavior can be observed for a variation of the out-of-plane dispersion in the media and the adventitia (not shown here).

The second and third columns in Fig. 6 depict the influence of various in-plane dispersions on the stress distribution. A lower in-plane dispersion in the media causes an increase of the circumferential stress and a decrease of the axial stress in the layer, and vice versa for a larger dispersion. A similar effect is present in the intima (not shown here). On the other hand, a lower in-plane dispersion in the adventitia decreases the circumferential stress and increases the axial stress, while a larger dispersion has the opposite effect. Collagen fibers are oriented close to the circumferential direction in the intima and the media, and the axial direction in the adventitia. With that in mind, it can be seen that a lower in-plane dispersion causes a higher stress in the fiber mean direction. Again, as for the various out-of-plane dispersions, for a larger inner diameter, the stress increases, and the differences between the cases are more pronounced.

In all cases illustrated in Fig. 6, a thinning of the media relative to the intima and the adventitia can be seen in the enlarged aorta. This is mainly caused by the degradation of elastin and the simultaneous degradation of SMCs (due to apoptosis) in the media. For a clearer view, the boundaries between the individual layers (vertical lines) are shown only for the case with median dispersion. For other cases, the layer thicknesses are slightly, but not significantly, different. A simultaneous increase of dispersion in all three layers (not shown here) tends to level the stresses across the thickness.

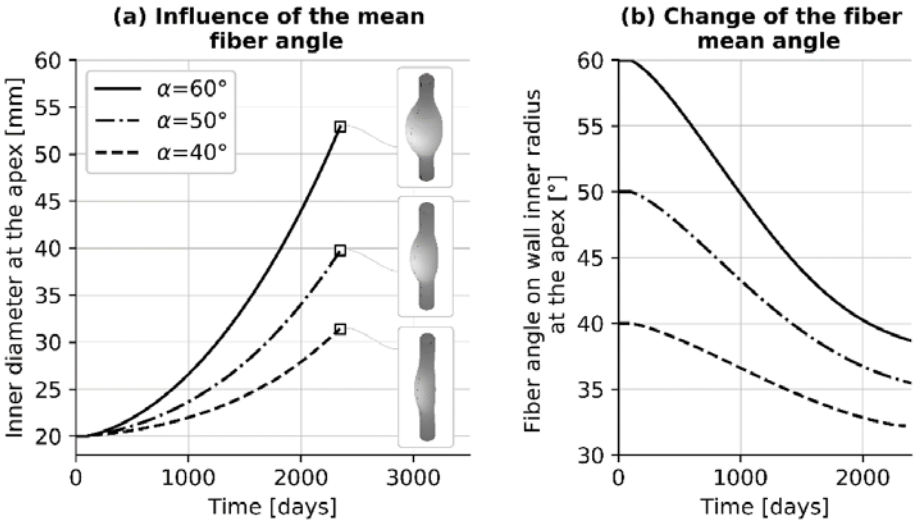

Fig. 7. Non-axisymmetric fusiform aneurysm model: (a) influence of the mean fiber angle on the growth for changes in the dispersion parameters from median healthy to median aneurysmal; (b) related evolution of collagen orientation. The inner diameter was measured at the aneurysm apex.

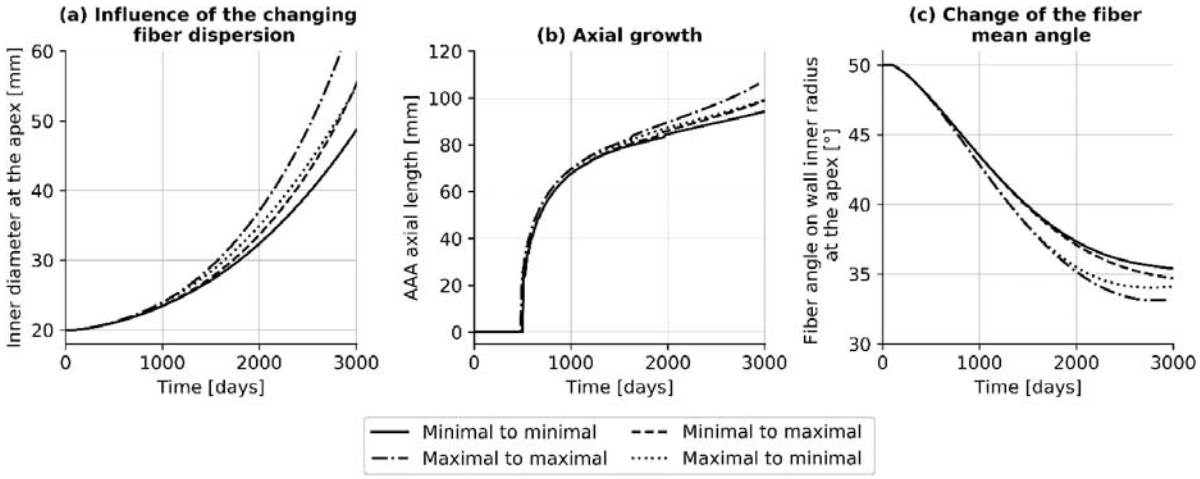

Fig. 8. Non-axisymmetric fusiform aneurysm model: (a) growth of aneurysm maximal diameter; (b) axial length; (c) change of the mean fiber angle for different evolutions of dispersion parameters.

3.4. Influence of fiber angles and change in dispersion on axially non-symmetric aneurysm growth

As was pointed out in Niestrawska et al. (2016) and Gasser et al. (2012), the structure of the healthy and aneurysmatic aortic wall is significantly different, in particular, there is a change in the collagen out-of-plane dispersion. Thus, it is not appropriate to use a constant dispersion parameter during the course of the G&R analysis, where the aortic wall structure changes from an initially healthy to an aneurysmal structure. Since the layer-specific structure is normally not present in the aneurysm after the inner and outer elastic laminae have degraded, the dispersion parameters obtained from SHG imaging in Niestrawska et al. (2016) were given for the entire aneurysmal wall. In this regard, we have used a one-layered aortic wall model to analyze the influence of the (variable) fiber dispersion on the axially non-symmetric aneurysm growth. Data on collagen orientation and dispersion are only known for health or disease. Unfortunately, there are no data from experimental studies available that show how and why the orientation and the dispersion are changing during disease development. Hence, linear interpolation based on the only known variable, i.e. the aneurysm diameter (and thus indirectly the stress), was the best guess we could choose. At each integration point, the dispersion parameters changed linearly between the local inner radii of $r_{\text{in,start}} = 11\text{mm}$ and $r_{\text{in,end}} = 36.5\,\text{mm}$ from the values measured in the healthy aortic wall (fourth row in Table 1) for $r_{\text{in}} \leq r_{\text{in,start}}$ to values measured in the aneurysmal wall (last row in Table 1) for $r_{\text{in}} \geq r_{\text{in,end}}$. The radius $r_{\text{in,end}} = 36.5\,\text{mm}$ was chosen as an average radius of eleven measured AAAs (Niestrawska et al., 2016).

For a simulation of axially non-symmetric aneurysms the elastin degradation function Q^{e} was expanded from Eq. (11) to include changes in the circular direction as

$$Q^{\text{e}}(z,s) = \phi^{\text{e}}_{\text{rem}} + \left(1-\phi^{\text{e}}_{\text{rem}}\right)\left[1-\exp\left(-s \,\Big/\, \tau^{\text{e}}_{1/2}\right) f_1(z) f_2(\vartheta)\right], \tag{13}$$

Table 3
Values of the pre-stretch tensor components for three extreme cases of fiber dispersion.

Case	G^k_m	G^k_p	G^k_n	κ_{ip}	κ_{op}
Perfectly aligned fibers (PA)	g	$1/\sqrt{g}$	$1/\sqrt{g}$	0	0.5
Isotropic dispersion in-plane and no dispersion out-of-plane (ID-IP)	g	g	$1/g^2$	0.5	0.5
Isotropic dispersion out-of-plane and no dispersion in-plane (ID-OP)	g	$1/g^2$	g	0	1/3

where $f_2(\vartheta) = \exp\left(-\frac{c_5\vartheta}{1.001\pi-\vartheta}\right)^2$. All parameters used here are defined in Horvat et al. (2019). Apart from the dispersion parameters, it is interesting to study the influence of initial collagen orientation on the aneurysmal growth, and its change during the growth of the aneurysm.

From Fig. 7(a) it can be seen that a decrease of the mean fiber angle (fibers closer to the circumferential direction) decreases the aneurysm growth rate and vice versa. Additionally, fibers located more towards the circumferential direction lead to a more pronounced non-axisymmetric growth.

Collagen orientation does not directly depend on time, i.e. it is not prescribed. It only changes as a function of the deformation of the artery and is controlled by the deformation gradient. The evolution of collagen angle during aneurysm growth is shown in Fig. 7(b). We show significant (8–22°) reorientation of collagen fibers towards the circumferential direction, which is very similar to what was experimentally observed. It should be noted that mechanical biaxial tests (see, e.g., Vande Geest et al., 2006) have shown an increase in the anisotropy of aneurysmal tissues compared to healthy aortic tissues. Imaging methods showed a more disorganized and dispersed tissue structure, which leads to a more isotropic behavior in which a substantial reorientation of the fibers in the circumferential direction is to be expected.

An examination of the influence of a change in dispersion on the growth rate for a variation from minimal healthy to minimal aneurysmal dispersion (i.e. the most anisotropic wall) – denoted by the solid curve in Fig. 8(a) – shows that growth is the slowest, as could be assumed. Similarly, for the least anisotropic wall (maximal-to-maximal dispersion), the aneurysm expands fastest, both radially and axially, see the dash-dotted curve in Fig. 8(a) and (b). Intriguingly, the reorientation of collagen appears to have reached a threshold that was not defined in any way in the model, see Fig. 8(c). When the fibers stopped reorienting themselves towards the circular direction, but the dispersion parameters continued to change to a more isotropic behavior, the rate of growth of the aneurysm increased.

Since the threshold for reorientation differs in four cases, it appears to depend on both dispersion parameters. It is to be expected that the dispersion reorientates itself less with minimal to minimal dispersion, and the maximal-to-maximal dispersion leads to an increased deformation, but reorientation does not continue. Although all aneurysm growths appear to be relatively similar, note that with a G&R time of 3000 days there is a difference in the maximal diameter of more than 1 cm, in which case the growth rates are very different.

By comparing the difference in maximal diameter of the same healthy dispersion parameter and the same diseased dispersion parameters (see Fig. 8), one can conclude that both the initial and final dispersion values are equally important. Thus, we suggest that more research should be done on the evolution of dispersion in the disease, either using animal models or non-invasive methods.

4. Conclusion

In the present study, a numerical model of collagen fiber dispersion based on the GST approach was implemented for the first time in a constrained mixture G&R model of an aortic wall. In addition, we proposed a new definition of the fiber pre-stretch tensor that is compatible with the fiber dispersion model; it takes into account pre-stretches perpendicular to the mean fiber direction. Similar to

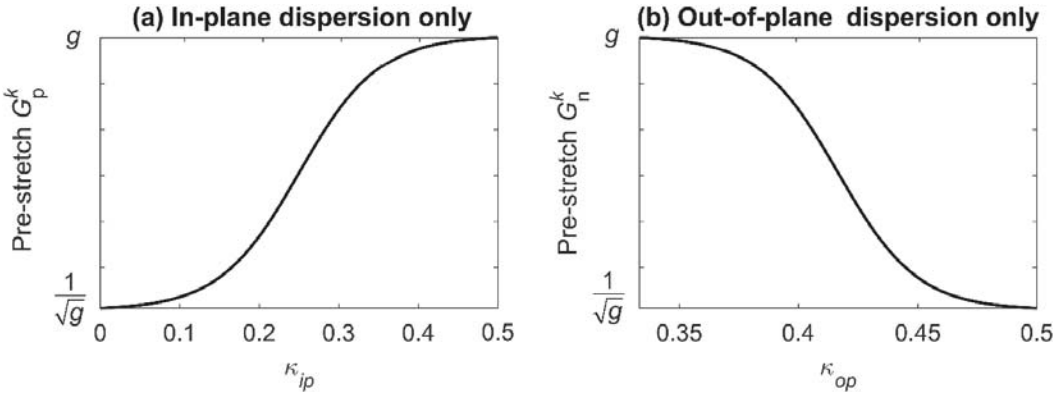

Fig. 9. Relationship between the pre-stretch components and the dispersion parameters: (a) with no out-of-plane dispersion; (b) with no in-plane dispersion.

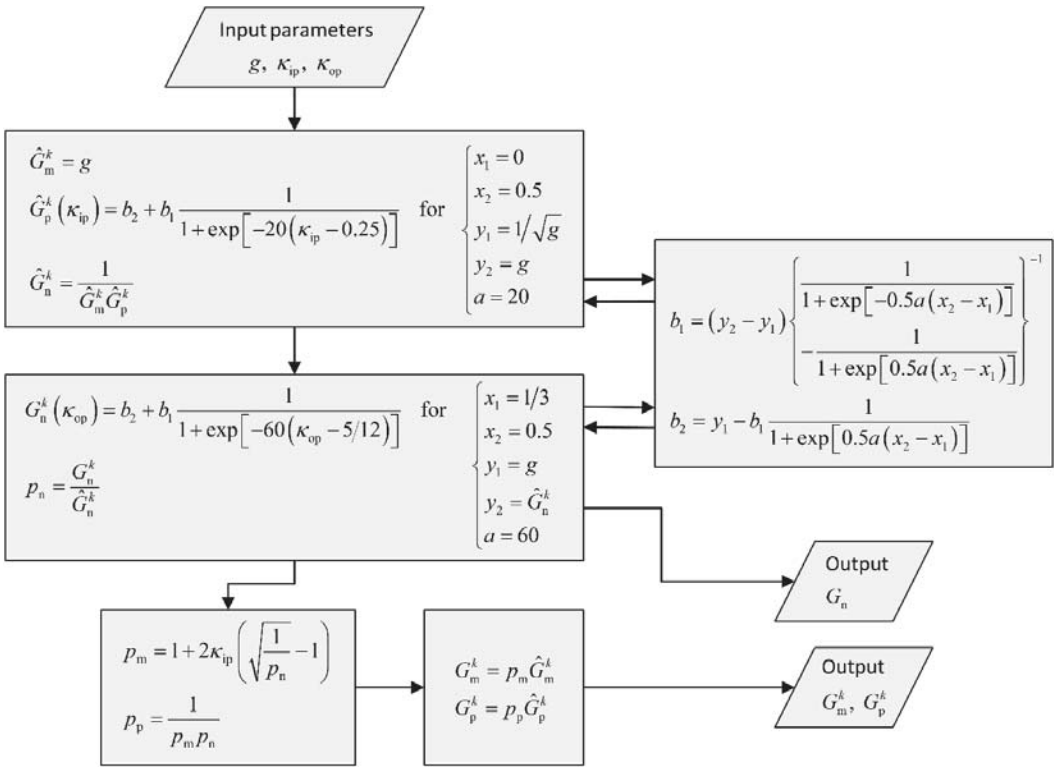

Fig. 10. Method for calculating pre-stretch components for a general case of fiber dispersion.

previous studies, inflation analyses of a straight cylindrical aortic wall model show that collagen fiber dispersions and mean fiber directions have significant effects on the mechanical response of the aortic wall. Particularly, a decrease in the fiber dispersion and a decrease in the mean fiber angle cause a stiffer pressure/diameter response. For a verification of the dispersion model implementation and the pre-stretch tensor definition, we investigated residual stresses during vascular adaptation due to hypertension. We showed a reasonable residual stress distribution (compression on the inner side and tension on the outer side) and a development of the opening angle that corresponds to the animal model. The mean angles in the *in vivo* and the unloaded states in health appear to be very similar.

Furthermore, the results, which compared the development of the inner diameter of an aneurysm for cases with different fiber dispersions and mean fiber angles, show that they play a significant and equally influential role in aneurysm growth. A smaller mean fiber angle (i.e. closer to the circumferential direction) results in slower aneurysm growth, while minimal dispersion in the intima and media and maximal dispersion in the adventitia result in faster aneurysm growth. From the stress analyses it can be concluded that lower in-plane dispersion causes an increase in stress in a given layer in the fiber mean direction (i.e. circumferential stress in the intima and media, and axial stress in the adventitia), and that lower out-of-plane dispersion in a given layer causes a decrease in both circumferential and axial stresses in the layer, while the stress in the other two layers is increased. The opposite behavior is true for larger in-plane and out-of-plane dispersions.

As explained in Niestrawska et al. (2016), the structure of the healthy and aneurysmatic aortic wall differs considerably, especially the collagen out-of-plane dispersion. To take this into account, in the last example, the fiber dispersion was changed over time with respect to the inner diameter of the aneurysm. The results of an axially non-symmetrical aneurysm show that changes in the initial collagen mean orientation towards circumferential direction result not only in a stiffer mechanical response (and consequently slower growth), but also in non-axisymmetric growth and more bending of the aneurysm. Moreover, we show a significant reorientation of the collagen fibers of around 10–20°. Finally, we show that reorientation can have a threshold and that both initial and final dispersion are equally important for the aneurysm. This suggests that temporal and spatial variations of the structural parameters should be considered in G&R simulations. For this purpose, however, more detailed measurements of the aneurysm structure are required.

Nevertheless, there are several limitations in the present study. Our analyses were performed for the *in vivo* state, whereas the dispersion parameters and the mean fiber angles used in the simulations were measured *ex vivo* on the unloaded configuration of the aortic wall (Niestrawska et al., 2016). Certainly, due to the constituent pre-stretches in the aortic wall, *in vivo* and *ex vivo* structural parameters are not equal. Since an aim of this study was to show the influence of fiber dispersions on AAA growth rather than modeling precise patient-specific conditions, we used available *ex vivo* parameters due to the lack of *in vivo* data. Almost all of the AAAs tested in (Niestrawska et al., 2016) contained an intraluminal thrombus. Virag et al. (Virag et al., 2015) have shown that the intraluminal thrombus has a significant effect on AAA growth, however, no thrombus was modeled in this work. Although we focused on AAA, the presented G&R model with the non-symmetrical fiber dispersion can also be used to model other arterial and fibrous tissues.

Neither the collagen dispersion nor the mean orientation depend on the development of the disease, the fiber stress, or the stretch. In order to integrate such mechanisms, it is necessary to formulate a thermodynamically consistent model, see, e.g., Karšaj et al.

(2009). Since such a formulation is computationally very demanding, we decided not to use it as no experimental or clinical data are required for model calibration.

From the results it is clear that changes in the aortic wall structure (i.e. change in fiber dispersion and mean fiber direction) have significant effects on mechanical response, stress distribution within the wall, and the growth of AAA. In order to improve the predictive capabilities of biomechanical simulations, the tissue structure must be modeled as precisely as possible. Therefore, we suggest that modeling of fiber dispersion should not be neglected in future numerical studies of abdominal aortic aneurysms.

CRediT authorship contribution statement

Nino Horvat: Visualization, Writing – original draft, Writing – review & editing, Data curtion, Investigation, Methodology, Software, Formal analysis. **Lana Virag:** Visualization, Writing – review & editing, Validation, Formal analysis. **Gerhard A. Holzapfel:** Conceptualization, Methodology, Validation. **Igor Karšaj:** Project administration, Funding acquisition, Supervision, Conceptualization, Methodology, Validation.

Declaration of Competing Interest

The authors declare that they have no known competing financial interests or personal relationships that could have appeared to influence the work reported in this paper.

Acknowledgment

This work was supported by a grant from the Croatian Science Foundation (project IP-2014-09-7382, I. Karšaj) and by a project Training of New Doctoral Students (DOK-2015-10-3164).

APPENDIX A

The pre-stretch tensor $\mathbf{G}^k$ in (9) is defined in terms of three diagonal components that describe pre-stretches in the three main directions of the fiber coordinate system (see Fig. 1). These components depend on the fiber dispersion parameters and they can easily be defined for three extreme cases of fiber dispersion, as shown in Table 3. In that table, the parameter g denotes a collagen deposition stretch, which was set to 1.08 for all analyses. Note that a case with isotropic dispersion both in-plane and out-of-plane is not mentioned in the table since it is not possible to define a pre-stretch tensor for an isotropic incompressible material. In that case, all three components of the pre-stretch tensor would have to be the same $G^k_{\mathrm{m}} = G^k_{\mathrm{p}} = G^k_{\mathrm{n}} = g$, and under the assumption of incompressibility, they would all be equal to one for any arbitrary value of g.

It is not known how the pre-stretch components change between these extremes, or how they can be defined in the general case with both in-plane and out-of-plane dispersion. We have assumed a change according to a sigmoid function, as shown in Fig. 9, however, the true change might be different. For example, between the PA and ID-IP extreme cases, where dispersion is present, only in-plane ($\kappa_{\mathrm{op}} = 0.5$), the pre-stretch component G^k_{m} remains constant and equal to g, the pre-stretch component G^k_{p} changes from $1/\sqrt{g}$ to g according to Fig. 9(a), whereas the pre-stretch component G^k_{n} is calculated from the incompressibility condition. Similarly, between the PA and ID-OP extreme cases the dispersion is present only out-of-plane ($\kappa_{\mathrm{ip}} = 0$). Then the pre-stretch component G^k_{n} changes from $1/\sqrt{g}$ to g according to Fig. 9(b), while the pre-stretch component G^k_{m} remains constant and equal to g, and G^k_{p} is again calculated from the incompressibility condition.

Sigmoid functions between two points (x_1, y_1) and (x_2, y_2) can be defined as:

$$S(x) = b_2 + b_1 \frac{1}{1 + \exp\{-a[x - 0.5(x_1 + x_2)]\}}, \tag{14}$$

$$b_1 = (y_2 - y_1)\left\{\frac{1}{1 + \exp[-0.5a(x_2 - x_1)]} - \frac{1}{1 + \exp[0.5a(x_2 - x_1)]}\right\}^{-1}, \tag{15}$$

$$b_2 = y_1 - b_1 \frac{1}{1 + \exp[0.5a(x_2 - x_1)]}, \tag{16}$$

where the parameter a defines the curvature of the function. Based on eq. (14), the sigmoid function in Fig. 9(a) is defined as

$$G^k_{\mathrm{p}}(\kappa_{\mathrm{ip}}) = b_2 + b_1 \frac{1}{1 + \exp\left[-20\left(\kappa_{\mathrm{ip}} - 0.25\right)\right]}, \tag{17}$$

with b_1 and b_2 calculated according to Eqs. (15) and (16) using $x_1 = 0$, $x_2 = 0.5$, $y_1 = 1/\sqrt{g}$, and $y_2 = g$. Similarly, the sigmoid function in Fig. 9(b) is defined as

$$G_{\mathrm{n}}^{k}(\kappa_{\mathrm{op}}) = b_2 + b_1 \frac{1}{1+\exp\left[-60\left(\kappa_{\mathrm{op}} - 5/12\right)\right]}, \tag{18}$$

with $x_1 = 1/3, x_2 = 0.5, y_1 = g$, and $y_2 = 1/\sqrt{g}$ being used to calculate b_1 and b_2. For the parameter a we have assumed $a = 20$ in (17) and $a = 60$ in (18).

So far we consider cases with only in-plane dispersion (between PA and ID-IP extreme cases) and with only out-of-plane dispersion (between PA and ID-OP extreme cases). In these cases, the pre-stretch component in the fiber mean direction was always $G_{\mathrm{m}}^{k} = g$, while the two other components were defined from the sigmoid functions and the incompressibility condition. However, in a general case with a dispersion both in-plane and out-of-plane, the pre-stretch component in the fiber mean direction G_{m}^{k} is not fixed, and the pre-stretch components are defined in two steps.

In the first step, the out-of-plane dispersion is ignored and the components are calculated as if there was only the in-plane dispersion. For the extreme cases between PA and ID-IP, the procedure is the same as mentioned above. The pre-stretch components calculated in the first step are label as $\widehat{G}_{\mathrm{m}}^{k}$, $\widehat{G}_{\mathrm{p}}^{k}$ and $\widehat{G}_{\mathrm{n}}^{k}$. In the second step, the pre-stretch component $\widehat{G}_{\mathrm{n}}^{k}$ has to increase to account for the out-of-plane dispersion. Simultaneously, due to the incompressibility condition, the components $\widehat{G}_{\mathrm{m}}^{k}$ and $\widehat{G}_{\mathrm{p}}^{k}$ have to decrease. The increase of G_{n}^{k} depends on κ_{op}, while the final value of G_{n}^{k} is calculated using the sigmoid function (18) with $x_1 = 1/3, x_2 = 0.5, y_1 = g$, and $y_2 = \widehat{G}_{\mathrm{n}}^{k}$ used to calculate b_1 and b_2. Note the change in the y_2 value. The factors $p_{\mathrm{m}}, p_{\mathrm{p}}$, and p_{n}, which describe the changes in $\widehat{G}_{\mathrm{m}}^{k}$, $\widehat{G}_{\mathrm{p}}^{k}$, and $\widehat{G}_{\mathrm{n}}^{k}$, are defined as

$$p_{\mathrm{m}} = \frac{G_{\mathrm{m}}^{k}}{\widehat{G}_{\mathrm{m}}^{k}},\ p_{\mathrm{p}} = \frac{G_{\mathrm{p}}^{k}}{\widehat{G}_{\mathrm{p}}^{k}},\ p_{\mathrm{n}} = \frac{G_{\mathrm{n}}^{k}}{\widehat{G}_{\mathrm{n}}^{k}}. \tag{19}$$

The changes in $\widehat{G}_{\mathrm{m}}^{k}$ and $\widehat{G}_{\mathrm{p}}^{k}$ depend on κ_{ip}, and the two extreme cases can be defined for the $\widehat{G}_{\mathrm{m}}^{k}$ change as

$$\begin{aligned} &p_{\mathrm{m}} = 1 \text{ for } \kappa_{\mathrm{ip}} = 0, \\ &p_{\mathrm{m}} = p_{\mathrm{p}} \text{ for} \kappa_{\mathrm{ip}} = 0.5. \end{aligned} \tag{20}$$

If we assume a linear correlation between p_{m} and κ_{ip}, and by using the incompressibility condition $p_{\mathrm{n}} p_{\mathrm{m}} p_{\mathrm{p}} = 1$, we can calculate p_{m} and p_{p} for an arbitrary κ_{ip} as

$$p_{\mathrm{m}} = 1 + 2\kappa_{\mathrm{ip}}\left(\sqrt{\frac{1}{p_{\mathrm{n}}}} - 1\right), p_{\mathrm{p}} = \frac{1}{p_{\mathrm{m}} p_{\mathrm{n}}}, \tag{21}$$

from where we can easily obtain G_{m}^{k} and G_{p}^{k}.

The method for calculating the pre-stretch components for a general case of fiber dispersion can also be seen in a flowchart shown in Fig. 10. Note that this method provides pre-stretch components that satisfy the extreme conditions shown in Table 3, however it is not correct for the cases with a high dispersion in both tangential plane and out-of-plane. Nevertheless, this does not pose a problem, as such cases of dispersion may not exist in the aortic wall and the pre-stretch tensor cannot be defined for incompressible isotropic materials.

References

Akintunde, A.R., Miller, K.S., 2018. Evaluation of microstructurally motivated constitutive models to describe age-dependent tendon healing. Biomech. Model. Mechanobiol. 17 (3), 793–814.

Baek, S., Rajagopal, K.R., Humphrey, J.D., 2006. A theoretical model of enlarging intracranial fusiform aneurysms. J. Biomech. Eng. 128 (1), 142–149.

Bersi, M.R., Khosravi, R., Wujciak, A.J., Harrison, D.G., Humphrey, J.D., 2017. Differential cell-matrix mechanoadaptations and inflammation drive regional propensities to aortic fibrosis, aneurysm or dissection in hypertension. J. R. Soc. Interface 14 (136).

Braeu, F.A., Seitz, A., Aydin, R.C., Cyron, C.J., 2017. Homogenized constrained mixture models for anisotropic volumetric growth and remodeling. Biomech. Model. Mechanobiol. 16 (3), 889–906.

Canham, P.B., Finlay, H.M., Dixon, J.G., Boughner, D.R., Chen, A., 1989. Measurements from light and polarised light microscopy of human coronary arteries fixed at distending pressure. Cardiovasc. Res. 23 (11), 973–982.

Cyron, C.J., Aydin, R.C., Humphrey, J.D., 2016. A homogenized constrained mixture (and mechanical analog) model for growth and remodeling of soft tissue. Biomech. Model. Mechanobiol. 15 (6), 1389–1403.

Eriksson, T.S.E., Watton, P.N., Luo, X.Y., Ventikos, Y., 2014. Modelling volumetric growth in a thick walled fibre reinforced artery. J. Mech. Phys. Solids 73, 134–150.

M. Farsad, S. Zeinali-davarani, J. Choi, and S. Baek, "Computational Growth and Remodeling of Abdominal Aortic Aneurysms Constrained by the Spine," vol. 137, no. September 2015, pp. 1–12, 2016.

Gasser, T.C., Gallinetti, S., Xing, X., Forsell, C., Swedenborg, J., Roy, J., 2012. Spatial orientation of collagen fibers in the abdominal aortic aneurysm ' s wall and its relation to wall mechanics. Acta Biomater 8 (8), 3091–3103.

Gasser, T.C., Ogden, R.W., Holzapfel, G.A., 2006. Hyperelastic modelling of arterial layers with distributed collagen fibre orientations. J. R. Soc. Interface 3 (6), 15–35.

Grytsan, A., Eriksson, T.S.E., Watton, P.N., Gasser, T.C., 2017. Growth description for vessel wall adaptation: a thick-walled mixture model of abdominal aortic aneurysm evolution. Materials (Basel) 10 (9), e994.

Grytsan, A., Watton, P.N., Holzapfel, G.A., 2015. A thick-walled fluid–solid-growth model of abdominal aortic aneurysm evolution: application to a patient-specific geometry. J. Biomech. Eng. 137 (3), 031008.
Hellenthal, F.A.M.V.I., Buurman, W.A., Wodzig, W.K.W.H., Schurink, G.W.H., 2009. Biomarkers of abdominal aortic aneurysm progression. Part 2: inflammation. Nat. Rev. Cardiol. 6, 543–552.
Holzapfel, G.A., 2008. Collagen in Arterial Walls: biomechanical Aspects. In: Fratzl, P. (Ed.), Collagen: Structure and Mechanics. Springer US, Boston, MA, pp. 285–324.
Holzapfel, G.A., Niestrawska, J.A., Ogden, R.W., Reinisch, A.J., Schriefl, A.J., 2015. Modelling non-symmetric collagen fibre dispersion in arterial walls. J. R. Soc. Interface 12, 20150188.
Holzapfel, G.A., Ogden, R.W., 2015. On the tension-compression switch in soft fibrous solids. Eur. J. Mech. /A Solids 49, 561–569.
Holzapfel, G.A., Ogden, R.W., 2017. On fiber dispersion models: exclusion of compressed fibers and spurious model comparisons. J. Elast. 129 (1–2), 49–68.
Holzapfel, G.A., Ogden, R.W., Sherifova, S., 2019. On fibre dispersion modelling of soft biological tissues : a review. Proc. R. Soc. A Math. Phys. Eng. Sci. 475 (2224), 20180736.
Horvat, N., Virag, L., Holzapfel, G.A., Sorić, J., Karšaj, I., 2019. A finite element implementation of a growth and remodeling model for soft biological tissues: verification and application to abdominal aortic aneurysms. Comput. Methods Appl. Mech. Eng. 352, 586–605.
Humphrey, J.D., Rajagopal, K.R., 2002. A constrained mixture model for growth and remodelling of soft tissues. Math. Model. Methods Appl. Sci. 12 (03), 407–430.
Karšaj, I., Humphrey, J.D., 2012. A multilayered wall model of arterial growth and remodeling. Mech. Mater. 44, 110–119.
Karšaj, I., Sansour, C., Sorić, J., 2009. The modelling of fibre reorientation in soft tissue. Biomech. Model. Mechanobiol. 8 (5), 359–370.
Karšaj, I., Sorić, J., Humphrey, J.D., 2010. A 3-D framework for arterial growth and remodeling in response to altered hemodynamics. Int. J. Eng. Sci. 48 (11), 1357–1372.
Lanir, Y., 1983. Constitutive equations for fibrous connective tissues. J. Biomech. 16 (1), 1–12.
Liu, S.Q., Fung, Y.C., 1989. Relationship between hypertension, hypertropy, and opening angle of zero-stress state of arteries following aortic constriction. J. Biomech. Eng. 111 (4), 325–335.
MacDonald, D.J., Finlay, H.M., Canham, P.B., 2000. Directional wall strength in saccular brain aneurysms from polarized light microscopy. Ann. Biomed. Eng. 28 (5), 533–542.
Matsumoto, T., Hayashi, K., 1994. Mechanical and dimensional adaptation of rat aorta to hypertension. J. Biomech. Eng. 116 (3), 278–283.
Niestrawska, J.A., Viertler, C., Regitnig, P., Cohnert, T.U., Sommer, G., Holzapfel, G.A., 2016. Microstructure and mechanics of healthy and aneurysmatic abdominal aortas: experimental analysis and modelling. J. R. Soc. Interface 13 (124), 20160620.
Niestrawska, J.A., Haspinger, D.Ch., Holzapfel, G.A., 2018. The influence of fiber dispersion on the mechanical response of aortic tissues in health and disease: a computational study. Comput. Methods Biomech. Biomed. Engin. 21 (2), 99–112.
Ren, J., 2013. Growth and residual stresses of arterial walls. J. Theor. Biol. 337, 80–88.
Schriefl, A.J., Zeindlinger, G., Pierce, D.M., Regitnig, P., Holzapfel, G.A., Jun. 2012. Determination of the layer-specific distributed collagen fibre orientations in human thoracic and abdominal aortas and common iliac arteries. J. R. Soc. Interface 9 (71), 1275–1286.
Smith, J.F.H., Canham, P.B., Starkey, J., 1981. Orientation of collagen in the tunica adventitia of the human cerebral artery measured with polarized light and the universal stage. J. Ultrasructure Res. 77 (2), 133–145.
Taber, L.A., Humphrey, J.D., 2001. Stress-modulated growth, residual stress, and vascular heterogeneity. J. Biomech. Eng. 123 (6), 528.
Taylor, R., 2013. FEAP - Finite Element Analysis Program, Version 8.4. University of California at Berkeley, Berkeley (CA).
Valentín, A., Humphrey, J.D., Holzapfel, G.A., 2013. A finite element-based constrained mixture implementation for arterial growth, remodeling, and adaptation: theory and numerical verification. Int. J. Numer. Method. Biomed. Eng. 29 (8), 822–849.
Vande Geest, J.P., Sacks, M.S., Vorp, D.A., 2006. The effects of aneurysm on the biaxial mechanical behavior of human abdominal aorta. J. Biomech. 39 (7), 1324–1334.
Virag, L., Wilson, J.S., Humphrey, J.D., Karšaj, I., 2015. A Computational model of biochemomechanical effects of intraluminal thrombus on the enlargement of abdominal aortic aneurysms. Ann. Biomed. Eng. 43 (12), 2852–2867.
Virag, L., Wilson, J.S., Humphrey, J.D., Karšaj, I., 2017. Potential biomechanical roles of risk factors in the evolution of thrombus-laden abdominal aortic aneurysms. Int. J. Numer. methods Biomed. wngineering 33 (12), e2893.
Wan, W., Hansen, L., Gleason, R.L., 2010. A 3-D constrained mixture model for mechanically mediated vascular growth and remodeling. Biomech. Model. Mechanobiol. 9 (4), 403–419.
Watton, P.N., Hill, N.A., Heil, M., 2004. A mathematical model for the growth of the abdominal aortic aneurysm. Biomech. Model. Mechanobiol. 3, 98–113.
Wilson, J.S., Baek, S., Humphrey, J.D., 2012a. Parametric study of effects of collagen turnover on the natural history of abdominal aortic aneurysms. Proc. R. Soc. A Math. Phys. Eng. Sci. 469 (2150), 20120556.
Wilson, J.S., Baek, S., Humphrey, J.D., 2012b. Importance of initial aortic properties on the evolving regional anisotropy, stiffness and wall thickness of human abdominal aortic aneurysms. J. R. Soc. Interface 9 (74), 2047–2058.
Witzenburg, C.M., Holmes, J.W., 2017. A comparison of phenomenologic growth laws for myocardial hypertrophy. J. Elast. 129 (1–2), 257–281.
Wu, J., Shadden, S.C., 2015. Coupled simulation of hemodynamics and vascular growth and remodeling in a subject-specific geometry. Ann. Biomed. Eng. 43 (7), 1543–1554.
Zeinali-Davarani, S., Sheidaei, A., Baek, S., 2011. A finite element model of stress-mediated vascular adaptation: application to abdominal aortic aneurysms. Comput. Methods Biomech. Biomed. Engin. 14 (9), 803–817.

PAPER 3

Horvat, Nino, Virag, Lana, Karšaj, Igor: Mechanical role of intraluminal thrombus in aneurysm growth: a computational study. Biomechanics and Modeling in Mechanobiology, 20(5):1819-1832, 2021, doi.org/10.1007/s10237-021-01478-w

Biomechanics and Modeling in Mechanobiology
https://doi.org/10.1007/s10237-021-01478-w

ORIGINAL PAPER

Mechanical role of intraluminal thrombus in aneurysm growth: A computational study

Nino Horvat[1] · **Lana Virag**[1] · **Igor Karšaj**[1]

Received: 24 November 2020 / Accepted: 7 June 2021

Abstract
Models that seek to improve our current understanding of biochemical processes and predict disease progression have been increasingly in use over the last decades. Recently, we proposed a finite element implementation of arterial wall growth and remodeling with application to abdominal aortic aneurysms (AAAs). The study focused on changes within the aortic wall and did not include the complex role of intraluminal thrombus (ILT) during the AAA evolution. Thus, in this work, we extend the model with a gradual deposition of ILT and its mechanical influence on AAA growth. Despite neglecting the increased biochemical activity due to the presence of a proteolytically active luminal layer of ILT, and thus underestimating rupture risk potential, we show that ILT helps to slow down the growth of the aneurysm in the axial direction by redirecting blood pressure loading from the axial-radial plane to predominately radial direction. This very likely lowers rupture potential. We also show that the ratio of ILT volume to volume sac is an important factor in AAA stabilization and that fully thrombosed aneurysms could stabilize quicker and at smaller maximum diameters compared to partially thrombosed ones. Furthermore, we show that ILT formation and the associated mural stress decrease negatively impact the wall constituent production and thickness. Although further studies that include increased biochemical degradation of the wall after the formation of ILT and ILT deposition based on hemodynamics are needed, the present findings highlight the dual role an ILT plays during AAA progression.

Keywords Growth and remodeling · Abdominal aortic aneurysm · Intraluminal thrombus · Finite element method

1 Introduction

It is well known that abdominal aortic aneurysms (AAAs) typically harbor intraluminal thrombus (ILT). According to a large population-based cohort study presented in (Behr-Rasmussen et al. 2014), its occurrence increases with AAA size: in the group of AAAs measuring 30–34 mm, by definition the smallest possible aneurysm size, already 42% contained ILT. In the group with a maximum AAA diameter of 35–39 mm, ILT occurrence increased to 60%, whereas all aneurysms with a diameter larger than 64 mm were thrombus-laden.

A key factor in the ILT formation is believed to be hemodynamics and the associated wall shear stress (WSS). WSS is likely responsible for inducing both platelet activation and endothelial dysfunction, two prerequisites for thrombus formation (Di Achille et al. 2014). Aggregation of activated platelets on injured endothelium leads to fibrin deposition. Fibrin fibers are stabilized by crosslinking into a network, while platelets and blood cells, most notably erythrocytes and leukocytes, get entwined into it, thus forming an intraluminal thrombus. Interestingly, unlike other blood clots, ILT does not heal by endothelial cell coverage or replacement of the fibrin with collagen fibers (Franck et al. 2013). Consequently, with new thrombus depositions over time, ILT can gradually become a layered structure. The three structurally, mechanically, and proteolytically distinct layers of a thrombus are the fresh luminal layer closest to the blood flow, the medial layer devoid of the cells, and the oldest, abluminal, layer with disorganized fibrin structure adjacent to the wall.

The role intraluminal thrombus plays in abdominal aortic aneurysm evolution is very controversial and not understood at all. Numerous clinical, experimental, and computational studies resulted in conflicting conclusions. For example, several studies found that AAA rupture is associated with

✉ Igor Karšaj
igor.karsaj@fsb.hr

[1] Faculty of Mechanical Engineering and Naval Architecture, University of Zagreb, Ivana Lučića 5, 10000 Zagreb, Croatia

Published online: 20 June 2021

larger ILT volumes (Hans et al. 2005; Parr et al. 2011); however, another study found no difference in ILT volumes in ruptured and intact AAA (Golledge et al. 2014). Another controversial measure is ILT thickness. Some studies claim that thicker thrombi lead to localized hypoxia, and consequentially, increased neovascularization and inflammation, as well as regional wall weakening (Vorp et al. 2001). Yet, some studies found that thicker thrombus slowed down the AAA growth and vice versa, smaller relative size of ILT was linked to the higher growth rate (Domonkos et al. 2019).

Similarly, several computational studies showed that the thrombus mechanically shields the aortic wall, starting with work presented by (Inzoli et al. 1993). Other studies (Mower et al. 1997; Di Martino et al. 1998) also confirmed the results on both idealized and 3-D patient-specific geometries (Gasser et al. 2010; Maier et al. 2010). However, others questioned the ability of soft, porous thrombus to shield the aortic wall. For example, (Meyer et al. 2010) showed the cushioning effect of the fully attached thrombus and thrombus-induced stress concentration when it is partially attached to the wall. Indeed, all previous studies assumed a perfect attachment of ILT to the wall. Although the connection of platelets and collagen is well studied, little is known about the attachment of fibrin to collagen. Additionally, some studies, e.g., (Fontaine et al. 2002; Swedenborg and Eriksson 2006), reported the "liquid phase" was found between thrombus and wall, leading to the conclusion that ILT is not always tightly bound to the aortic wall. Additionally, Tong et al. (Tong et al. 2011) reported that some abluminal layers were degraded to the point they had almost no tensile strength and could not be mechanically tested, further raising the question of the connection between the ILT and the wall.

Our previous growth and remodeling (G&R) study on a simplified cylindrical model allowed us to hypothesize about the role of the ILT on AAA growth. We have shown that ILT has an essential role in aneurysm evolution and should not be neglected during modeling (Virag et al. 2015, 2017). The model shows a great agreement with smoking- and hypertension-induced increases in growth rate (Virag et al. 2017), both of which are clinically observed (Bhak et al. 2015). The model confirmed and offered additional support to the age, female gender, smoking, and hypertension being factors that increase rupture risk. Additionally, it also supported animal models in the claim that inhibition of inflammation, both elastin- and collagen-based, decreases growth rate (Parodi et al. 2005; Steinmetz et al. 2005), but at the same time agrees with the trial on humans (Arnoud Meijer et al. 2013) that the decrease might not be sufficient to prevent AAA growth enough for the surgery to be avoided (Virag et al. 2017). In addition to confirming already accepted hypotheses, the model also yielded in some new insights into bio-chemo-mechanical processes within AAA. We hypothesized that it could cause commonly observed staccato growth (Kurvers et al. 2004). The model can explain why thin thrombus contributes to rapid expansion, whereas thick ILT decreases dilatation rate (Domonkos et al. 2019), despite ILT thickness being proposed to be a rupture risk factor (Vorp et al. 2001).

For verification of these hypotheses, it is necessary to model an aneurysm with more realistic geometry. As the first step in hypotheses verification, we implemented the G&R model of the aortic wall into a finite element environment (Horvat et al. 2019). The implementation validation was performed by analyses of homeostasis and aortic adaptations to changes in the hemodynamics, i.e., changes in blood flow and pressure, of a non-idealized aorta. The obtained results show an excellent agreement with the membrane theory estimation, animal models, and clinical observations. When applied to an axisymmetric fusiform aneurysm, the model shows that intramural and wall shear stress-mediated mass productions of fibers might be one of the key features determining the outcome of aneurysm growth, with the higher deposition of collagen leading to an aneurysm stabilization. This was also suggested in the animal model presented in (Franck et al. 2013). Furthermore, the application of the model to non-axisymmetric aneurysms showed an increase in the arterial curvature, which is also typically clinically observed, likely caused by the high axial stresses in the aneurysmal sac and the local weakening of the aortic wall.

In this work, we expand that model with the inclusion of thrombus elements and investigate the mechanical influence of intraluminal thrombus on aneurysm growth in axially symmetrical AAAs, the importance of ILT to aneurysm sac volume ratios as well as the moment of the first thrombus deposition. Although the biochemical influence of the ILT is neglected in this work, this is the first G&R finite element model investigating the effect of thrombus deposition on AAA evolution.

2 Methodology

2.1 Aortic wall growth and remodeling

The implementation of constrained mixture growth and remodeling model of the arterial wall, proposed in (Humphrey and Rajagopal 2002), into the finite element analysis program (FEAP, (Taylor 2013)) was first presented in (Horvat et al. 2019) in detail. Briefly, the aortic wall is considered a mixture of four collagen families, elastin, and smooth muscle. Collagen and smooth muscle are allowed to turnover continuously, with their production rate increasing with increased wall stresses and decreased wall shear stresses compared to the homeostatic levels. Although each constituent produced in each time step is

allowed to possess their own natural, stress-free configuration, they deform as a constrained mixture.

The aortic wall is assumed to be incompressible, and thus an appropriate finite element formulation free from locking at the incompressible or nearly incompressible limit was chosen, i.e., a mixed variational approach using the Hu-Washizu variational principle. Hexahedral 8-node elements with three degrees of freedom at each node were employed; for axially symmetric fusiform aneurysm model, a 2° three-layered cylindrical segment of height $L = 350$ mm was discretized with 1440 elements (120 non-uniform elements in the axial direction, one in the circumferential direction, and 12 throughout the thickness of the wall). Proximal–distal symmetry was assumed to restrict axial lengthening or shortening of the aortic segment.

Additionally, in order to minimize numerical instabilities introduced by large gradients and discontinuities at the interfaces between layers, transition zones with a gradual change in the structure from one layer to another were defined. Histological imaging on aortic tissue also indicated the presence of transition zones: on the intensity plots showing collagen fiber orientation and dispersion through the healthy aortic wall thickness, the "transition layers" in between the layers with different fiber orientations were visible (Niestrawska et al. 2016). Therefore, the width of the transition zones was chosen to correspond to the width of the transition layers observed in these findings.

Enlargement of aneurysms is believed to be initiated by the local irreversible loss of elastin. Elevated oxidative stress levels are believed to be responsible for the initial elastin damage (Martinez-Pinna et al. 2010). In the thrombus-laden aneurysm, elastin is further degraded by proteolytic activity of deposited ILT, as well as increased neovascularization. However, in the current model, the biochemical influence of thrombus is neglected, and thus loss of elastin is simplified to a spatiotemporal function, adopted from (Wilson et al. 2012), and similar to other studies that focused on fusiform aneurysm growth (Braeu et al. 2017; Grytsan et al. 2017; Lin et al. 2017). Thus, the fraction of elastin remaining at the current time s is defined as

$$Q^{\mathrm{e}}(z,\tau) = \phi^{\mathrm{e}}_{\mathrm{rem}} + \left(1-\phi^{\mathrm{e}}_{\mathrm{rem}}\right)\left[1-\exp\left(-s/\tau^{\mathrm{e}}_{1/2}\right)f_1(z)\right] \quad (1)$$

where $\phi^{\mathrm{e}}_{\mathrm{rem}} = 0.2$ is the remaining functional elastin set to correspond with data of (Tong et al. 2014) showing that even in large aneurysms some functional elastin remained, and $\tau^{\mathrm{e}}_{1/2}$ is the half-life of elastin. The function $f_1(z)$ is describing local, non-uniform degradation of elastin in the axial direction z, and is defined as

$$f_1(z) = \begin{cases} \exp\left[-0.7\left(z-z_{\mathrm{down}}\right)^2\right] & z < z_{\mathrm{down}}, \\ \exp\left[-0.7\left(z-z_{\mathrm{up}}\right)^2\right] & z > z_{\mathrm{up}}, \\ 1 & z_{\mathrm{down}} \le z \le z_{\mathrm{up}}. \end{cases} \quad (2)$$

In between coordinates $z_{\mathrm{down}} = 165$ mm and $z_{\mathrm{up}} = 185$ mm from Eq. (2) degradation of elastin is maximal and constant, while as axial coordinate z approaches 0 or L, $f_1(z)$ gradually approaches zero, leaving elastin intact in the healthy part of the aorta. All other model equations and parameters for the aortic wall without thrombus, an interested reader can find in (Horvat et al. 2019).

2.2 Intraluminal thrombus deposition and mechanics

In the aortic wall, the turnover of constituents happens internally, e.g., fibroblasts and smooth muscle cells present in the wall are responsible for collagen production. On the other hand, ILT grows by a continuous conversion of constantly renewed fibrinogen from the blood into fibrin. Thus, the mass of the aortic wall increases only several fold during aneurysm progression. Yet, the thrombus is continuously being deposited, with its mass changing from zero in a healthy artery or small aneurysm to a potentially huge thrombus mass in large AAAs. Therefore, it is convenient to model an aortic wall with a constant number of finite elements and keep track of changes in constituent mass fractions, whereas, for ILT, it is more appropriate to increase the number of finite elements at each deposition time and preserve the mass of each element constant. It is still possible to monitor the conversion of fibrin to fibrin degradation products or voids as well as cell apoptosis within the constant ILT finite elements, allowing the associated mechanical properties to vary in time or with the depth of the thrombus layer.

The first thrombus deposition is likely related to hemodynamic changes introduced by the creation of an aneurysmal sac. It was proposed that high shear stress is needed for the activation of platelets, which can then be presented to a susceptible endothelium at low wall shear stresses (Di Achille et al. 2014). Other, more precise, proposed measures of likelihood of thrombus formation, such as platelet activation potential (Shadden and Hendabadi 2013) or thrombus formation potential (TFP) (Di Achille et al. 2017), were likewise all based on wall shear stress and hemodynamics. The computational prediction of ILT formation obtained using TFP resulted in a satisfying first estimate compared to medical imaging from follow-ups on six patients. However, little is known about further thrombus deposition. The same model and model parameters do not seem to predict further thrombus deposition well. That is possibly due to different biochemical processes occurring during thrombus

deposition on damaged endothelium during the formation of the ILT, compared to the deposition on the existing luminal layer of thrombus with a high concentration of active plasmin (i.e., enzyme that degrades fibrin).

Considering that not much is understood about ILT growth, in this study, we used a simple criterion for deposition of new thrombus: a new thrombus layer is deposited at each time τ in which radial distance from the current luminal surface $r_{\text{lum}}(\tau)$ to a targeted luminal surface $\rho_{\text{lum}}(\tau)$ is greater than a predefined value $\Delta\rho_{\text{lum}}$. The definition of radii used in the model and in Fig. 1 is presented in the Table 1.

To model ILT formation and growth, we have developed and implemented a method for adding new finite elements into the finite element analysis program (FEAP, (Taylor 2013)). The new elements represent fresh thrombus and are added to the finite element model of a growing aneurysm. The procedure can be seen in detail in the flowchart in Fig. 2. When a criterion for deposition of a new thrombus layer is fulfilled, the G&R simulation is paused, and an algorithm for generating new thrombus finite elements is initiated. New thrombus elements are added within a space between the existing luminal surface and the targeted luminal surface. For every new element, the algorithm defines coordinates and connectivity of nodes and element boundary conditions where necessary. The coordinates are generated in such a way that thrombus growth is perpendicular to the underlying aortic wall surface. We used the same eight-node hexahedral elements for the thrombus as we did for the aortic wall. Furthermore, coinciding nodes on the boundary between two thrombus layers or between the first layer of the thrombus and the aortic wall are mutually linked. Note that new elements are added up to the targeted luminal surface in the undeformed state on the current, deformed configuration of an aneurysm model. After deposition of the new thrombus layer, the blood pressure loading is transferred on the new thrombus luminal surface, and G&R simulation continues until the criterion for thrombus deposition is fulfilled once again. Thrombus element thickness was set to 0.25 mm in here presented results, and, depending on the chosen thrombus layer thickness, more than one thrombus finite element might be added in the radial direction in a single thrombus deposition. Note that we have investigated the influence of different thrombus element thicknesses in the range 0.1–1 mm on the AAA evolution, yet the differences in aneurysm progression were not significant (results not shown here).

Figure 1b illustrates the finite element model of an aneurysm before ILT deposition, after deposition of the first thrombus layer, and after significant growth of ILT. Note that, for illustrative purpose, the model in Fig. 1b was cut at the apex and revolved to 90°, while, as mentioned in Sect. 2.1, a 2° segment with one element in a circular direction and proximal–distal symmetry was used in the analysis.

We first let AAA grow to a specific diameter without ILT, Fig. 1a, b, left. At a certain point, ILT is formed (Fig. 1b, middle) and continues to grow (Fig. 1b, right). Two different scenarios are investigated in this work, as illustrated in Fig. 1c, d, showing the growth of ILT.

2.3 *Scenario 1: ILT deposition to the predefined diameter—Fig. 1c*

Considering that ILT formation and deposition are likely driven by hemodynamics, meaning it is mainly based on geometry, the first scenario studied in this work is continuous thrombus deposition to the diameter of thrombus formation ($2R_{\text{lum}}$). This assumption is supported by medical imaging of large AAAs, suggesting that the overall luminal diameter tends to be preserved, although at a higher value compared to the healthy aorta (e.g., see cases P-6, P-8, and P-9 in Figure 9 in (Zambrano et al. 2016)). In this case, the thrombus is first deposited at a predefined luminal diameter ($2R_{\text{ILTstart}}$), and during AAA growth, the aneurysm sac is constantly filled with thrombus to that same luminal diameter value ($r_{\text{lum}}(\tau) = R_{\text{lum}} = R_{\text{ILTstart}}$). This scenario is illustrated in Fig. 1c. With the growth of an aneurysm, ILT is deposited so that the luminal area remains constant yet larger than the healthy lumen. Note

Table 1 Definitions of radii used in the model. Note, r, R, ρ represent current (computed) radii, predefined (input) value, and numerical targeted radius values, respectively

Label	Description
$r_{\text{lum}}(\tau)$	Current radius of luminal surface
$r_{\text{in}}(\tau)$	Current radius of aortic inner wall surface, with special case $r_{\text{in}}(0)$ denoting the initial healthy inner radius
$r_{\text{out}}(\tau)$	Current radius of aortic outer wall surface
$\rho_{\text{lum}}(s)$	Targeted ILT luminal surface radius in the current time step
R_{lum}	Predefined ILT final luminal surface radius
R_{ILTstart}	Predefined radius at which ILT first starts to deposit (Scenario 2)
$\Delta\rho_{\text{lum}}$	Predefined change of ρ_{lum} at each time step during the thrombus deposition

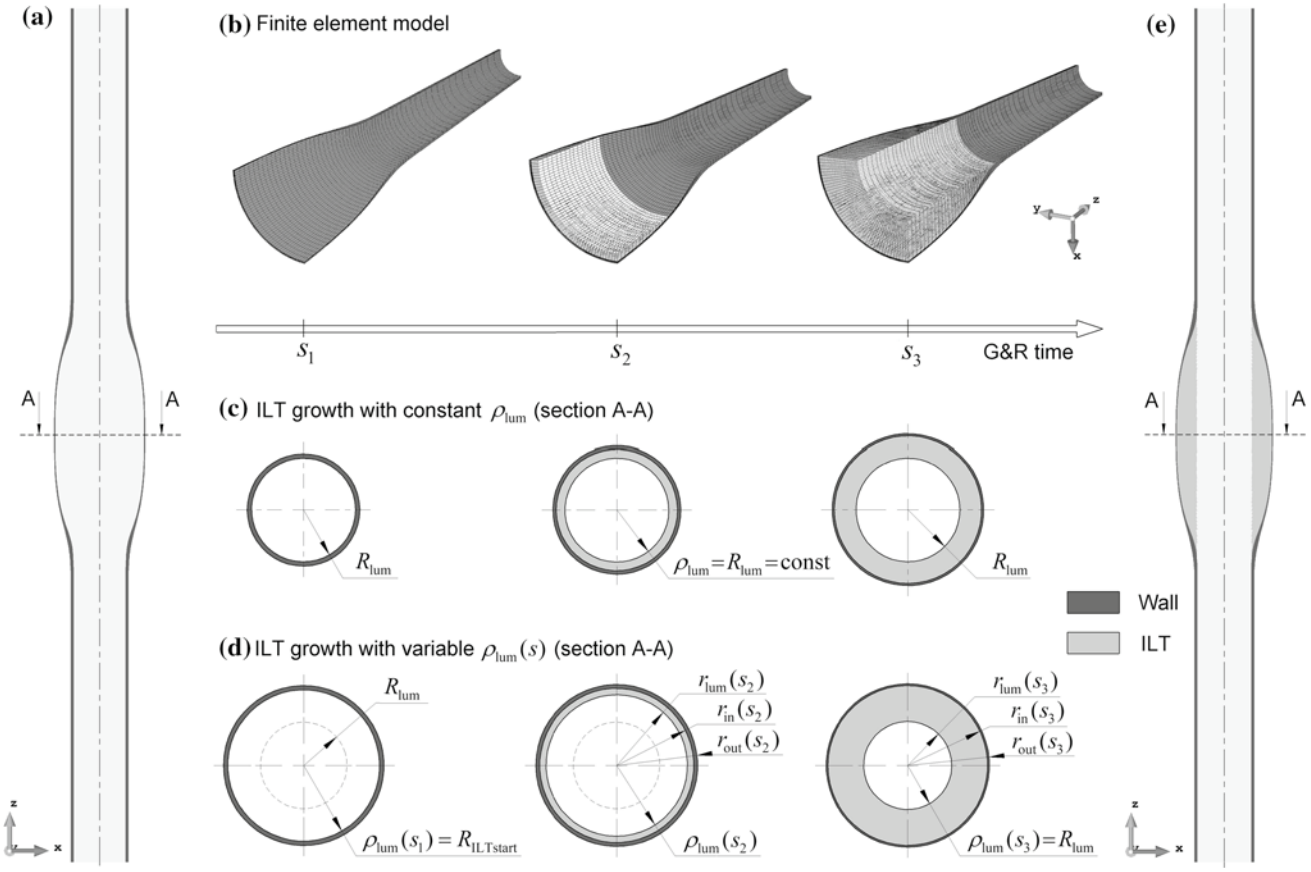

Fig. 1 Contours of the aorta before ILT formation (**a**); finite element model before ILT deposition, after first thrombus formation, and after growth of ILT (**b**); Scenario 1: growth of AAA with constant, expanded lumen area in several G&R time instances (**c**); Scenario 2: growth of AAA with lumen tending to maintain healthy area in several G&R time instances (**d**); contours of a fully thrombosed aneurysm (**e**)

that, in this scenario, the targeted luminal surface is constant, $\rho_{lum}(s) = R_{lum}$, (Fig. 1c).

2.4 *Scenario 2: Maintaining of the healthy lumen diameter—Fig. 1d*

Similar to our previous works (Virag et al. 2015, 2017), in the second case, we assumed a fully thrombosed aneurysm sac ($r_{lum} = r_{in}(0)$). This presumption also arose from medical imaging showing that the lumen area can remain the same as in the healthy part (e.g., see patients 1, 2, and 4 in Fig. 2 in (Metaxa et al. 2015)). Noting that the AAA size at the point when the ILT is formed can vary from patient to patient (Behr-Rasmussen et al. 2014), we investigated the influence of different times of ILT formation ($R_{ILTstart}$) on AAA growth. This scenario is illustrated in Fig. 1d: after the first ILT deposition (at $R_{ILTstart}$), new ILT elements are constantly added until the aneurysm sac is fully thrombosed, i.e., until the lumen area returns to the initial, homeostatic value ($r_{in}(\tau) = R_{lum} = r_{in}(0)$). The targeted luminal surface is moving in this scenario, $\rho_{lum}(s_1) = R_{ILTstart}$, $\rho_{lum}(s_2) = r_{lum}(s_2)$, … , $\rho_{lum}(s_i) = R_{lum}$ see Fig. 1d. After that, thrombus elements are added to maintain the luminal area constant ($r_{in}(\tau) = R_{lum} = r_{in}(0)$). The final thrombus-laden aneurysm contours are illustrated in Fig. 1e, showing a fully thrombosed aneurysm sac.

Please refer to the videos in the supplement for the spatiotemporal illustration of thrombus-laden aneurysm growth for these two scenarios. For both cases, we investigated the influence of the moment (i.e., AAA diameter) at which ILT forms, keeping in mind that almost half of AAAs with a maximum diameter of 30 mm already contain ILT and that some bigger ones do not (Behr-Rasmussen et al. 2014). Blood pressure was always applied to the luminal surface, i.e., at the radius r_{lum} (see definitions of radii in Fig. 1d). The criteria for thrombus deposition and all processes are further illustrated in the flowchart in Fig. 2 for the two mentioned deposition scenarios.

ILT was modeled as incompressible, as suggested by (Vorp et al. 1996), homogeneous elastic material. The constitutive model of intraluminal thrombus was based on histological analysis and mechanical testing of separate human

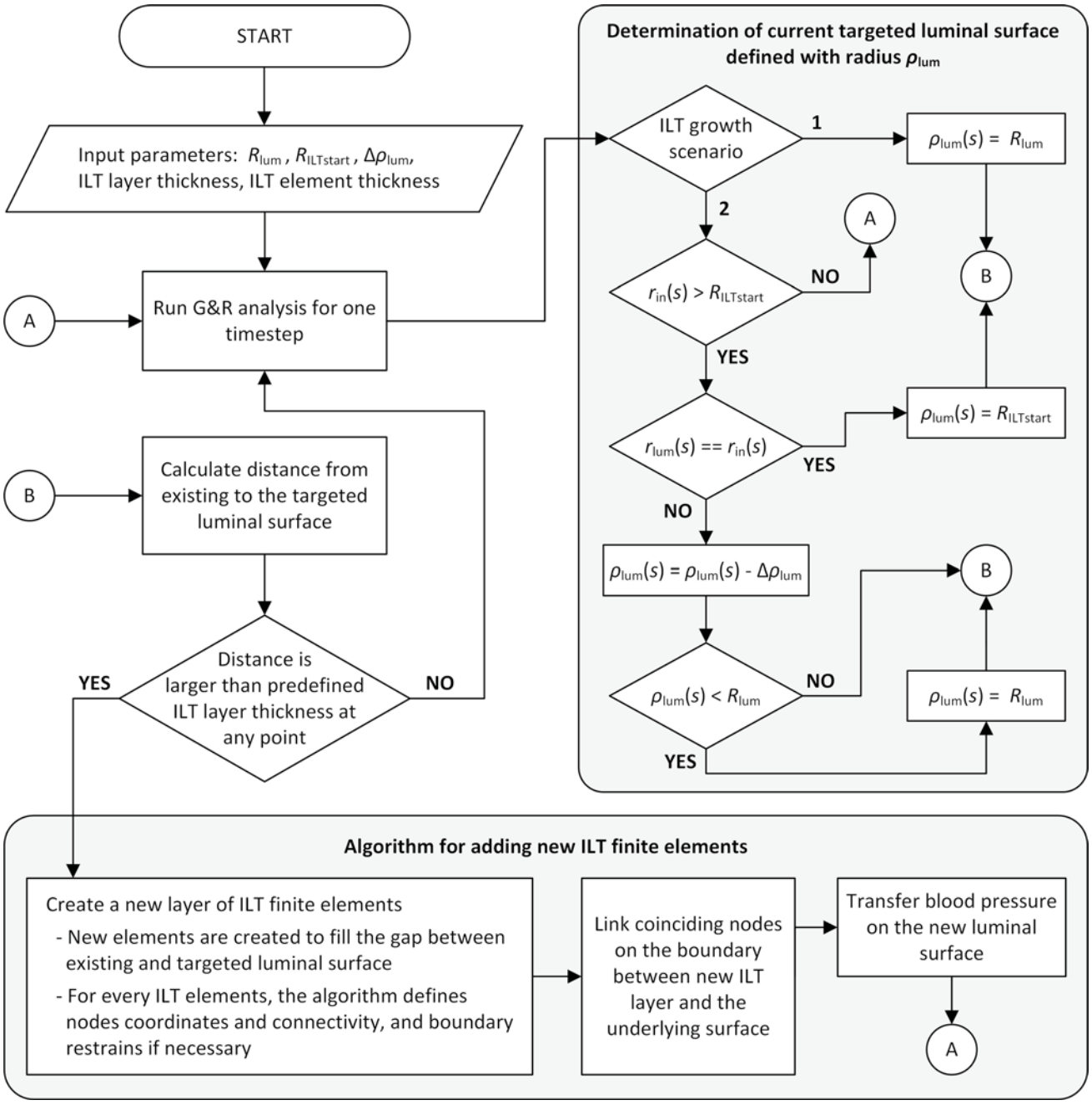

Fig. 2 Flowchart of the thrombus deposition process

thrombus layers in (Tong et al. 2011). Thus, strain-energy function characterizing thrombus mechanical behavior was defined as:

$$\widehat{W}_{\mathrm{ILT}} = \mu(I_1 - 3) + \frac{k_1}{k_2}\left(\exp\left(k_2(I_1 - 3)^2\right) - 1\right) \tag{3}$$

where I_1 is the trace of Cauchy-Green tensor, μ and k_1 are stress-like parameters and k_2 is a dimensionless material parameter that differs for each layer. Thrombus layers (luminal and medial-abluminal) were in our previous work (Virag et al. 2015) differentiated by mass fractions of constituents—fibrin, erythrocytes, fibrin degradation products, and voids. In this work, luminal layer thickness was defined to be constant 2 mm, as a clinically observed average (Vande Geest et al. 2006; Tong et al. 2011), and associated with stiffness of isotropic luminal layer estimated in (Tong et al. 2011). Due to a lack of platelets in the deeper ILT layers, fibrin fibers cannot be cleaved anymore. Hence, without production, they can only degrade with time and amount of

present plasmin (see Tong et al. 2011; Virag et al. 2015) for clarification). Noting that fibrin acts as the main mechanical scaffold of thrombus, the change in stiffness within the medial-abluminal layer was simplified as an exponential decay of fibrin mass fraction, which corresponds to the results in (Virag et al. 2015) (e.g., see Fig. 6). Thus, local thrombus stiffness k_2 was defined to depend on the depth d of an integration point as:

$$k_2(d) = \begin{cases} k_{2,\mathrm{lum}} & \text{for } d \le d_{\mathrm{lum}} \\ k_{2,\mathrm{abl}} + \left(k_{2,\mathrm{lum}} - k_{2,\mathrm{abl}}\right) \exp\left[-K\left(d - d_{\mathrm{lum}}\right)\right] & \text{for } d > d_{\mathrm{lum}} \end{cases} \tag{4}$$

where $k_{2,\mathrm{lum}}$ and $k_{2,\mathrm{abl}}$ are values obtained from mechanical testing for luminal and abluminal layers in (Tong et al. 2011), $d_{\mathrm{lum}} = 2$ mm is a thickness of the luminal layer, and $K = 0.2$ is a decay parameter. The parameter value was chosen in order for the average k_2 in the medial layer to correspond to experimental data. Other material parameters from Eq. (3), k_1 and k_1, were modeled in the same way.

Additionally, because fibrinolysis is not modeled here directly, and noting that fibrin mesh in the abluminal layer adjacent to the wall is disrupted and disorganized and that abluminal elements that are deposited the earliest would withstand unrealistically large deformations, a decrease in fibrin prestretch was modeled similar to the stiffness:

$$G_{\mathrm{f}}(d) = \begin{cases} G_{\mathrm{f,lum}} & \text{for } d \le d_{\mathrm{lum}} \\ G_{\mathrm{f,abl}} + \left(G_{\mathrm{f,lum}} - G_{\mathrm{f,abl}}\right) \exp\left[-K\left(d - d_{\mathrm{lum}}\right)\right] & \text{for } d > d_{\mathrm{lum}} \end{cases} \tag{5}$$

where $G_{\mathrm{f,abl}} = 1$ is a prestretch of fibrin in the abluminal layer and $G_{\mathrm{f,lum}} = 1.15$ is a prestretch of newly deposited fibrin in the luminal layer before application of blood pressure. A relatively high value of prestretch was selected, such that after loading, it decreases to approximately 1.08, as used in (Virag et al. 2015, 2017). Above-mentioned scalar values of prestretch were set in the axial and circumferential direction, while in the radial direction, due to the material incompressibility, prestretch was calculated as $G_{\mathrm{f}}^{r}(d) = 1/G_{\mathrm{f}}(d)^2$.

3 Results

In order to investigate the mechanical influence of thrombus on aneurysm evolution, we compared AAA growth without and with ILT for both scenarios described above Fig. 1c and d, for otherwise same wall model parameters. Moreover, we investigated the effect of the moment of the first thrombus deposition and thrombus stiffness in realistic ranges on aneurysm progress.

3.1 Comparison of AAA evolutions with and without thrombus: Geometrical changes and stress distributions

The evolution of the maximal inner radius of the aneurysm without thrombus (line with no marker) compared to two different cases of thrombus-laden aneurysms, with otherwise identical model parameters, is shown in Fig. 3a. The full dot (•) denotes the moment of the ILT formation. Note that before the full dot, i.e., first thrombus deposition, all three lines coincide. The line marked with a triangle marker (Δ) represents AAA growth of a fully thrombosed aneurysm in case ILT was first formed at the radius R_{ILTstart} of 14 mm and filled to the luminal radius of a healthy artery $R_{\mathrm{lum}} = r_{\mathrm{lum}}(0) = 10$ mm (Scenario 2). In the other case (Scenario 1), marked with a diamond (◇), a luminal radius was kept constant at a specific value,

in this case, $R_{\mathrm{lum}} = 13.5$ mm. Note that for the formation of thrombus, the luminal radius needed to expand 0.5 mm more (value of $\Delta\rho_{\mathrm{lum}}$) to allow thrombus deposition. Thus, the full dot marking the time of ILT formation is at a 14 mm AAA radius. In every time step in which luminal surface $r_{\mathrm{lum}}(\tau)$ (defined in Fig. 1d, right) dilated $\Delta\rho_{\mathrm{lum}}$, new thrombus elements were added. In both cases, thrombus deposition led to the stabilization of AAA. Stabilization of growth was achieved quicker in the case of a fully thrombosed aneurysm sac. This can be explained by a faster accumulation of thicker thrombus leading to a steep decrease in circumferential and axial stresses, as shown in Fig. 3e, showing the time evolution of stresses at the inner side of the aneurysm apex. Rapid filling of aneurysm sac from 14 to 10 mm leads to a quick recovery of stresses to the homeostatic value and, thus, cessation of AAA growth, despite thrombus being significantly softer than the aortic wall. On the other hand, continuous thrombus deposition to a larger lumen area (in this case, luminal radius increased from 10 to 13.5 mm) also leads to decreased AAA growth rate, albeit the decrease is lower. Unlike AAA without thrombus, the stress evolution at the apex of a thrombus-laden AAA is not a smooth curve because the deposition of new thrombus layers introduces abrupt changes.

Additional insight into differences in stress distributions for two different thrombus deposition cases can be seen in Fig. 3f, showing the spatial distribution of circumferential and axial stresses at the apex (section A-A in luminal radius Fig. 1e) at the G&R time 2500 days, as marked by a vertical line in Fig. 3a. In AAA without thrombus (no marker), circumferential stresses are much higher than axial and in this time step already close to the critical wall strength of 460 kPa reported by (Fillinger et al. 2003). At the same time instant of 2500 days, if the thrombus is deposited continuously to the value of (increased) luminal radius (diamond

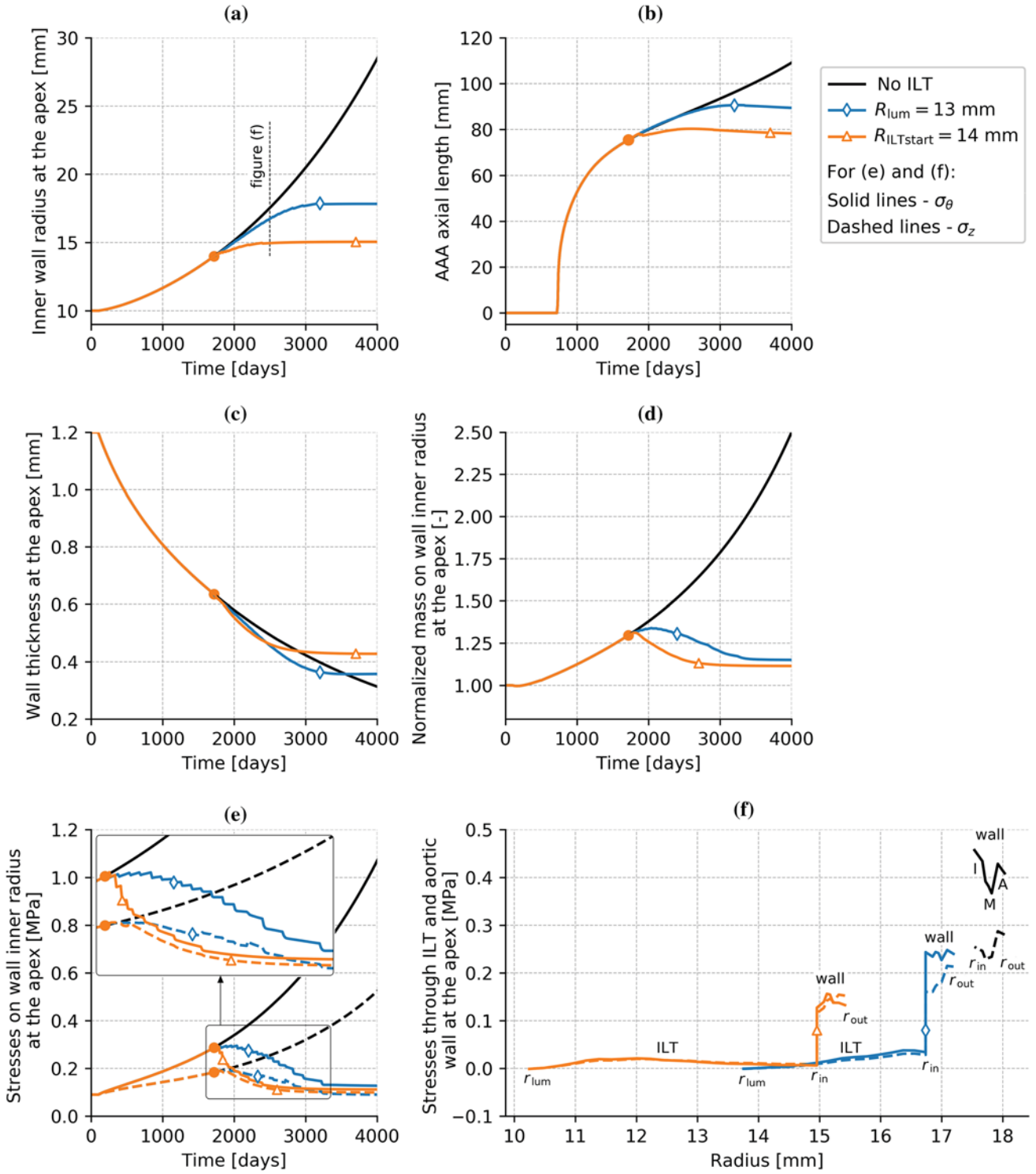

Fig. 3 Growth of AAA inner diameter over time for aneurysm without ILT (no marker) and two thrombus-laden aneurysms: Scenario 1 (diamond) and Scenario 2 (triangle) (**a**); axial growth of aneurysms (**b**); evolution on the wall thickness at the apex (**c**); evolution of a normalized wall element mass at the inner side at the apex (**d**); evolution of circular (solid lines) and axial (dashed lines) stresses at the inner side of aneurysm apex (**e**); spatial distribution of normal stress through thrombus and aortic wall at the apex at the G&R time of 2500 days (**f**). Radius r_{lum} defines an interface between blood flow and thrombus, r_{in} is an inner radius and defines an interface between the wall and ILT (or blood), and r_{out} is the outer wall radius. Layers of the aortic wall are labeled as I (intima), M (media), and A (adventitia). The moment of the first ILT deposition is denoted with a full dot

marker), the thrombus elements deposited the earliest are stretched more, bearing more load. However, fibrin mesh in the deeper layers becomes more degraded, disrupted, and disorganized, and its load-bearing capabilities decrease (with Eq. (5)). It can be noted that the peak stresses in ILT are at the radius of 16.5 mm, and not at the r_{in}.

When the whole aneurysm sac was rapidly filled with thrombus (triangle marker), circumferential stress in the thrombus was significantly lowered. Interestingly, circumferential and axial wall stresses are similar. Noting in Fig. 3a that this aneurysm has not expanded much since the first thrombus deposition, meaning the thrombus is not very stretched, and it can be seen in Fig. 3f that it does not bear much load. One might wonder why the aneurysm stabilized if the thrombus is bearing barely any load. The answer might be another interesting effect of thrombus deposition shown in Fig. 3b, showing the axial growth of the aneurysm. In order to measure the length of an aneurysm, positions of the neck were defined at the axial coordinates where the radius reached 110% of a healthy inner radius (i.e., 11 mm). Because of such a definition, the length of an aneurysm is zero for the first 750 days. Figure 3b clearly shows that thrombus influences not only radial but also axial growth. In case a thrombus is not present, aneurysm length keeps increasing, whereas its growth slows down and stabilizes when the thrombus is present.

Another interesting consequence of ILT deposition is the reduced production of collagen and smooth muscle. The lowered mural stresses lead to a decrease in mass, Fig. 3d, and, as a result, in wall thickness, Fig. 3c. The reduction in both mass and thickness is greater for rapidly filled AAA to the healthy luminal radius. Although in both ILT deposition scenarios increased thinning of the wall can be seen, the final thickness is stabilized at a higher value compared to AAA without ILT, partially due to decreased axial stretching. Additionally, it can be seen that the final wall thickness is also higher with thicker thrombus than with thinner ILT.

3.2 Influence of ILT deposition on axial growth

While it is apparent from Fig. 3 that ILT influences the axial growth of an aneurysm, it does not show how. A possible explanation is illustrated in Fig. 4 and Fig. 5. Blood pressure within AAA without thrombus stretches the aneurysm apex in axial direction considerably, as can be seen in Fig. 4a. This leads to higher axial stresses shown in Fig. 3e. The deposition of thrombus changes pressure distribution and significantly reduces axial tensile force at the apex as seen in Fig. 4b, whereas radial force remains the same. It can also be seen with thicker ILT (line with triangle marker in Fig. 3f) axial stresses decrease more than with thinner ILT (diamond marker).

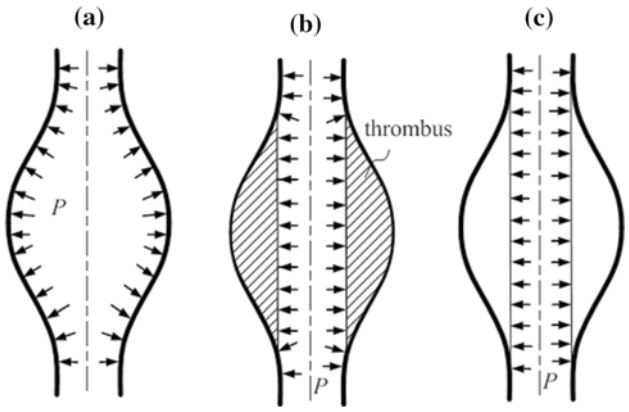

Fig. 4 Pressure (P) distribution in aneurysm without thrombus (**a**), with thrombus (**b**), and pressure acting on reference configuration (**c**)

In order to verify whether axial growth is really halted because of pressure redirection or thrombus mechanically shielding the wall, we considered an additional example. A simple way to model a fully thrombosed aneurysm while simultaneously neglecting mechanical properties of ILT can be achieved by letting the pressure always act on the reference (healthy) configuration, as illustrated in Fig. 4c. By doing so, no ILT elements need to be added, and therefore ILT can bear no load. The comparison of radial and axial growth of AAAs without thrombus and fully thrombosed AAAs with and without thrombus stiffness is shown in Fig. 5.

To allow ILT elements to be deposited, the luminal radius needs to enlarge at least for $\Delta\rho_{lum} = 0.5$ mm. This means the luminal radius ($r_{in}(\tau)$) constantly varies between 10 and 10.5 mm. Consequently, before ILT formation, as well as at every time instance when the luminal radius is larger than a healthy radius, a small axial force exists due to pressure distribution in the shoulder region (see Fig. 4b). In contrast, if pressure is always applied to a referent configuration, axial component of a pressure loading will not exist at any time. For this reason, initial AAA growth in the first 500 days is slightly slower for AAA with neglected ILT stiffness (but constant luminal radius) compared to the other two cases, Fig. 5a. After ILT deposition, due to the hindered collagen production, a certain time is needed before the size of AAA with ILT elements becomes smaller than AAA filled with ILT without stiffness. Additionally, the results show that even if ILT stiffness is ignored, fully thrombosed AAA will expand twice as slow as the AAA without thrombus, with a tendency to stabilize (after G&R time 5000 days stresses started to decrease toward homeostatic values, results not shown here).

Furthermore, despite ILT with neglected stiffness being unable to provide resistance to axial growth by carrying part of the load, the length of the aneurysms ceases to grow,

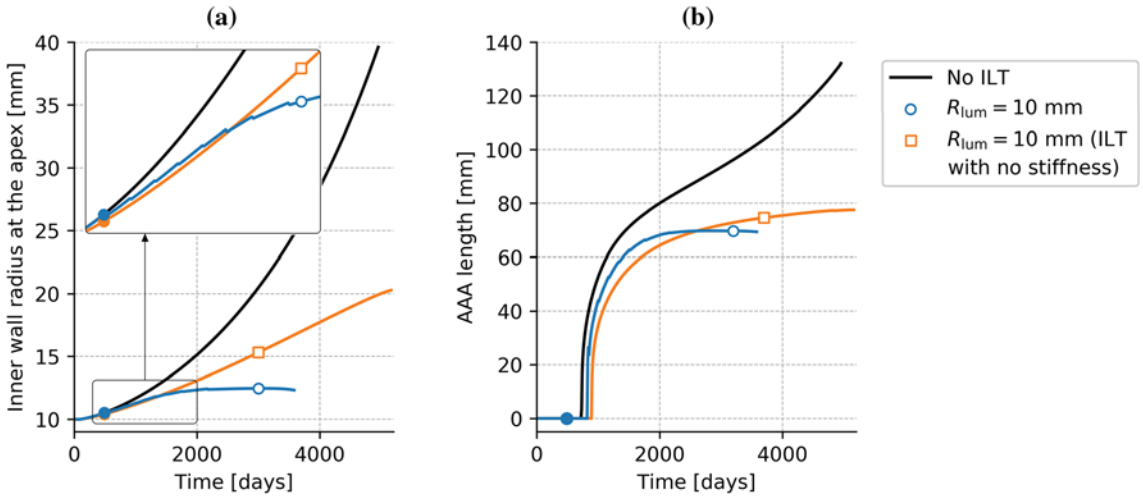

Fig. 5 Radial (**a**) and axial (**b**) growth of AAA without ILT (no marker), fully thrombosed AAA with ILT stiffness (circle marker), and fully thrombosed AAA without ILT stiffness (square marker). The moment of the first ILT deposition is denoted with a full dot

Fig. 5b. The final length is only slightly larger compared to fully attached ILT with stiffness. As already shown in Fig. 3b, if there is no thrombus present, AAA length will continue to increase.

Thus, we believe the redirection of pressure plays an important role in ILT during aneurysm growth. Interestingly, according to the machine learning model for predicting rupture presented by Shum et al. (Shum et al. 2011), the length of the aneurysmal sac is the most crucial feature for rupture prediction.

3.3 *Influence lumen dilatation within the aneurysmal sac (*Scenario 1*)*

Noting that wall thickness decreases quicker after ILT deposition indicates that the moment of ILT formation might be an important factor in thrombus-laden AAA evolution and its final outcome, as an older aneurysmal wall is less elastic and less capable of adapting to abrupt changes. As can be seen in Fig. 6a, later ILT formation (i.e., formation at a higher inner radius) lowers the likelihood of stabilization and increases further growth and time necessary for AAA

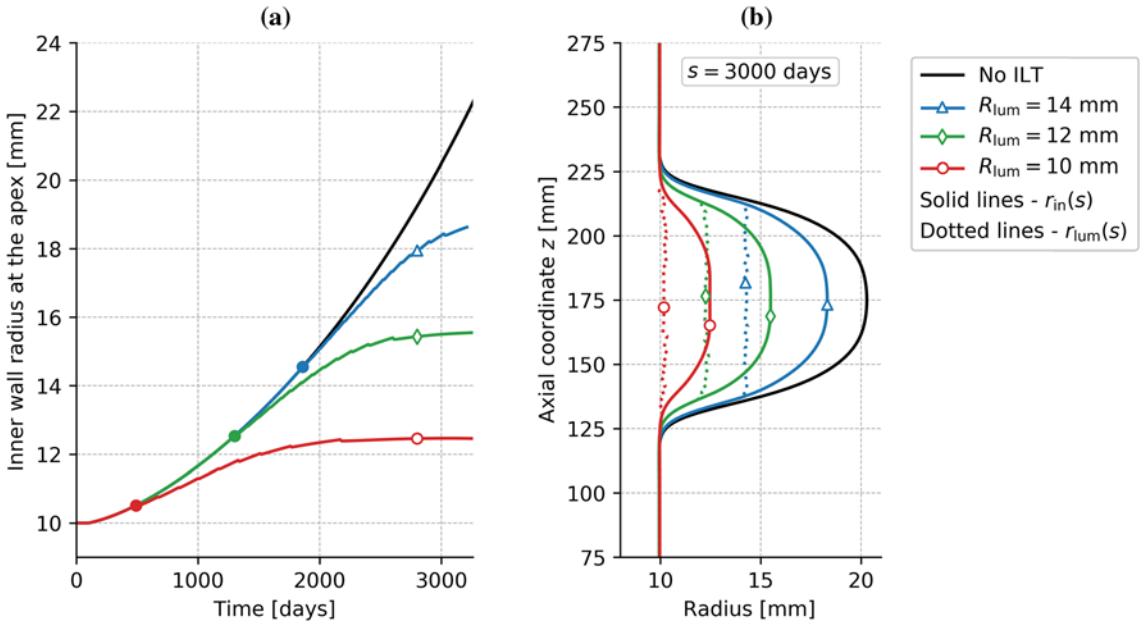

Fig. 6 Evolution of maximum inner radius (**a**) and contours of the inner wall (solid lines) and luminal surface (dotted lines) at the G&R time 3200 days (**b**) for aneurysms with different lumen areas. The moment of the first ILT deposition is denoted with a full dot

stabilization. These results are also in agreement with a machine learning study from (Shum et al. 2011). The authors showed that one of the four most important geometrical indices is the ILT to aneurysm sac volume ratio, with a lower volume ratio leading to rupture.

Note that in the case when ILT formed immediately and continued to fill the aneurysmal sac to the healthy radius value ($R_{\text{lum}} = r_{\text{in}}(0)$, the line marked with an empty circle), i.e., fully thrombosed aneurysm shown in a previous example, the final radius is 12.5 mm (i.e., diameter 25 mm), which is not considered to be aneurysmal aortic dilatation.

It is also interesting to note the difference in the axial length of the AAA sac, clearly visible in Fig. 6b. Although the contours are plotted for the same G&R time, meaning elastin is degraded equally in all four aneurysms, AAA length increases with later ILT deposition.

3.4 *Influence of the thrombus formation time for fully thrombosed aneurysm (*Scenario 2*)*

As mentioned in methodology section, the influence of thrombus formation time for fully thrombosed AAA was investigated as well. As can be seen from Fig. 7a, when neglecting the biochemical influence of thin thrombus, fully thrombosed aneurysms are likely to stabilize. Interestingly, if thrombus forms at the smaller maximum diameter, further AAA growth will be lower; however, the time necessary for stabilization might be longer. This might be explained by the fact that the thrombus is not strained much and is bearing very little load in either case; however, for later ILT formation, it will be thicker and thus carry more load, therefore leading to a quicker stabilization. When comparing geometries at G&R time 3000 days, it is evident from Fig. 7b that AAA without thrombus is the largest, and with earlier thrombus deposition, AAA growth is halted earlier. The dotted line that denotes the luminal surface is the same for all the cases shown in this example.

Note that deposition at smaller radii is not shown here because aneurysms stabilized at maximum diameters that are not considered aneurysms.

3.5 Influence of the thrombus stiffness

For all the results shown above, ILT material parameters were chosen as the mid-range value estimation from (Tong et al. 2011). Aneurysm evolutions for lower and upper stiffness range, and otherwise the same parameters, are shown in Fig. 8a. The results shown here are for the case when ILT was constantly filled to an increased luminal radius $r_{\text{lum}} = 12$ mm (Scenario 1); however, similar conclusions can be drawn for other luminal radii or fully thrombosed sac. As might be expected, the stiffer the thrombus is, the aneurysm stabilizes quicker and at a smaller maximum size. Although all thrombi decrease wall stresses, in the case of a compliant thrombus, both circumferential and axial stresses continue to increase at first, before decreasing to the new homeostatic value. This is likely because a compliant thrombus needs to be thick enough in order to bear a notable part of loading. A thin compliant thrombus

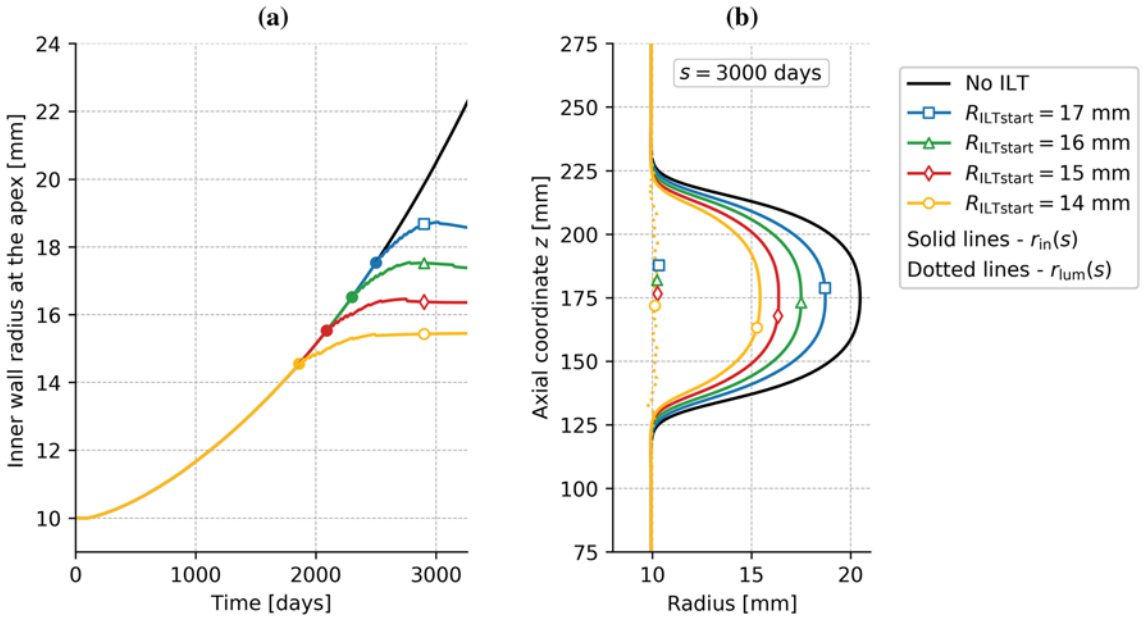

Fig. 7 Evolution of maximum inner radius (**a**) and contours of the inner wall and thrombus surface at the end of the simulation (**b**) for aneurysms with different moments of the first thrombus deposition, denoted by a full dot

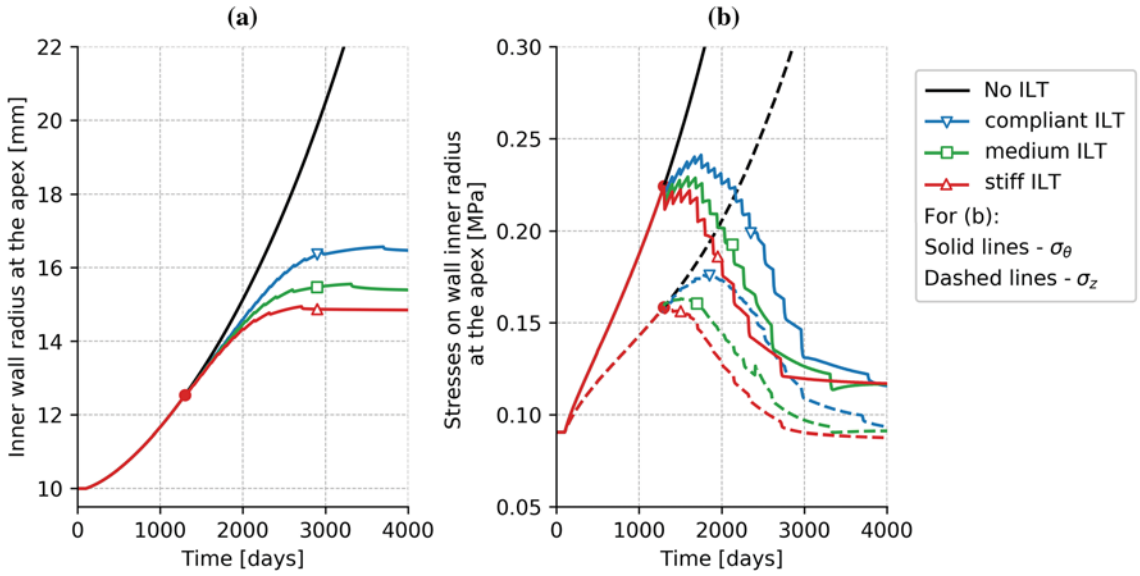

Fig. 8 Evolution of maximum inner radius (**a**) and stress evolution of the inner radius at the apex (b) for intraluminal thrombi with different stiffness. The moment of the first ILT deposition is denoted with a full dot

reduces stresses slightly compared to the values in AAAs without thrombus; however, it is unable to induce a stress recovery to homeostatic value until it is sufficiently thick.

4 Conclusions and discussion

The influence of intraluminal thrombus in AAA evolution is very controversial and unclear. A comprehensive bio-chemo-mechanical finite element model is needed for the investigation of ILT impact on AAA growth. Toward this end, the addition of thrombus finite elements is presented in this work. The results presented here show that the thrombus mechanically shields the wall and could lead to a decrease in growth rate and increase in aneurysm stability. However, before jumping to conclusions, it is important to note that the biochemical activity is modeled as a predefined spatiotemporal function, and increased proteolytical activity due to the presence of thrombus is not considered. Thus, this model presumably overestimates the stability of aneurysm growth.

Yet, regardless of biochemical activity, the results show a significant decrease in axial length and axial growth rate of thrombus-laden aneurysms compared to aneurysms without thrombus. This is largely because of redirection of blood pressure loading from axial-radial plain to predominately radial direction, reduction of the total force, and, in smaller part, due to the partial transfer of load to the soft thrombus. While redirection of the load from axial to the radial direction might not intuitively lead to aneurysm growth retardation, according to the machine learning model for predicting rupture presented by (Shum et al. 2011), the length of the aneurysmal sac is the highest-ranked feature in the decision tree as well as the feature that provides the highest information gain. In the aneurysms without thrombus, the axial stress value at the apex can be comparable to circumferential stress (see Fig.5 in (Horvat et al. 2019)). As blood pressure stretches the aneurysm sac axially, it increases tensile stress in the apex and compresses the shoulder regions. This further influences wall thickness distribution.

Additionally, we show that a thin thrombus has a negative impact on an aortic wall thickness—while lowering stresses is generally good for postponing rupture, it also means the collagen and smooth muscle production is lowered and that the wall becomes thinner. Apart from lowering wall stress-driven constituent productions, ILT likely also inhibits wall shear stress-driven mass production by covering endothelial cells. Endothelial cells on the inner side of the wall are in charge of signaling changes in blood flow to cells and molecules in the wall. After receiving the signal, they initiate or adjust the G&R process. However, after thrombus formation, endothelial cells are covered and unable to register changes in the wall shear stress.

On the other hand, due to pressure redirection by thick thrombus, the axial stretching is reduced, positively impacting the wall thickness. Additionally, thick thrombus carries more load and allows wall stresses to decrease to the homeostatic value.

Furthermore, we show that for the fully thrombosed aneurysms, the impact of the moment of the first thrombus deposition is twofold: for the earlier deposition, further AAA growth will be lesser; however, the time necessary for stabilization might be longer. If an aneurysm is not fully

thrombosed, a lower ratio of ILT to sac volume impacts AAA outcome negatively. Moreover, an increase in stiffness has a positive effect on the likelihood of AAA stabilization.

The hypotheses that can be derived from here presented results are:

(1) It is possible that thrombus is a "natural protection" against the rapid axial expansion of the lesion and, consequently, the rupture. Radial and axial stabilization either happen simultaneously, or axial stabilization leads to the cessation of radial growth (see Fig. 3a, b and Fig. 5). Thus, by lowering axial loading, ILT might allow axial stabilization, and consequently, radial as well. Keeping in mind that G&R models use constant mean blood pressure, it could be interesting to investigate how vessel compliance influences pressure distribution within the thrombosed aneurysm sac using a fluid–structure interaction model.

(2) Thin thrombus is likely perilous: it slightly shields the wall mechanically, but that also lowers the production of wall constituents. Biochemically, it is well known that the luminal layer is proteolytically the most active (Wilson et al. 2013), degrading the wall further. In contrast, thick thrombus decreases axial stretching of the aneurysm, which reduces the negative impact of a lowered constituent production, but it also lowers the degradation from the proteolytical activity by distancing the luminal layer of ILT from the wall. Unfortunately, every thick thrombus was thin at some point, and thus, the underlying wall is likely degraded, especially the elastin that cannot be produced in maturity. This conclusion was already indirectly suggested by several clinical studies: (Shum et al. 2011) concluded that smaller ILT to aneurysm sac volume ratio leads to rupture, (Domonkos et al. 2019) claimed that thicker thrombus slowed down the AAA growth and vice versa, the smaller relative size of ILT was linked to the higher growth rate. Additionally, (Metaxa et al. 2015) found that aneurysms with higher asymmetrical thrombus deposition index (i.e., larger surface covered by thin thrombus) are associated with higher growth rates. Thus, we propose that a biomarker for rupture based on a surface covered by a thin thrombus might be worth investigating.

(3) We hypothesize that the later first ILT deposition is more dangerous than a deposition in younger AAAs. This hypothesis can be derived from the above-presented results but also noting that the more degraded wall is less able to adapt to a new bio-chemo-mechanical situation.

In order to verify these hypotheses, it is necessary to model the comprehensive bio-chemo-mechanical influence of thrombus, preferably using a fluid–solid–growth (FSG) model to predict thrombus deposition more accurately.

Supplementary Information The online version contains supplementary material available at https://doi.org/10.1007/s10237-021-01478-w.

Acknowledgements This work was supported by grants from the Croatian Science Foundation (project IP-2014-09-7382, I. Karšaj and IP-2018-01-3796, D. Ozretić)

References

Arnoud Meijer C, Stijnen T, Wasser MNJM et al (2013) Doxycycline for stabilization of abdominal aortic aneurysms: a randomized trial. Ann Intern Med 159:815–823. https://doi.org/10.1016/j.jvs.2014.02.035

Behr-Rasmussen C, Grondal N, Bramsen MB et al (2014) Mural thrombus and the progression of abdominal aortic aneurysms: a large population-based prospective cohort study. Eur J Vasc Endovasc Surg 48:301–307. https://doi.org/10.1016/j.ejvs.2014.05.014

Bhak RH, Wininger M, Johnson GR et al (2015) Factors associated with small abdominal aortic aneurysm expansion rate. JAMA Surg 150:44–50. https://doi.org/10.1001/jamasurg.2014.2025

Braeu FA, Seitz A, Aydin RC, Cyron CJ (2017) Homogenized constrained mixture models for anisotropic volumetric growth and remodeling. Biomech Model Mechanobiol 16:889–906. https://doi.org/10.1007/s10237-016-0859-1

Di Achille P, Tellides G, Figueroa CA, Humphrey JD (2014) A haemodynamic predictor of intraluminal thrombus formation in abdominal aortic aneurysms. Proc R Soc A Math Phys Eng Sci 470:20140163–20140163. https://doi.org/10.1098/rspa.2014.0163

Di Achille P, Tellides G, Humphrey JD (2017) Hemodynamics-driven deposition of intraluminal thrombus in abdominal aortic aneurysms. Int J Numer Method Biomed Eng 33:1–17. https://doi.org/10.1002/cnm.2828

Di Martino E, Mantero S, Inzoli F et al (1998) Biomechanics of abdominal aortic aneurysm in the presence of endoluminal thrombus: experimental characterisation and structural static computational analysis. Eur J Vasc Endovasc Surg 15:290–299. https://doi.org/10.1016/S1078-5884(98)80031-2

Domonkos A, Staffa R, Kubíček L (2019) Effect of intraluminal thrombus on growth rate of abdominal aortic aneurysms. Int Angiol 38:39–45

Fillinger MF, Marra SP, Raghavan ML, Kennedy FE (2003) Prediction of rupture risk in abdominal aortic aneurysm during observation: wall stress versus diameter. J Vasc Surg 37:724–732. https://doi.org/10.1067/mva.2003.213

Fontaine V, Jacob MP, Houard X et al (2002) Involvement of the mural thrombus as a site of protease release and activation in human aortic aneurysms. Am J Pathol 161:1701–1710. https://doi.org/10.1016/S0002-9440(10)64447-1

Franck G, Dai J, Fifre A et al (2013) Reestablishment of the endothelial lining by endothelial cell therapy stabilizes experimental abdominal aortic aneurysms. Circulation 127:1877–1887. https://doi.org/10.1161/CIRCULATIONAHA.113.001677

Gasser TC, Auer M, Labruto F et al (2010) Biomechanical rupture risk assessment of abdominal aortic aneurysms: model complexity versus predictability of finite element simulations. Eur J Vasc Endovasc Surg 40:176–185. https://doi.org/10.1016/j.ejvs.2010.04.003

Golledge J, Iyer V, Jenkins J et al (2014) Thrombus volume is similar in patients with ruptured and intact abdominal aortic aneurysms. J Vasc Surg 59:315–320. https://doi.org/10.1016/j.jvs.2013.08.036

Grytsan A, Eriksson TSE, Watton PN, Gasser TC (2017) Growth description for vessel wall adaptation: a thick-walled mixture model of abdominal aortic aneurysm evolution. Materials (basel) 10:e994. https://doi.org/10.3390/ma10090994

Hans SS, Jareunpoon O, Balasubramaniam M, Zelenock GB (2005) Size and location of thrombus in intact and ruptured abdominal aortic aneurysms. J Vasc Surg 41:584–588. https://doi.org/10.1016/j.jvs.2005.01.004

Horvat N, Virag L, Holzapfel GA et al (2019) A finite element implementation of a growth and remodeling model for soft biological tissues : verification and application to abdominal aortic aneurysms. Comput Methods Appl Mech Eng 352:586–605. https://doi.org/10.1016/j.cma.2019.04.041

Humphrey JD, Rajagopal KR (2002) A constrained mixture model for growth and remodelling of soft tissues. Math Model Methods Appl Sci 12:407–430. https://doi.org/10.1142/S0218202502001714

Inzoli F, Boschettp F, Zappa M et al (1993) Biomechanical factors in abdominal aortic aneurysm rupture. Eur J Vasc Surg 7:667–674

Kurvers H, Veith FJ, Lipsitz EC et al (2004) Discontinuous, staccato growth of abdominal aortic aneurysms. J Am Coll Surg 199:709–715. https://doi.org/10.1016/j.jamcollsurg.2004.07.031

Lin WJ, Iafrati MD, Peattie RA, Dorfmann L (2017) Growth and remodeling with application to abdominal aortic aneurysms. J Eng Math 109:113–137. https://doi.org/10.1007/s10665-017-9915-9

Maier A, Gee MW, Reeps C et al (2010) A comparison of diameter, wall stress, and rupture potential index for abdominal aortic aneurysm rupture risk prediction. Ann Biomed Eng 38:3124–3134. https://doi.org/10.1007/s10439-010-0067-6

Martinez-Pinna R, Lindholt JS, Blanco-Colio LM et al (2010) Increased levels of thioredoxin in patients with abdominal aortic aneurysms (AAAs). A potential link of oxidative stress with AAA evolution. Atherosclerosis 212:333–338. https://doi.org/10.1016/j.atherosclerosis.2010.05.031

Metaxa E, Kontopodis N, Tzirakis K et al (2015) Effect of intraluminal thrombus asymmetrical deposition on abdominal aortic aneurysm growth rate. J Endovasc Ther 22:406–412. https://doi.org/10.1177/1526602815584018

Meyer CA, Guivier-Curien C, Moore JE (2010) Trans-thrombus blood pressure effects in abdominal aortic aneurysms. J Biomech Eng 132:071005. https://doi.org/10.1115/1.4001253

Mower WR, Quinones WJ, Gambhir SS (1997) Effect of intraluminal thrombus on abdominal aortic aneurysm wall stress. J Vasc Surg 26:602–608. https://doi.org/10.1016/S0741-5214(97)70058-2

Niestrawska JA, Viertler C, Regitnig P et al (2016) Microstructure and mechanics of healthy and aneurysmatic abdominal aortas: experimental analysis and modelling. J R Soc Interface 13:20160620. https://doi.org/10.1098/rsif.2016.0620

Parodi FE, Mao D, Ennis TL et al (2005) Suppression of experimental abdominal aortic aneurysms in mice by treatment with pyrrolidine dithiocarbamate, an antioxidant inhibitor of nuclear factor-kB. J Vasc Surg 41:479–489. https://doi.org/10.1016/j.jvs.2004.12.030

Parr A, McCann M, Bradshaw B et al (2011) Thrombus volume is associated with cardiovascular events and aneurysm growth in patients who have abdominal aortic aneurysms. J Vasc Surg 53:28–35. https://doi.org/10.1016/j.jvs.2010.08.013

Shadden SC, Hendabadi S (2013) Potential fluid mechanic pathways of platelet activation. Biomech Model Mechanobiol 12:467–474. https://doi.org/10.1007/s10237-012-0417-4

Shum J, Martufi G, Di Martino E et al (2011) Quantitative assessment of abdominal aortic aneurysm geometry. Ann Biomed Eng 39:277–286. https://doi.org/10.1007/s10439-010-0175-3

Steinmetz EF, Buckley C, Shames ML et al (2005) Treatment with simvastatin suppresses the development of experimental abdominal aortic aneurysms in normal and hypercholesterolemic mice. Ann Surg 241:92–101. https://doi.org/10.1097/01.sla.0000150258.36236.e0

Swedenborg J, Eriksson P (2006) The intraluminal thrombus as a source of proteolytic activity. Ann N Y Acad Sci 1085:133–138. https://doi.org/10.1196/annals.1383.044

Taylor R (2013) FEAP - Finite Element Analysis Program. Version 8:4

Tong J, Cohnert T, Regitnig P, Holzapfel GA (2011) Effects of age on the elastic properties of the intraluminal thrombus and the thrombus-covered wall in abdominal aortic aneurysms: Biaxial extension behaviour and material modelling. Eur J Vasc Endovasc Surg 42:207–219. https://doi.org/10.1016/j.ejvs.2011.02.017

Tong J, Cohnert T, Regitnig P et al (2014) Variations of dissection properties and mass fractions with thrombus age in human abdominal aortic aneurysms. J Biomech 47:14–23. https://doi.org/10.1016/j.jbiomech.2013.10.027

Vande Geest JP, Sacks MS, Vorp DA (2006) A planar biaxial constitutive relation for the luminal layer of intra-luminal thrombus in abdominal aortic aneurysms. J Biomech 39:2347–2354. https://doi.org/10.1016/j.jbiomech.2006.05.011

Virag L, Wilson JS, Humphrey JD, Karšaj I (2015) A computational model of biochemomechanical effects of intraluminal thrombus on the enlargement of abdominal aortic aneurysms. Ann Biomed Eng 43:2852–2867. https://doi.org/10.1007/s10439-015-1354-z

Virag L, Wilson JS, Humphrey JD, Karšaj I (2017) Potential biomechanical roles of risk factors in the evolution of thrombus-laden abdominal aortic aneurysms. Int J Numer Methods Biomed Wngineering 33:e2893. https://doi.org/10.1002/cnm.2893

Vorp DA, Mandarino WA, Webster MW, Gorcsan J (1996) Potential influence of intraluminal thrombus on abdominal aortic aneurysm as assessed by a new non-invasive method. Cardiovasc Surg 4:732–739

Vorp DA, Lee PC, Wang DHJ et al (2001) Association of intraluminal thrombus in abdominal aortic aneurysm with local hypoxia and wall weakening. J Vasc Surg 34:291–299. https://doi.org/10.1067/mva.2001.114813

Wilson JS, Baek S, Humphrey JD (2012) Parametric study of effects of collagen turnover on the natural history of abdominal aortic aneurysms. Proc R Soc A Math Phys Eng Sci 469:20120556. https://doi.org/10.1098/rspa.2012.0556

Wilson JS, Virag L, Di Achille P et al (2013) Biochemomechanics of intraluminal thrombus in abdominal aortic aneurysms. J Biomech Eng 135:021011. https://doi.org/10.1115/1.4023437

Zambrano BA, Gharahi H, Lim CY et al (2016) Association of intraluminal thrombus, hemodynamic forces, and abdominal aortic aneurysm expansion using longitudinal CT images. Ann Biomed Eng 44:1502–1514. https://doi.org/10.1007/s10439-015-1461-x

PAPER 4

Submitted Manuscript of a journal article.

Virag, Lana, **Horvat, Nino**, Karšaj, Igor: A computational study of bio-chemo-mechanics of thrombus-laden aneurysms. The manuscript has been submitted to Journal of the Mechanics and Physics of Solids

A computational study of bio-chemo-mechanics of thrombus-laden aneurysms

Lana Virag, Nino Horvat, Igor Karšaj[#]

University of Zagreb, Faculty of Mechanical Engineering and Naval Architecture, Zagreb, Croatia

Address for Correspondence

Igor Karšaj, Ph.D.
University of Zagreb
Faculty of Mechanical Engineering and Naval Architecture
Ivana Lučića 5
Zagreb, 10000
Croatia
Phone: +385 1 6168 125
Fax: +385 1 6168 187
igor.karsaj@fsb.hr

Abstract

The role of intraluminal thrombus (ILT) in abdominal aortic aneurysm (AAA) development has been controversial for decades, yet the researchers and clinicians agree that thrombus is not an innocent bystander in disease progression. In an effort to increase our understanding of its role, in this work, we present a bio-chemo-mechanical mathematical model of thrombus-laden aneurysms. Unlike all previous finite element studies, where AAAs grow due to prescribed irreversible time-dependent elastin degradation, in this study, protein degradation depends on protease activity. Enzymes degrading collagen and elastin are believed to come from the luminal layer of intraluminal thrombus and the increasing area of chemotactic *vasa vasorum* in the wall. The geometrical and structural spatiotemporal changes in the aneurysmal wall at the apex and shoulder region of the thrombus-laden aneurysm are explained in detail. Furthermore, we show that later ILT formation is more perilous than its early deposition, despite lower peak protease activity and related extracellular matrix degradation. Interestingly, the radial growth rate is slightly slower for fully thrombosed AAAs compared to the partially thrombosed ones, however, their axial growth is much more pronounced. Additionally, we show that thrombus deposition greatly impacts the aneurysmal sac shape and volume.

Keywords: growth and remodelling, abdominal aortic aneurysm, intraluminal thrombus, proteolytic activity, finite element method

1. Introduction

Intraluminal thrombus (ILT) is usually clinically perceived negatively. It hinders the endovascular treatment and is believed to hasten the rupture. Nevertheless, various clinical, histological, experimental, and computational studies came to conflicting results, some confirming the presumption that ILT negatively impacts AAA outcome and others presenting opposing results. For example, one study showed that AAAs with ILT had faster growth rates compared to AAA without ILT: small AAAs (size range, 3–4 cm) with ILT grew 1.9-fold faster than did those without ILT and medium AAAs (size range, 4–5 cm) with ILT had 1.2-fold faster growth than did those without ILT [1]. Yet, another study [2] showed a weak, nonsignificant correlation between the AAA growth rate and ILT volume (with $p=0.054$), which disappeared after adjusting for the initial AAA size. Also, despite some studies claiming ILT volume is a good predictor of AAA rupture (e.g., [3]), others found no correlation ([4]). A recent systematic review and meta-analysis of the association between intraluminal thrombus volume and abdominal aortic aneurysm rupture concluded that while ILT volumes are bigger in ruptured AAAs, it is very likely due to the larger diameter of ruptured AAAs [5]. Namely, as AAAs grow, the increase in sac volume is occupied by additional ILT deposition, with minimal change in lumen volume, [2].

However, all studies agree that ILT plays an important role in disease development and its outcome. Thrombus does not appear to be an innocent bystander in AAA pathophysiology. However, its exact role remains elusive and controversial. Despite computational evidence of a possible protective role of the ILT in reducing wall stress, increasing evidence has shown that the ILT promotes AAA wall degeneration in humans and animal models [6]. One of the current hypotheses on role of ILT in AAA progression is that thin thrombus is perilous, while thick one provides protection. Thrombus is known to be much more compliant compared to the wall [7], and mechanical shielding capabilities of thin thrombus are very limited. On the other hand, it is well known that the luminal layer is proteolytically the most active [8]. Newer studies also showed that thin thrombus (<10mm) has higher oxidative stress and proteolytic enzyme expression compared to thicker ones (>10 mm) [9]. In contrast, a thick thrombus is not only proteolytically less active but possibly lowers axial stretching of the aneurysm [10]. Many studies have presented cushioning effect of large thrombus, mostly assuming its homogeneity (e.g., [11, 12]), but some also accounted for its heterogeneous composition using MR imaging [13].

Several clinical studies indirectly indicated this hypothesis: Shum et al. [14] concluded that a smaller ILT to aneurysm sac volume ratio leads to rupture, Domonkos et al. [15] claimed that thicker thrombus slowed down the AAA growth and vice versa, the smaller relative size of ILT was linked to the higher growth rate. Additionally, Metaxa et al. [16] found that aneurysms with higher asymmetrical thrombus deposition index (i.e., larger surface covered by thin thrombus) are associated with higher growth rates.

Thus, this study aims to comprehensively investigate the role ILT plays during AAA progression. We expand the finite element implementation of the arterial wall growth and remodelling presented in [17] with a bio-chemo-mechanical model of ILT. The implementation was previously used to clarify the importance of collagen fibre dispersion [18] and examine mechanical influence of ILT [10] on the aneurysm progression. The new bio-chemo-mechanical model is based on work given in [19], adapted to be functional in finite element environment. This model showed promising results, as it was able to replicate clinical expectations for different rupture risk and stabilisation factors [20]. However, it was applied to a simplified cylindrical geometry that does not represent aneurysms well, and consequently, it was unable to track changes in the shoulder region. Using the finite element method to describe more realistic AAA geometry, we seek to investigate 3D diffusion of enzymes and related heterogeneous degradation of extracellular matrix, with special attention to shoulder region. Furthermore, we investigate AAA growth after later ILT formation, on stiffer wall, compared to earlier thrombus deposition.

2. Methodology

2.1. Influence of thrombus formation on kinetics of G&R

The growth and remodelling model of arteries has been outlined in detail in many previous studies, [21, 22]. For an overview of original G&R model of aortic wall, please check Appendix A in [17]. Herein, we present only the most important equations concerning G&R of the wall and thoroughly the

mathematical model of bio-chemical and bio-mechanical effect of the thrombus on a aortic wall kinetics and kinematics. The new model of bio-chemo-mechanics of intraluminal thrombus, based on a complex model presented in Virag et al. [19], herein is for the first time implemented into the 3D finite element environment. The formulation of intraluminal thrombus is optimized to enable robust and efficient implementation, with a special attention given not to lose accuracy of model predictions from [19]. Figure 1 shows the schematic representation of the model, with denoted equation numbers describing listed relationships.

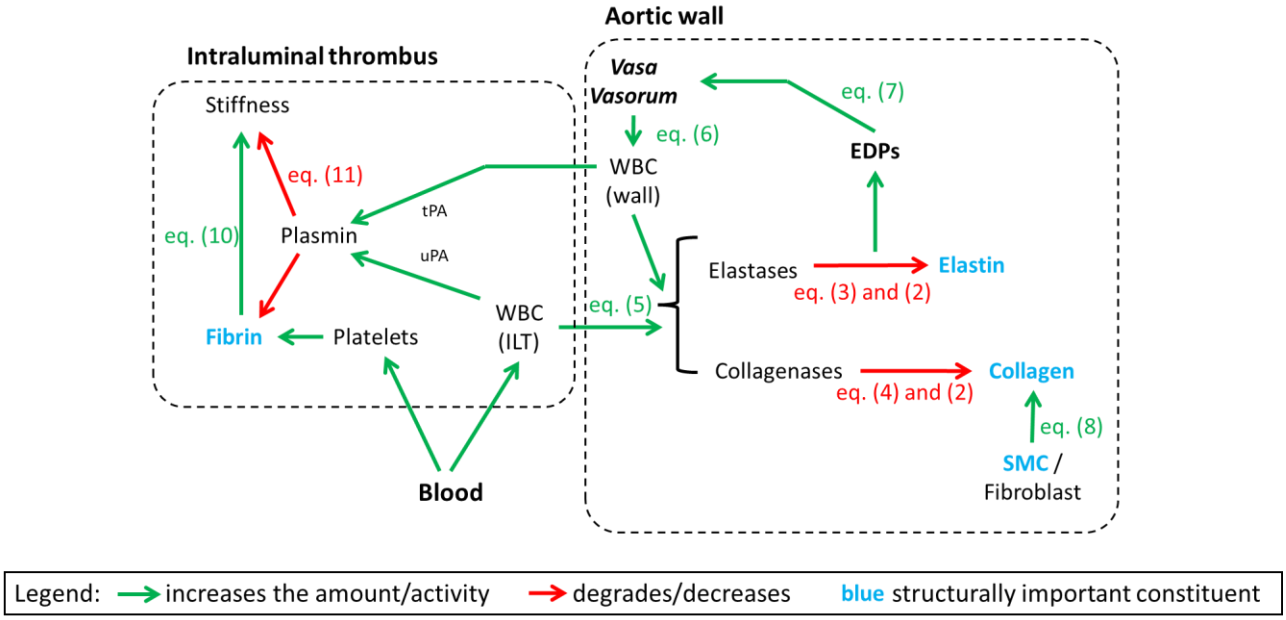

Fig. 1 The schematic representation of the model with denoted equations describing relations (abbreviations: WBC – white blood cells, EDPs – elastin degradation products, SMC – smooth muscle cells, ILT – intraluminal thrombus)

Briefly, current mass of wall constituent k (elastin, collagen or smooth muscle cells), $M^k(s)$, is calculated as

$$M^k(s) = M^k(0)Q^k(s) + \int_0^s \dot{m}^k(\tau)\, q^k(s-\tau)\, \mathrm{d}\tau\,, \qquad (1)$$

where $M^k(0)$ is its initial mass, $\dot{m}^k$ is production rate for each constituent, and $q^k(s-\tau)$ is a survival function determining how much mass produced in arbitrary time τ remained in current time s. The main difference in this work to other available studies is that the degradation of elastin, Q^{e} (e.g. see eq. (1) in [10]), in aneurysms is not described as a predefined spatiotemporal function but it is outcome of complex biochemomechanical mechanisms in a wall and intraluminal thrombus. Complex nature of AAA initiation is still unclear and as such not modeled in this study. Assuming the initial sac becomes large enough, thrombus forms. With the deposition of the proteolytically active luminal layer of ILT, degradation of mural proteins (elastin and collagen) increases. Thus, protein degradation depends on the spatial distribution of proteases coming from both luminal layer of ILT and the wall itself (mostly *vasa vasorum*). Additional degradation by the increased amount of collagenases is also described.

This was achieved by expanding the degradation rate K_q^k from the commonly used survival function q_i^k between the arbitrary G&R time τ and current time s

$$q_i^k(s-\tau) = \exp\left(-\int_\tau^s K_q^k(\tilde{\tau})\, \mathrm{d}\tilde{\tau}\right) \qquad (2)$$

for elastin to

$$K_q^{\mathrm{e}}(r,\varphi,z,\tau) = k_q^{\mathrm{e}} + w_{q,\mathrm{elas}}^{\mathrm{e}} M^{\mathrm{elas}}(r,\varphi,z,\tau)\,, \qquad (3)$$

and for collagen to

$$K_q^{\mathrm{c}}(r,\varphi,z,\tau)=\left\|\frac{\partial W^{\mathrm{c}}}{\partial \mathbf{F}^{\mathrm{c}}_{n(\tau)}}\right\| \Big/ \left\|\frac{\partial W^{\mathrm{c}}}{\partial \mathbf{F}^{\mathrm{c}}_{n(0)}}\right\| k_q^{\mathrm{c}} + w^{\mathrm{c}}_{q,\mathrm{MMP}} M^{\mathrm{MMP}}(r,\varphi,z,\tau)\,. \tag{4}$$

In eq. (3) and (4), k_q^{e} and k_q^{c} are degradation rates associated with a half-life of elastin and collagen respectively, i.e. for constituent *k* degradation rate is defined as $k_q^k=\ln(2)/(\tau^k_{(1/2)})$. Furthermore, $w^{\mathrm{e}}_{q,\mathrm{elas}}$ and $w^{\mathrm{c}}_{q,\mathrm{MMP}}$ are weighting factors defining protein degradation rate by increased concertation of elastases M^{elas} and collagenase M^{MMP}, and $\left\|\partial W^{\mathrm{c}}/\partial \mathbf{F}^{\mathrm{c}}_{n(\tau)}\right\| \Big/ \left\|\partial W^{\mathrm{c}}/\partial \mathbf{F}^{\mathrm{c}}_{n(0)}\right\|$ is the ratio of current to the homeostatic stretch of collagen fibres. Protease amount changes both spatially and in time. Based on the literature review [8, 23–25] and similar to our previous model applied to cylindrical geometry [19], we assume two primary sources of activated proteases: the luminal layer of thrombus and *vasa vasorum* in the aortic wall. Fresh thrombus next to the blood flow is characterised by a low amount of fibrin and a high amount of blood cells and proteins, such as platelets, neutrophils, macrophages, fibrinogen, and plasminogen [26]. Some of these cells (neutrophils) are responsible for protease extraction. Because deeper layers of intraluminal thrombus are mostly devoid of cells [27], the first protease source was assumed to be at the luminal radius. The number of the produced active proteases was set to be

$$M^k\left(r_{\mathrm{L}},\varphi,z,s\right)=K^k_{\mathrm{N}}M^{\mathrm{N}}_{\mathrm{tot}}\left(\varphi,z,s\right). \tag{5}$$

Here, *k* denotes either elastases or collagenases, r_{L} luminal radius, K^k_{N} is a correlation parameter denoting the amount of the extracted proteases per unit of neutrophils (N) per time step, and $M^{\mathrm{N}}_{\mathrm{tot}}$ is the total amount of neutrophils in the luminal layer. Because the distribution of neutrophils was assumed to be constant throughout the luminal layer, their total amount directly depended on the luminal layer thickness. Note that we retain notation from [19] and write $K^{\mathrm{elas}}_{\mathrm{N}}$ for elastases and $K^{\mathrm{MMP}}_{\mathrm{N}}$ for collagenases.

In the wall, *vasa vasorum* has been linked with increased proteases extraction, and thus the amount of elastases and collagenases M^k at the outer wall radius r_{o} can be calculated as

$$M^k\left(r_{\mathrm{o}},\varphi,z,s\right)=K^k_{\mathrm{VV}}A^{\mathrm{VV}}_{\mathrm{tot}}(\varphi,z,s)\,. \tag{6}$$

In the above equation, K^k_{VV} is a correlation factor that relates the *vasa vasorum* area with a unit of proteases per unit time and $A^{\mathrm{VV}}_{\mathrm{tot}}$ is a total current area of neovascularisation.

Neovascularisation of the wall is related to the mass of elastin degradation products (EDPs), which are also chemoattractants for inflammatory cells [28]. The development of *vasa vasorum* has also been connected with increased hypoxia due to thick ILTs [29]. However, a clinical study [25] reported that the expression of genes associated with intramural neovascularisation is the same or only slightly increased in thrombus-covered vs thrombus-free walls in AAAs. A recent computational study [30] showed that ILT did not affect oxygen flow to the aneurysm wall, further disproving the theory that thrombus causes local hypoxia. Thus, change in amount and area of *vasa vasorum* $A^{\mathrm{VV}}_{\mathrm{tot}}(s)$ is assumed to be

$$A^{\mathrm{VV}}_{\mathrm{tot}}(r_{\mathrm{o}},\varphi,z,s)=A^{\mathrm{VV}}_0+\int_0^s K^{\mathrm{VV}}_{\mathrm{EDP}}M^{\mathrm{EDP}}_{\mathrm{tot}}(\varphi,z,s)\,\mathrm{d}\tau\,. \tag{7}$$

In eq. (7), A^{VV}_0 is the homeostatic area of *vasa vasorum* in the healthy aorta, taken from [29], $K^{\mathrm{VV}}_{\mathrm{EDP}}$ is a correlation factor that relates *vasa vasorum* growth per unit of EDPs per unit time, and $M^{\mathrm{EDP}}_{\mathrm{tot}}$ is the total amount of EDPs in the wall. In the original model [19], the mass of EDPs was calculated similar to the mass of wall constituents, i.e. with associated production and degradation by macrophages. Here, we simplified it to a percentage of degraded elastin.

On the cylindrical model, from [19], it was reasonable to calculate the spatial distribution of proteases by solving Fick's low for radial diffusion with two sources. Since an axisymmetric 3D model of the fusiform aneurysm was used in this work, we will show results of 3D diffusion, solved in FEAP [31] with a thermal analysis solver.

Production of wall constituents $\dot{m}^k(\tau)$, see eq. (1), depends on its basal value m_B^k and deviations in wall stresses $\Delta\sigma$ and wall shear stresses determining change in concentration of vasodilators/constrictors ΔC,

$$\dot{m}^k(\tau) = m_B^k\left(1 + K_\sigma^k \Delta\sigma + K_C^k \Delta C\right). \qquad (8)$$

K_σ^k and K_C^k are rate parameters governing constituent level stress-driven mass production.

2.2. Aortic wall stress analysis

Cauchy wall stress $\boldsymbol{\sigma}$ is calculated using the rule of mixtures as

$$\boldsymbol{\sigma} = \phi^{\mathrm{e}}\boldsymbol{\sigma}^{\mathrm{e}} + \phi^{\mathrm{c}}\boldsymbol{\sigma}^{\mathrm{c}} + \phi^{\mathrm{m}}\boldsymbol{\sigma}^{\mathrm{m}} + \phi^{\mathrm{m}}\sigma^{\mathrm{active}}\mathbf{e}_{\mathrm{m}} \otimes \mathbf{e}_{\mathrm{m}}, \qquad (9)$$

where ϕ denotes mass fraction of elastin, collagen, and smooth muscle, and $\mathbf{e}_{\mathrm{m}}$ orientation of smooth muscle cells. Elastin is modelled as isotropic neo-Hookean material, while collagen and smooth muscle that exhibit exponential stress-strain relationship are modelled with exponential stored energy function. For details on wall mechanics please check [17].

2.3. Constitutive formulation and stress analysis of intraluminal thrombus

A thrombus is a continuously evolving structure composed of fibrin and blood cells embedded into the fibrin mesh [32]. Fibrin accumulates as activated thrombin cleaves fibrinogen into fibrin and is stabilised via crosslinking by activated factor XIIIa. Fibrinolysis occurs when plasmin degrades fibrin clots. Plasmin is generated by the activation of plasminogen by numerous factors, most importantly tissue- or urokinase-type plasminogen activators (tPA and uPA). However, activation of plasminogen can be hindered by plasminogen activator inhibitor (PAI-1). Thus, fibrin turnover is a complex process that, to be modelled realistically, requires understanding spatiotemporal distributions of many cells and molecules, such as fibrinogen, activated platelets, crosslinking factors, plasminogen and its activators and activator inhibitors. Clearly, there is a serious lack of such data. Nevertheless, platelets can be found in ILT only in the thin luminal layer [27]. Thus, fibrin cannot be cleaved in medial and abluminal layers and is only degraded. This potentially allows us to simplify the growth and remodelling of ILT.

The finite element implementation model of ILT into FEAP [31] has been described in detail in [10]. Briefly, we assume that the luminal layer is 2 mm thick, as shown in many studies, e.g. [33]. Thrombus is modelled as incompressible material [34]. The strain energy function characterising thrombus mechanical behaviour was based on histological analysis and mechanical testing of human thrombus layers in [7] as

$$W_{\mathrm{ILT}} = \mu(I_1 - 3) + \frac{k_1}{k_2}\left(\exp\left(k_2(I_1 - 3)^2\right) - 1\right), \qquad (10)$$

with I_1 being the trace of Cauchy-Green tensor, μ and k_1 stress-like parameters and k_2 a dimensionless material parameter. Constitutive parameters were fitted in Tong et al. [7] for each thrombus layer. However, it is difficult to differentiate between medial and abluminal layers numerically. Thus, we change all ILT stiffness parameters with the depth of thrombus d. For example, the parameter k_1 is defined as a constant $k_{1,\mathrm{lum}}$ in the luminal layer (i.e., for $d \le d_{\mathrm{lum}} = 2$ mm), and in deeper layers can be calculated as

$$k_1(d) = k_{1,\mathrm{abl}} + \left(k_{1,\mathrm{lum}} - k_{1,\mathrm{abl}}\right)\exp\left[-K\left(d - d_{\mathrm{lum}}\right)\right]. \qquad (11)$$

In eq. (11) $k_{1,\mathrm{lum}}$ and $k_{1,\mathrm{abl}}$ are stiffness parameters of luminal and abluminal layer, respectively, and K is a decay parameter chosen to allow a realistic thickness of the medial layer.

3. Calibration of intraluminal thrombus model parameters

The model parameter values related to the growth and remodelling of the aortic wall remain unchanged to previous studies [10, 17] and listed in the Table A.1 in the Appendix A. However, prior to analysing the bio-chemo-mechanical influence of intraluminal thrombus on aneurysm progression, parameter calibration and verification of the ILT model must be performed. This is necessary for several reasons: first, this is an altered variation of the of the ILT G&R model from [19], adapted for

the 3D finite element environment. While the growth of ILT is still considered, its remodelling is neglected due to the immense computational requirements. Unlike wall finite elements, whose number remains constant during the analysis, the number of ILT finite elements increases by hundreds every several time steps. Additionally, storage of history variables required for aortic wall FE can be reduced to the last 50 time steps (or approximately 500 days, see Appendix D in [17] for details), whereas this could not be done for fibrin comprising the thrombus.

Second, biomechanical parameters from [19] were defined for 2D geometry, meaning that all mass-related variables are defined by the unit of length. This is further complicated by the uneven mesh in the axial direction (with larger finite elements near the boundaries and smaller elements in the area of the AAA sac), axially inhomogeneous growth of the element mass, and different numbers of integration points per element (8 for 3D FE implementation vs 1 for the semi-analytical solution from [19]). As a result, these parameters, unfortunately, cannot be directly used for the full 3D FE formulation.

Therefore, both mechanical and biochemical parameters of intraluminal thrombus needed to be adjusted to replicate the results from a fully thrombosed cylindrical model from [19, 20] best possible. The parameter calibration is managed in two steps. First, biochemical model parameters need to be chosen to replicate the spatial (i.e., radial) distributions of elastases and collagenases during the AAA progression, as well as temporal changes of their total count in the wall. Mechanical parameters can be calibrated subsequently to depict appropriate aneurysm growth rates and spatiotemporal changes in stresses, both within the wall and thrombus.

Table 1 shows the calibrated values and ranges of ILT model parameters. Briefly, five correlation factors (K_{N}^{k} and K_{VV}^{k} for elastases and collagenases, and $K_{\mathrm{EDP}}^{\mathrm{VV}}$) define the boundary conditions for the protease diffusion. They were chosen so that in larger cylindrical aneurysms amount of proteases in the fully formed luminal layer is approximately 4-8 times higher than in the aortic wall, as was presented in histological studies [35, 36].

Table 1 Default values and reasonable ranges of bio-chemo-mechanical ILT model parameters obtained by calibration on cylindrical model

	Parameter	Default value [range]	Unit	Calibrated to / taken from
Biomechanical model parameters	$K_{\mathrm{N}}^{\mathrm{elas}}$	0.12	$\mathrm{g_{elas}/g_N}$	As was used in [19, 20]
	$K_{\mathrm{N}}^{\mathrm{MMP}}$	5.5	$\mathrm{g_{MMP}/g_N}$	
	$K_{\mathrm{EDP}}^{\mathrm{VV}}$	150	$\mathrm{mm_{VV}^2 / g_{EDP}}$	
	$K_{\mathrm{VV}}^{\mathrm{elas}}$	0.2 [0.15 – 0.25]	$\mathrm{g_{elas}/mm_{VV}^2}$	Calibrated to 4-8 times higher proteolytical activity of luminal layer compared to the wall [35, 36]
	$K_{\mathrm{VV}}^{\mathrm{MMP}}$	4.5 [4 – 5]	$\mathrm{g_{MMP}/mm_{VV}^2}$	
	A_0^{VV}	5e-4	$\mathrm{mm_{VV}^2}$	Taken from [29], as used in [19]
	$w_{q,\mathrm{elas}}^{\mathrm{e}}$	0.035 [0.02 – 0.05]	$\left(\mathrm{g_{elas}day}\right)^{-1}$	Calibrated to ensure a fraction of functional elastin after 20 years [37]
	$w_{q,\mathrm{MMP}}^{c}$	0.035 [0.01 – 0.1]	$\left(\mathrm{g_{MMP}day}\right)^{-1}$	Calibrated to ensure realistic growth rates
Mechanical parameters	μ_{lum}	1.625	kPa	Calibrated for realistic radial stress and pressure through the thrombus depth [38]
	$k_{1,\mathrm{lum}}$	2.15	kPa	
	$k_{2,\mathrm{lum}}$	0.0075	-	
	μ_{abl}	1	kPa	
	$k_{1,\mathrm{abl}}$	0.475	kPa	
	$k_{2,\mathrm{abl}}$	0.005	-	
	K	0.3 [0.15 – 0.4]	-	Calibrated for realistic thickness of the medial layer of ILT [7]

Weighting factors ($w^{e}_{q,\mathrm{elas}}$ and $w^{c}_{q,\mathrm{MMP}}$) specify the rate of increased elastin and collagen degradation due to increased proteolytic activity introduced by thrombus formation. This factor for elastin $w^{e}_{q,\mathrm{elas}}$ was chosen such that 20 years after the formation of an aneurysm, 10-20% of functional elastin still remain in the aneurysm, based on a study presented in [37]. For collagen, a range of $w^{c}_{q,\mathrm{MMP}}$ values was chosen after all other parameters were calibrated in order for AAA growth rates to be realistic, i.e., several mm/year. Note that a decrease in weighting factors can describe patients on anti-inflammatory therapy.

For the original mechanical properties of thrombus layers from [7], the thrombus bears almost 90% of radial stress in large aneurysms. Thus, these parameter values were reduced so that radial stress and pressure (calculated as $p = -1/3\,\mathrm{tr}(\boldsymbol{\sigma})$) through the thrombus depth are realistic. An experimental study [38] reported that the ratio of pressure within the thrombus to that within the flowing blood should be 0.90 ± 0.09, 0.86 ± 0.10, and 0.81 ± 0.09 at depths of 1, 2, and 3 cm, respectively. This was an additional calibration criterium. The range of values for decay parameter *K* defines the thickness of the medial layer of ILT, which varies between 5-15 mm according to [7].

4. Results

Using the calibrated parameters, we can finally investigate the influence of ILT on an axially symmetric fusiform AAA evolution. First, we show geometrical and structural changes during fully thrombosed AAA. Furthermore, similar to work in [10], we investigate two different thrombus deposition cases: fully thrombosed aneurysm with the delayed formation of ILT and partially thrombosed AAAs.

4.1. Geometrical and structural changes

As the initial insult, we suddenly locally degrade 15% of elastin. Due to irreversible structure change, the artery starts to bulge locally. In case there are no additional stimuli for aneurysm formation, the adaptation of the aorta to the insult mostly depends on the collagen production rate (i.e. production rate parameters in eq. (8)). If there is sufficient collagen production (upper range value of K^{k}_{C} from Table A.1), an aneurysm might not form, and the aorta will find a new equilibrium at a locally slightly dilated non-aneurysmal radius, as can be seen in Fig. 2(a), black line. However, if the proteolytically active thrombus forms and further degrades the wall, an aneurysm will develop. This case is appropriate for studying the bio-chemo-mechanical effect of ILT on AAA progression, as aneurysm growth depends solely on thrombus and no other factors.

We let the thrombus deposit in every time step in which the difference between current luminal radius and healthy inner radius is larger than 0.4 mm, i.e., in this case, thrombus forms at G&R time of approximately 1000 days, when the inner radius is 10.4 mm. The evolution of the maximal inner radius and axial length of the fully thrombosed AAA can be seen in Fig. 2 (orange lines). After thrombus deposits, a thin, proteolytically active luminal thrombus is adjacent to the wall and starts to progressively degrade proteins in the wall. As a consequence, the aorta starts to dilate more rapidly. Unlike an artery without a thrombus that stabilises at 11 mm radius, an aneurysm with a thrombus shows near-linear growth of maximal diameter.

The length of an aneurysm is here defined similarly to the definition in [39]; it is calculated as the distance between the sections with a diameter 10% larger compared to the healthy one (i.e. 11 mm). If the thrombus does not deposit, the diameter never reaches this value, and AAA length remains zero (black line in Fig. 2(b)). However, if thrombus deposits, AAA length expands steeply at first, and after the first medial layer of ILT forms, the growth slows down (orange line in Fig. 2(b)). Note that the moment when length becomes non-zero is delayed compared to the increase in radial growth (1500 vs 1000 days). This is because ILT forms at a radius of 10.4 mm, at which point the length is still zero. Medial layer of ILT forms at the moment when total ILT thickness exceeds 2 mm and the inner wall radius increases from 10 mm to 12 mm, which is at a G&R time of 2000 days. A more pronounced decrease in axial growth can be seen after that point in Fig. 2(b)).

The growth of AAA can be understood easier when observing contours of inner radius, as shown in Fig. 2(c)), for different G&R times: full, dashed and dotted lines represent G&R times 2000, 3000 and 4000 days, respectively. Again, black lines signify the contours of the weakened artery without ILT. It

is evident that the length of local dilatation does not change because no additional elastin degradation is introduced. In the case where ILT brings in proteases that can migrate in both radial and axial directions, local dilatation expands.

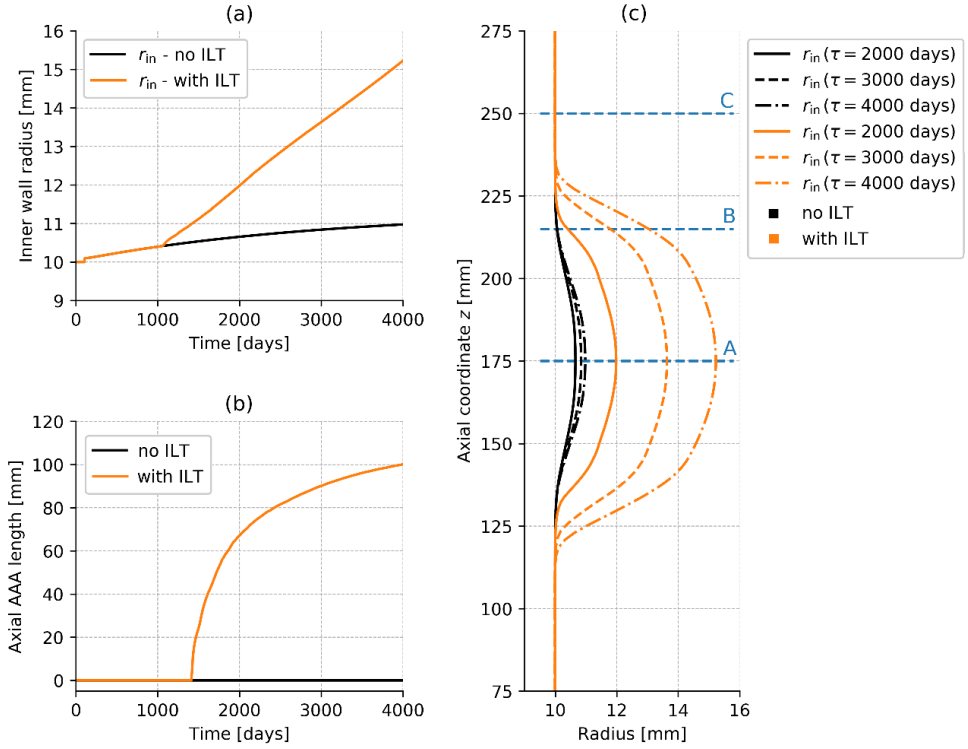

Fig. 2 The radial (a) and axial (b) growth of artery without thrombus after sudden degradation of 15% of elastin (black line) and evolution of a fully thrombosed aneurysm (orange line), and contours of inner radius at different G&R times (c)

Unlike previous studies, where degradation of elastin was prescribed, in this study, it depends on elastase distribution. It is interesting to see normalised axial elastase distribution at the inner and outer radius of the aortic wall, Fig. 3(a). Elastase amount was normalised by their initial amount at the apex on the outer radius of the wall. Note that 15% elastin was degraded as the initial insult, meaning that a significant mass of EDPs exists in the wall at the moment of thrombus deposition, and consequently, so do increased *vasa vasorum* and proteases. This can be seen as a jump in Fig. 3(b), full green line, to the normalised value 1.

Numerous intriguing findings can be observed from Fig. 3. First, at the healthy part (cross section C in Fig. 2(c)), elastases concentration is zero, as there are no protease sources in close proximity (neither ILT nor increase neovascularisation). Second, at G&R time of 2000 days (full lines in Fig. 3(a)), only the luminal layer exists, and its thickness changes axially: at the apex, it is maximal (2 mm), and towards neck regions, it decreases to 0. Because the number of proteases coming from the ILT is directly proportional to the luminal layer thickness, the distribution of proteases at the inner wall is comparable to the ILT shape. Furthermore, after the medial layer of ILT forms, at G&R times 3000 and 4000 days, at the shoulder region (e.g., around $z = 230$ mm and $z = 120$ mm for G&R time 4000 days) luminal layer is adjacent to the wall, and the elastase amount at the inner radius of the wall is very high. Approaching the apex, ILT becomes thicker, and the proteolytically active luminal layer is further from the wall. Therefore, a steep decrease in elastase concentration can be seen. With the thickest thrombus at the apex, a local minimum in proteolytic activity can be seen.

It is also interesting to note that enzyme activity in the neck region increases with time (peak of the dashed line at G&R time 3000 days compared to the peak of dash-dotted line illustrating protease amount at G&R time 4000 days). This is because with axial growth of AAA, the length of the luminal layer, and consequently its total volume, increases. In the larger luminal layer, more neutrophils from the blood can be embedded, which implies that more proteases can be extracted and then migrate to the aortic wall.

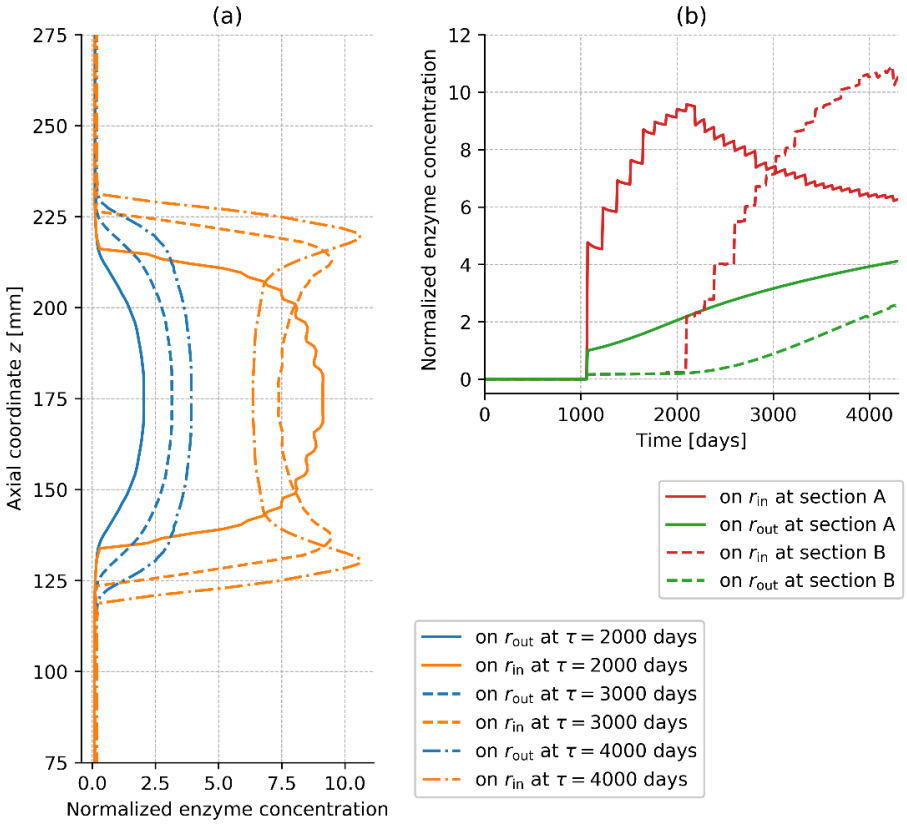

Fig. 3 Axial distribution of normalised elastases concentration at inner and outer radius at different G&R times (a), evolution of normalised elastases activity at the inner and outer radius at sections A and B (b)

On the outer wall radius, protease amount depends on the area of *vasa vasorum*, which in turn depends on the elastin degradation products. Because in the healthy part, elastin is not degraded, and there is no increase in the neovascularisation from homeostatic value, there is also no source of additional proteolytic activity. With most elastin degraded at the apex, the highest activity of elastases and collagenases is at the outer radius. Interestingly, however, from the blue lines in Fig. 3(a), it can be seen that curves flatten in time, and the distribution of elastases becomes more and more uniform in the axial direction.

When observing the evolution of elastase activity at the apex, shown in Fig. 3(b), before thrombus formation at G&R time 1000 days, it is zero. After the first ILT deposition, it increases significantly at the apex (section A defined in Fig. 2(c)). Enzyme concentration continues to increase with every further deposition until the luminal layer is fully formed. After the ILT thickness exceeds 2 mm, and the first part of the medial layer forms, it acts as a barrier for protease diffusion, and elastase concentration at the inner wall radius starts to decrease. In between thrombus depositions, existing ILT deforms with the growth of AAA and becomes slightly thinner, which results in a minor decrease in protease amount.

Section B is, at the moment of thrombus formation, at the healthy part of the aorta. Only after sufficient axial aneurysm growth protease can reach this section. This can be observed as a delay in the increase of elastase concentration in Fig. 3(b), full vs dashed lines. Again, as already explained, the peak of elastase amount is higher in section B than in section A.

At the outer radius (green lines), where the concentration of elastases depends on EDPs, a monotonous increase in elastase can be seen due to continuous elastin degradation. It can be seen that in section B, the elastase amount increases steeper at section B compared to apex A, resulting in flattening of the axial distribution in Fig. 3(a).

It might be valuable to mention that the spatiotemporal distribution of collagenases qualitatively looks very similar to elastases and will not be shown here.

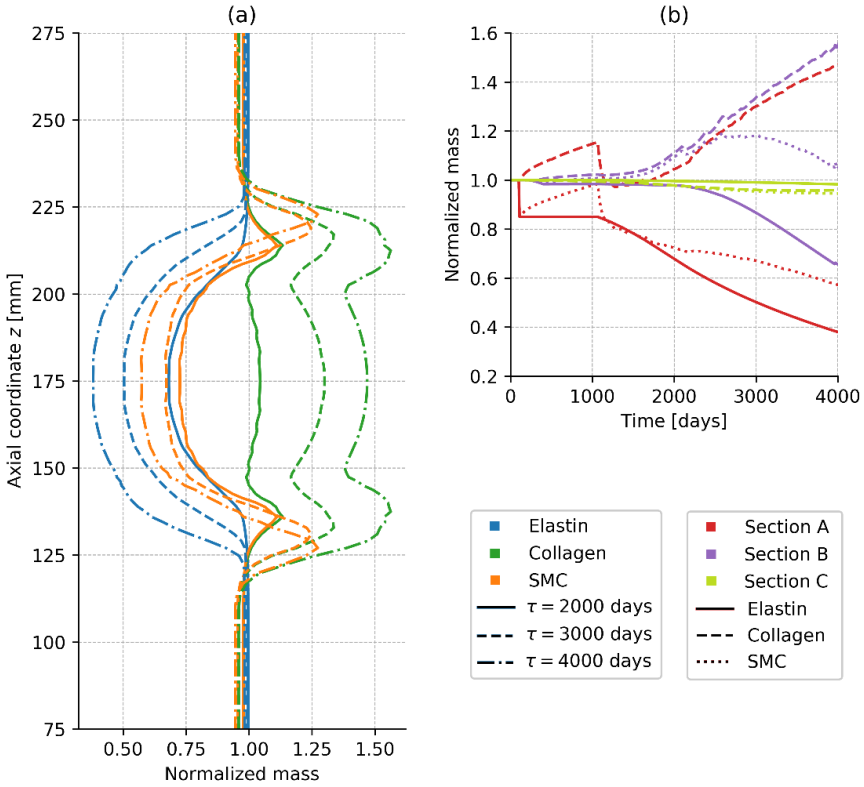

Fig. 4 The axial distribution of cumulative wall constituent masses through the thickness, normalised by their initial mass, at G&R time $s = 4000$ days (a), evolution of the wall constituent masses at points A, B and C (b)

Based on elastase distribution from the Fig. 3, elastin mass can be calculated as shown in Fig. 4. Masses are normalised by their homeostatic value. Cumulative masses through thickness at different sections are shown in Fig. 4(b). At the apex (red lines), elastin is initially degraded by 15%, and a jump from 100% to 85% can be seen. Before ILT formation, elastin mass remains unchanged, and after its first deposition, approximately at time 1000 days, elastin continues to degrade. Because anoikis, i.e. apoptosis of smooth muscle cells with loss of elastin, is modelled (for cf. see [17, 40]), smooth muscle mass also decreases with initial loss of elastin. However, because of increased wall stresses that trigger the turnover of SMCs and collagen, during adaptation of the aorta to the insult, both smooth muscle and collagen mass increase. The formation of ILT brings in proteases, and masses of all constituent masses decrease. During further growth and remodelling process, collagen mass production increases due to increased stresses, and collagen mass continues to grow monotonously. Smooth muscle mass decreases with elastin degradation, yet because it can still be produced, the loss of SMC is not as prominent as elastin mass.

Section B was initially a healthy part, and elastin mass was nearly constant until the introduction of proteases (purple lines) after sufficient axial growth of AAA. Unlike elastin, a significant increase in SMC and collagen mass can be observed before ILT deposition near the section. The moment elastin starts degrading depends on the elastase activity from Fig. 3(b). With the loss of elastin, SMC mass starts to visibly lower, yet at G&R time 4000 days, it is still at a value higher than homeostatic. Intriguingly, while collagen mass at the apex considerably decreased after ILT formation, at section B, it continues to rise, albeit somewhat slower. Also, because the sudden decline did not happen, collagen mass at section B is higher compared to the apex.

In section C, homeostasis is preserved, and wall constituent masses are mostly preserved.

Note that aneurysmal wall composition was not one of the calibration preconditions and can therefore be used for model verification. The changes in mass correspond well to data obtained from histochemical methods in He and Roach [41]. Tong et al. [37] also noted a decrease in dry weight of elastin mass and an increase in collagen mass (see Fig. 10 in [37]), as we show in Fig. 4(b). They also measured elastin to collagen ratio in adventitia and intima-media under different thrombus ages: under

phase II thrombus (corresponding to fully developed luminal layer), phase III thrombus (medial layer), and phase IV (abluminal layer). In intima undelaying the luminal layer, the reported collagen to elastin ratio was 0.53±0.4, under the phase III it was 0.44±0.35, and under phase IV thrombus it was 0.2±0.2. Our model at G&R time 2000 days (the moment when the luminal layer is fully formed) returns values of this ratio at the inner node of 0.52, and time 3000 days 0.26 and at 4000 days 0.15. The sharp decrease in the ratio is the consequence both of the degradation of elastin (with higher degradation in intima than in adventitia) and higher production of collagen.

When inspecting axial constituent mass distribution, Fig. 5(a), elastin mass directly depends on the elastase distribution (Fig. 3(a)). In the area around the apex, SMC mass is lower than homeostatic, yet in the shoulder region, its production is still higher than apoptosis. Collagen mass is at all locations higher than healthy value but the highest in the neck. Note that intimal thickening in shoulder regions thickening despite inflammatory infiltration was noted in [42].

Collagen production depends on the increase in stresses compared to the homeostatic value. Fig. 4(a) and (b) show circumferential and axial stresses through the thickness at a G&R time of 4000 days. The thrombus is much softer than the aortic wall, and ILT layers rupture at stress values of approximately 25 kPa [7]. Noting that all turnover in ILT happens exclusively in the luminal layer of thrombus, fibrin at radii r > 12mm can only degrade and deform substantially with the wall. Thus, although stresses at 3.5 mm ILT thickness seem to be low, they would increase with the growth of AAA.

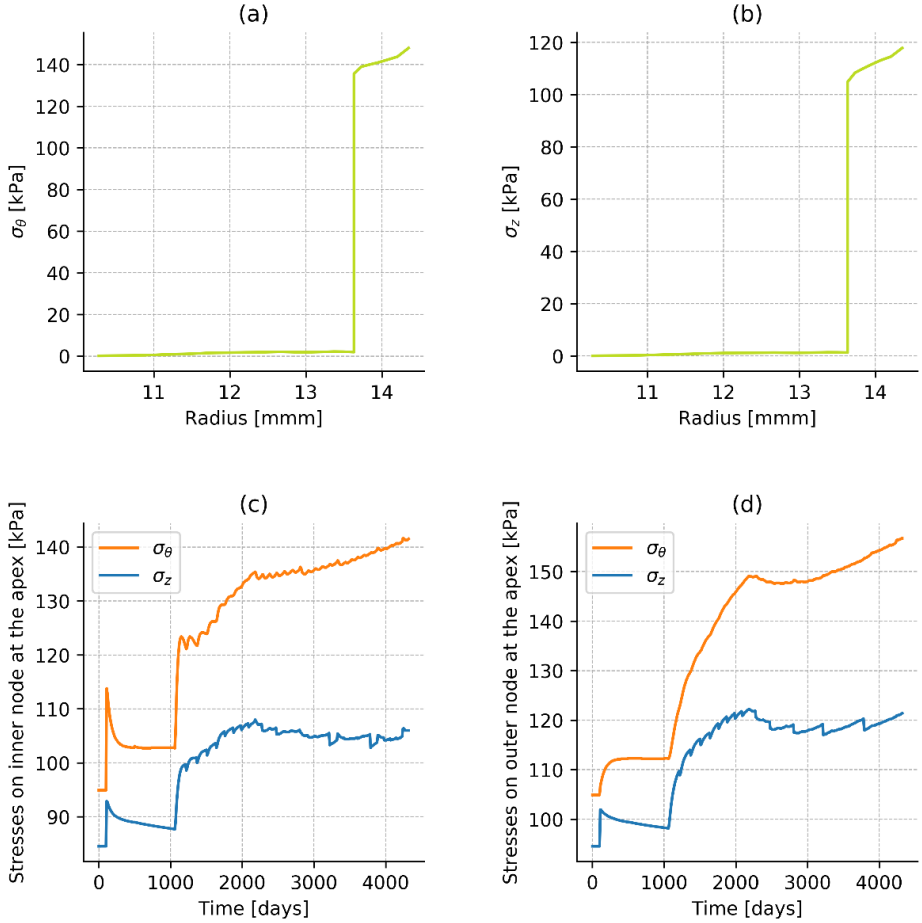

Fig. 4 Distribution of the circumferential (a) and axial stress (b) through the ILT and wall thickness at the apex at G&R time 4000 days; circumferential and axial wall stresses evolution at the apex on the inner radius (c) and outer radius (d)

Several crucial pieces of information can be studied in Fig. 4(c) and (d), showing stress evolutions at the apex at the inner and outer nodes. After initial insult, with degradation of elastin, sudden dilation of the aorta causes an increase in stresses. Circumferential stress at the outer node is the only stress without an immediate response. As collagen and SMC mass adapted to the insult, stress values

lowered and found a new equilibrium state. The formation of the thrombus caused a very sharp increase in stresses. This can be explained by increased degradation of both elastin and collagen that are stretched more than their homeostatic value and bear a significant load. This results in initially very steep growth of AAA diameter and an increase in stresses. Axial and circumferential stresses at all locations at the apex continue to quickly grow until the first medial layer of ILT is formed (G&R time 2000 days). After the medial layer is formed, axial stresses at the apex seem to stop increasing (blue lines in Fig. 4(c) and (d)). Yet, circumferential stresses keep increasing with the growth of AAA (Fig. 1(a)). Small fluctuations can be observed at moments of thrombus depositions.

4.2. Influence of increase in luminal area

Based on medical imaging data of large AAAs, it seems that the overall luminal diameter tends to be preserved, although sometimes at a higher value than the healthy aorta [43]. Thus, we let the thrombus first form at a predefined luminal diameter and deposit ILT constantly during AAA progression to that same increased luminal diameter r_{lum}.

In the previous section, when exploring the geometrical and structural changes introduced by the bio-chemo-mechanical thrombus model during AAA growth, we let the aorta stabilise at a slightly dilated radius of 11 mm (Fig. (a), black line) after the initial insult of 15% elastin degradation in order to separate factors from the aortic wall and ILT in the greatest possible extent.

Obviously, when investigating the influence of later ILT formation, at radii of 12, 14 or 16 mm, the aorta must dilate to that radius for a thrombus to form. For that to happen, we decreased the collagen production in the wall (lower range value of K_C^k from Table A.1). When collagen production is not sufficient for the aorta to adapt to the insult, aneurysm forms even without other stimuli, see blue line in Fig. 6(a).

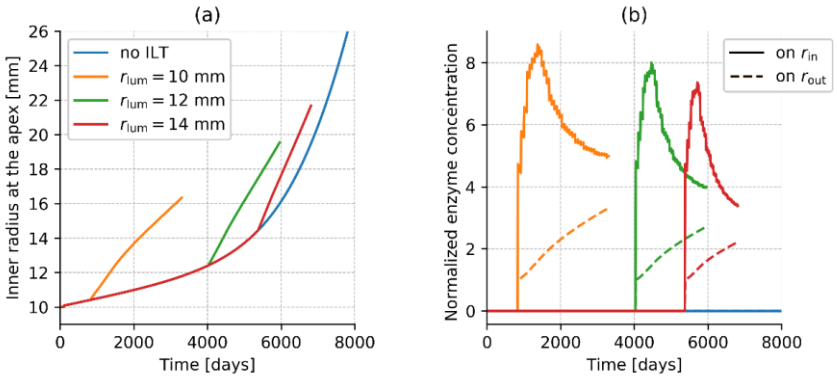

Fig. 6 The evolution of the AAA inner radii for aneurysm with an increased luminal area (a), evolution of elastase concentration at the inner and outer radius at the apex (b)

Progression of AAA for different luminal radii can be seen in Fig. 6(a) – orange line represents the growth of fully thrombosed AAA (but with different collagen production compared to the previous example in Fig. 2), green line AAA with luminal radius in the aneurysmal sac of 12 mm, and red line for change in luminal radius to 14 mm. It is easy to see that slopes of curves are progressively steeper with later ILT formation. Interestingly, peak protease activity at the inner wall radius at the apex is reduced for delayed ILT formation, Fig. 6(b). This can be explained by the shorter axial length of the luminal layer for higher values of luminal radius (see contours in Fig. 10(c) and online resource videos for clarification), which implies a lower total volume of luminal layer and thus also the total amount of proteases.

On the outer wall, protease activity starts from the same amount of elastin degradation products. With slightly lower elastase concentration on the inner node, EDP mass increases slower, and slopes on the outer radius are, to some extent, milder, dashed lines in Fig. 6(b).

Thus, despite slower degradation of extracellular matrix, higher growth rates for later ILT formation likely happen due to higher values of wall stress with an increase in AAA diameter. At later ILT formation, wall stresses are higher, and so are stresses collagen and elastin bear; see blue lines in Fig.

7. This means that degradation of extracellular matrix by proteolytically active luminal layer introduces larger insult.

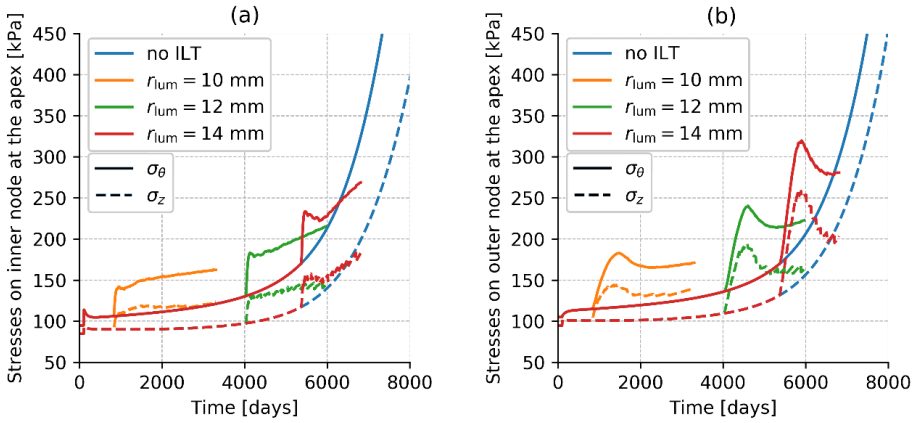

Fig. 7 Circumferential and axial stress evolutions at the inner (a) and outer radius (b) at the apex for AAA with different luminal radii

Curiously, axial stresses at the inner wall and all stresses at the outer apex wall seem to find an equilibrium quickly after the formation of the medial layer. Only the circumferential stress at the inner wall increases. Even with smaller values of all stress components, the growth rate is higher for a partially thrombosed aneurysm compared to one without a thrombus. This is probably due to constant degradation of elastin when ILT is introduced vs constant elastin mass at 85% of healthy value for AAA without thrombus.

4.3. Influence of the moment of ILT formation

Some medical imaging shows that the lumen area can remain the same in the aneurysmal sac as in the healthy part [16]. However, only 42% of the patients with AAAs sizing 30-34 mm have ILT [44]. This means that moment of ILT formation varies from patient to patient. Thus, we investigated the influence of different times of ILT formation on fully thrombosed AAA growth. In this case, we let the aneurysm dilate to a predefined radius r_{ILTstart} before the formation of the thrombus. After the formation, ILT quickly fills the whole aneurysmal sac until it becomes fully thrombosed.

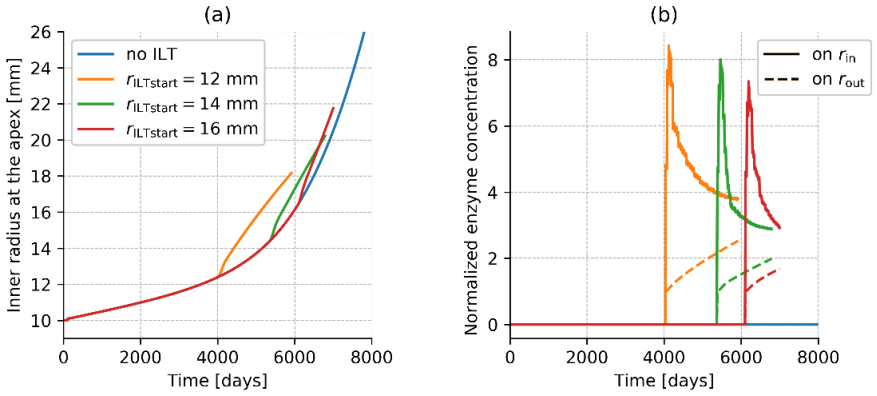

Fig. 8 The evolution of the AAA inner radii (a), evolution of elastase concentration at the inner and outer radius at the apex (b) for fully thrombosed aneurysms with different times of ILT formation

Fig. 8(a) shows the evolution of maximum inner radius for fully thrombosed aneurysms if an ILT first formed at inner apex radii r_{ILTstart} of 12, 14, and 16 mm. Again, similar to Fig. 6(a), an evident increase in slope steepness can be observed for the later ILT formation. Also, peak enzyme concentration decreases with the formation of ILT in the more dilated aneurysmal sac, Fig. 8(b). However, because new thrombus layers are deposited until the whole aneurysmal sac is thrombus-laden, and not only depending on AAA growth, a decrease in enzyme activity with the distancing of the luminal layer is

much sharper in the fully thrombosed case compared to the increased luminal radius in Fig. 6(b). Again, the increase in proteolytic activity on the outer radius is very similar for all simulations.
When observing stresses, the initial jump after thrombus deposition is higher for later ILT formation, e.g., for circumferential stress at inner radius, stresses rise for 75, 90 and 100 kPa for formation at 12-, 14-, and 16- mm inner radius, respectively, see Fig. 9(a). Yet, after the quick formation of the medial layer, a decrease in the same stress is also larger for the later ILT deposition. A further change in stresses, possibly due to axial growth shown in Fig. 10(b), depends significantly on the moment of ILT deposition. Similar behaviour can be seen for the evolution of axial stresses and evolution of stresses on the outer wall at the apex Fig. 9(b). Again, while stresses increase slower for thrombus-laden compared to the AAA without thrombus, Fig. 9, the same cannot necessarily be said for the geometry, Fig. 8(a).

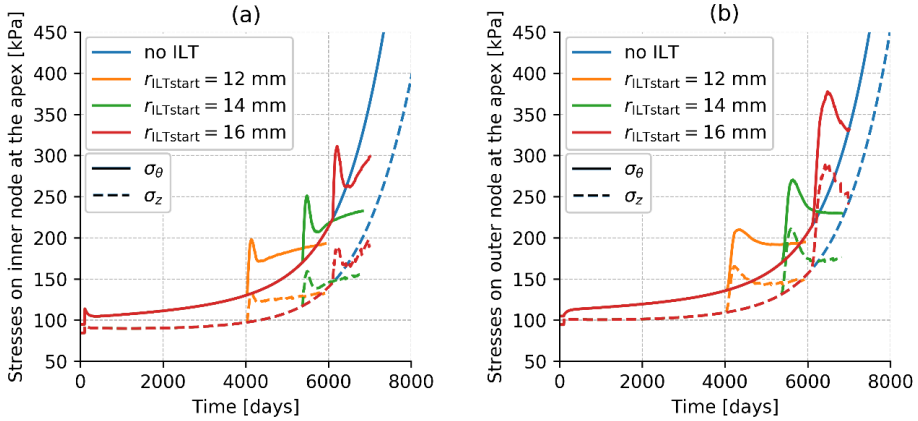

Fig. 9 Circumferential and axial stress evolutions at the inner (a) and outer radius (b) at the apex for fully thrombosed aneurysms with different times of ILT formation

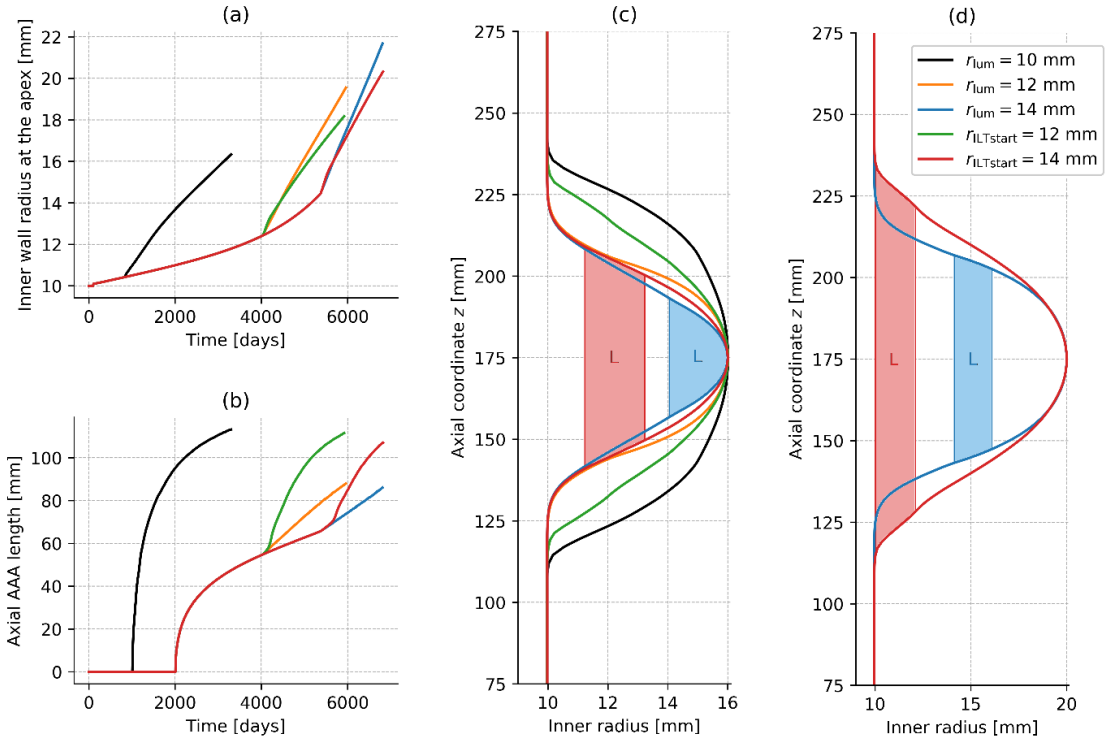

Fig. 10 Comparison of the radial (a) and axial growth (b), contours of inner wall radius for three thrombus deposition cases in the moment of the same maximal inner wall radius of 16 mm (c), contours of inner wall radius and denoted coloured area of the luminal layer of ILT (L) for partially and fully thrombosed aneurysm with ILT deposition formation moment at the inner radius of 14 mm at the maximal inner radius of 20 mm (d)

It is fascinating to examine geometrical changes and differences in aneurysmal sac for three different ILT depositions, Fig. 10. Based on the evolution of maximal radius, a fully thrombosed aneurysm with immediate ILT deposition (black line in Fig. 10(a)) seems to have the most stabilisation potential. When comparing ILT formation at the expended radii (green vs orange and red vs blue lines), the evolution of AAA diameter is very similar, yet aneurysms that eventually become fully thrombosed grow slightly slower compared to the partially thrombosed ones. This is because in the fully thrombosed AAAs, the distance between the luminal layer and wall at the apex increases more rapidly, and wall degradation is lower.

However, the difference between aneurysms with an increased lumen area and a healthy one is much more prominent when studying axial length growth, Fig. 10(b). In partially thrombosed AAAs luminal layer always stays positioned at the same location (at inner wall radius 14-16 mm) far away from the shoulder region; see denoted blue luminal layer in Fig. 10(c) and (d). This means fewer proteases migrate to the neck region, and AAAs remain smaller in the axial direction. For an aneurysm with thrombus formation at $r_{\mathrm{ILTstart}} = 14$ mm that eventually becomes fully thrombosed (red lines in Fig. 10), thrombus quickly fills in the aneurysmal sac. From the red luminal layer denoted in Fig. 10(c) and (d), it is obvious that as AAA grows, the luminal layer moves further inward, actively degrading the whole aneurysmal wall. Already at a maximal inner radius of 16 mm (Fig. 10(c)), it can already be seen that the red contour is slightly wider than the blue one.

Please refer to the videos (online resource) for the spatiotemporal illustration of thrombus-laden aneurysm growth and distribution of proteases for these three cases.

5. Conclusions and discussion

Intraluminal thrombus (ILT) plays a controversial role in abdominal aortic aneurysm (AAA) development. Whether it mechanically stabilises an aneurysm or degrades the underlying aortic wall and causes rupture is unknown, but it is certain that thrombus is not an innocent bystander in aneurysm progression [6].

In this work, we attempt to broaden our understanding of the role the thrombus plays from a comprehensive bio-chemo-mechanical point of view. We build on previous work [10], where we investigated the mechanical influence of ILT alone. In the present bio-chemo-mechanical model of thrombus-laden aneurysms, protein degradation depends on protease activity, unlike previous finite element studies, where AAAs growth was initiated by prescribed irreversible time-dependent elastin degradation, e.g., [17, 22, 45, 46]. Collagenases and elastases are believed to originate both from blood-borne cells embedded in the luminal layer of intraluminal thrombus and from the increasing area of chemotactic *vasa vasorum* in the wall. Based on enzyme distribution, we show a very heterogeneous structure and wall constituent mass distribution. Comparing our results to histological studies from [37, 41], evolution in masses and elastin to collagen ratio during the AAA growth is within the expected range.

It is thought-provoking to note that most of the numerical studies correlate the collagen mass and its mechanical properties to rupture, with a rationale that most of the functional elastin is degraded in an aneurysm and that smooth muscle underwent related apoptosis, e.g. [21, 47]. Yet, recent animal studies focused on vascular smooth muscle turnover as a potential key factor for cessation of AAA growth. For example, Bi et al. [48] concluded that irreversible degeneration of SMCs is critical to the rapid formation of the elastase-induced rabbit AAA model, and excessive regeneration of SMC accounts for the self-healing process. Similarly, another recent animal model [49] showed that aortic wall aneurysm development could be limited through reductions in oxidative stress and vascular smooth muscle cell apoptosis. This would lead to the conclusion that an increase in SMC mass in the shoulder region, as seen in Fig. 4(a), might not have an insignificant role when determining the AAA outcome.

Furthermore, our results show that later ILT formation leads to higher growth rates of maximal AAA diameter compared to its early deposition, despite peak protease activity and related degradation of the extracellular matrix being lower. Additionally, thrombus deposition has a large impact on the aneurysmal sac shape and volume.

Interestingly, here presented results show that the radial growth rate is slightly slower for fully thrombosed AAAs compared to the partially thrombosed ones; however, their axial growth is much more pronounced. Conversely, the length of an AAA was determined as the feature with the most information gained by machine learning performed in Shum et al. [14]. A similar conclusion was reached in our numerical analysis of the influence of AAA morphology without thrombus on rupture [39]. Here, however, the results show that the radial growth rate is smaller for aneurysms that axially grow more. It is important to note, though, that in longer AAAs the wall is weaker, and the extracellular matrix is axially more degraded, as luminal thrombus was adjacent to the wall at all heights. This means that AAA would likely be much less adaptive to the additional insults, e.g., hypertension development, injury, or increased elastin degradation due to smoking and related increase in reactive oxygen species. Moreover, the opposite tendencies of growth rate in radial and axial direction could also potentially explain very conflicting clinical results when investigating relation between ILT volume and rupture.

Regarding the limitation and assumption of the model, we neglected the surrounding tissue and the spine and assumed the laminar blood flow, as is often the case in G&R models. Additionally, little is known about the causes of AAA formation and protease distribution or their sources in AAAs without thrombus. For this reason, we simplified the initial insult as sudden degradation of elastin. Although with elastin degradation, we could define the mass of elastin degradation products and, therefore, the growth of neovascularisation and increase in proteases in the wall, it is difficult to determine the boundary conditions for enzyme distribution before ILT forms. This led to a jump in protease activity after the formation of the thrombus. Despite not being completely realistic, this assumption allowed us to investigate the bio-chemical influence of ILT separately from other factors.

Despite the limitations, the presented results bring very intriguing insight into the role of ILT in AAA development. One could hypothesise that neither wall nor ILT alone should be predictors of growth rate and rupture, but rather the moment of ILT formation and history of ILT further deposition (i.e., does fresh luminal layer deposit in the vicinity of already very weakened wall). The moment of thrombus formation needs to be defined by the composition of the underlying wall, its compliance, amount of remaining elastin and smooth muscle, how stretched the collagen is, and how fast collagen mass can be produced (i.e., factors defining the ability of the wall to adapt to the new insult), rather than G&R time/follow-up time itself. Admittedly, most of these are very difficult to assess noninvasively. Nevertheless, we believe that these results are bringing exciting insights into thrombus-laden aneurysm pathology.

Acknowledgements

This work was supported by grant from the Croatian Science Foundation (IP-2020-02-4016, Ž. Tuković).

Appendix A

In Table A.1 model parameters related to the G&R of the aortic wall are shown. Note that some parameters are observed (e.g., properties of blood or healthy aortic radius), some are fixed (e.g., initial mass fractions, homeostatic values of stretch and stress, and some mechanical properties), and others are calculated to ensure equilibrium.

Table A.1 Model parameters related to the growth and remodelling of the aortic wall

	Role	Default value [range]	Ref.
Observed	Physical constants	$\rho = 1050$ kg m^{-3}	[50]
		$\mu = 0.0037$ Pa s	
		$d_{\text{in}} = 20$ mm	
	Initial loading	$P_{\text{h}} = 90$ mmHg	[50]
		$\tau_{\text{h}}^{\text{w}} = 0.506$ Pa	
		$\sigma_{\text{h}} = 100$ kPa	
		$\sigma_{\text{h}}^{\text{c}} = 200$ kPa	
	Composition by layer	$\phi_{\text{int}} = 0.16$, $\phi_{\text{med}} = 0.52$, $\phi_{\text{adv}} = 0.32$	[51, 52]
		$\phi_{\text{int}}^{\text{e}} = 0.1$, $\phi_{\text{med}}^{\text{e}} = 0.55$, $\phi_{\text{adv}}^{\text{e}} = 0.25$	
		$\phi_{\text{med}}^{\text{SMC}} = 0.20$	
		$\phi_{\text{int}}^{\text{c}} = 0.9$, $\phi_{\text{med}}^{\text{c}} = 0.25$, $\phi_{\text{adv}}^{\text{c}} = 0.75$	
	Homeostatic kinetics	$\tau_{1/2}^{\text{c}} = \tau_{1/2}^{\text{SMC}} = 80$ days	[50]
		$\tau_{1/2}^{\text{e}} = 40$ years	
	Passive elasticity	$c_3^{\text{c}} = 22$	[51]
		$c_3^{\text{SMC}} = 3.5$	
Bounded	Pre-stretches	$G_{\Theta\Theta}^{\text{e}} = G_{zz}^{\text{e}} = 1.4$	[53]
		$G_{\text{h}}^{\text{SMC}} = 1.2$	
		$G_{\text{h}}^{\text{c}} = 1.08$	
	SMC activation	$T_{\text{m}} = 100$ kPa	[53]
		$\lambda_{\text{m}} = 2$	
		$\lambda_0 = 0.4$	
		$K_{\text{act}} = 0.05$	
	Production	$K_\sigma^{\text{c}} = K_\sigma^{\text{SMC}} = 2$	[17, 54]
		$K_C^{\text{c}} = K_C^{\text{SMC}} = 0.1$ $[0.02 - 0.1]$	
Calculated	Passive elasticity	$c_2^{\text{c}} = 560.3$ kPa	
		$c_2^{\text{SMC}} = 62.1$ kPa	
		$c^{\text{e}} = 33.96$ kPa	

References

1. Zhu C, Leach JR, Wang Y, et al (2020) Intraluminal thrombus predicts rapid growth of abdominal aortic aneurysms. Radiology 294:707–713. https://doi.org/10.1148/radiol.2020191723

2. Paraskevas KI, Torella F, Swaelens C, et al (2018) Temporal Changes in Intraluminal Thrombus Volume Within Abdominal Aortic Aneurysms : Implications for Planning Endovascular Aneurysm Sealing. https://doi.org/10.1177/1526602817748585

3. Parr A, McCann M, Bradshaw B, et al (2011) Thrombus volume is associated with cardiovascular events and aneurysm growth in patients who have abdominal aortic aneurysms. J Vasc Surg 53:28–35. https://doi.org/10.1016/j.jvs.2010.08.013

4. Golledge J, Iyer V, Jenkins J, et al (2014) Thrombus volume is similar in patients with ruptured and intact abdominal aortic aneurysms. J Vasc Surg 59:315–320. https://doi.org/10.1016/j.jvs.2013.08.036

5. Singh TP, Wong SA, Moxon J V., et al (2019) Systematic review and meta-analysis of the association between intraluminal thrombus volume and abdominal aortic aneurysm rupture. J Vasc Surg 70:2065-2073.e10. https://doi.org/10.1016/j.jvs.2019.03.057

6. Boyd AJ (2021) Intraluminal thrombus: Innocent bystander or factor in abdominal aortic aneurysm pathogenesis? JVS Vasc Sci 2:159–169. https://doi.org/10.1016/j.jvssci.2021.02.001

7. Tong J, Cohnert T, Regitnig P, Holzapfel GA (2011) Effects of age on the elastic properties of the intraluminal thrombus and the thrombus-covered wall in abdominal aortic aneurysms: Biaxial extension behaviour and material modelling. Eur J Vasc Endovasc Surg 42:207–219. https://doi.org/10.1016/j.ejvs.2011.02.017

8. Wilson JS, Virag L, Di Achille P, et al (2013) Biochemomechanics of Intraluminal Thrombus in Abdominal Aortic Aneurysms. J Biomech Eng 135:021011. https://doi.org/10.1115/1.4023437

9. Wiernicki I, Parafiniuk M, Kolasa-Wolosiuk A, et al (2019) Relationship between aortic wall oxidative stress/proteolytic enzyme expression and intraluminal thrombus thickness indicates a novel pathomechanism in the progression of human abdominal aortic aneurysm. FASEB J 33:885–895. https://doi.org/10.1096/fj.201800633R

10. Horvat N, Virag L, Karšaj I (2021) Mechanical role of intraluminal thrombus in aneurysm growth: A computational study. Biomech Model Mechanobiol. https://doi.org/10.1007/s10237-021-01478-w

11. Inzoli F, Boschettp F, Zappa M, et al (1993) Biomechanical Factors in Abdominal Aortic Aneurysm Rupture. Eur J Vasc Surg 7:667–674

12. Maier A, Gee MW, Reeps C, et al (2010) A comparison of diameter, wall stress, and rupture potential index for abdominal aortic aneurysm rupture risk prediction. Ann Biomed Eng 38:3124–3134. https://doi.org/10.1007/s10439-010-0067-6

13. Leach JR, Kao E, Zhu C, et al (2019) On the Relative Impact of Intraluminal Thrombus Heterogeneity on Abdominal Aortic Aneurysm Mechanics. J Biomech Eng 141:. https://doi.org/10.1115/1.4044143

14. Shum J, Martufi G, Di Martino E, et al (2011) Quantitative assessment of abdominal aortic aneurysm geometry. Ann Biomed Eng 39:277–286. https://doi.org/10.1007/s10439-010-0175-3

15. Domonkos A, Staffa R, Kubíček L (2019) Effect of intraluminal thrombus on growth rate of abdominal aortic aneurysms. Int Angiol 38:39–45. https://doi.org/10.23736/S0392-9590.18.04006-3

16. Metaxa E, Kontopodis N, Tzirakis K, et al (2015) Effect of intraluminal thrombus asymmetrical deposition on abdominal aortic aneurysm growth rate. J Endovasc Ther 22:406–412. https://doi.org/10.1177/1526602815584018

17. Horvat N, Virag L, Holzapfel GA, et al (2019) A finite element implementation of a growth and remodeling model for soft biological tissues : Verification and application to abdominal aortic aneurysms. Comput Methods Appl Mech Eng 352:586–605. https://doi.org/10.1016/j.cma.2019.04.041

18. Horvat N, Virag L, Holzapfel GA, Karšaj I (2021) Implementation of collagen fiber dispersion in a growth and remodeling model of arterial walls. J Mech Phys Solids 153:104498.

https://doi.org/10.1016/j.jmps.2021.104498

19. Virag L, Wilson JS, Humphrey JD, Karšaj I (2015) A computational model of biochemomechanical effects of intraluminal thrombus on the enlargement of abdominal aortic aneurysms. Ann Biomed Eng 43:2852–2867. https://doi.org/10.1007/s10439-015-1354-z

20. Virag L, Wilson JS, Humphrey JD, Karšaj I (2017) Potential biomechanical roles of risk factors in the evolution of thrombus-laden abdominal aortic aneurysms. Int J Numer methods Biomed wngineering 33:e2893. https://doi.org/10.1002/cnm.2893

21. Wilson JS, Baek S, Humphrey JD (2012) Parametric study of effects of collagen turnover on the natural history of abdominal aortic aneurysms. Proc R Soc A Math Phys Eng Sci 469:20120556. https://doi.org/10.1098/rspa.2012.0556

22. Grytsan A, Eriksson TSE, Watton PN, Gasser TC (2017) Growth description for vessel wall adaptation: a thick-walled mixture model of abdominal aortic aneurysm evolution. Materials (Basel) 10:e994. https://doi.org/10.3390/ma10090994

23. Fontaine V, Jacob MP, Houard X, et al (2002) Involvement of the mural thrombus as a site of protease release and activation in human aortic aneurysms. Am J Pathol 161:1701–1710. https://doi.org/10.1016/S0002-9440(10)64447-1

24. Houard X, Leclercq A, Fontaine V, et al (2006) Retention and Activation of Blood-Borne Proteases in the Arterial Wall. Implications for Atherothrombosis. J. Am. Coll. Cardiol. 48:A3–9

25. Mäyränpää MI, Trosien JA, Fontaine V, et al (2009) Mast cells associate with neovessels in the media and adventitia of abdominal aortic aneurysms. J Vasc Surg 50:388–395. https://doi.org/10.1016/j.jvs.2009.03.055

26. Adolph R, Vorp DA, Steed DL, et al (1997) Cellular content and permeability of intraluminal thrombus in abdominal aortic aneurysm. J Vasc Surg 25:916–926. https://doi.org/10.1016/S0741-5214(97)70223-4

27. Touat Z, Ollivier V, Dai J, et al (2006) Renewal of mural thrombus releases plasma markers and is involved in aortic abdominal aneurysm evolution. Am J Pathol 168:1022–1030. https://doi.org/10.2353/ajpath.2006.050868

28. Nackman GB, Karkowski FJ, Halpern VJ, et al (1997) Elastin degradation products induce adventitial angiogenesis in the Anidjar/Dobrin rat aneurysm model. Surgery 122:39–44

29. Vorp DA, Lee PC, Wang DHJ, et al (2001) Association of intraluminal thrombus in abdominal aortic aneurysm with local hypoxia and wall weakening. J Vasc Surg 34:291–299. https://doi.org/10.1067/mva.2001.114813

30. Almijalli M (2021) Does the intraluminal thrombus provoke the rupture of the abdominal aortic aneurysm wall? Appl Sci 11:. https://doi.org/10.3390/app11219941

31. Taylor R (2013) FEAP - Finite Element Analysis Program, Version 8.4

32. Matusik P, Mazur P, Stępień E, et al (2010) Architecture of intraluminal thrombus removed from abdominal aortic aneurysm. J Thromb Thrombolysis 30:7–9. https://doi.org/10.1007/s11239-009-0430-3

33. Vande Geest JP, Sacks MS, Vorp DA (2006) A planar biaxial constitutive relation for the luminal layer of intra-luminal thrombus in abdominal aortic aneurysms. J Biomech 39:2347–2354. https://doi.org/10.1016/j.jbiomech.2006.05.011

34. Vorp DA, Mandarino WA, Webster MW, Gorcsan J (1996) Potential influence of intraluminal thrombus on abdominal aortic aneurysm as assessed by a new non-invasive method. Cardiovasc Surg 4:732–739

35. Houard X, Ollivier V, Louedec L, et al (2009) Differential inflammatory activity across human abdominal aortic aneurysms reveals neutrophil- derived leukotriene B 4 as a major chemotactic factor released from the intraluminal thrombus. FASEB J 23:1376–1383. https://doi.org/10.1096/fj.08-116202

36. Houard X, Touat Z, Ollivier V, et al (2009) Mediators of neutrophil recruitment in human abdominal aortic aneurysms. Cardiovasc Res 82:532–541. https://doi.org/10.1093/cvr/cvp048

37. Tong J, Cohnert T, Regitnig P, et al (2014) Variations of dissection properties and mass fractions with thrombus age in human abdominal aortic aneurysms. J Biomech 47:14–23. https://doi.org/10.1016/j.jbiomech.2013.10.027

38. Hinnen JW, Koning OHJ, Visser MJT, Van Bockel HJ (2005) Effect of intraluminal thrombus on pressure transmission in the abdominal aortic aneurysm. J Vasc Surg 42:1176–82. https://doi.org/10.1016/j.jvs.2005.08.027

39. Živić J, Virag L, Horvat N, Karšaj I (2021) The risk of rupture and abdominal aortic aneurysm morphology : A computational study. Int J Numer Method Biomed Eng 1–17. https://doi.org/10.1002/cnm.3566

40. Mtairag EM, Houard X, Rais S, et al (2002) Pharmacological Potentiation of Natriuretic Peptide Limits Polymorphonuclear Neutrophil–Vascular Cell Interactions. Arterioscler Thromb Vasc Biol 22:1824–1831. https://doi.org/10.1161/01.ATV.0000037102.31086.F4

41. He CM, Roach MR (1994) The composition and mechanical properties of abdominal aortic aneurysms. J Vasc Surg 20:6–13

42. Sluimer JC, Gasc JM, van Wanroij JL, et al (2008) Hypoxia, Hypoxia-Inducible Transcription Factor, and Macrophages in Human Atherosclerotic Plaques Are Correlated With Intraplaque Angiogenesis. J Am Coll Cardiol 51:1258–1265. https://doi.org/10.1016/j.jacc.2007.12.025

43. Zambrano BA, Gharahi H, Lim CY, et al (2016) Association of Intraluminal Thrombus, Hemodynamic Forces, and Abdominal Aortic Aneurysm Expansion Using Longitudinal CT Images. Ann Biomed Eng 44:1502–1514. https://doi.org/10.1007/s10439-015-1461-x

44. Behr-Rasmussen C, Grondal N, Bramsen MB, et al (2014) Mural thrombus and the progression of abdominal aortic aneurysms: A large population-based prospective cohort study. Eur J Vasc Endovasc Surg 48:301–307. https://doi.org/10.1016/j.ejvs.2014.05.014

45. Lin WJ, Iafrati MD, Peattie RA, Dorfmann L (2017) Growth and remodeling with application to abdominal aortic aneurysms. J Eng Math 109:113–137. https://doi.org/10.1007/s10665-017-9915-9

46. Braeu FA, Seitz A, Aydin RC, Cyron CJ (2017) Homogenized constrained mixture models for anisotropic volumetric growth and remodeling. Biomech Model Mechanobiol 16:889–906. https://doi.org/10.1007/s10237-016-0859-1

47. Wilson JS, Baek S, Humphrey JD (2012) Importance of initial aortic properties on the evolving regional anisotropy, stiffness and wall thickness of human abdominal aortic aneurysms. J R Soc Interface 9:2047–2058. https://doi.org/10.1098/rsif.2012.0097

48. Bi Y, Guo J, Yi M, et al (2022) Degeneration and Regeneration of Smooth Muscle Cells in Two Different Abdominal Aortic Aneurysm Models in Rabbits. Ann Vasc Surg 79:290–297. https://doi.org/https://doi.org/10.1016/j.avsg.2021.09.019

49. Krishna SM, Li J, Wang Y, et al (2021) Kallistatin limits abdominal aortic aneurysm by attenuating generation of reactive oxygen species and apoptosis. Sci Rep 1–15. https://doi.org/10.1038/s41598-021-97042-8

50. Humphrey JD (2002) Cardiovascular Solid Mechanics: Cells, Tissues, and Organs. Springer Science+Business Media New York

51. Cardamone L, Valentín A, Eberth JF, Humphrey JD (2009) Origin of axial prestretch and residual stress in arteries. Biomech Model Mechanobiol 8:431–46. https://doi.org/10.1007/s10237-008-0146-x

52. Karšaj I, Humphrey JD (2012) A multilayered wall model of arterial growth and remodeling. Mech Mater 44:110–119. https://doi.org/10.1016/j.mechmat.2011.05.006

53. Valentín A, Humphrey JD, Holzapfel GA, et al (2011) A multi-layered computational model of coupled elastin degradation, vasoactive dysfunction, and collagenous stiffening in aortic aging. Ann Biomed Eng 39:2027–2045. https://doi.org/10.1007/s10439-011-0287-4

54. Valentín A, Humphrey JD (2009) Parameter sensitivity study of a constrained mixture model of arterial growth and remodeling. J Biomech Eng 131:101006. https://doi.org/10.1115/1.3192144

PAPER 5

Accepted Manuscript of the book chapter reproduced with permission from Springer Naturel.

Virag, Lana, **Horvat Nino**, Karšaj Igor: Bio-chemo-mechanical role of intraluminal thrombus deposition on arterial tissue growth and remodeling. In: Solid (Bio)mechanics: Challenges of the Next Decade, editors: Gerhard Sommer, Kewei Li, Daniel Ch. Haspinger, Raymond W. Ogden, publisher: Springer Cham, 2022, doi.org/10.1007/978-3-030-92339-6_5

Bio-chemo-mechanical role of intraluminal thrombus deposition on arterial tissue growth and remodeling

Lana Virag, Nino Horvat and Igor Karšaj

Abstract Intraluminal thrombus (ILT) is present in various arterial lesions, such as aneurysms or dissections. The role thrombus plays during the development of these diseases is still controversial and unclear. The extraction of ILT is a standard procedure only during an open abdominal aortic aneurysm (AAA) repair. Thus a wide variety of histological analyses and mechanical testing is available mostly for AAA thrombus, whereas much less is known about other thrombi. This chapter investigates the possible, sometimes opposing, roles ILT has in arterial growth and remodeling, with a focus on AAAs, using computational methods. Based on available experimental data, a bio-chemo-mechanical ILT model is developed. The results suggest that an ILT can significantly influence AAA expansion and its rupture risk. When a luminal layer with high proteolytic activity is in proximity to the remodeling wall it may increase AAA expansion rate. ILT may also contribute to clinically-observed discontinuous expansion patterns. Mechanically, ILT shields the wall and reduces the AAA axial growth. Additionally, thrombus deposition is believed to be driven by hemodynamic factors, meaning that the typically used growth and remodeling model of soft tissue might not suffice for a complete understanding of ILT influences; for more comprehensive modeling, a fluid-solid-growth (FSG) model is needed. Using the FSG model, asymmetrical thrombus deposition is predicted, increasing the area covered by thin thrombus.

Lana Virag
University of Zagreb, Faculty of Mechanical Engineering and Naval Architecture, Ivana Lučića 5, Zagreb, Croatia

Nino Horvat
University of Zagreb, Faculty of Mechanical Engineering and Naval Architecture, Ivana Lučića 5, Zagreb, Croatia

Igor Karšaj
University of Zagreb, Faculty of Mechanical Engineering and Naval Architecture, Ivana Lučića 5, Zagreb, Croatia, e-mail: igor.karsaj@fsb.hr

1 Introduction

Intraluminal thrombus (ILT) is a fibrin-rich structure with intertwined red and white blood cells, platelets, and other cells and molecules from the blood. It is present in many cardiovascular diseases; it causes myocardial infarction and stroke by obstruction of blood flow; whereas in aneurysms or dissections it simultaneously degrades and shields the underlying wall. Thrombus is known to significantly influence the outcome of the diseases: for example, a study by Tsai et al. [1] showed that partial thrombosis, as compared to full potency or no thrombus, is a independent predictor of rupture. Rupture of intracranial aneurysms (IA) was also related to a thin thrombus [2]. However, the treatment of IAs with flow diverters is based on disruption of blood flow within the aneurysm to induce pro-thrombotic conditions [3]. In the thrombus-laden abdominal aortic aneurysms (AAA), a thicker thrombus was shown to slow down the AAA growth; however, smaller relative size of ILT was linked to a higher growth rate [4]. In conclusion, ILT has a very complex, but undoubtedly important role in the evolution and outcome of various vascular diseases. Noting the high incidence of thrombus presence (around 70% in IA [2], 45% in AD [1], and 80% in AAA [5, 6]), it should not be neglected, neither during clinical decision making nor during numerical modeling.

Treatment of these diseases is mostly endovascular and thrombus is not extracted during the procedure. The only exemption is the open surgical repair of AAAs, during which ILT can be removed, histologically analyzed, and mechanically tested. Because of that, there is a vast amount of data about ILT from AAA, while much less is known about other thrombi that can be examined only after autopsy. The work presented in this chapter will, consequently, be focused mostly on abdominal aortic aneurysms, but with appropriate adjustments can be applied to other thrombus-laden arterial lesions.

Formation and further growth of intraluminal thrombus are believed to be hemodynamically driven. It is proposed that for the formation of ILT within aneurysms two main conditions need to be fulfilled – platelets must be activated within a shear flow and then be presented to a susceptible endothelium [7]. Besides the wall shear stress (WSS), there were several other attempts to define a measure of the likelihood of thrombus formation: Shadden et al. [8] proposed a non-dimensional scalar index that represents the magnitude of shear rates that a fluid particle accumulates while travelling throughout the fluid domain named platelet activation potential (PLAP). Furthermore, an index referred to as thrombus formation potential (TFP) which identifies local regions of the wall that were simultaneously exposed to pro-thrombotic WSS stimuli and a flow rich in activated platelets showed promising results. Comparisons between the computational prediction of intraluminal thrombus deposition within AAA using TFP and medical data from follow-ups on six patients gave a satisfying first estimate of thrombus deposition [9]. Similarly, Naim et al. [10] performed computational fluid dynamics analysis of AD to illustrate the potential mechanism behind the formation of thrombus and predict possible locations based on WSS.

An intraluminal thrombus, unlike other blood clots, shows few signs of healing, i.e. fibrin fibers are not replaced with collagen during the disease evolution, [11],

at least before treatment. Yet, follow-up imaging after treatment of aneurysms and dissections typically show shrinkage of the lesion and, in some cases, even complete disappearance of intraluminal thrombi (whether by replacement by collagen or by the degradation of fibrin). Thus, for modelling ILT after treatment, herein presented model could be expanded with a model describing the longitudinal changes in structure and mechanical properties during the transformation of a clot from an initially fibrin-based mesh to a predominantly collagenous mass, e.g. see [12].

Depending on the thrombus size and age, ILT can consist of up to three structurally and proteolytical different layers. The portion closest to the flowing blood (i.e., the luminal layer) is characterized by an aggregation of activated platelets as well as the entrapment of erythrocytes and leukocytes within a continuously evolving fibrin mesh. Luminal layer thickness is possibly limited by the depth to which blood components can penetrate the fibrin mesh, as it is usually 2 mm thick [13]. Leukocytes within the luminal layer are responsible for producing enzymes that degrade the arterial wall (matrix metalloproteinases (MMPs); collagenases and elastases) or indirectly activating them (e.g., by activating urokinase plasminogen activator (uPA), which turns plasminogen to plasmin. In turn, plasmin not only degrades fibrin but also activates latent MMPs). In deeper layers (medial and abluminal), due to lack of platelets and blood cells [14], fibrin is not produced anymore, and fibrin mesh becomes more degraded and disorganized. The degradation of fibrin mesh in some human abluminal layers, i.e. the first deposited thrombus layer adjacent to the arterial wall, can reach a point where the layer has barely any tensile strength and cannot be mechanically tested. [15].

Despite overwhelming evidence that thin ILT biochemically degrades arterial wall [14, 16], and thick mechanically shields it [17], thrombus has been either modelled as inert, homogeneous material in static models that focus on the stress state in the wall (e.g., [18]) or neglected in most numerical growth and remodeling (G&R) studies (e.g., [19, 20]). There is, therefore, a pressing need for a greater understanding of ILT's influences on the arterial wall and lesion evolution.

The goal of this research was to develop a growth and remodeling model of enlargement and possible rupture of thrombus-laden AAAs. Additionally, potential differences in model predictions for physiological ranges of parameter values related to the risk of rupture were examined. Furthermore, by coupling computational fluid dynamics analysis to predict time and position of thrombus deposition with G&R model, fluid-solid-growth (FSG) model was formulated and used to predict natural history of AAAs.

2 Arterial growth and remodeling

Arterial wall and intraluminal thrombus interact with each other (e.g., ILT introduces increased proteases to the wall and the wall constrains thrombus deformation) and thus they cannot be modeled separately.

G&R of healthy arteries. The growth and remodeling (G&R) model of soft tissues, used herein for the arterial wall, was first proposed by Humphrey and Rajagopal [21]. All the details about implementation into finite element framework and model parameters can be found in Horvat et al. [22]. Briefly, G&R models consider changes in arterial mass due to the turnover (i.e. degradation and deposition) of collagen and smooth muscle (SMC) continuous.

The current mass of each constituent k evolves as

$$M^k(s) = M^k(0)Q^k(0) + \int_0^s \dot{m}^k(\tau) q^k(s-\tau)\mathrm{d}\tau, \tag{1}$$

where k represents specific wall constituent (i.e. elastin, specific direction of collagen and SMC), $q^k(s-\tau)$ is a survival function that defines a percentage of constituent produced at the past time τ that remains at the current time s, with a special case that $Q^k(s) = q^k(s-0)$. Unlike collagen and smooth muscle, elastin is not produced in maturity [21]. Given that $M^k(0)$ is the initial mass of constituent k, note that Eq. (1) is simplified to $M^e(s) = M^e(0)Q^e(s)$ for elastin. Collagen deposition $\dot{m}^k(\tau)$ is a constant at a basal production rate m_B^k during homeostasis (health) but it may be altered in response to deviations in intramural or wall shear stress from respective homeostatic values due to injury, disease, or inflammation. Thus, it can be claimed that

$$\dot{m}^k(\tau) = m_B^k \left(1 + K_\sigma^k \Delta\sigma + K_C^k \Delta\tau_\mathrm{w}\right), \tag{2}$$

where $\Delta\sigma$ and $\Delta\tau_\mathrm{w}$ are deviations of the mural and wall shear stress (WSS) from homeostatic value, and K_σ^k and K_C^k are parameters governing constituent level mural and wall shear stress-driven mass production, respectively.

The calculation of intramural stresses is based on constrained mixture theory and theory of evolving configurations. The constrained theory assumes that each constituent (elastin, collagen, smooth muscle) experiences the same deformation as the mixture (arterial wall), while simultaneously allowing them individual natural, stress-free configurations. This means that any constituent k deposited at a generic G&R time τ is incorporated within the extant extracellular matrix with its own pre-stretch $\mathbf{G}^k(\tau)$. Theory of the evolving configurations states that the total deformation a constituent produced at time τ feels in a current loaded (*in vivo*) mixture configuration at time s, defined by a deformation gradient $\mathbf{F}^k_{n(\tau)}(s)$, depends, thus, on the initial deposition pre-stretch $\mathbf{G}^k(\tau)$ and overall deformation gradient of the mixture ${}^s_\tau\mathbf{F}$ from deposition time τ to current time s (see Fig. 1 in Karšaj and Humphrey [23] for clarification). The associated right Cauchy-Green tensor $\mathbf{C}^k_{n(\tau)}(s)$ is thus $\mathbf{C}^k_{n(\tau)}(s) = \mathbf{F}^k_{n(\tau)}(s)^\mathrm{T}\mathbf{F}^k_{n(\tau)}(s)$ and can be used to calculate the inherent stored-energy for each constituent ($\hat{W}^k$). Isotropic elastin is modelled as neo-Hookean material, while collagen and smooth muscle are modelled using the standard exponential model in tension and no compressive stiffness, as in [21]. Noting that fibers of the same constituent deposited into the extracellular matrix at different times have different associated deformation gradients, the total stored

energy of a constituent is a sum of the unique stored energies of each fiber and their mass fraction, namely

$$W^k(s) = \frac{M^k(0)}{\sum\limits_k M^k(s)} \hat{W}^k Q^k(s) + \int_0^s \frac{\dot{m}^k(\tau)}{\sum\limits_k M^k(s)} \hat{W}^k q^k(s-\tau) \mathrm{d}\tau. \tag{3}$$

The Cauchy stress within the aortic wall can then be calculated as a constrained mixture:

$$\boldsymbol{\sigma} = \frac{2}{\det(\mathbf{F})} \mathbf{F} \frac{\partial W}{\partial \mathbf{C}} \mathbf{F}^{\mathrm{T}} + \sigma^{\mathrm{active}} \boldsymbol{\sigma}_\theta \otimes \boldsymbol{\sigma}_\theta, \tag{4}$$

with $W = \sum\limits_k W^k$ the overall stored energy function, and σ^{active} the active stress contribution from circumferentially oriented smooth muscle contractility.

Illustrative example. When hemodynamic factors, such as blood pressure or flow, are altered, the arterial wall adapts to the new conditions. In order to verify G&R model implementation into a finite element environment but also to illustrate vascular adaptation to perturbations from homeostasis, remodeling of the wall after an abrupt change in flow is presented here. An increase in blood flow causes the widening of arteries, as has been observed clinically both in animal models (e.g., using anastomosis to increase blood flow of rabbits [24]) and in humans [25]. The animal model reported that the time needed for vascular adaptation after an abrupt blood flow increase by 60% was approximately 2 months for rabbits. Interestingly, the increase in diameter of the artery with altered blood flow compared to the diameters of the control arteries was 19%, which reasonably matches the membrane theory which predicts a 17% increase in the arterial diameter. An increase in blood flow in humans is typically caused by exercise, rather than a surgical procedure, making the change less abrupt and measurements more difficult to control. However, the difference in diameter was observed in all arteries between athletes and sedentary subjects, although quantitatively the change varies among arteries (e.g., the difference in diameter of femoral arteries was reported to be 11–17.3%, carotid arteries were only slightly dilated [25]).

Numerically obtained results are presented in Fig. 1. For the first 400 days of the G&R process, hemostasis is preserved, so there is no change in luminal diameter (Fig. 1(a)) or wall thickness (Fig. 1(b)). At the G&R time of 400 days the blood flow was abruptly increased by 20%. The increase in flow led to wall shear stress-induced changes in the production of fibers (see Eq. (2)) and active response of smooth muscle cells. This triggered growth and a remodeling process. Note that if WSS driven production rate (K_C) was zero, the vessel would stay in homeostasis, as an increase in blood flow did not affect intramural stress in the wall, and thus the equilibrium would not be disturbed. Change in the flow initially decreased mass production, which was, in turn, reflected by the thinning of the wall and its expansion. Both thinning and dilatation of the wall induced an increase in wall stresses, and thus also production rate. With the growth of the mass, stresses began to decrease back to the homeostatic value and the new equilibrium was found. Figure 1 also shows that the parameter K_C influences the time needed for the vessel to find a new

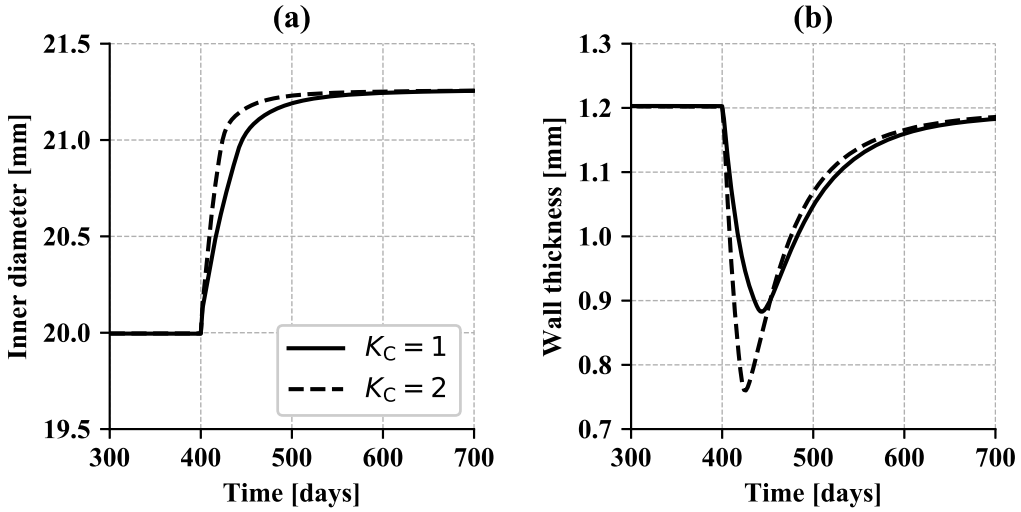

Fig. 1 Evolution of the inner diameter (a), and the wall thickness (b) for different wall shear stress driven production rates (K_C) after a 20% increase in the blood flow.

equilibrium, but it does not change the new equilibrium state, i.e. the final inner radius and thickness. For the larger value of K_C initially lost mass was greater, and, consequently, so were the dilatation and change in wall stresses. This led to a quicker deposition of the new mass, and thus the equilibrium state was reached faster. Depending on the model parameter, the time needed for the vessel to reach a new equilibrium diameter was between 60 and 150 days, which is roughly in accordance with the animal model. For other model parameters and all clarifications, see [22] .

The new equilibrium state after changes in blood flow or pressure, but not the G&R process, can be estimated using a membrane theory approximation. According to membrane theory, when blood flow is 20% above its homeostatic (normal) value, both the inner radius and the thickness should change $1.2^{1/3} = 1.06266$ times compared to the initial, healthy value. Hence, for an aorta with an inner diameter of 20 mm, the terminal inner diameter would amount to 21.25 mm. As can be seen in Fig. 1, the terminal diameter reached the exact same value, whereas thickness was slightly overestimated by the membrane theory approximation. In conclusion, the results obtained by the G&R model show great agreement both with clinical observations and membrane theory.

G&R of diseased arteries. When modeling arteries in disease, the above described G&R model must be slightly adjusted. For example, elastin has a very long half-life in health, estimated to be 40 years. In the illustrative example, the mass of elastin was assumed to be constant, since observed time of several hundred days was relatively short. On the other hand, aneurysms are characterized by lengthy progression (measured in decades) and local irreversible loss of elastin, which must be taken into account. Along with the loss of elastin, programmed death of smooth muscle cells caused by a loss of attachment to the surrounding matrix, including elastin fibers, was also observed in aneurysms. Therefore, the degradation of smooth

muscle should be linked to the degradation of elastin. Additionally, phenotypic transitioning of smooth muscle cells from a contractile to synthetic state causing a decrease in maximal active stress should be considered, similar to Valentín et al. [26].

3 Intraluminal thrombus model

The growth process (i.e. change of mass) in the aortic wall happens internally – fibroblasts and smooth muscle in the wall are responsible for the production of collagen. During the growth of an aneurysm, clinically observed aortic wall thickness does not change significantly, meaning the wall mass typically increases several times compared to a healthy artery because of the expansion. Conversely, a thrombus is continuously being deposited by conversion of the constantly renewed fibrinogen from the blood, with its mass changing significantly – from zero in a healthy artery or small aneurysm to a potentially huge thrombus mass in large AAAs. Although a complete understanding of the spatially evolving deposition of thrombus remains wanting, many medical images of large AAAs suggest that the luminal diameter tends to be maintained, [60]. Thus, while it is convenient to model an aortic wall with a constant number of finite elements and keeping track of changes in its mass, for ILT it is more suitable to increase the number of finite elements at each deposition time, but preserve the mass of each element constant. Within the constant thrombus element mass, it is still possible to monitor the turnover of fibrin and cell apoptosis, and thus change associated mechanical properties. Because thrombus deposition is likely linked to the hemodynamics, i.e. aneurysm geometry, in the G&R model the lumen area was assumed to remain constant. This means that the additional ILT elements were deposited on the inner side of the aneurysm in every time step in which the lesion enlarged sufficiently. Previously deposited portions of the luminal layer were buried and gradually became medial and abluminal layers. Moreover, based on experimental findings [15], fibrin, fibrin degradation products (FDPs), erythrocytes (RBCs), and voids were considered to be the most significant space-filling constituents of a layered ILT. Leukocytes, platelets, and non-collagenous extracellular proteins were neglected as load-bearing constituents but were nevertheless crucial for the biological activity of the thrombus. The model was based on diverse experimental and clinical results reviewed in Wilson et al. [27].

Fibrin. During fibrinogenesis, platelets release thrombin, which helps to convert soluble fibrinogen into fibrin. Fibrin polymerizes to form a cross-linked mesh. Changes in the mass of fibrin depend on its deposition and degradation, similar to changes in wall constituents (see Eq.(2)). Based on experimental findings, it can be assumed that the production rate of fibrin depends on the mass of platelets M_i^{plt} and decreases with increased fibrin density ϕ_i^f through a correlation parameter $K_{plt,\phi}^f$, such that

$$\dot{m}_i^f(\tau) = K_{plt,\phi}^f M_i^{plt}(\tau)\left(1 - \phi_i^f(\tau)\right). \tag{5}$$

On the other hand, fibrinolysis is governed by plasmin. Moreover, since fibrinolysis has been reported to be inversely proportional to the density of the fibrin mesh and its current stretch [28], a mass removal rate-type parameter $K_q^f(\tau)$ used for the survival function

$$q^k(s-\tau) = \exp\left(-\int_\tau^s K_q^f(\tilde{\tau})\mathrm{d}\tilde{\tau}\right) \tag{6}$$

was considered to be

$$K_q^f(\tau) = k_q^f + w_q^f M_i^{pls}(\tau)\frac{1-\phi_i^f(\tau)}{\lambda_i(\tau)}, \tag{7}$$

where k_q^f is a homeostatic value depending on the natural half-life of fibrin, M_i^{pls} is the mass of plasmin, λ_i is fibrin stretch, and w_q^f is a weighting function.

Mechanically, ILT can bear stress and possibly reduce the peak wall stress. Cauchy stress in the ILT was modelled using a stored energy function for an isotropic fibrin mesh based on [15] while a neo-Hookean strain energy function was used for the FDPs.

Cells and Platelets. Several studies reported that blood-derived cells were found mostly in the luminal layer ([29, 30]), presumably because flowing blood can replenish and sustain cells only to a certain depth. Thus, the defined boundary of the luminal layer was a depth beyond which cells could not be replenished, either because a critical fibrin mesh density $\phi_{crit}^{f,RBC}$ was reached or because a critical radius $r_{crit}(\tau)$ was attained. This critical radius was defined in each instant by a critical mass of fibrin M_{crit}^f, such that

$$\sum_{r_l}^{r_{crit}} M^f(r,\tau) = M_{crit}^f, \tag{8}$$

where M_i^f is the mass of fibrin in layer i and r_l is the luminal radius. The quantity of blood-borne cells was assumed to be constant in the luminal layer (e.g. M_l^{plt} for platelets) and decreased with a first-order decay process (with a half-life $\tau_{1/2}^{plt}$ of 7 to 11 days for platelets and $\tau_{1/2}^{RBC} = 120$ days for erythrocytes) in deeper layers. In summary, the mass of platelets (and similarly for leukocytes, primarily neutrophils, M_i^N) was calculated as

$$M_i^{plt}(\tau) = \begin{cases} M_l^{plt}(\tau) & \text{except if} \\ M_l^{plt}(\tau_{crit}^{i,1})\cdot e^{-K_q^{plt}(\tau-\tau_{crit}^{i,1})} & r_i(\tau) \geq r_{crit}(\tau) \\ M_l^{plt}(\tau_{crit}^{i,2})\cdot e^{-K_q^{plt}(\tau-\tau_{crit}^{i,2})} & \phi_j^f(\tau) \geq \phi_{crit}^{f,plt}, \quad \forall j \geq i \end{cases} \tag{9}$$

where $\tau_{crit}^{i,1}$ is the time at which a critical mass of fibrin (i.e., r_{crit}) was achieved, thus transitioning the layer from luminal to medial. Similarly, $\tau_{crit}^{i,2}$ represents the time

at which the limit of the luminal layer was achieved by reaching the critical mass fraction of fibrin (i.e., mesh density). Due to smaller size and number of leukocytes compared to the erythrocytes, their volume was neglected when modeling the total ILT volume; nonetheless, their presence is important for biochemical activity (e.g., production of plasmin, MMPs, or other elastases). The distribution of erythrocytes within the ILT was defined similarly to platelets, with the exception of using a mass fraction instead of the mass, because it is more convenient for calculation of the overall stored energy of ILT.

Plasmin, EDPs, and neovascularization. Conversion of plasminogen to plasmin is a complex process catalyzed by multiple enzymes, including a key step that includes activation either by tissue plasminogen activator (tPA, found on endothelial cells) or urokinase plasminogen activator (uPA, coming mainly from the blood stream via mesenchymal and inflammatory cells). Conversely, activation may be inhibited by plasmin activation inhibitor (PAI-1) and alpha-2 antiplasmin. Noting that not much is known about their distributions, a simplified model was used, capturing the overall increase in activated plasmin phenomenologically. It considered plasmin diffusion from two primary sources: the leukocyte-rich luminal layer of the ILT and the inflamed aneurysmal wall (to which leukocytes invade via the *vasa vasorum*). This increased production of plasmin within the wall is consistent with immunohistological reports [31]. The mass of activated plasmin M_i^{pls} that degrades fibrin is given as

$$M_i^{pls}(\tau) = K_N^{pls} M_i^N(\tau) + \underbrace{M_{wall}^{pls}(\tau) - \sum_{j=1}^{i} K_f^{pls} M_j^f(\tau)}_{\geq 0}, \tag{10}$$

where K_N^{pls} is a correlation factor between plasmin and neutrophils in the thrombus, K_f^{pls} is the amount of plasmin consumed per unit of fibrin, and $M_{wall}^{pls}(\tau)$ is the mass of plasmin in the wall, calculated as $M_{wall}^{pls}(\tau) = K_{EDP}^{pls} M_{tot}^{EDP}(\tau) + K_{VV}^{pls} A_{tot}^{VV}(\tau)$. The plasmin generated within the wall depended largely on the total mass of elastin degradation products M_{tot}^{EDP}, which are chemo-attractants for inflammatory cells and stimulate neovascularization of the wall (i.e., increase the area of *vasa vasorum* A_{tot}^{VV}, [32]). Correlations between plasmin and EDPs/*vasa vasorum* were accounted for by K_{EDP}^{pls} and K_{VV}^{pls} , respectively. The production rate of EDPs directly depended on the amount of elastin degraded per time step, while their degradation was modelled as a first-order decay with a constant half-life. The total mass of EDPs can then be calculated by Eq.(1).

Due to the controversial influence of hypoxia on neovascularisation, it was neglected. Instead, based on studies that showed EDPs alone promote neovascularization [32], the development of *vasa vasorum* was modeled solely as a function of the mass of EDPs, such that

$$A_{tot}^{VV}(s) = A_0^{VV} + \int_0^s K_{EDP}^{VV} M_{tot}^{EDP} \mathrm{d}\tau, \tag{11}$$

where A_0^{VV} is the area of *vasa vasorum* in the healthy aorta, and K_{EDP}^{VV} is a correlation factor that relates *vasa vasorum* growth per unit of EDPs per unit of time.

Fibrin degradation products and voids. The luminal layer contains entrapped erythrocytes, platelets, and other blood-borne molecules within a thick fibrin mesh. Once the luminal layer is buried deeper within the thrombus, erythrocytes cannot be replenished. Likewise, the amount of platelets necessary for fibrin deposition decreases steeply, thus allowing degradation to outpace deposition. Dissolution of fibrin and apoptosis of red blood cells can leave small interconnected channels ("voids" or "canaliculi") throughout the ILT [30]. Degrading fibrin was assumed to convert partly into fibrin degradation products (FDPs) and partly into canaliculi (as fibrin was removed by macrophages) in a 7:3 ratio.

Biochemical interaction of ILT and aneurysmal wall. An increase in proteolytical activity due to the presence of the ILT was integrated via additional terms in the mass removal rate-type parameter K_q^k in survival function. For example, the elastin in normally aging aorta depends solely on its natural half-life $\tau_{1/2}^e$ on the order of forty to fifty years: $K_q^e(\tau) = k_q^e = \ln 2/\tau_{1/2}^e$. Increased degradation of elastin in an aneurysm due to inflammation was incorporated via an additional term,

$$K_q^e(\tau) = k_q^e + w_{q,elas}^e M^{elas}(r,\tau) \tag{12}$$

where amount of elastases, M^{elas}, were modulated by a weighting factor $w_{q,elas}^e$. Correspondingly for collagen, we write (cf. [23])

$$K_q^c(\tau) = \frac{\partial W^c/\partial \mathbf{F}^c_{n(\tau)}}{\partial W^c/\partial \mathbf{F}^c_{n(0)}} k_q^c + w_{q,MMP}^c M^{MMP}(r,\tau), \tag{13}$$

where the collagen mass removal parameter K_q^c depends on the ratio of the current $\partial W^c/\partial \mathbf{F}^c_{n(\tau)}$ to the homeostatic $\partial W^c/\partial \mathbf{F}^c_{n(0)}$ tension, and k_q^c is the rate-type removal parameter associated with homeostatic half-life; the second terms relates to the distribution of active MMPs (i.e. collagenases).

Similar to plasmin, MMPs may arise from two sources: the luminal layer in ILT or the *vasa vasorum* in the aortic wall. A first approximation, quasi-static transport, was determined easily from the diffusion equation, $\partial M^{elas}/\partial t = \nabla \cdot \left[D \nabla M^{elas}\right]$, where D is the diffusion coefficient that can be estimated based on available data of the radial distribution of proteases [16, 29]. The available elastase/MMPs from the luminal layer was defined as $K_N^{elas} M_{tot}^N$ (or $K_N^{MMP} M_{tot}^N$ for MMPs), where $K_N^{elas/MMP}$ described how much elastase/MMP was produced per unit of leukocytes per time step, at a point at radius r_L which was defined as

$$r_L(s) = \frac{1}{M_{tot}^N(s)} \sum_i M_i^N(s) r_i(s), \tag{14}$$

similar to a center of mass. The concentration of elastase/MMPs available at the outer radius depended on the area of *vasa vasorum* and the number of inflammatory cells: $K_{WBC}^{elas} M_{tot}^{WBC}(s) + K_{VV}^{elas} A_{tot}^{VV}(s)$. Thus, by solving the diffusion equation, the

overall distribution of proteases was:

$$M^k(r,s) = \frac{K_N^k M_{tot}^N(s) - K_{WBC}^k M_{tot}^{WBC}(s) - K_{VV}^k A_{tot}^{VV}(s)}{\ln(r_L(s)/r_o)} \ln\frac{r(s)}{r_o} + K_N^k M_{tot}^N(s), \quad (15)$$

where k indicates elastases or collagenases. Mass of inflammatory cells in the wall, M_{tot}^{WBC}, was modelled similar to Eq.(1) with degradation depending on the cellular half-life, and production $\dot{m}_{tot}^{WBC}$ increasing with the growth of EPD mass and *vasa vasorum*, such that

$$\dot{m}_{tot}^{WBC}(\tau) = K_{EDP,VV}^{WBC} \left(\frac{A_{tot}^{VV}(\tau)}{A_0^{VV}}\right)^{\alpha} M_{tot}^{EDP}(\tau), \quad (16)$$

where $K_{EDP,VV}^{WBC}$ is a correlation factor that relates the proliferation of white blood cells with EDPs and neovascularisation, and α is a power parameter. Schematic presentation of the whole ILT/wall interaction model is presented by Fig. 2 in [21].

Model predictions – biochemical influence of ILT. The full potential of the described ILT model is presented in [21, 33]. Very briefly, Fig. 2(a) shows predicted distributions of mass fractions of constituents within the ILT. The boundary between the luminal and medial layer is evident by the steep decrease in fibrin and RBCs, as cells could not penetrate further into the thrombus. Similarly, platelets were unable to reach deeper parts of the ILT, disenabling fibrin production. Consequently, with fibrin degradation exceeding its production, the mass fraction of fibrin decreased. The ILT that is deposited the latest is next to the blood flow (i.e., near a radius of 10 mm) and is characterized by low amounts of fibrin and large numbers of RBCs. In the older, buried parts of the luminal layer, fibrin fraction increased and RBCs diminished. Unlike the distinctive luminal layer, the border between intermediate and abluminal layers was less evident; both were characterized by disruption of fibrin mesh and devoid of blood cells and platelets. These results correspond qualitatively to the reported distribution of constituents from histological analysis from Tong et al. [15], where four phases of thrombus aging were defined as: phase I (fresh thrombus, new luminal layer in the model) characterized by 90% RBCs and 10% thin fibrin bundles; phase II (matches older luminal layer) with less than 10% RBCs, some condensed proteins (FDPs), and increasing thin and thick fibrin fibers; phases III and IV (i.e., older thrombus) with degraded fibrin.

It can be seen from Fig. 2(a) that the thickness of the luminal layer is approximately 2 mm, which is in accordance with clinical observations [13, 15]. This is not a predefined value, as luminal layer thickness, or depth to which platelets and blood cells penetrate through the fibrin mesh, is defined by (9). For quickly expanding aneurysms luminal layer thickness increases, because fibrin production is slow compared to aneurysm expansion. Likewise, for slow expanding or stabilized aneurysm, the luminal layer becomes thinner. During a non-linearly expanding aneurysm, luminal layer thickness varies in time.

The evolution of total normalized metalloproteinases describing proteolytical activity in the underlying wall is highlighted in Fig. 2(b). In the early years, when

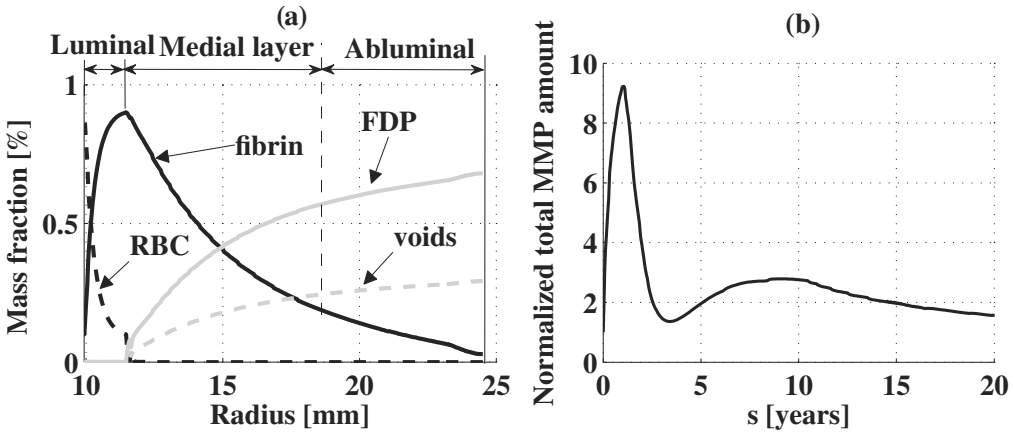

Fig. 2 Predicted radial distribution of mass fractions of structurally important constituents 20 years after aneurysm initialization. The solid black line represents fibrin, the dashed black line red blood cells, the gray solid line voids (canaliculi), and the gray dashed line fibrin degradation products (FDPs) (a), the evolution of the normalized amount of matrix metalloproteinases (MMPs) in the aortic wall (b).

ILT is thin, the amount of MMPs within the adjacent wall increased very steeply. At the instant when the blood cells and molecules are unable to reach the oldest ILT layer, it becomes much less proteolytically active medial layer and acts as a barrier for diffusion of proteases. Consequently, the MMP activity sharply decreased after formation of medial layer. Twenty years after aneurysm initialization, the MMP count was reduced ~4 fold relative to the peak value, but was still higher than the initial value. This happened due to increased inflammation in the wall itself, due to *vasa vasorum* and chemotactic EDPs.

Model predictions – biomechanical influence of ILT. As noted above, many medical images of large AAAs suggest that the luminal area tends to be maintained at the constant value (e.g. see Fig. 9 in [34]), either equal or greater than healthy value. The choice of the new luminal diameter is also an important factor for aneurysm progression and stabilization. Figure 3 shows evolutions of thrombus-laden aneurysms with different lumen areas compared to AAA without thrombus. Full black dots in Fig. 3(a) denote the moment of the first ILT deposition. While AAA without thrombus continued to grow exponentially (and ruptured), radius to which ILT was constantly filled determined whether AAA will stabilize, how long the stabilization will take and how much will the AAA further expand. In case of fully thrombosed aneurysms (square marker), i.e. if lumen area was kept constant at a healthy value (with lumen radius of 10 mm), the dilatation stabilized at the diameter of 25 mm, which is not considered an aneurysm. When lumen area was kept constant at a larger values, both time necessary for AAA stabilization and further AAA growth increased. Note that likelihood of stabilization decreased with increased lumen radius.

Model predictions – influence of rupture risk factors. The model was further used to investigate the influence of rupture risk factors (smoking, age, sex, hypertension) and stabilization factors on AAA growth [33]. The focus here is on smoking and MMP inhibition. Smoking is known to elevate oxidative stress, and thus injure the

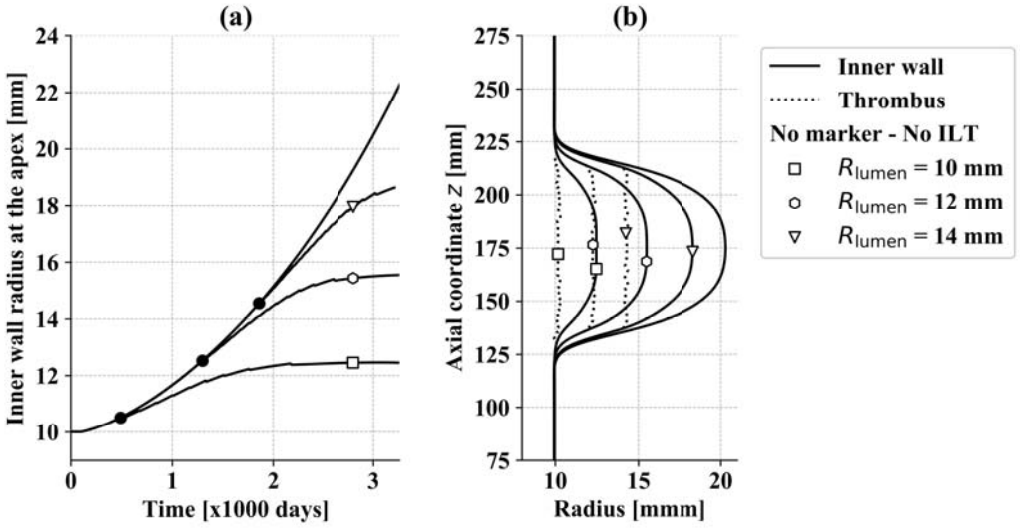

Fig. 3 Evolution of inner AAA radius (a), contours of ILT/wall interface and luminal area (b) for different luminal areas of thrombus deposition

arterial endothelium and promote atherogenesis [35]. Furthermore, it also increases inflammation in the vascular wall [36] as well as the concentration of fibrinogen in plasma and alters the activity of platelets. Raised platelet activity and increased fibrinogen potentiate thrombosis along the dysfunctional endothelium [36]. Finally, it correlates strongly with increased aortic blood pressure, heart rate, and arterial stiffness [37]. Smoking-induced arterial stiffening is suggested to be isotropic, as reflected by a consistent increase in both elastin- and collagen-associated parameters [38].

All these cardiovascular detriments, that smoking introduces in health, negatively influence the propagation of diseases. Thus, smoking is associated with both larger AAAs [6, 39] and expansion rates [40]. Cessation of smoking does not help instantly with lowering AAA expansion rate: it has been shown that two years after cessation of smoking arterial stiffness was not reduced [41] and that it can take up to a decade for the stiffness to return to the level of never-smokers [42]. Lowering inflammation rates also likely takes years, as it was estimated five years of abstinence are necessary to reduce fibrinogen concentrations to the range of never-smokers [43].

Based on these studies, smoking was modeled by increased elastin stiffness, inflammation, and platelet activity. Some other aspects smoking introduces to vascular health, such as endothelial and smooth muscle cell dysfunction, are also characteristics of aneurysms independent of smoking and were implicitly included in the model for smokers and non-smokers alike. All other G&R parameters were identical among the groups.

Figure 4(a) shows numerically predicted 20-year-growth of non-smoker and smoker. Predicted maximal AAA diameter was greater for smokers (5.39 cm) than non-smokers (4.40 cm). The average increase in dilatation rate due to smoking can easily be calculated as 0.0495 cm/year. This shows a great agreement with clinical observations, as reported expansion rate increase associated with smoking was

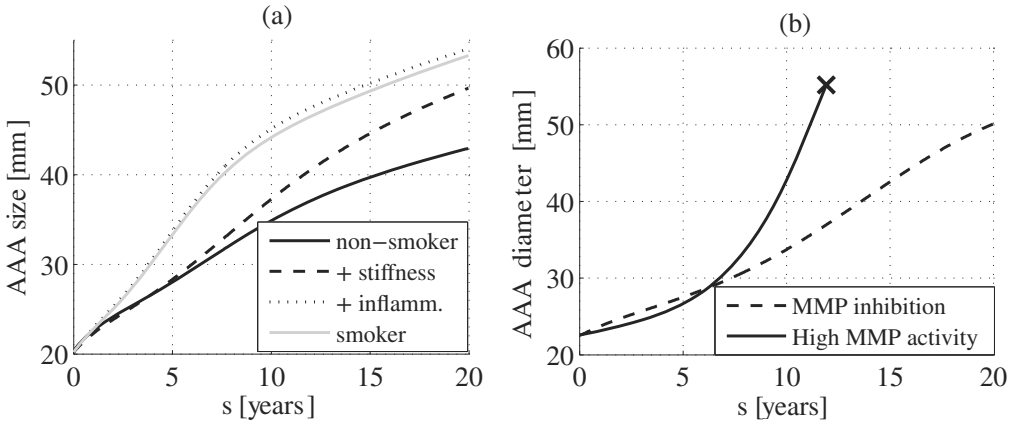

Fig. 4 Simulated evolution of an AAA in a non-smoker (solid line), in cases of increased stiffness (dash line), increased stiffness plus elevated inflammation (dotted line), and increased stiffness, higher inflammation, and increased platelet activity (gray line) – that is, full effects of smoking (a), simulated AAA evolution in cases of rapid versus slow collagen degradation (b). Rupture is denoted by "×".

0.05 ± 0.01 cm/year [39]. In order to determine which of the smoking-induced alterations introduces rupture risk the most, changes were simulated gradually: first only influence of an increase in stiffness was simulated, then increase in both stiffness and inflammation and finally also platelet activity (i.e. smoker). The results suggest that inflammation played the greatest role in early aneurysmal progression, although increased stiffness also significantly increases the growth rate (Fig. 4(a). Fibrinogen concentration and platelet activity (present in the smoker group) did not have a major influence on AAA evolution (dotted vs. dashed line). Interestingly, the high activity of platelets resulted in slightly decreased AAA size, because increased production of fibrin resulted in a slightly stiffer, thinner luminal layer. This influences AAA growth positively because a stiffer luminal layer reduces the peak wall stress more, whereas a thinner luminal layer means it will be distanced from the arterial wall earlier. Note that this does not mean that an increased platelet activity could potentially stabilize AAAs since lower wall stress means collagen production is decreased with lower deviation from homeostatic stress value (refer to (1)). Additionally, platelets are chemotactic for neutrophils and monocytes [44] and can cause higher inflammation and expansion rates.

Model predictions – influence of stabilization factors. Although there is no cure for aneurysm, some studies have proposed the use of anti-inflammatory drugs for the reduction or arrest of the AAA enlargement. Some of the proposed drugs act directly on MMPs [45, 46] and others reduce extracellular matrix degradation indirectly, e.g. via platelet inhibitors [47] or immunosuppressive agents [48]. The hypothesis was investigated on animal models: a study on mice showed that preservation of medial elastin can lessen aneurysmal dilatation [45] while another study showed that non-specific inhibition of collagenases can lead to lesion stabilization [46]. Unfortunately, non-specific MMP inhibition has not reduced aneurysmal progression in human patients [49]. There is clearly a need for an increased understanding of the biochemical mechanisms of aneurysm formation and evolution.

Figure 4(b) shows that the thrombus-laden aneurysm model supports results from animal models, with attenuation of collagenase activity (i.e., decreasing the parameter describing collagen degradation by MMPs $w^c_{q,MMP}$ in Eq.(13)) helped to decrease the likelihood of rupture. However, the results also agree with the study showing the failure of drug effects in humans, as after 20 years of disease progression the maximum diameter was 5 cm, at which point surgical treatment would be recommended. Thus, the current results suggest that rates of degradation of both collagen and elastin (results not shown here) may strongly influence aneurysmal evolution. The model suggests that high rates of collagen degradation lead to progressive enlargement, and reduced inflammation could perhaps prevent rupture, although the reduction of inflammation alone might not suffice.

4 Fluid-solid-growth

Hemodynamic changes are undoubtedly an important factor in the progression of arterial lesions. As discussed in previous sections, they can be sensed by vascular cells and cause the arterial wall to adapt. For example, hemodynamics is believed to play a crucial role in intracranial aneurysm (IA) evolution and thus hemodynamical analyses, such as computational fluid dynamics (CFD) and fluid-structure-interaction (FSI) simulations, of IAs are much more common than G&R studies. Note that CFD assumes the wall to be rigid and does not consider the influence of deformation and movement of the aortic wall on the hemodynamic output, whereas FSI considers the compliance of the wall and, as a result, provides a more accurate description of hemodynamics [50, 51], but is computationally much more expensive. Furthermore, considering ILT formation and deposition are likely dependent on hemodynamics, the logical new phase in numerical modeling is combining the hemodynamics analysis with modeling of G&R of the wall. This loose coupling of CFD or FSI models over a cardiac cycle (time scale in milliseconds) with long-term G&R models of the evolving wall (time scale in days) is referred as fluid-solid-growth (FSG) model. The concept of the FSG framework was first proposed by Humphrey & Taylor in 2008 [52], and implemented by Figueroa et al. [53] on a basilar artery the following year. There were very few attempts applying the FSG model to IAs ([54, 55]) and AAAs ([56]), but all neglecting thrombus. Currently, there are no studies that applied the FSG framework to model AD.

In addition to using hemodynamic analysis as an input for calculation of collagen production rate, it can also be used as an indicator of when, where, and how much thrombus will be deposited. The general framework is shown in Fig. 5: long-term G&R model runs until maximal luminal diameter increases sufficiently (e.g. 1 mm). At that time G&R analysis is interrupted, luminal surface for CFD simulation is generated, and hemodynamic analysis over several cardiac cycles is performed. If predefined conditions for thrombus deposition are not met (e.g. time averaged wall shear stress (TAWSS) did not decrease below the threshold value), G&R continues without adjustments. However, when requirements are fulfilled, new thrombus finite

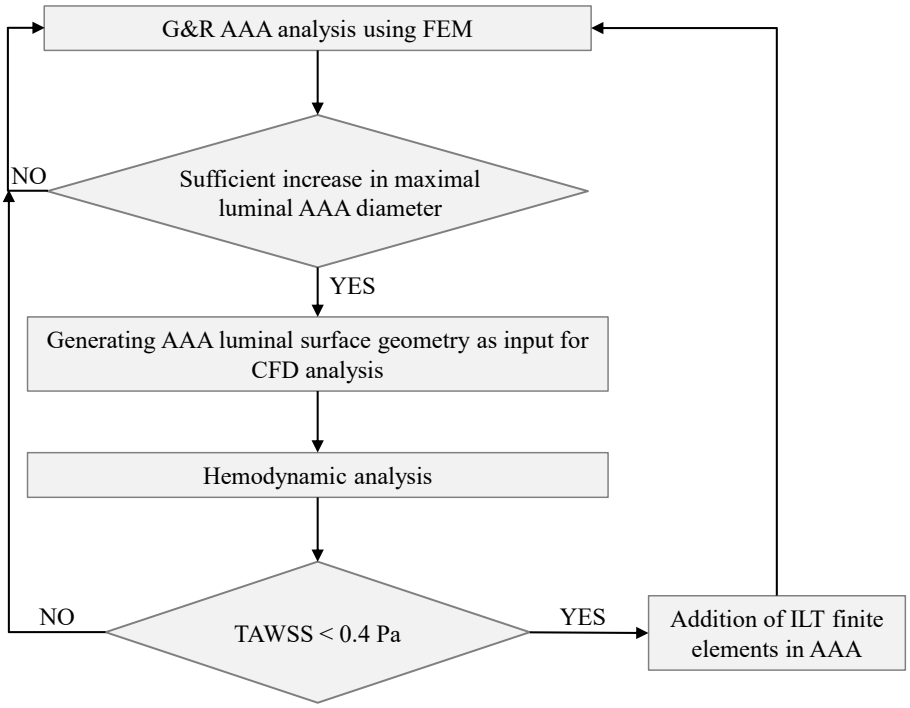

Fig. 5 Schematic representation of FSG model used in this work.

elements are added to the aneurysm finite element model at the location defined by hemodynamic analysis. Interestingly, with lower defined threshold values of TAWSS that defines the thrombus deposition, not only the lumen area dilates more, but the deposition becomes more asymmetrical (Fig. 6(a)). This asymmetrical deposition consequently leads to a reduced AAA expansion of the shielded distal part of the aneurysmal sac and apex is no longer at the middle surface but shifts upward. This effect can be seen in Fig. 6(b): the first thrombus was deposited at the AAA diameter of 30 mm, up to which point a clear symmetry of inner wall radius over axial coordinate $z = 175$ mm can be seen. With ILT deposition, the maximum diameter shifts to coordinate $z = 185$ mm. Moreover, with delayed ILT deposition at the proximal part of the aneurysm, the area covered by thin, proteolytically active ILT is increased. In the results shown here, the biochemical influence of ILT was neglected; however additional expansion of the proximal side and further deformation of the aneurysm sac can be expected due to increased degradation of the underlying wall.

Figure 6(a) also shows that thrombus reduces not only radial but also axial growth. A possible explanation for this is that in AAA without thrombus, blood pressure stretches the aneurysm apex a lot, which results in high axial stresses. The formation of thrombus changes pressure distribution and significantly reduces axial tensile force at the apex. Interestingly, according to a machine learning model of rupture prediction presented by Shum et al. [57], the length of the aneurysmal sac is the most important feature.

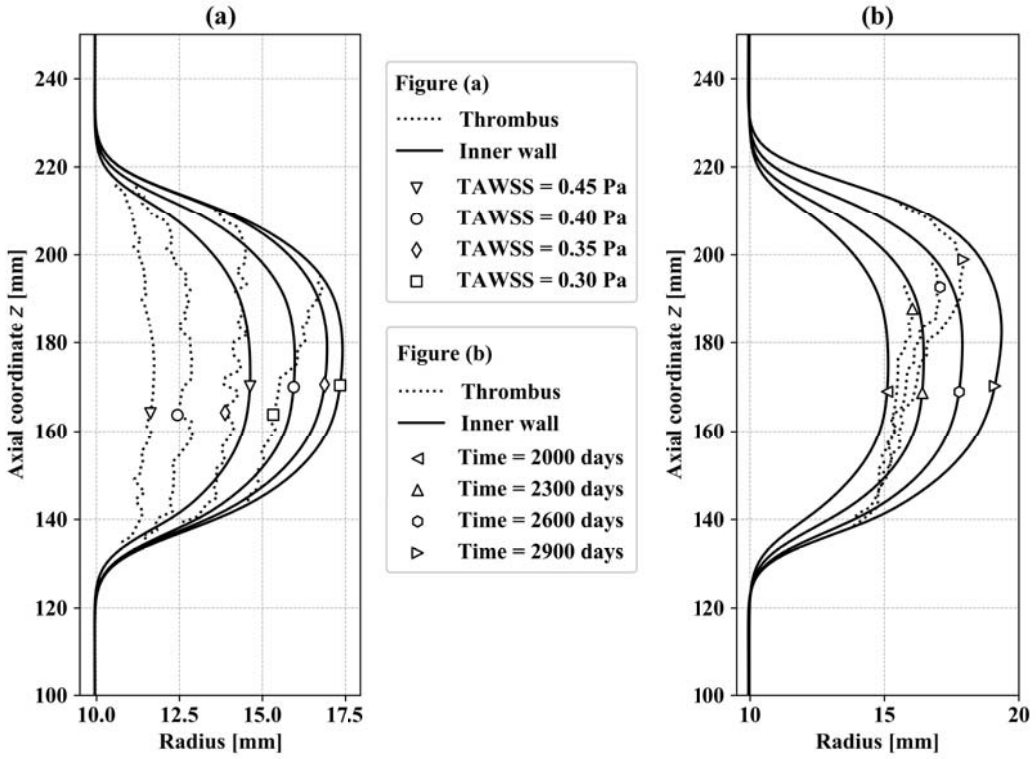

Fig. 6 Contours of ILT/wall interface radius (full lines) and luminal radius (dotted lines) at the same G&R time (2500 days) for different threshold values of TAWSS (a), and contours at different times during evolutions of AAA when threshold value is 0.3 Pa (b)

5 Conclusions

Intraluminal thrombus has a very complex, controversial, and unclear role in the progression of cardiovascular diseases. Because many clinical and experimental studies resulted in conflicting conclusions, ILT presence is usually perceived negatively; however, it might be a natural protection against the rapid expansion of the vascular lesion. The numerical G&R and FSG modeling could be very useful tools for the investigation of bio-chemo-mechanical processes introduced by thrombus deposition, the guidance of experiments, and recommendation of more accurate rupture risk factors or better treatments. However, intraluminal thrombus should not be neglected in the models, as it has a fundamental influence on disease evolution. For example, during follow-up imaging of AAAs, it was observed that radial enlargement of aneurysm often occurs via stepwise dilatations, with periods of stability alternating with periods of enlargement [58]. Prior G&R models of aortic aneurysms that were considering only aortic wall (e.g., [19, 20]) did not manage to capture this effect. When the influence of ILT is taken into account, it was possible to model the first stagnation on a simplified geometry (see [21] for details).

The growth and remodeling model of intraluminal thrombus presented in this chapter is partially based on *in vitro* experiments that are true for any blood clot (e.g. information about fibrinogenesis and fibrinolysis), and partially on ILT within AAAs,

as histological and mechanical data available in the literature were needed for the development of the model. Before applying the model to some other vascular lesion, minor adjustments and assumptions would probably be necessary. For example, MMPs from the thrombus in false lumen of aortic dissection would likely diffuse in two directions, both to intima and media-adventitia.

On a positive note, the model shows a great agreement with clinical observations and animal models. An increase in smoking induced expansion rates was calculated to be ~0.050 cm/year, and hypertension increased expansion ~0.022 cm/year per 10 mmHg, both of which are clinically observed [39]. The model confirms and offers additional support to the female gender, smoking, and hypertension being factors that increase rupture-risk. Additionally, it also supports animal models in the claim that inhibition of inflammation, both elastin- and collagen-based, decreases growth rate, but at the same time agrees with the trial on humans that the inflammation inhibition might not hinder AAA growth sufficiently for the surgery to be avoided.

In addition to confirming already accepted hypotheses, the model also brought in some new insights into bio-chemo-mechanical processes within AAA. It can explain why thin thrombus contributes to rapid expansion, whereas thick ILT decreases dilatation rate [4], despite ILT thickness being proposed to be a rupture risk factor [59]. Several hypotheses can be formulated from the numerical results, e.g. that ILT likely causes stepwise growth of AAAs or that thrombus indirectly slows down radial growth by prevention of axial expansion.

In conclusion, careful consideration of the mechanical, chemical, and biological influences of proteolytically active, multi-layered intraluminal thrombus on vascular lesions is advised and necessary for maximization of the potential of numerical models to increase our understanding of cardiovascular diseases and to identify rupture-risk and stabilization factors.

References

1. Tsai TT, Evangelista A, Nienaber CA, et al (2007) Partial thrombosis of the false lumen in patients with acute type B aortic dissection. N Engl J Med **357**, 349–359
2. Frösen J, Piippo A, Paetau A, Kangasniemi M, Niemelä M, Hernesniemi J, Jääskeläinen J (2004) Remodeling of saccular cerebral artery aneurysm wall is associated with rupture: Histological analysis of 24 unruptured and 42 ruptured cases. Stroke **35**, 2287–2293
3. Paliwal N, Damiano RJ, Davies JM, Siddiqui AH, Meng H (2017) Association between hemodynamic modifications and clinical outcome of intracranial aneurysms treated using flow diverters. Proc SPIE Int Soc Opt Eng. https://doi.org/10.1002/nbm.3369.Three
4. Domonkos A, Staffa R, Kubíček L (2019) Effect of intraluminal thrombus on growth rate of abdominal aortic aneurysms. Int Angiol **38**, 39–45
5. Simão Da Silva E, Rodrigues AJ, Magalhães Castro De Tolosa E, Rodrigues CJ, Villas Boas Do Prado G, Nakamoto JC (2000) Morphology and diameter of infrarenal aortic aneurysms: A prospective autopsy study. Cardiovasc Surg **8**, 526–532
6. Behr-Rasmussen C, Grondal N, Bramsen MB, Thomsen MD, Lindholt JS (2014) Mural thrombus and the progression of abdominal aortic aneurysms: A large population-based prospective cohort study. Eur J Vasc Endovasc Surg **48**, 301–307

7. Di Achille P, Tellides G, Figueroa CA, Humphrey JD (2014) A haemodynamic predictor of intraluminal thrombus formation in abdominal aortic aneurysms. Proc R Soc A Math Phys Eng Sci **470**, 20140163–20140163
8. Shadden SC, Hendabadi S (2013) Potential fluid mechanic pathways of platelet activation. Biomech Model Mechanobiol **12**, 467–474
9. Di Achille P, Tellides G, Humphrey JD (2017) Hemodynamics-driven deposition of intraluminal thrombus in abdominal aortic aneurysms. Int j numer method biomed eng **33**, 1–17
10. Naim WNWA, Ganesan PB, Sun Z, Liew YM, Qian Y, Lee CJ, Jansen S, Hashim SA, Lim E (2016) Prediction of thrombus formation using vortical structures presentation in Stanford type B aortic dissection: A preliminary study using CFD approach. Appl Math Model **40**, 3115–3127
11. Schriefl AJ, Collins MJ, Pierce DM, Holzapfel GA, Niklason LE, Humphrey JD (2012) Remodeling of intramural thrombus and collagen in an Ang-II infusion ApoE-/-model of dissecting aortic aneurysms. Thromb Res **130**, e139–e146
12. Karšaj I, Humphrey JD (2009) A mathematical model of evolving mechanical properties of intraluminal thrombus. Biorheology. https://doi.org/10.3233/BIR-2009-0556
13. Vande Geest JP, Sacks MS, Vorp DA (2006) A planar biaxial constitutive relation for the luminal layer of intra-luminal thrombus in abdominal aortic aneurysms. J Biomech **39**, 2347–2354
14. Houard X, Rouzet F, Touat Z, et al (2007) Topology of the fibrinolytic system within the mural thrombus of human abdominal aortic aneurysms. J Pathol **212**, 20–28
15. Tong J, Cohnert T, Regitnig P, Holzapfel GA (2011) Effects of age on the elastic properties of the intraluminal thrombus and the thrombus-covered wall in abdominal aortic aneurysms: Biaxial extension behaviour and material modelling. Eur J Vasc Endovasc Surg. https://doi.org/10.1016/j.ejvs.2011.02.017
16. Fontaine V, Touat Z, Mtairag EM, et al (2004) Role of leukocyte elastase in preventing cellular re-colonization of the mural thrombus. Am J Pathol **164**, 2077–87
17. Inzoli F, Boschettp F, Zappa M, Longo T, Fumero R (1993) Biomechanical Factors in Abdominal Aortic Aneurysm Rupture. Eur J Vasc Surg **7**, 667–674
18. Wang DHJ, Makaroun MS, Webster MW, Vorp DA (2002) Effect of intraluminal thrombus on wall stress in patient-specific models of abdominal aortic aneurysm. J Vasc Surg **36**, 598–604
19. Watton PN, Hill NA (2009) Evolving mechanical properties of a model of abdominal aortic aneurysm. Biomech Model Mechanobiol **8**, 25–42
20. Wilson JS, Baek S, Humphrey JD (2012) Importance of initial aortic properties on the evolving regional anisotropy, stiffness and wall thickness of human abdominal aortic aneurysms. J R Soc Interface **9**, 2047–2058
21. Virag L, Wilson JS, Humphrey JD, Karšaj I (2015) A Computational Model of Biochemomechanical Effects of Intraluminal Thrombus on the Enlargement of Abdominal Aortic Aneurysms. Ann Biomed Eng. https://doi.org/10.1007/s10439-015-1354-z
22. Horvat N, Virag L, Holzapfel GA, Sorić J, Karšaj I (2019) A finite element implementation of a growth and remodeling model for soft biological tissues: Verification and application to abdominal aortic aneurysms. Comput Methods Appl Mech Eng **352**, 586–605
23. Karšaj I, Humphrey JD (2012) A multilayered wall model of arterial growth and remodeling. Mech Mater **44**, 110–119
24. Brownlee RD, Langille BL (1991) Arterial adaptations to altered blood flow. Can J Physiol Pharmacol **69**, 978–983
25. Fridez P, Zulliger M, Bobard F, Montorzi G, Miyazaki H, Hayashi K, Stergiopulos N (2003) Geometrical, functional, and histomorphometric adaptation of rat carotid artery in induced hypertension. J Biomech **36**, 671–680
26. Valentín A, Humphrey JD, Holzapfel GA (2011) A multi-layered computational model of coupled elastin degradation, vasoactive dysfunction, and collagenous stiffening in aortic aging. Ann Biomed Eng **39**, 2027–2045
27. Wilson JS, Virag L, Di Achille P, Karšaj I, Humphrey JD (2013) Biochemomechanics of Intraluminal Thrombus in Abdominal Aortic Aneurysms. J Biomech Eng **135**, 021011
28. Scott DJA, Prasad P, Philippou H, et al (2011) Clot architecture is altered in abdominal aortic aneurysms and correlates with aneurysm size. Arterioscler Thromb Vasc Biol **31**, 3004–10

29. Houard X, Touat Z, Ollivier V, Louedec L, Philippe M, Sebbag U, Meilhac O, Rossignol P, Michel JB (2009) Mediators of neutrophil recruitment in human abdominal aortic aneurysms. Cardiovasc Res **82**, 532–541
30. Adolph R, Vorp DA, Steed DL, Webster MW, Kameneva M V, Watkins SC (1997) Cellular content and permeability of intraluminal thrombus in abdominal aortic aneurysm. J Vasc Surg **25**, 916–26
31. Fontaine V, Jacob MP, Houard X, Rossignol P, Plissonnier D, Angles-Cano E, Michel JB (2002) Involvement of the mural thrombus as a site of protease release and activation in human aortic aneurysms. Am J Pathol **161**, 1701–1710
32. Nackman GB, Karkowski FJ, Halpern VJ, Gaetz HP, Tilson MD (1997) Elastin degradation products induce adventitial angiogenesis in the Anidjar/Dobrin rat aneurysm model. Surgery **122**, 39–44
33. Virag L, Wilson JS, Humphrey JD, Karšaj I (2017) Potential biomechanical roles of risk factors in the evolution of thrombus-laden abdominal aortic aneurysms. Int j numer method biomed eng **33**, e2893
34. Zambrano BA, Gharahi H, Lim CY, Jaberi FA, Choi J, Lee W, Baek S (2016) Association of Intraluminal Thrombus, Hemodynamic Forces, and Abdominal Aortic Aneurysm Expansion Using Longitudinal CT Images. Ann Biomed Eng **44**, 1502–1514
35. Burke A, FitzGerald GA (2003) Oxidative stress and smoking-induced vascular injury. Prog Cardiovasc Dis **46**, 79–90
36. Powell JT (1998) Vascular damage from smoking: disease mechanisms at the arterial wall. Vasc Med **3**, 21–28
37. Mahmud A, Feely J (2003) Effect of smoking on arterial stiffness and pulse pressure amplification. Hypertension **41**, 183–187
38. Enevoldsen MS, Henneberg KA, Jensen JA, Lönn L, Humphrey JD (2011) New interpretation of arterial stiffening due to cigarette smoking using a structurally motivated constitutive model. J Biomech **44**, 1209–1211
39. Bhak RH, Wininger M, Johnson GR, Lederle FA, Messina LM, Ballard DJ, Wilson SE (2015) Factors associated with small abdominal aortic aneurysm expansion rate. JAMA Surg **150**, 44–50
40. Al-Barjas HS, Ariëns R, Grant P, Scott JA (2006) Raised plasma fibrinogen concentration in patients with abdominal aortic aneurysm. Angiology **57**, 607–614
41. van den Berkmortel FWPJ, Wollersheim H, van Langen H, Smilde TJ, den Arend J, Thien T (2004) Two years of smoking cessation does not reduce arterial wall thickness and stiffness. Neth J Med **62**, 235–241
42. Jatoi NA, Jerrard-Dunne P, Feely J, Mahmud A (2007) Impact of smoking and smoking cessation on arterial stiffness and aortic wave reflection in hypertension. Hypertension **49**, 981–985
43. Meade TW, Imeson J, Stirling Y (1987) Effects of changes in smoking and other characteristics on clotting factors and the risk of ischaemic heart disease. Lancet **330**, 986–988
44. Deuel TF, Senior RM, Chang D, Griffint GL, Heinrikson RL, Kaiser ET (1981) Platelet factor 4 is chemotactic for neutrophils and monocytes. Proc Natl Acad Sci **78**, 4584–4687
45. Parodi FE, Mao D, Ennis TL, Bartoli MA, Thompson RW (2005) Suppression of experimental abdominal aortic aneurysms in mice by treatment with pyrrolidine dithiocarbamate, an antioxidant inhibitor of nuclear factor-kB. J Vasc Surg **41**, 479–489
46. Steinmetz EF, Buckley C, Shames ML, Ennis TL, Vanvickle-Chavez SJ, Mao D, Goeddel LA, Hawkins CJ, Thompson RW (2005) Treatment with simvastatin suppresses the development of experimental abdominal aortic aneurysms in normal and hypercholesterolemic mice. Ann Surg **241**, 92–101
47. Owens AP, Edwards TL, Antoniak S, et al (2015) Platelet inhibitors reduce rupture in a mouse model of established abdominal aortic aneurysm. Arterioscler Thromb Vasc Biol **35**, 2032–2041
48. Lawrence DM, Singh RS, Franklin DP, Carey DJ, Elmore JR (2004) Rapamycin suppresses experimental aortic aneurysm growth. J Vasc Surg **40**, 334–338

49. Arnoud Meijer C, Stijnen T, Wasser MNJM, Hamming JF, Van Bockel JH, Lindeman JHN (2013) Doxycycline for stabilization of abdominal aortic aneurysms: A randomized trial. Ann Intern Med **159**, 815–823
50. Caballero AD, Laín S (2013) A Review on Computational Fluid Dynamics Modelling in Human Thoracic Aorta. Cardiovasc Eng Technol **4**, 103–130
51. Alimohammadi M, Agu O, Balabani S, Díaz-Zuccarini V (2014) Development of a patient-specific simulation tool to analyse aortic dissections: Assessment of mixed patient-specific flow and pressure boundary conditions. Med Eng Phys **36**, 275–284
52. Humphrey JD, Taylor CA (2008) Intracranial and Abdominal Aortic Aneurysms: Similarities, Differences, and Need for a New Class of Computational Models. Annu Rev Biomed Eng **10**, 221–246
53. Figueroa CA, Baek S, Taylor CA, Humphrey JD (2009) A Computational Framework for Fluid-Solid-Growth Modeling in Cardiovascular Simulations. Comput Methods Appl Mech Eng **198**, 3583–3602
54. Watton PN, Selimovic A, Raberger NB, Huang P, Holzapfel GA, Ventikos Y (2011) Modelling evolution and the evolving mechanical environment of saccular cerebral aneurysms. Biomech Model Mechanobiol **10**, 109–132
55. Selimovic A, Ventikos Y, Watton PN (2013) Modelling the evolution of cerebral aneurysms: Biomechanics, mechanobiology and multiscale modelling. Procedia IUTAM **10**, 396–409
56. Grytsan A, Watton PN, Holzapfel GA (2015) A Thick-Walled Fluid-Solid-Growth Model of Abdominal Aortic Aneurysm Evolution: Application to a Patient-Specific Geometry. J Biomech Eng **137**, 031008
57. Shum J, Martufi G, Di Martino E, Washington CB, Grisafi J, Muluk SC, Finol EA (2011) Quantitative assessment of abdominal aortic aneurysm geometry. Ann Biomed Eng **39**, 277–286
58. Kurvers H, Veith FJ, Lipsitz EC, et al (2004) Discontinuous, staccato growth of abdominal aortic aneurysms. J Am Coll Surg **199**, 709–15
59. Vorp DA, Lee PC, Wang DHJ, Makaroun MS, Nemoto EM, Ogawa S, Webster MW (2001) Association of intraluminal thrombus in abdominal aortic aneurysm with local hypoxia and wall weakening. J Vasc Surg **34**, 291–299
60. Zambrano BA, Gharahi H, Lim CY, Jaberi FA, Choi J, Lee W, Baek S (2016) Association of Intraluminal Thrombus, Hemodynamic Forces, and Abdominal Aortic Aneurysm Expansion Using Longitudinal CT Images. Ann Biomed Eng **44**, 1502–1514